Title
Combustion Dynamics of Liquid Droplets and Turbulent Jets Relevant to Rocket Engines

Author
Plascencia Quiroz, Miguel Angel

Publication Date
2021

Peer reviewed|Thesis/dissertation

UNIVERSITY OF CALIFORNIA
Los Angeles

Combustion Dynamics of Liquid Droplets and Turbulent Jets Relevant to Rocket Engines

A dissertation submitted in partial satisfaction
of the requirements for the degree
Doctor of Philosophy in Mechanical Engineering

by

Miguel Angel Plascencia Quiroz

2021

ABSTRACT OF THE DISSERTATION

Combustion Dynamics of Liquid Droplets and Turbulent Jets Relevant to Rocket Engines

by

Miguel Angel Plascencia Quiroz
Doctor of Philosophy in Mechanical Engineering
University of California, Los Angeles, 2021
Professor Ann R. Karagozian, Chair

These experiments examined the reactive processes involving nanoparicle laden liquid droplets, and turbulent jet flames as two separate sets of studies. The first part of this dissertation (Chapters 2 and 3) deals with the combustion of ethanol liquid droplets loaded with nano particulate additives using different droplet formation methods. For this study, an apparatus at the Energy and Propulsion Research Laboratory at UCLA was used to keep the droplet in a quiescent environment. Three different types of droplet combustion experiments were performed, involving: (I) the classic single droplet suspended from a quartz fiber, (II) a single droplet suspended from a quartz capillary, (III) a burning droplet that has continual fuel deliver to sustain the droplet for longer periods of time during the combustion process. Two alternative nanoparticles were explored to demonstrate the effect of energetic additives: reactive nano aluminum (nAl) and inert nano silicon dioxide ($nSiO_2$), each having nominal average diameters of 80 nm. Simultaneous high speed visible and OH* chemiluminescence images were taken to determine the shape of the droplet over time and hence the burning rate constant (K), flame standoff distance (δ_f), and mean OH* chemiluminescence intensity (I_{mean}) with varying particulate concentrations. Visible imaging showed particle/vapor

ejections and jetting in continuously fed droplet experiments, while rod-suspended burning droplets showed limited particle ejection, usually towards the end of the droplet lifetime. The $nSiO_2$-laden, rod-suspended droplets formed a porous, shell-like structure resembling the shape of a droplet at higher $nSiO_2$ concentrations, in contrast to smaller residue structures left for nAl-laden droplets. A systematic increase in the burning rate constant was observed as the loading concentration of nAl was increased from 1wt%-6wt%. The droplet with continual fuel delivery had the greatest improvement in K of 13% over the pure fuel value. For $nSiO_2$, the continuously fed droplet showed the greatest increase of 5% at 1 wt% loading concentrations, and no consistent trend was observed for $nSiO_2$, likely due to the large shell-like residue structures in the latter stages of combustion. Transmission electron microscopy (TEM) images of particle residue revealed additional insights.

The second part of this dissertation (Chapters 4 and 5) studied reacting gaseous turbulent jets in a newly constructed experiment at the Air Force Research Laboratory (AFRL/RQR) located at Edwards Air Force base. This experimental study aimed to characterize the coupling of an acoustic field with a turbulent gaseous methane nonpremixed flame under atmospheric pressure conditions. Two separate injection configurations were examined: one that involved a classic single methane jet surrounded by a minimal velocity oxidizer co-flow and a second coaxial jet configuration with annular oxidizer flow and the same low-velocity co-flow. The different jets were placed within an acoustic waveguide in which standing waves could be created using several speakers. The reacting jets could thus be situated at either a pressure node or a pressure anti-node location. High-speed Schlieren and OH* chemiluminescence images recorded the near field behavior of the flame under both unforced and acoustically forced conditions. High-speed imaging showed two different phenomena associated with these standing waves. When the flame was forced while situated at a pressure node, a sinuous oscillatory response of the flame was observed, in addition to transverse oscillations of the center fuel jet, which shortened the intact fuel core length. The flame "flattened" into an ellipsoidal shape in the direction of the acoustic waves. Conversely, at

a pressure anti-node, the coupling of the acoustics and flame gave rise to an axisymmetric response (puff-like oscillations), which prompted the flame to become unstable at the anchoring region. This could lead to periodic liftoff or permanent flame liftoff.

A receptivity study for a methane jet at Reynolds number of 5,300 and an ambient oxygen concentration of 40% showed that the reacting jet was able to respond at the frequency of the unsteady acoustic field for a range of frequencies, but with a diminishing response of the flame for both the pressure node and the pressure anti-node under high frequency excitation. Proper Orthogonal Decomposition (POD) analysis was able to extract mode shapes and frequencies based on pixel intensity fluctuations. For the cases of pressure node forcing, this analysis method illustrated the different modes of flame oscillation, in many cases which were similar to corresponding low Reynolds number fuel jet experiments with pressure node excitation conducted at UCLA. A forcing susceptibility diagram was created to map the three different anchoring stability regimes the flame experienced under pressure anti-node forcing, demonstrating the need for higher amplitude excitation required for the flame to lift off when forced at higher frequency pressure anti-node conditions.

As an extension to the single jet, the shear coaxial jet configuration kept the center fuel and surrounding oxidizer co-flow constant. Only the outer annular oxidizer flowrate was varied, with annular-to-inner jet velocity ratios ranging from R = 0.05 to 0.3, to investigate its impact on the flame's ability to respond to the acoustics. In the absence of acoustic excitation, the coaxial jet did demonstrate natural shear layer/wake like instabilities at higher annular-to-jet velocity ratios, for R = 0.17 and 0.3. The dynamical response of the coaxial jet to pressure node excitation exhibited similar characteristics to that of the single jet for a range of forcing frequencies. But when forced at a pressure anti-node, a notable difference between the two configurations was found. The shear coaxial jet was more responsive to the acoustic forcing at higher forcing frequencies, for example, than the single fuel jet. The susceptibility diagrams for the full range of annular-to-inner jet velocity ratios demonstrated opposite trends when compared to the single jet, that is, that the coaxial jet

was more responsive to excitation at a given excitation amplitude when the forcing frequency was higher, and thus closer to the natural coaxial jet instability frequency. Hence evidence suggests that the natural instabilities of the coaxial jet shear layer may be causing the difference in susceptibility diagrams.

Both sets of experimental studies here, the nanofuel droplet combustion studies and the acoustically-coupled turbulent fuel jet combustion experiments, provide useful advances to our understanding of reactive flows relevant to liquid rocket engine systems. Enhancement in burning rates with nanoparticulate additives show potential benefits for rocket fuels, and attendant benefits are documented in the presence of acoustic disturbances, studied separately [1]. AFRL-based acoustically coupled turbulent fuel jet studies reveal different dynamical characteristics, depending on the injection system and the acoustic frequency and amplitude range. Different characteristic signatures extracted via POD analysis are both relevant in understanding combustion instabilities and in developing reduced order models underlying control of such instabilities. The present studies contribute to these goals in important ways.

The dissertation of Miguel Angel Plascencia Quiroz is approved.

Adrienne Lavine

Jeff Eldredge

Mitchell Spearrin

Douglas Talley

Ann R. Karagozian, Committee Chair

University of California, Los Angeles

2021

To my parents

TABLE OF CONTENTS

LIST OF FIGURES

LIST OF TABLES

Nomenclature

a	Semi-major axis of ellipse
b	Minor axis of ellipse
c	Speed of Sound
d	Droplet diameter
d_0	Initial droplet diameter
$\dot{d}$	Time derivative of droplet diameter
d_{eqvs}	Equivalent volume of a sphere diameter of the droplet
δ_f	Flame standoff distance
f_a	Resonant frequencies
G	Rayleigh index
I_{mean}	Mean OH* chemiluminescence intensity
K	Burning rate constant, units of mm^2/s
$K_{non-fed}$	Classic single droplet burning rate constant
K_{fed}	Continuously fed single droplet burning rate constant
λ	Wavelength associated to resonant frequencies
$\dot{m}$	mass flowrate
MR	Mass ratio (Annular-to-inner jet)
PAN	Pressure anti-node
PN	Pressure node
p'	Pressure oscillation amplitude
p'_{max}	Pressure oscillation amplitude at pressure anti-node
q'	Heat release oscillation amplitude
R	Velocity ratio (Annular-to- inner jet)
$Re_{1,2}$	Reynolds number based on diameter
T_{bp}	Boiling temperature

T_{vol} Volatilization temperature

u' Velocity oscillation amplitude

u'_{max} Velocity oscillation amplitude at pressure anti-node

ACKNOWLEDGMENTS

First I am extremely grateful to my advisor Professor Ann Karagozian for her invaluable advice, continuous support, and patience during my PhD study. She provided me the opportunity to join her lab at UCLA, where I was able to establish a foundation of my experimental skills and fundamental combustion knowledge. Her guidance was not only through scientific research but also on personal and career growth. I am thankful for the experiences I obtained while being part of her research group. I am equally as grateful to my second advisor Dr. Douglas Talley who guided my research at the Air Force Research Laboratory (AFRL). He entrusted me with designing and building a new experiment in his laboratory. Due to this experience, I was able to learn an invaluable amount of engineering knowledge that I would otherwise not have. He always emphasized scientific education and research which enabled the completion of my graduate studies. Thanks to these opportunities I feel ready and capable of conducting research in any laboratory setting in the future.

I would like to offer a special thank you to Dr. John Bennewitz, Dr. Hyung Sub Sim, and Dr. Mario Roa. I had the pleasure of conducting research alongside each one of them at different periods of my graduate studies. The scientific knowledge and experimental skills they passed onto me helped shape the engineer that I am today. I am grateful not only for the mentorship but also for the friendships that we built. Additionally, I want to give a special thanks to Professor Owen Smith for all his advice related to the droplet combustion experiment; especially when I started to handle nanoparticles and create fuel mixtures with them. I would also like to express my sincere gratitude to Randy Harvey, an experienced technician at AFRL. When I first got to AFRL my hands-on skills were limited to say the least, but Randy taught me the necessary skills to be able to design, build, and machine facility components. His patience with me is truly admirable. Another technician who I would like to thank is David Hill, who helped me order a lot of the component I needed early on. I am also grateful to all the brilliant members in the UCLA Energy and

Propulsion Research Laboratory. I had the opportunity to work alongside: Andres Vargas, Dario Valentini, Takeshi Shoji, Andrea Besnard, Elijah Harris, Richard Abrantes, Ayaboe Edoh, Stephen Schein, Mathias Ross, Rosa Padilla, Salvador Badillo Rios, Jonathan Tran, Daniel Kerr, and David Ren. The group had a collaborative and supportive environment which made daily life in the lab enjoyable.

Without the support and encouragement of my family, it would have been impossible for me to complete my PhD. First I want to thank my parents, who gave me a great childhood in which education was always promoted. The work ethic and sense of responsibility that they taught me early on in life has been essential to my success. Special thanks to my two older sisters, who have been great role models since my early childhood. Also thanks to my brother who has always boosted my spirits and been a friend I could spend time with to escape from my research.

Lastly, I am thankful for the Eugene V. Cota-Robles Fellowship I received from the UCLA Graduate Division, which supported my graduate school studies for two academic years. Additionally, this research has been supported by the AFRL-UCLA Educational Partnership Agreement 16-EPA-RQ-09; the Air Force Office of Scientific Research (Dr. M. Birkan, Program Officer); ERC, Inc. (subcontract PO PS180038); and Jacobs Tech, Inc. (subcontract RAPT1-0000000003).

VITA

2011–2015	Chancellor's Excellence Scholar, UCI
2013–2014	Undergraduate Student Researcher, Lasers, Flames, and Aerosols Research Group, UCI
2014–2015	Mechanical engineer intern at Parker Aerospace, Irvine, CA
2015	B.S., Mechanical Engineering, UCI
2015-2016	Eugene V. Cota-Robles Fellowship, UCLA
2015-2018	Graduate Student Researcher, Energy and Propulsion Research Laboratory, UCLA
2017	M.S. in Mechanical Engineering, UCLA.
2018-2019	Eugene V. Cota-Robles Fellowship, UCLA
2018	Boeing Fellowship, UCLA
2018-2021	Graduate Student Researcher, AFRL, Edwards AFB, CA

PUBLICATIONS AND PRESENTATIONS

H. S. Sim, M. A. Plascencia, A. Vargas, and A. R. Karagozian, *Acoustically Forced Droplet Combustion of Liquid Fuel with Reactive Aluminum Nanoparticulates*, Combustion Science and Technology, Vol. 192, pp. 761–785, 2019.

H. S. Sim, M. A. Plascencia, A. Vargas, J. W. Bennewitz, O. I. Smith, and A. R. Karagozian, *Effects of Inert and Energetic Nanoparticles on Burning Liquid Ethanol Droplets*, Combustion Science and Technology, Vol. 191, pp. 1079-1100, 2018.

J. W. Bennewitz, D. Valentini, M. A. Plascencia, A. Vargas, H. S. Sim, B. Lopez, O. I. Smith, and A. R. Karagozian, *Periodic partial extinction in acoustically coupled fuel droplet combustion. Combustion and Flame*, Vol. 189, pp. 46–61, 2017.

M. A. Plascencia, M. Roa, A. R. Karagozian, D. G. Talley, *Turbulent Nonpremixed Jet Flames under Transverse Acoustic Forcing*, 2020 AIAA Propulsion Energy Forum, Virtual, August 2020.

M. A. Plascencia, H. S. Sim, A. Vargas, O. I. Smith, A. R. Karagozian, *Effects of Energetic and Inert Nano Particles on Burning Liquid Ethanol Droplets*, 70th Annual Meeting of the American Physical Society Division of Fluid Dynamics, Denver, CO, November 2017.

M. A. Plascencia, J. W. Bennewitz, A. Vargas, H. S. Sim, O. I. Smith, A. R. Karagozian, *Periodic Partial Extinction Regime in Acoustically Coupled Fuel Droplet Combustion*, 69th Annual Meeting of the American Physical Society Division of Fluid Dynamics, Portland, OR, November, 2016.

CHAPTER 1

Introduction and Background

Chemical propulsion is the current method of choice used by almost all rocket launch vehicles. Chemical propulsion systems can be liquid rocket engines (LREs), solid rocket motors (SRMs), or hybrid engines (solid fuel with liquid or gaseous oxidizer). Of these, LREs have been the main engine for the core stages of launch vehicles because of their higher performance (i.e., specific impulse I_{SP}, which is the thrust scaled by the weight flow rate of the exhaust, in units of time) and controllability during operation. Performance of these LREs highly depends on the combustion chamber processes such as injection, atomization, vaporization, mixing and ignition of the propellants. Like most chemical reacting systems, LREs have challenging combustion related problems that have been continuously worked on since early liquid rocket engine development [2, 3, 4, 5]. This is especially the case for hydrocarbon-fueled LREs, which are known to have greater problems with combustion instabilities than hydrogen-fueled LREs, and with the advent of an increasing proportion of hydrocarbon-fueled US launch vehicles, an understanding of such instabilities is increasingly important.

This study contributes to the field by investigating various aspects of combustion chamber processes, especially with respect to combustion-acoustic coupling. Part one was a set of experiments conducted at the UCLA Energy and Propulsion Research Laboratory which investigated the combustion of liquid fuel droplets as part of a larger study involving combustion-acoustic interactions in a small scale, atmospheric waveguide. The liquid droplets were loaded with nanoparticles, used as a fuel additive, to investigate vaporiza-

tion (burning rate) characteristics. Part two was conducted at a new facility at Air Force Research Laboratory at Edwards AFB where jet flames of various geometries were subject to acoustic forcing. This study focused on the injection and combustion processes related to liquid rocket engines, specifically the coupling phenomena of acoustic fluctuations and a reacting jet.

1.1 Liquid Rocket Engines

Historically LREs have been primarily used for launch vehicles that take different types and sizes of payloads into earth's orbit or space. Since the initial space launches in the late 1950's, rockets have been used for space exploration, satellite deployment (communication and weather), and for military missions [6]. Depending on the requirements of the mission these launch vehicles can have multiple stages, each with their own propulsion system. As previously stated, liquid rocket engines typically achieve high specific impulse (I_{SP}) as well as high thrust as compared to solid or hybrid engines which is why they are chosen for larger payload missions. With the higher performance comes a more complex system with more components. Some of the additional components include tanks, valves, turbomachinery, and relatively elaborate combustion/thrust chambers. See figure 1.1 for more details.

The goal of an LRE is to generate thrust to move the rocket which is held stationary on the ground by earths gravitational field. To produce thrust the propellants carried by the rocket must chemically react inside the chamber to convert the chemical potential energy into thermal enthalpy. Temperatures in the combustion chamber can be between 2500 C to 4100 C (2773 K-4373 K). The thermal enthalpy expands the combustion products through the nozzle to convert the thermal enthalpy into kinetic energy. In the nozzle the hot gases expand and can reach velocities anywhere from 1800 to 4300 m/sec at the exit [6]. The expelled exhaust gases produce thrust which can be explained by newtons third law; where the rocket pushes on the gas, and the gas in turn pushes on the rocket. The research topics

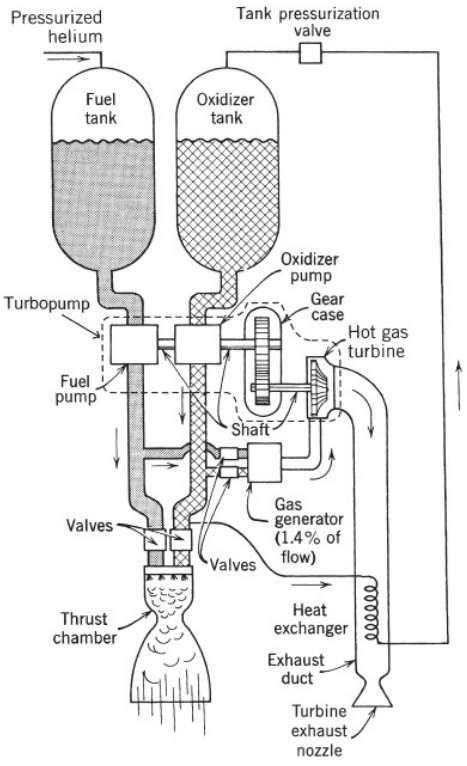

Figure 1.1: Propellant delivery system for typical liquid rocket engines: taken and edited from [6].

of this study are related to the combustion processes that occur inside the thrust chamber. Therefore, the focus will be on the combustion chamber processes: injection, atomization, vaporization, mixing and combustion of the propellants. Along with these topics, combustion dynamics in the combustion chamber resulting in combustion instabilities will be reviewed.

1.1.1 Injection Systems

In operation the liquid propellants enter the thrust chamber through the injector plate first. Injectors plates are designed specifically to create uniform atomization and mixing over the chamber cross section, although the mixture ratio can be biased rich near walls. Historically injector plates consisted of hole patterns that introduced the fuel and oxidizer separately. Many injector designs consist of individual cylindrical elements that are assembled into arrays on the injector plate. In this injection scheme, each injector element is equipped

with an inner and outer flow path for the fuel and oxidizer, where a difference in velocity exists between the propellant flows. Typical configurations included classic straight coaxial injectors, swirl coaxial injectors, and impinging coaxial injectors; in liquid rocket engines the oxidizer typically flows through the inner path and fuel flows through the outer flow path. Both liquids and gases have historically been used in the inner and outer flows, depending on engine requirements. Here attention is given to the case where the inner flow is liquid oxygen and the outer flow is gaseous hydrogen. This differential velocity causes a shearing between the flows which helps to break up the oxygen stream into small droplets [6].

1.1.2 Atomization

As the propellants enter the combustion chamber atomization must begin in order to have sufficient time for combustion. The injectors are design specifically to promote atomization by creating a turbulent shear layer between the two different density fluids, which also makes it susceptible to hydrodynamic instabilities. Depending on the injector design, the jets produced could be unstable naturally or the injector exit could cause flow instabilities. To breakup the liquid jets some sort of instability in the propellant streams must occur [4]. Atomization is achieved when thin liquid sheets are formed which subsequently become unstable and then break up to form ligaments and large drops, which then break down further into small droplets [7]. It is important to note that the atomization process described applies to subcritical propellant injection. When the propellant is supercritical there is no definitive atomization process. It becomes difficult to distinguish the difference between gaseous and liquid phases of the flow.

1.1.3 Vaporization

Vaporization in LREs can be described as droplet gasification and diffusion. Similarly to atomization, vaporization is another process that only occurs during subcritical propellant

injection. Vaporization rates are influenced by turbulence, pressure or temperature oscillations and acoustic waves. Evaporation of droplets occurs as heat release from the nearby reactions cause the droplet surface to heat up through radiation, convection, and conduction heat transfer. The liquid evaporates when the droplet surface approaches its boiling temperature. The droplet surface must vaporize at a rate rapid enough for efficient Fuel-oxidizer mixing to occur for combustion [8, 9, 10].

1.1.4 Mixing

Mixing of the fuel and oxidizer propellants is the step before combustion. With the oxidizer and fuel now in the same phase after vaporization the last step is to mix the two. In LREs the propellant flows are turbulent in all locations of the combustion chamber. Thus, molecular mixing takes place through turbulent mass diffusion of the fuel and oxidizer towards each other from regions of high to low species concentration [11]. Concentration gradients will form locally on either side of the chemical reaction zone. Adequate mixing is essential to sustain combustion for the entirety of the engine operation.

1.1.5 Combustion

The final step for the propellants is to undergo sustained combustion for the desired time of operation. After successful ignition, the chamber contains heterogeneous zones containing liquids, vaporized propellants, and areas of chemical reactions characterized by chemical oxidation of the fuel. As breakdown of propellant chemicals into smaller fractions and simpler chemicals transpire, rapid chemical reactions occur at increasingly higher temperatures. The high temperature will quickly vaporize any remaining liquid droplets through convective heating, and turbulent diffusion continues to mix pockets of fuel-rich and fuel-lean gases. Reaction zones inside the chamber are characterized by high heat release. Even with precise design of the injectors, uniform combustion inside the chamber is never quite achieved, and

is often not desired to maintain chamber walls relatively cool. Because of these pockets of fuel rich or fuel lean mixtures, fluctuations of heat release will be present and could stimulate potential instabilities inside the chamber [6, 12].

1.2 Droplet Combustion

Individual burning droplets have been investigated as a basis of fundamental combustion studies for decades [13, 14, 2, 15, 16]. Combustion of a droplet represents a heterogeneous reactive process involving condensed phase combustion. This simple model can help understand the characteristics of current and future fuels used by LREs. Injectors for these systems are designed to create liquid sprays consisting of droplet groups which typically burn as a collection. Before trying to understand how the collection burns the combustion of a single droplet is required. Several physical and chemical phenomena are involved in the combustion of a single droplet, which involve fluid dynamics, chemical reactions, and heat transfer.

In most practical systems, fluid motion arises from the flow field surrounding the droplet as well as the inertia of the droplet itself. In contrast stationary droplets, in the laboratory under gravity, establish natural motion of the surrounding fluid through buoyancy forces. As the droplets enter the combustion zone (or heat source) heat transfer to the droplet increases vapor pressure and the liquid evaporates into the gas phase and diffuses outward creating a flame zone. A non-premixed flame encompasses the liquid droplet with the fuel vapor on the inside reacting with the surrounding oxidizer. This category of flames is limited by the diffusion speed of the oxidizer and fuel towards the reaction zone. Since the oxidizer and fuel are entering the reaction from opposite sides, the flames contain both fuel lean and fuel rich regions. Figure 1.2 illustrates the different mechanisms described here.

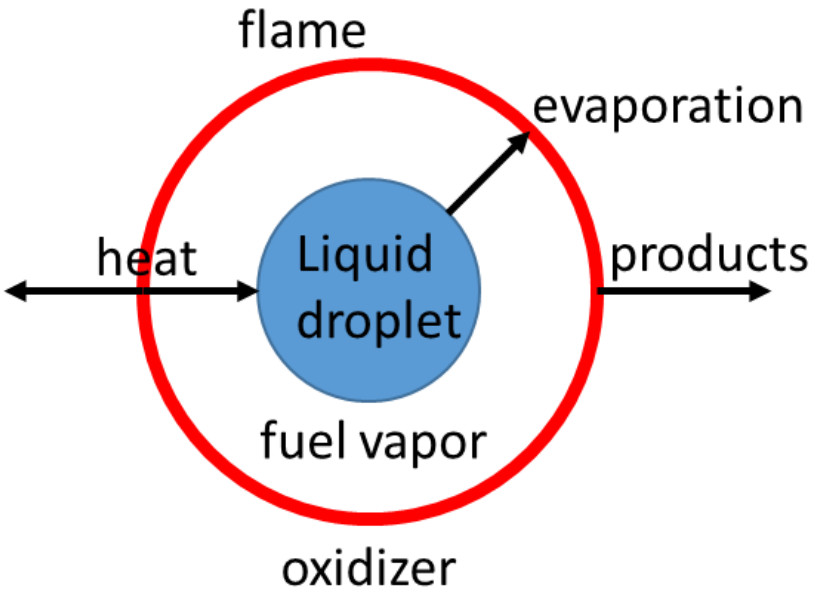

Figure 1.2: Physical and chemical processes of a burning droplet [17].

The rate at which the surface of the droplet regresses is predominantly dependent on the transport and thermodynamic properties of the liquid fuel and surrounding ambient gas, and it is often quantified by the well-established d^2 law [10, 11, 18]. This equation may be derived from the continuity equation by which mass is lost from a spherical droplet of initial diameter d_0, resulting in the variation in droplet diameter d(t) over time, indicated by the following equation,

$$d^2(t) = d_0^2 - Kt. \tag{1.1}$$

Equation 1.1 holds after the initial transient period associated with ignition and heating of the droplet [17]. During quasi-steady droplet burning the equation represents a linear relation between the droplet diameter squared (surface area) vs time. The slope (K) is known as the burning rate constant and has units of mm^2/s. The d^2 law has been shown to accurately describe spherical droplets burning in micro-gravity [19, 20] and semi-spherical droplets in normal gravity [13, 14, 15, 21, 22], but in the latter case the length scale associated with

the oblong droplet should be corrected. There are various methods in the literature used to calculate the equivalent diameter to replace the sphere-based diameter in the d^2 law [23]. One method is a diameter based on the equivalent area of a circle (d_{eqac}), defined by the diameter of a circle which has the same projected area (A_P) as that of the imaged droplet, Eqn. 1.2. Another method is the diameter based on the equivalent volume of a sphere (d_{eqvs}), the diameter of a sphere which has the same volume as that of the body of revolution of the droplet image about its vertical axis, Eqn. 1.3.

$$d_{eqac} = \sqrt{4A_p/\pi} \tag{1.2}$$

$$d_{eqvs} = \sqrt[3]{6V/\pi} \tag{1.3}$$

Historically three different experimental methods have been used to study fundamental physics of droplet combustion. The three methods are fiber suspended droplets, an array of falling droplets, and a porous sphere that has fuel feeding the surface continuously [17]. Fiber suspended droplets in a controlled environment (usually surrounded by stationary gas) allows for easy probing of the droplet regression, but the intrusion of the fiber can cause heat loss and changes in the droplet shape (i.e. away from spherical). In the case of falling droplets, the disadvantages of the fiber are removed and droplet size can be evaluated via optical imaging. But probing the droplet instantaneously becomes more difficult and convective heat transfer is introduced for falling droplets. Lastly, the porous sphere allows for a true quasi-steady burning of the droplet and probing for long periods of time but once again the droplet is affected by the presence of the sphere and the dynamics associated with the regression of the droplet cannot be studied. Porous sphere experiments are mainly for the study of gas phase processes.

1.2.1 Fuel Additives

Recent advances in nanoscale materials have revived the desire to explore liquid fuels laden with energetic nanoparticles (nanofuels). The use of these nanofuels containing reactive, energetic, and/or catalytic nanoscale additives is thought to have the potential to improve combustion characteristics by modifying the base fuels' physical and chemical properties. Materials such as magnesium, aluminum, boron, titanium, and others have been manufactured to form particles with diameters in the 1-100 nm range. Enhanced properties such as increase volumetric energy density, shortened ignition delays, higher volumetric heat release rates, and enhanced thermal conductivity are suggested to be present in these energetic nanoparticles [24, 25].

The potential benefits of nanoscale particles compared to micron scale and above are: 1) nanoparticles offer a significantly larger surface area to volume ratio, which theoretically corresponds to enhanced reactivity and 2) decreasing particle size generally provides lower ignition temperature and energy. Surface atoms can have different thermo-physical and electrical properties compared to the bulk atoms, thus with small enough particles the properties of the surface atoms can dominate the overall particles' properties. There is a limit to how small these metal particles can be in order to take advantage of the enhanced properties, because the metal oxide layer is a few nanometers thick (3 nm). When this layer constitutes a large mass fraction of the nanoparticle then the properties of the particle are no longer that of the metal core but that of the metal oxide [25].

Metal combustion can transpire in the vapor phase or as a heterogeneous process. For a metal to burn as a vapor the oxide volatilization temperature must be greater than that of the metal boiling temperature, otherwise it will burn heterogeneously on the surface [8]. This is known as the Glassman Criterion temperature. Table 1.1 show the volatilization (T_{vol}) and boiling temperatures (T_{bp}) for a few different metals and their oxides. For aluminum T_{vol} is greater than T_{bp} and according to the Glassman criterion this metal will burn in the

vapor phase with a detached diffusion flame.

Metal	T_{bp} [K]	Oxide	T_{vol} [K]
Mg	1366	MgO	3430
Al	2791	Al_2O_3	4000
B	4139	B_2O_3	2340
Ti	3631	Ti_3O_5	4000

Table 1.1: Physical Properties of Metal and Metal oxides [8]

Recently there have been numerous fundamental droplet combustion studies focusing on nanofuels using a variety of liquid base fuels and additive mixtures. In terms of the nanoparticles the following materials have been studied; aluminum [26, 27, 28, 29, 30, 31, 32, 33], boron and iron [34], magnesium oxide [35, 33], carbon-based particles [36, 37, 38, 33], and titanium dioxide [39, 40]. These metallic nanoparticles are theorized to enhance combustion by increasing the energy density of the base fuel. A common approach taken to measure the impact of these nanoparticles on the burning characteristics is by determining the burning rate constant K of the different nanofuels.

Aluminum nanoparticles (nAl) have been studied as potential liquid fuel additives by multiple research groups for their high reactivity and catalytic properties. For example, Tanvir et al. studied a stream of falling droplets on the order of 200-400 microns, where the nanofuel was composed of ethanol and aluminum nanoparticles (nAl) [28]. Their results showed that the burning rate constant (K) increased as the loading concentrations of nAl with a maximum enhancement in the burning rate constant over the pure ethanol case of 140%, observed for 5wt% nAl loading concentration [28]. Another set of results by Pfeil et al. looked at fiber suspended droplets for the addition of nAl to ethanol and JP-8. The addition of 1wt.% nAl to ethanol gave a 10 % increase in K and 1wt% nAl in JP-8 had no effect on K [26]. Javed et al. tested kerosene droplets containing 0.1%, 0.5%, or 1.0% nAl at elevated temperatures (400-800 $^{\circ}C$) [30]. The nAl laden droplets exhibited disruptive behavior of the

burning droplet causing reduced ignition delay, lowered minimum ignition temperature, and the burning rates were enhanced. The work presented later on in the results section has been published which shows droplet combustion experiments with 1.3-1.9 mm diameter ethanol droplets exhibit moderate increases (10%) in K at increasing nAl loading concentrations, up to 6 wt.% [32]. This work is consistent with the previously mentioned work by Pfeil et al. in 2010.

Not all experimental results have been favorable when adding energetic nanoparticles to liquid fuels; some have been neutral, and others have reported negative impact on the burning characteristics. The difference in findings can be largely attributed to the different types of experiments and different additives-fuel combinations. Guerieri et al. performed falling droplet experiments to compare the effects of nAl with that of nAl plus nitrocellulose particles through a comparative analysis of kerosene that had a surfactant for suspension stability (TOPO) [31]. In contrast to other observations, a reduction of 12% in K was reported when 6.1wt. % nAl was added to a kerosene droplet. The nature by which nanoparticle agglomerates/aggregates and their structural geometry within the droplet are thought to cause a wide range in the observed values of K. A comprehensive study by Bennewitz et al. looked at various energetic nanoparticle, including nAl, in RP-2 and ethanol. In general, the findings were not significant in enhancing the burning rate constant or reducing ignition delays in rod suspended droplets. The loading concentrations were taken as high as 6 wt.%; most of the particle burning was seen at the end of the droplet lifetime. The enhanced particle burning at the end of the droplet was also seen by Pfeil et al. (2010) and Sim et al. (2018).

Other experiments exploring nanofuels have involved synthesizing nanoparticles or using nanoparticles with different properties other than metals. Javed et al. studied the effects of coating nAl particles with oleic acid. This was done for fiber suspended burning heptane [29] and kerosene [30] droplets at elevated temperatures. Their results reveal a significant increase in K in a high temperature environment for both fuels. In a second study, Pfeil et al.

added ammonia borane to ethanol for combustion of fiber suspended droplets. An increase of up to 16% is observed in the value of K but the burning behavior from combustion with nAl. The droplet experiences expansion and contraction, ultimately shattering and atomizing into smaller droplets [41], in contrast to more systematic regression of the nAl-laden droplet surface before the influence of agglomerate becomes large.

Lastly, some experiments have investigated how nanoparticle laden fuels can be used to control combustion dynamics in liquid rocket engines. First it is important to look at the natural instabilities that arise in nanoparticle laden droplets. Instabilities could arise in the suspension of NPs in fuel droplets due to inhomogeneities in the fuel mixture as well as heterogeneous bubble nucleation associated with a surface reaction of NPs [42]. Such instabilities, including droplet deformation (in a swell-shrink cycle), along with flame perturbations due to micro- explosions and/or ligament/jet formation, have been observed in many studies for nano- fuel droplets. Recent studies have explored the initiation mechanisms of these natural instabilities and coupling between the phenomena and burning processes for NP-laden fuel droplets [40, 43, 44]. In terms of combustion dynamics control in LREs one study looked at ammonia borane (AB) as an additive in ethanol fuel [45] to study the effect on a variable resonance combustor. The results surprisingly showed a bimodal heat release distribution when the liquid fuel was composed of 6wt.% AB. This significantly altered the stable combustion range by making the system unstable over a wider range of geometric configurations. A study by our group looked at acoustically coupled nanofuel droplets with ethanol as the base fuel and nAl as the additive. Acoustic excitation allows droplets with nAl additives to burn for longer periods of time than in the absence of acoustics, likely due to a reduction in particle agglomeration as well as a suppression of particle jetting observed in the absence of acoustic excitation. Additionally, improved resistance to acoustic excitation, along with an increase in mean flame extinction strain rate of burning nanofuel droplets (by up to 44%). These findings suggested several potential benefits for nAl particle additive for LRE applications.

1.3 Combustion Instabilities

The occurrence of combustion instabilities in LREs continues to pose significant challenges due to the complex and nonlinear nature of turbulent combustion and multi-phase processes. High frequency combustion instabilities are considered to be the most destructive and are usually characterized by well-defined frequencies and mode shapes corresponding to the natural acoustic modes of the chamber [3]. A combustor theoretically has an infinity of resonant acoustical modes with corresponding resonant frequencies, but enhanced losses tend to attenuate the higher frequencies. Naturally, combustion chambers experience random background noise (smooth combustion) due to chemical reactions and gas expansion. When pressure amplitudes exceed the average noise amplitude it is said to be combustion instability, or in some cases, rough combustion. Combustion instabilities are considered to be present when pressure fluctuations during operation exceed $\pm 5\%$ of the mean chamber pressure. The instabilities are characterized by well-defined periodic pressure peaks that may be continual, may amplify, or dampen [6, 2].

Classification of combustion instability can be done through the frequency at which they are oscillating. The first category are low frequency instabilities less than 400Hz. They are termed "chugging" instabilities. Interactions between the propellant feed system and the combustion chamber can create these low frequency instabilities. The second category of instabilities are in the intermediate range of frequencies between 400Hz-1,000Hz and commonly related to vibrations of the engine structure but can also be caused by combustion processes. Lastly, high frequency instabilities (above 1,000Hz) are known to be the most destructive type. They are linked to combustion processes and chamber acoustical resonance modes [6].

The unsteady heat release associated with combustion can be thought of as an acoustic source which propagates sound disturbances throughout the combustor. The pressure waves travel across the chamber and reflect off the walls to make their way upstream to the injector

plate. Therefore, incoming flow is perturbed and further causes mass flow and heat release oscillations. This process could be thought of as a feedback cycle, as shown in figure 1.3, where flow/mixture perturbations create unsteady oscillations in the heat release rate, which in turn trigger acoustic oscillations that disturb the flow.

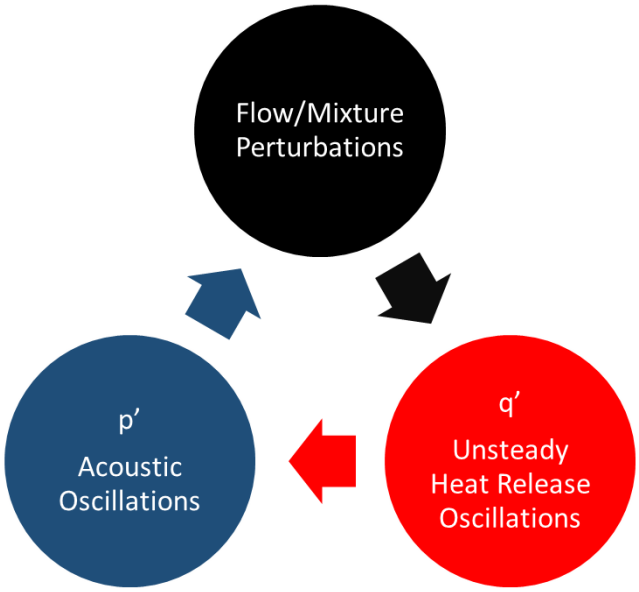

Figure 1.3: Thermo-acoustic Feedback Cycle

During the combustion process if the timing between heat release and pressure oscillations is right it can increase chamber pressure amplitudes significantly. The Rayleigh criterion describes the coupling between pressure and heat release oscillations; when heat is given at the moment of the greatest condensation or taken at the moment of the greatest rarefaction, vibration is amplified. The opposite would cause vibrations to dampen [46]. In other words, when heat release oscillations and pressure oscillations are in phase, or nearly so, there is an amplification of the disturbance; if they are out of phase, the disturbance dampens. Combustion instabilities can be quantified mathematically over an acoustic period (T) by the following equation,

$$G = \frac{1}{T}\int_V p'q'dV, \tag{1.4}$$

where p' represents the pressure perturbations, q' represents the heat release oscillations, V is the volume of interest, and G is is the Rayleigh index. This equation is derived assuming only linear perturbations. When pressure and heat release fluctuations are nearly in phase it results in a positive G value indicating unstable combustion. Conversely when p' and q' are out of phase, G is negative, which is thought to denote stable combustion.

1.3.1 Longitudinal and Transverse Instabilities

High-frequency instabilities occur in two basic modes, longitudinal and transverse. A combination of longitudinal and transverse modes is also possible, but not as common. These instabilities occur at frequencies greater than 1,000 Hz and generally involve excitation of acoustically resonant chamber modes. They can rapidly amplify to destructive magnitudes. Large acoustic pressure and velocity fluctuations are contained throughout the chamber. An oscillatory source of energy is required for sustaining an instability. For high frequency instabilities, this energy must come from the propellant combustion and can be only weakly dependent upon the feed system [2].

Longitudinal modes occur along the axial direction of the chamber. They depend on the boundary conditions on the upstream and downstream interfaces (e.g. injector and converging nozzle entrance). Because pressure waves are reflected off the boundaries and travel though the combustion zone, natural dampening of these waves occurs making them less harmful. However, longitudinal instabilities can still occur in LREs and are important to consider during the design of these engines.

Transverse modes are defined by the cross-sectional geometry of the chamber. For cylindrical chambers, they can be broken down into radial and spinning tangential and standing tangential modes. Spinning tangential modes travel clockwise or counterclockwise around the chamber at the instability frequency. This waveform contains a constant amplitude as it races around the combustion chamber. These modes have circular pressure node lines oriented orthogonal to the radial axis of the combustor. Standing tangential modes are char-

acterized by a waveform with fixed node(s) locations fluctuating amplitudes. These waves have the velocity perturbation 90° out of phase with the pressure in the space dimension. Combinations of transverse and longitudinal modes may also occur. The combination of modes will have nodes lines that split the chamber cross section as well as node lines in the radial direction [2]. Refer to figure 1.4 for visualization of the first transverse modes of each type.

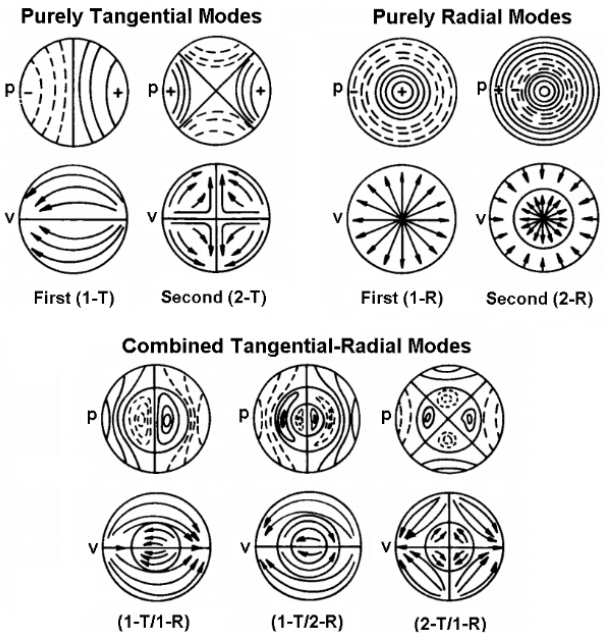

Figure 1.4: Acoustic Pressure and Velocity Distributions for Common Transverse Modes [2]

1.3.2 Historical example: Combustion Instabilities in F-1 Engines

One of the noteworthy cases of a rocket experiencing catastrophic combustion instabilities was in the development of Rocketdyne's F-1 engine for NASA's Apollo program. Five of these engines were used on the first stage of the Saturn V in from the mid-1960s to early 1970s. One of the major issues found during the first decade of developing this engine was severe failures due to combustion instabilities. In 1962 a program named Project First was

formed to develop a stable F-1 engine and to understand the parameters that make a LREs stable. A total of 2000 full-scale tests were conducted during Project First that focused on injection patterns and baffle configurations [2].

After approximately 3200 full-scale tests of the F-1 engine an appropriate injector design and baffle pattern was found that kept the engine stable. The baffles minimize any influential coupling and amplification within the chamber particularly with transverse oscillations [2]. These baffles protruded enough into the chamber to be effective, yet not so far that it would change affect the chamber performance. While these efforts delivered a stable combustor, it took many design iterations and full-scale tests to find a workable solution. It is important to note that the solution found for the F-1 engine was not a universal one. Different engines with different injectors and acoustic resonances will behave differently. Thus, a fundamental understanding behind the phenomenon of thermo-acoustic instabilities is vital to avoid costly liquid rocket engine development in the future.

1.3.3 Reacting Jets Exposed to Transverse Acoustic Excitation

Over the past few decades, researchers have studied the dynamic coupling between transverse acoustics and heat release oscillations in the near field of the injector with the goal of understanding the underlying physical mechanisms responsible for the high-frequency transverse mode instabilities. Small changes in injector geometry and associated flow field variables, including fuel–oxidizer velocity ratio, momentum flux ratio, injection temperature, and injection pressure drop, are found to have potentially significant effects on the overall stability of the engine. The focus of this section will be to highlight studies on gaseous flames under oscillatory pressure fields. Specifically, transverse forcing of jets in pressure nodes and pressure anti-node configuration will be discussed.

Several fundamental studies on gaseous non-premixed flames under transverse oscillatory pressure fields have been conducted in the past. For example, Ghosh and Diao [47, 48] investigated how varying parameters such as density, velocity ratio, and momentum flux

ratios of a shear coaxial flame affects its response to acoustics. The flame acoustic interaction was most significantly affected by the density ratio, which was varied by introducing noble gases to both the oxidizer and the fuel. Experiments by Sim et al. [49] with laminar micro jet flames exposed to transverse acoustic excitation suggest that as forcing amplitude increases, flame dynamics transition from weakly oscillatory combustion to full-scale flame coupling and lock-in to multi-mode flame dynamics, involving periodic liftoff and reattachment.

Transverse forcing of premixed burners have shown interesting flame dynamics that could be related to non-premixed flames. For example, Pun et al. [50] found that an aerodynamically stabilized flame is more susceptible to chamber acoustics compared to one that is stabilized by a bluff-body. In the low frequency range, the frequency-driven global Rayleigh index resulted in lower magnitudes for the bluff-body stabilized flame. O'Connor et al. [51, 52, 53] investigated the response of a premixed swirl flame to transverse acoustic excitation. Investigations included in phase and out-of-phase forcing of the acoustic field. In the near field the velocity fluctuations are dominant in the shear layer including the vortex roll-up. In-phase forcing disturbed the flame symmetrically and out-of-phase forcing created helical disturbances in the flame. In the downstream region the transverse acoustics motion takes over the flame. The conclusion of this work was that the unstable shear layer created by the swirl burner is highly susceptible to acoustic forcing, which has a significant effect on flame response. In a similar experiment Saurabh and Paschereit [54] subjected a swirl stabilized premixed flame to axial and transverse acoustic forcing. At low frequencies, the two different types of forcing produced qualitatively similar results characterized by axisymmetric fluctuations of the flame. Quantitatively the two forcing methods were different. The flame response to transverse forcing is higher than the response to axial forcing as seen through plotting the flame transfer function. Additionally, when the two forcing methods were turned on simultaneously, the flame responses were shown to be asymmetric. The authors attributed this to amplitude and phasing differences between the axial and transverse forcing.

It is important to discuss some of the findings related to forcing reacting gaseous jets up stream of the injector because they could be related to pressure anti-node forcing. For example, Juniper et al. [55] studied self-excited jet nonpremixed flames as well as low density jets. In the reacting cases, a large forcing amplitude was required in order for heat release to lock-in to the forcing frequency and to overcome natural instabilities. In a study of the well know Delft burner, Rocha et al. [56] introduced acoustic forcing to the burner to examine temperature and gas concentrations. It was found that the forced flames exhibited notable differences with unforced flames, such as altered flame liftoff dynamics. Chao and Jeng [57] found that forcing in the turbulent amplification regime of frequencies helped with flame stability and extended the blow-out limit. Work by Demare and Baillot [58] show a reduction in the liftoff height which they attribute to the enhanced mixing and disruption of the streamwise structures. Alternatively, Zheng et al. [59] looked at laminar premixed flames under acoustic excitation; their results showed that external excitation could promote periodic liftoff and reattachment of the flame.

Acoustically forced jets have revealed important dynamics in flame behavior that can be related to LRE. Fundamental studies such as the ones presented are still needed to test new injectors and fuels for future LRE development. With that in mind part two of this work looks to investigate flame-acoustic coupling.

1.4 Research Goals

Over the years, in the context of studying combustion instabilities relevant to pure liquid fuels, our research group at UCLA has utilized an experiment where fuel is continuously delivered through a thin capillary that forms a droplet on the tip and is maintained at roughly a constant diameter during combustion and is stabilized due to surface tension. This method allows for acquiring phase locked imaging and other localized data for a single burning droplet placed in an acoustic field, and this experiment has been done in both

micro-gravity [60] and normal gravity [61, 62]. Fuels such as Ethanol, Methanol, JP-8, and liquid synthetic fuels derived via the Fischer Tropsch process have been studied. Bulk flame deflection and alterations in droplet burning characteristics in the presence of standing acoustic waves (in the vicinity of either a pressure node or pressure anti-node) have been interpreted in the context of an acoustic radiation force from a quantitative perspective [63, 60]. Studies done by Rodriguez [64] and Teshome [65] in normal gravity explored droplet combustion response in acoustic environments established by both dual speaker and speaker-reflector configurations, with evaluation of acoustically- resonant combustion features such as burning rate constant and acoustic acceleration. Wegener [66] and Sevilla [67, 61] performed phase-locked OH* chemiluminescence imaging that revealed temporal coupling between the acoustic forcing and flame, enabling for the first time a local quantification of the Rayleigh index and ability to relate burning rate increases to the nature of the combustion-acoustic coupling. More recently, Bennewitz et al. [62] found for several alternative fuels (ethanol, JP-8, and Fischer-Tropsch) that high enough forcing amplitudes cause the diffusion flame around the droplet to experience periodic partial extinction and re-ignition caused by periodic straining of the flame.

Part one of this study looks at a systematic set of tests for nanofuel droplets burning in a quiescent environment at atmospheric conditions, to explore fundamental phenomena in the absence of acoustic perturbations. We are not only motivated by the reported benefits of nanofuels and contradictory findings reported in the literature, but we are also interested in finding ways to overcome some of the challenges such as their natural tendency to form aggregates which hinders homogeneity of the nanofuel. The goal in part one of this work is to look at different droplet formation methods and to study differences and similarities in perceived nanofuel droplet combustion behavior: the alternatives being the fiber suspended droplet, droplets suspended on a capillary, and droplet continuously fed via a capillary. Of the fuels explored by our group ethanol was used because nanoparticles can be suspended without the use of surfactants. The nanoparticles explored to date include reactive nano Aluminum

(nAl), as done by others in non-fed experiments, but also inert nano Silica (nSiO2), as a means of examining the effect of the actual dynamics of a nanoparticulate in liquid fuel as contrasted with its contribution to the fuel's energetic content. Several combustion parameters were explored here, including the burning rate constant, flame standoff distance, and OH* chemiluminescent flame intensity. These studies form the foundation for separate ongoing experiments involving the exposure of such nanofuel droplets to acoustic perturbations in normal gravity [68].

Part two of this work involved reactive gaseous jet experiments conducted at the Air Force Research Laboratory (AFRL). Our research group has performed acoustically coupled jet experiments for over a decade. In earlier experiments, non-reacting liquid nitrogen coaxial jets under transverse forcing were investigated. Parameters such as jet spread angle and dark core length were measured [69, 70, 71, 72, 73]. In a similar experimental setup, forced reacting jets were studied containing rocket relevant propellants, GO2/RP-2 or GH2/LOX. Acoustic-flame coupling was quantified by OH* chemiluminescence wave tracking [74, 75, 76, 77]. Current experiments examined turbulent nonpremixed flames created by shear coaxial jet configurations using gaseous methane and enriched air. The jet is situated at either a pressure node or pressure anti-node. The purpose of this study is to examine the dynamic coupling between flame and acoustics during the onset of combustion instability. Understanding the coupling and synchronization between flame and acoustics can give insight on the growth/decay of combustion instabilities per the Rayleigh criterion, with more contemporary analysis tools to explore the dynamics with the ultimate goal of controlling them.

CHAPTER 2

Nanofuel Droplet Combustion: Experimental Setup and Methods

The information presented in this chapter is taken with slight modification from the article: *Hyung Sub Sim, Miguel A. Plascencia, Andres Vargas, John W. Bennewitz, Owen I. Smith & Ann R. Karagozian (2018): "Effects of Inert and Energetic Nanoparticles on Burning Liquid Ethanol Droplets", Combustion Science and Technology, DOI: 10.1080/00102202.2018.1509857.*

2.1 Nanofuel Characterization and Preparation

The nanoparticles (NPs) chosen for this study included energetic aluminum (nAl) and inert silicon dioxide ($nSiO_2$) both were purchased from Nanostructured and Amorphous Materials Inc. The particles were advertised as having an average nominal diameter of 80 nm. Upon receiving the nano materials, transmission electron microscopy (TEM) imaging was performed to confirm the size distribution of the particles, Figure 2.1 shows samples of each material with a 200 nm resolution. The as received particle images indicate a particle diameter range of tens to several hundreds of nanometers. Figure 2.1.a indicates that nAl had spherical shapes and particle sizes ranging from tens to several hundreds of nanometers (consistent with the nominal diameter of 80 nm). Some nAl particles show an Al_2O_3 layer of approximately 2-4 nm. This layer is significant because compared to the aluminum core the oxide layer's melting temperature is approximately 1400 K larger [8]; table 2.1 provides more details on these values as reported by Nanostructured and Amorphous Materials Inc. These

articles were stored in a vacuum desiccator upon opening to prevent further oxidation on the surface of the nAl particles. The as-received $nSiO_2$ (shown in 2.1.b) appeared to consist of much smaller amorphous particles, with average sizes on the order of tens of nanometers in diameter but with larger aggregates as compared with nAl.

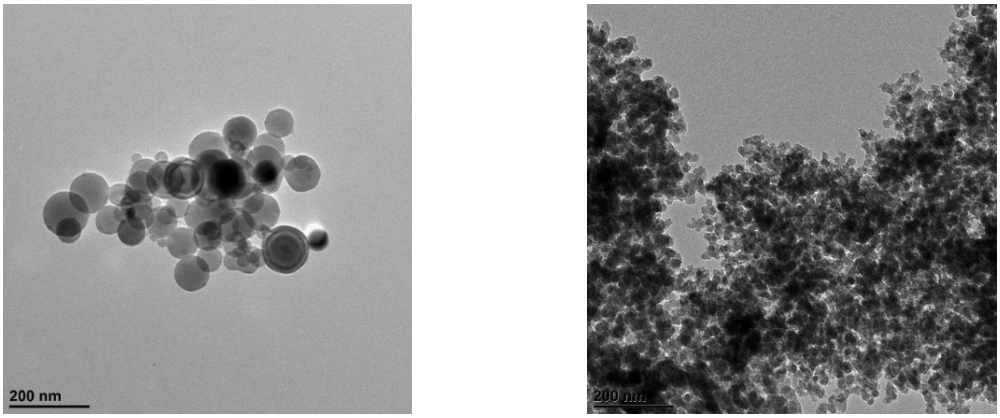

(a) nAl (b) $nSiO_2$

Figure 2.1: TEM Images of received material with a scale of 200 nm.

Name	Density [g/cm^3]	Melting Temperature [k]
Aluminum	2.7	933
Aluminum Dioxide	4.0	2,345
Silicon Dioxide	2.2-2.6	1,873

Table 2.1: Bulk properties of Aluminum, Aluminum Oxide, and Silicon Dioxide.

Preparation of the fuel was done in a fume hood to prevent any contamination to the laboratory environment. The target mixture volume made for a typical set of tests was 20 ml and loading concentrations were varied from 1 to 6 weight percent of the liquid fuel. To prepare the mixture, a weighing dish, beaker, and an analytical scale (Torbal, AGZN120) were used to measure out the correct quantity of nanoparticles and liquid ethanol (purchased from Sigma-Aldrich), which were then poured into a glass vial. Stable suspension of the

mixtures was achieved by placing the mixture vials inside a horn sonicator (Qsonica, Q125) for 5-10 minutes. The sonicator contained an ice bath to prevent ethanol from naturally evaporating. The sonicator was operated at 100 percent amplitude (10 Watts) with an 8 second pulse at 50 percent duty cycle. The suspension stability of NPs was monitored by measuring particle loading concentrations at the beginning and end of the experiments. The samples were poured on to a weighing dish which was placed in a vacuum oven to dry out the sample. Sampled measurements, in Figure 2.2, showed good dispersion of NPs, maintaining the target loading concentration in ethanol for at least 2–3 hours.

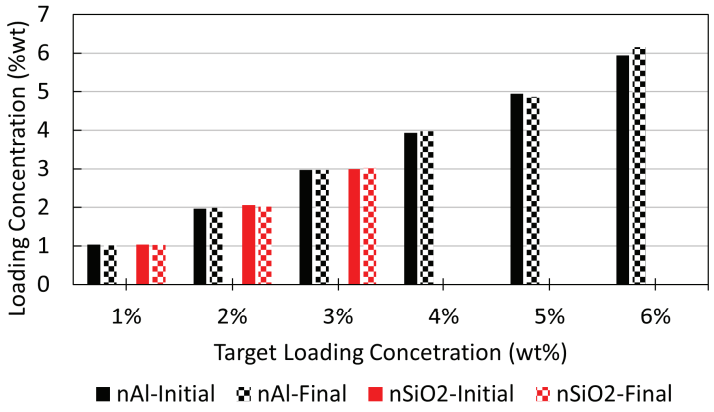

Figure 2.2: Suspension stability of nAl and $nSiO_2$ mixtures (final refers to 3 hours after sonication process).

2.2 Experimental Apparatus

The present droplet combustion experiments were conducted in a closed, atmospheric pressure acoustic waveguide in which the burning fuel droplet was suspended in the center. The apparatus is identical as the one used in prior studies [63, 64, 65, 67, 66, 78]. In the current experiments, various modifications have been made to improve flame/droplet imaging and acoustic characterization, among other features. Figure 2.3 shows the acoustic waveguide along with other components used to collect data.

The waveguide is made of hollow aluminum round stock with an inner diameter of 11.4 cm and a length of 90 cm. A speaker assembly, consisting of two speakers (Dayton Audio, DS115-8) and three rods 61 cm long, is placed inside the acoustic waveguide. The rod assembly enable fixing the distance between the speakers while moving them relative to the geometric center of the waveguide. The waveguide is equipped with pressure taps along the outer surface which are approximately 2.5 mm in diameter to allow the insertion of miniature pressure transducers (Kulite, XCE-093-50D) with a diameter 2.4 mm. There are four ports on the waveguide which are utilized all located at/near the center. First located at the top center of the waveguide a threaded port which allows for different fuel delivery methods to be used. A port for ignition is located near the bottom center where the droplet is formed; where a heating element can be inserted and removed. Lastly, for optical access to the droplet there are two quartz windows located on the waveguide such that the droplet can be imaged perpendicularly.

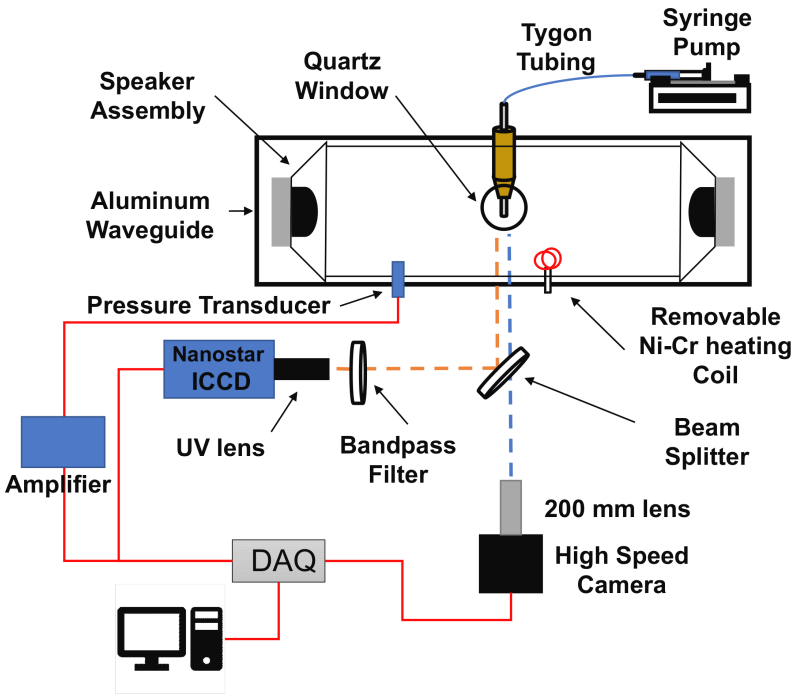

Figure 2.3: Schematic of the experimental apparatus for the combustion of a fuel droplets.

2.2.1 Acoustic Field

Instrument control and data recording was done using LabView software in combination with a data acquisition board (DAQ) (NI USB-6251 BNC), although that was not the focus of the present studies, but rather, separate studies [1]. This is described here because of the relevance to the AFRL-based experiments. A sinusoidal signal is generated in LabView and sent though the DAQ to a speaker amplifier (Radioshack, MPA-250B) before the signal reaches the two speakers. After the amplifier, the speakers can be wired in-phase or out-of-phase to create a standing wave. Simultaneously the pressure transducer signal is being acquired to adjust the output sinusoidal signal to establish the desired pressure amplitude at the nearest pressure anti-node. The speakers were forced at frequencies low enough to create effectively one-dimensional planar waves along the length of the waveguide. In separate studies to examine the effects of acoustic excitation on burning droplets, the speakers are moved, together, to the right or left, relative to the burning droplet, to explore the effect of the position of the droplet relative to a pressure node (PN) or anti-node (PAN) [61, 62].

The acoustic field inside the waveguide has been characterized using pressure transducers as well as a hot wire anemometer (Dantec Dynamics, 55P11) to measure both pressure ($p'(x,t)$) and velocity ($v'(x,t)$) amplitudes. Theoretical values were calculated using the linearized momentum equation relating pressure and velocity amplitudes.

$$p'(x,t) = Re(-p'_{max} \sin(\frac{2\pi x}{\lambda}) \exp(i\omega t)) \tag{2.1}$$

$$u'(x,t) = Re(-i\frac{p'_{max}}{\rho c} \cos(\frac{2\pi x}{\lambda}) \exp(i\omega t)) \tag{2.2}$$

First the hot-wire had to be calibrated; for this the hot-wire was placed at the geometric center of the waveguide. The calibration procedure was taken from Huelsz and López-Alquicira [79] which implemented hot-wire anemometry to an oscillatory flow field arising from acoustic forcing. Voltage measurements were acquired for acoustic excitation ampli-

tudes ranging from 0 to 280 Pa in increments of 10 Pa. These voltage measurements were correlated with the theoretical velocity at the probe location from Eqn. 2.2, and repeated for each of the three acoustic forcing frequencies.

Experimental results showing velocity perturbation amplitudes in the vicinity of the PN for each of the three forcing frequencies, at an excitation amplitude $p'_{max} = 200$ Pa (measured at the nearest PAN), are shown in Fig. 2.4. For each forcing frequency, there was close agreement observed between the theoretical and experimental velocity perturbation amplitudes; this reassured that the pressure amplitude (p') measurement in the vicinity of the droplet location is a good estimate of the local (u') during droplet burning experiments via Eqn. 2.2. These results have been published by Bennewitz et al. [62].

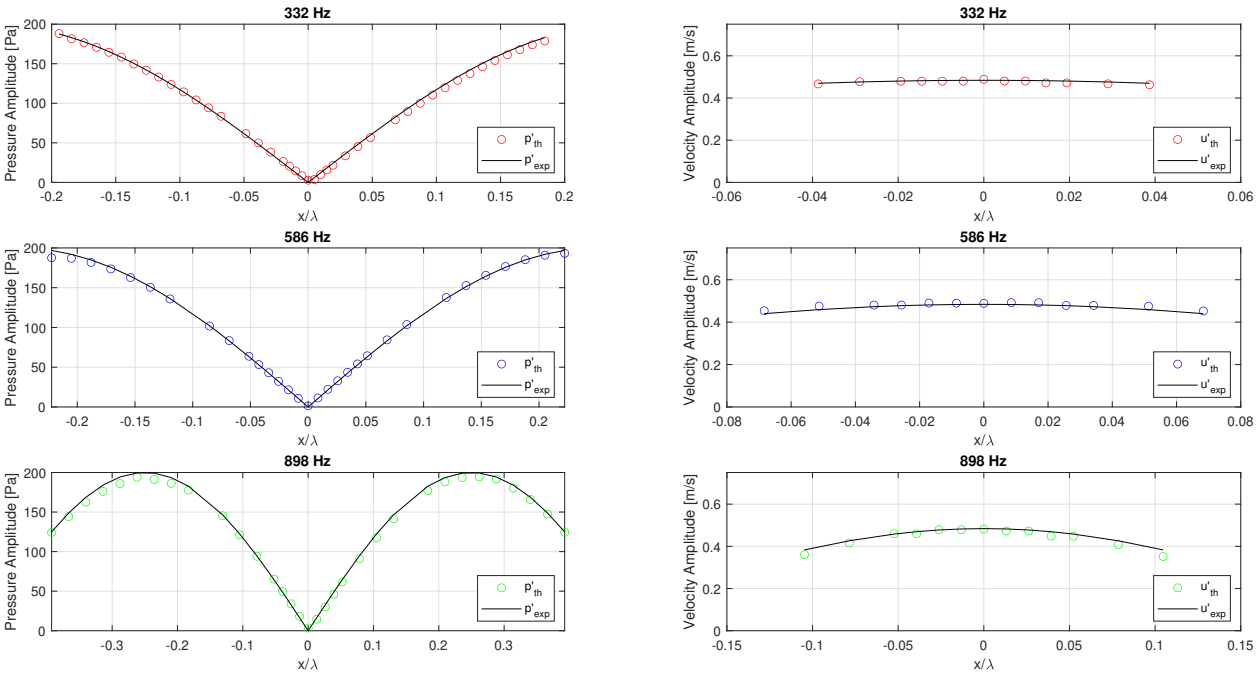

Figure 2.4: Experimental and theoretical acoustic pressure oscillation amplitude profiles are shown at forcing frequencies 332 Hz, 586 Hz, and 898 Hz.

For this particular study the acoustic aspect of this apparatus was not used although separate studies use the acoustic field to explore nanofuels[1]. Additional details regarding

the effects of acoustic excitation on burning droplets and the methods for exploration in the present waveguide can be found in [61, 62].

2.2.2 Fuel Delivery Methods

This study looks at three distinct fuel delivery techniques each involving a different method of generating a droplet. The experiments here were conducted in three different ways (see Figure 2.5): (1) with a burning droplet suspended from a quartz fiber (case I); (2) a droplet suspended from a quartz capillary without continuous fuel delivery during combustion (case II); and (3) a droplet suspended from the capillary with continuous fuel delivery at a volumetric flow rate, Q_v via a syringe pump (case III).

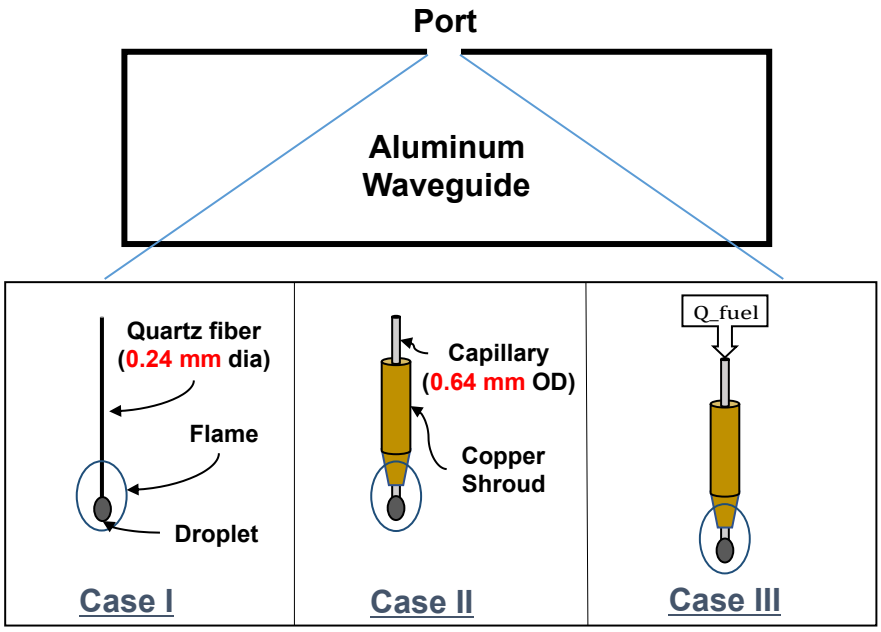

Figure 2.5: Schematic describing the three droplet formation methods.

The fibers and capillaries were manufactured in house using an oxygen/MAP hand torch from Bernzomatic, where the fibers started from a 2 mm rod and the capillaries from a 2 mm tube. To make the fibers, the rod had to be drawn to approximately 240 microns

in diameter. Once the fiber was created a bead of approximately 100 microns larger was formed at the tip to help suspend the droplet. The capillaries were drawn by placing them on a rotating stand to heat the quarts material uniformly. The capillaries were drawn at approximately half the length to form a taper down to 640 microns. Table 2.2 summarizes average dimensions of both the capillaries and fibers used for these experiments.

	Fiber [μm]	Fiber Bead [μm]	Capillary, OD [μm]
Diameter	240	360	640

Table 2.2: Diameters of quartz fibers and capillaries.

Case I is the classic fiber suspended experiment where a single droplet was deposited on the quartz bead using a small capillary. These tests were performed for comparison purposes to past/current work being done on nanofuels [26, 27, 28]. Case II included a quartz capillary where a single droplet was formed at the tip of the capillary similar to case I. These tests enabled for the direct assessment of the effect of a quartz capillary, which had a larger diameter, as compared to a quartz fiber. Experiments from case III allow for a quasi-state approach of continuous fuel delivery to enable probing the flame for longer periods of time. Fuel is continuously delivered to the droplet to replenish the fuel that evaporates on the surface due to the presence of the high temperature flame. As shown in the diagram, the capillary is placed inside a copper shroud to protect the capillary from excess heating for both case II and III.

2.2.3 Image Acquisition

The droplets were imaged perpendicularly to the waveguide length (see Figure 2.3). Front and rear quartz windows were used for imaging and back-lighting the droplets. Two cameras were used for these experiments, one was Nanostar ICCD camera (LaVision) permitting the

capture of chemiluminescence from the electronically excited hydroxyl radical, OH*, within the flame surrounding the droplet. The second was a high-speed visible camera (Photron Mini AX200) used for recording shadowgraph images.

For fiber-suspended (case I) and continuously fed droplets (Case III) simultaneous imaging of the droplet was recorded. A beam splitter (Andover Corp. 325SC01-50) was utilized to image the droplet from one single port, giving the same angle of the burning droplet. The beam splitter was oriented at 45° based on incident light, reflecting 90% of the incident light below 350 nm and allowing 90% transmission at wavelengths above 350 nm. An ultraviolet (UV)-B light bulb was used for backlighting the droplet. The NanoStar camera was equipped with a 105 mm UV lens and a narrow-band filter (ZBPA 310) centered at 310 nm with a full width at half maximum (FWHM) of 20 nm. The high- speed visible camera with a 200 mm micro lens was employed for visualizing the droplet diameter behavior, as well as particle expulsion events and their ignition. The two cameras were synchronously operated using a LabVIEW script in conjunction with a data acquisition board (NI USB-6251) and a programmable timing unit (PTU). Synchronization of the cameras for case I and III was achieved using a TTL signal generated in LabVIEW. The two cameras were on standby waiting for the trigger which synchronized the images with the pressure signal.

For case (II) only the NanoStar camera operating in the ultraviolet range was used. Attached to the camera was a U-330 band-pass filter with a wavelength centered at 330 nm, (FWHM) of 140 nm, with back-lighting of the droplet via a far red (730 nm) light-emitting diode (LED). Table 2.3 reports the recording rates for the different cases.

	Lavision, NanoStar	Photron, Mini AX200
case (I)	15	3000
case (II)	28	NA
case (III)	10	1000

Table 2.3: Recording Rates (fps) for experiment cases I, II, and III.

2.2.4 Experimental Procedure

A streamlined procedure was used to conduct the experiments due to the fast evaporation of ethanol and sedimentation of the particles. First the nanofuel was prepared as mentioned in section 2.1 then immediately was loaded into a 20 ml plastic syringe. Additionally, a Tygon tube with a capillary at one end was attached to the syringe. Next, one of two droplet formation methods were used: for case I a single droplet was placed on the fiber using a small capillary. For case II and III the capillary was placed inside the copper shroud and the syringe was placed on a pump (KD Scientific, 100 Series). Using the syringe pump a single droplet could be formed or a droplet that had constant volume flow rate. Lastly, the droplets were ignited using a removable nichrome wire. After a test the rod or capillary was cleaned by ultrasonic bath or manually wide between experiment trials. Also, in between trials the waveguide was purged to refresh the air, and the syringe with the nanofuel was manually shaken to maintain stability of the mixture. The maximum testing time for a batch of nanofuel was 3 hours corresponding to the mixture stability results presented in section 2.1.

2.3 Measurement Methods

2.3.1 Burning Rate Constant

The burning rate constant for a suspended droplet (case I and II) and a continuously fed droplet (case III) are calculated using the following two equations, respectively.

$$K_{non-fed} = -\frac{d(d^2)}{dt} = -2d\dot{d} \tag{2.3}$$

$$K_{fed} = \frac{4Q_v}{\pi d} - 2d\dot{d} \tag{2.4}$$

where d is the droplet diameter and Q_v is the volume flowrate. These two equations are derived from continuity; the second equation accounts for the replenishing of fuel to the droplet in addition to the droplet surface regression rate [60, 61]. The droplet was approximated as an ellipsoidal so that the diameter with the equivalent volume of a sphere takes the form,

$$d_{eqvs} = 2a^{1/3}b^{2/3} \tag{2.5}$$

where a and b are the semi-major and minor axis lengths determined by tracking the edge of the droplet in MATLAB which uses the Canny edge detection method. With the edge of the droplet found it was then possible to fit an ellipse to the points, as seen in Figure 2.6, then assuming vertical symmetry the volume of an ellipsoid is calculated. To calculate the equivalent droplet diameter (d_{eqvs}), Eqn. 2.5, the volume of the ellipsoid is equating to the volume of a sphere [63]. Having the droplet diameter history, K was extracted as the slope via linear regression using the middle 80 percent of the data which represents Eqn. 2.3, this would be for case I and II. For the case III, Eqn. 2.4 is used where (d_{eqvs}) is nearly constant throughout the experiment due to the droplets reaching quasi-steady burning with a constant fuel flow rate Q_v, therefore the second term in Eqn. 2.4 is typically very small. Nevertheless, this term is still quantified in the instantaneous calculations for K; the K values were averaged over the quasi-steady period to provide the mean burning rate constant for the experiments in Case III.

2.3.2 Mean OH* Chemiluminescence Intensity and Standoff Distance

The electronically excited hydroxyl radical is created during hydrocarbon combustion through the intermediate reaction involving methylidyne (CH) and diatomic oxygen [80], given by

$$\mathrm{CH}(^2\Pi_u) + \mathrm{O_2}(^3\Sigma_g) \rightarrow \mathrm{CO}(^1\Sigma^+) + \mathrm{OH}^*(^2\Sigma^+). \tag{2.6}$$

Then the de-excitation reaction of the OH* radical

$$\mathrm{OH}^*(^2\Sigma^+) \rightarrow \mathrm{OH}(^2\Pi) + h\nu \tag{2.7}$$

gives an electronic transition ($^2\Sigma^+ - ^2\Pi$) in the ultraviolet (UV) band centered around 308 nm.

The mean OH* chemiluminescent intensity was calculated using the images obtained from the intensified camera. To compute the overall integrated intensity of each image multiple post processing steps were performed, first the images are background subtracted to remove any light not emitted from the flame. Secondly, the images are filtered to isolate the area corresponding to the flame [78]. An example of a processed image can be seen in Figure 2.6. The goal of processing the images to obtain electronically excited OH* chemiluminescent intensity of the flame which is said to be a good indicator of heat release [20, 81, 82, 83, 84, 85, 86].

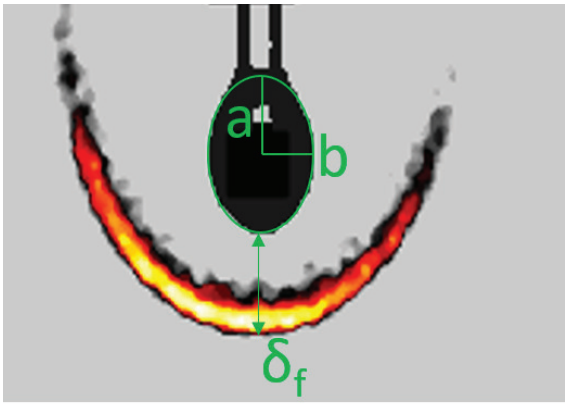

Figure 2.6: OH* chemiluminescence image showing relevant dimensions for calculating burning rate constant and standoff distance.

The analysis of the flame standoff distance δ_f focused on the stagnation region of the flame which is established at the lower part of the droplet due to buoyancy. This standoff distance was calculated using the processed images as used for the calculating mean intensity. In Figure 2.6 the standoff distance δ_f is defined as the distance from the edge of the droplet to the maximum OH* chemiluminescence intensity point of the flame keeping the vertical position constant, corresponding to the center of the droplet and capillary system. Results for both the mean intensity and standoff distance will be discussed in the next chapter.

2.4 Temperature Measurements

Temperature measurements of the droplet were made using a S-type thermocouple (Omega, P10R-005) made of Platinum–Rhodium (Pt-10-Rh/Pt) with 0.125 mm wire diameter. The thermocouple (TC) was held vertically to match the conditions as that in case I. This was done for a single droplet by suspending it directly on the TC junction and igniting it. Results for neat fuel (pure ethanol), nAl + Ethanol and $nSiO_2$ + Ethanol will be presented in the next chapter. In between testing the nanofuels the TC was cleaned using an ultrasonic bath with ethanol and a neat fuel droplet was burned on the same TC before running another nanofuel test.

2.5 Simple Model for Nanofuel Burning Rate

This section is taken from a paper from our group; Sim et al. [32] presented the development of a theoretical burning rate constant was formulated for nanofuels. Given that characterization of nanofuels was largely done by investigating the burning rate it was of interest to predict the effects of nanoparticle additives on theoretical droplet burning rate constants as well as adiabatic flame temperature. A simple droplet combustion model was developed to better understand the mechanisms for enhancement in K for nanofuels. The theoretical burning rate constant (K_0) for a single droplet may be determined from the following relation [18],

$$K_0 = \frac{8\lambda_g}{C_{p,g}\rho_l} \ln(1+B), \tag{2.8}$$

where λ_g, $C_{p,g}$, and ρ_l denote the average thermal conductivity, specific heat of the fuel and oxidizer in the gas phase, and the density of fuel (here, ethanol) at the boiling point, respectively. B is the transfer number given by,

$$B = \frac{C_{p,g}(T_\infty - T_{boil}) + \frac{q}{i}}{h_{fg}}, \tag{2.9}$$

in which h_{fg} is the latent heat of vaporization of the fuel at the boiling point, T_∞ is the ambient temperature, T_{boil} is the boiling temperature of the ethanol droplet, q is the heat of combustion of fuel, and i is the stoichiometric oxygen to fuel mass ratio. Suitable species properties such as heat capacity and thermal conductivity were determined based on approaches described in [87].

To incorporate the effects of NPs in this droplet combustion model, all properties in eqn. 2.8 were determined for the present nanofuels with various nanoparticle types and loading concentrations from the following equations, after the analysis of [88],

$$\frac{\lambda_{nf}}{\lambda_{bf}} = 1 + \frac{3(\alpha - 1)\phi}{(\alpha + 2) - (\alpha - 1)\phi}, \tag{2.10}$$

$$\rho_{nf} = (1 - \phi)\rho_{bf} + \phi\rho_{np}, \tag{2.11}$$

and

$$C_{p,nf} = \frac{(1 - \phi)\rho_{bf}C_{p,bf} + \phi\rho_{np}C_{p,np}}{\rho_{nf}}. \tag{2.12}$$

Here α is the thermal conductivity ratio between the NP and the base fuel and ϕ is the volume fraction of NP within the liquid. The subscripts np, nf, and bf identify nanoparticle, nanofuel, and base (neat) fuel. Heats of combustion were estimated for all fuel constituents, including nAl and $nSiO_2$, and the latent heat of vaporization of nAl-ethanol mixtures was adopted as well, from measurements in [28]. Temperature-dependent properties used in these calculations for ethanol, nAl, and $nSiO_2$ are adopted from [89, 90, 91, 92, 93, 94, 95].

Theoretical calculations were also performed to understand changes in the adiabatic temperatures of ethanol flames with the addition of $nSiO_2$ and nAl. The adiabatic flame temperature was determined for various loading concentrations, using the NASA CEA program [96], 1 atm and an initial temperature of 300 K. The adiabatic flame temperature for

ethanol in air with an equivalence ratio of unity, most relevant for flames here, was estimated to increase from the value for neat fuel, 2,195 K, to approximately 2,250 K in the presence of 6 wt.% Al, resulting from exothermic oxidation of Al. With the addition of $nSiO_2$ to the flames in the computation, the theoretical flame temperature was not significantly changed for various loading concentrations up to 6 wt.%.

CHAPTER 3

Nanofuel Droplet Combustion: Results and Discussion

The information presented in this chapter is taken with slight modification from the article: *Hyung Sub Sim, Miguel A. Plascencia, Andres Vargas, John W. Bennewitz, Owen I. Smith & Ann R. Karagozian (2018): "Effects of Inert and Energetic Nanoparticles on Burning Liquid Ethanol Droplets", Combustion Science and Technology, DOI: 10.1080/00102202.2018.1509857.*

This study aims to understand the effects of adding energetic nanoparticles (nAl) to liquid ethanol fuel (nanofuels). To do this, three different types of experiments were carried out as mentioned in section 2.2.2. In addition, inert nanoparticles ($nSiO_2$) were used as alternative additives to compare results against the nAl energetic nanoparticles. The main parameter quantified in this investigation is the burning rate constant (K) but others such as the flame standoff distance, OH* chemiluminescent intensity and droplet temperature are evaluated. Before looking at the nanofuels a series of baseline tests were conducted to understand the differences between neat fuel (pure ethanol) and nanofuels.

3.1 Baseline Experiments

3.1.1 Case I: Droplet suspended from a quartz fiber

The first set of tests completed were for case I. As mentioned in section 2.2.4, droplets were transferred to the quartz fibers using a small capillary that would disperse a consistent size droplet on the fiber of approximately 1.3 mm in diameter. Simultaneous visible and UV

imaging allowed for tracking of the droplet as well as of the flame. Normalized droplet diameter history shown in Figure 3.1 is in good agreement with the classical d squared law [17], so that K may be extracted from the slope of the line given by $(d/d_0)^2$ vs. t/d^2. From section 2.3, the droplet diameter is determined from back-lit imaging and edge detection, where d is based on the equivalent volume of a sphere.

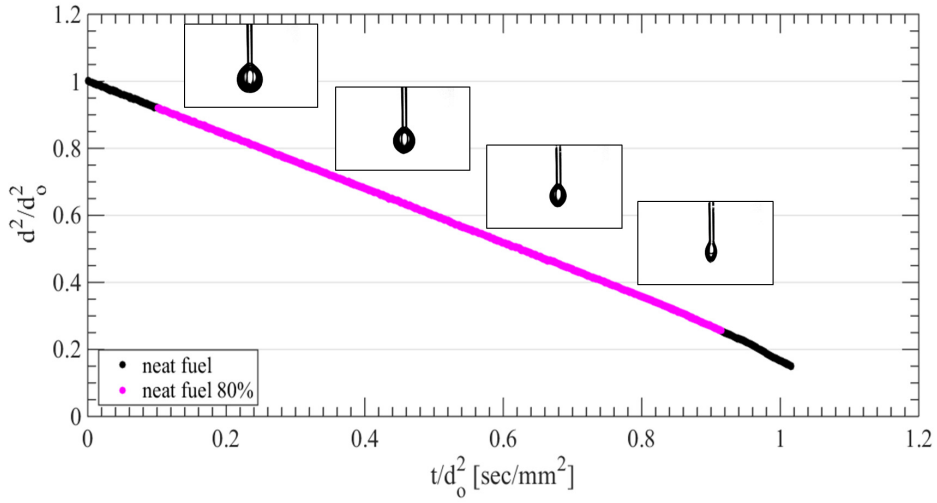

Figure 3.1: Normalized droplet diameter regression for neat ethanol fuel with images depicting this process for Case I. The droplet was burned in atmospheric conditions.

Four representative images show the droplet evaporating on the fiber over approximately 1-2 seconds. When calculating K using the slope of the normalized droplet diameter squared only the middle 80 percent of the data range is used. The middle portion of the data best represents quasi-steady burning (i.e., linear slope). The first ten percent of the data accounts for ignition time and the last ten percent has a droplet with a liquid volume approximately equal to the bead's volume. Overall, 48 baseline tests were conducted for case I to reduce the uncertainty. For example, the burning rate constant was not influenced by the variation in the fiber dimensions, trends for which are show in Figure 3.2. The average burning rate constant for case I was 0.810 $[mm^2/s]$ with a 98 percent confidence interval of $\pm$ 0.002.

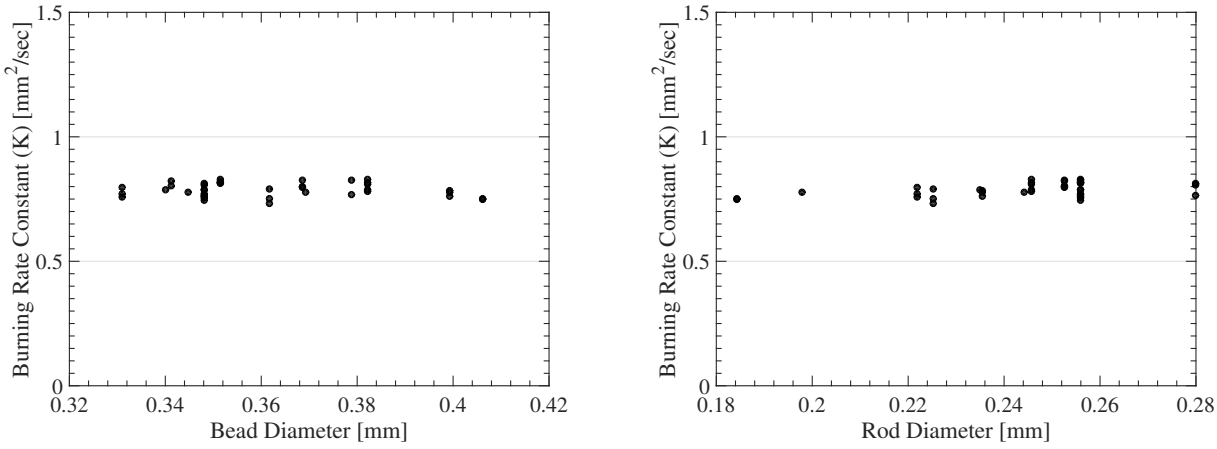

(a) Bead

(b) Rod

Figure 3.2: Burning rate constant versus a) fiber bead diameter and b) fiber diameter.

The flame standoff distance (δ_f) for case I was calculated as the distance from the edge of the droplet to the point where the flame has the highest intensity. As indicated in Figure 2.6, the flame standoff distance δ_f was typically measured from the bottom of the droplet to the bottom of the flame surface; this was not the case when acoustic excitation disturbed the droplet and caused flame deflection [61]. Figure 3.3 depicts the evolution of the standoff distance for several neat fuel tests. For an easy way of comparing the standoff distance to the plots of nanofuel droplets, the vertical axis of the plot has a normalized standoff distance. This non-dimensional standoff distance is defined as δ_f divided by the instantaneous droplet diameter with time. From the plot in Figure 3.3 it can be seen that the general trends for all the cases show continuous increase in normalized δ_f as time evolves. This rate of increase in the flame standoff distance becomes larger through the lifetime of the droplet because the droplet surface recedes and the total amount of fuel vapor increases as the droplet burns. These results are consistent with those found by Law et al. for ocatane droplets [97].

The spatially averaged, normalized OH* chemiluminescence intensity of the transient flame is plotted in Figure 3.4. In early part of combustion, the flame intensity remains nearly constant but approximately halfway through the burn time the intensity begins to

decrease. The decline in the flame intestine is due to the depletion of fuel vapor and especially oxygen in the vicinity of the droplet. The intensity profile does not go to zero because it corresponds to the amount of data used for tracking the diameter, which is cut off when the droplet is on the same order of size as the bead.

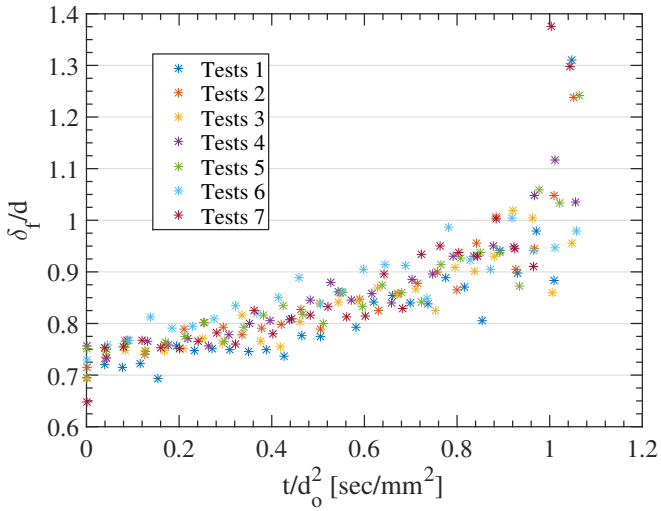

Figure 3.3: Normalized standoff distance time evolution for several representative neat fuel cases.

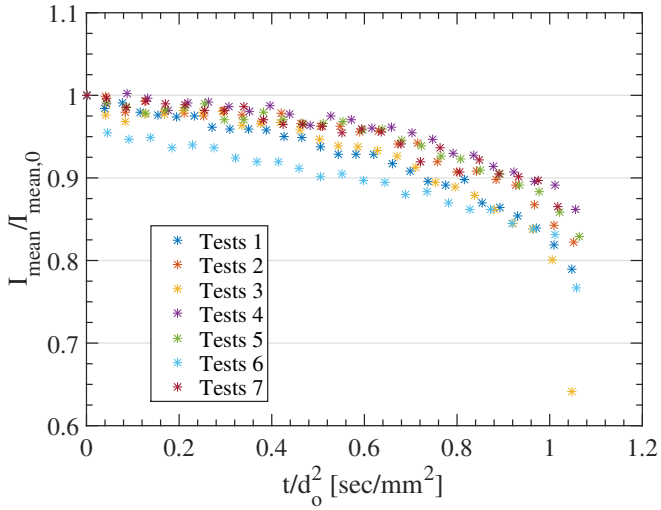

Figure 3.4: Transient profile of the normalized OH* chemiluminescence intensities for neat fuel.

3.1.2 Case II: Droplet suspended from a quartz capillary

Separate experiments of burning ethanol droplets suspended from the quartz capillary, but without continuous feeding of fuel, were performed for comparison with the fiber-suspended droplets (case I) without feeding. Similar to case I, the droplet diameter history $(d/d_0)^2$ varies linearly in time. For these tests only the intensified camera was used to acquire images at 28 fps. Figure 3.5, includes images of the burning ethanol droplet. The average

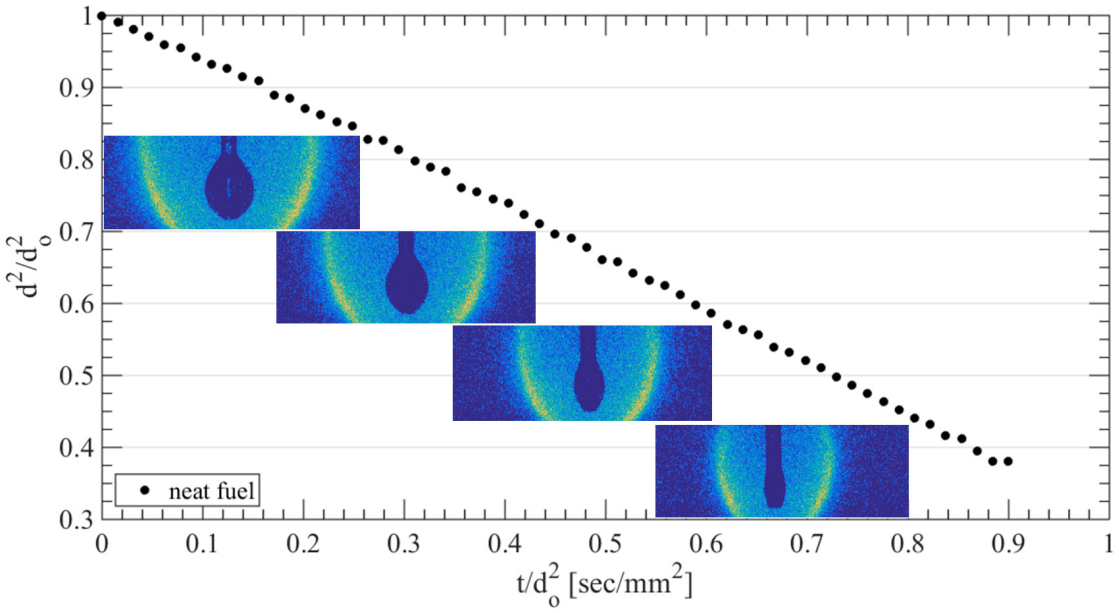

Figure 3.5: Normalized droplet diameter regression for neat fuel with images depicting this processes for case II. Droplet was burned in atmospheric conditions.

burning rate constant is 0.740 $[mm^2/s]$ with a 98 percent confidence interval of $\pm$ 0.013. These average burning rates for pure ethanol are systematically lower than those in case I, even when accounting for experimental uncertainties (1.38%) in the evaluation of K [61]. Case II had larger droplet diameters (1.5 mm) compared to case I; this was due to the capillary having a lager diameter than the fibers used for case I. This leads to a lower relative liquid surface area for the droplet exposed to hot gases, thus with lower relative evaporation rates

as well as possibly a higher heat loss to the capillary, so there is less energy to vaporize the ethanol. Only having the intensified Nanostar camera caused the resolution of the camera to be less than half. Hence, in order to resolve the droplet shape and interface as accurately as possible, only a portion of the actual burning droplet was imaged with the UV camera, as can be seen in Figure 3.5 where the flame is cut off. For this reason, the standoff distance and flame chemiluminescent intensity could not be calculated.

3.1.3 Case III: Continuously fed droplet via a quartz capillary

In these experiments in which fuel is continuously fed to the burning fuel droplet, the burning process is effectively quasi-steady; the variation of the droplet diameter is small because the droplet is continuously being replenished with new fuel via a syringe pump delivering fuel at a constant volume flow rate. Figure 3.6 shows pure ethanol droplets exhibited quasi-steady combustion for over 20 sec, much longer than that for nonfed droplets in cases I and II (which burned for 1.5–1.8 sec).

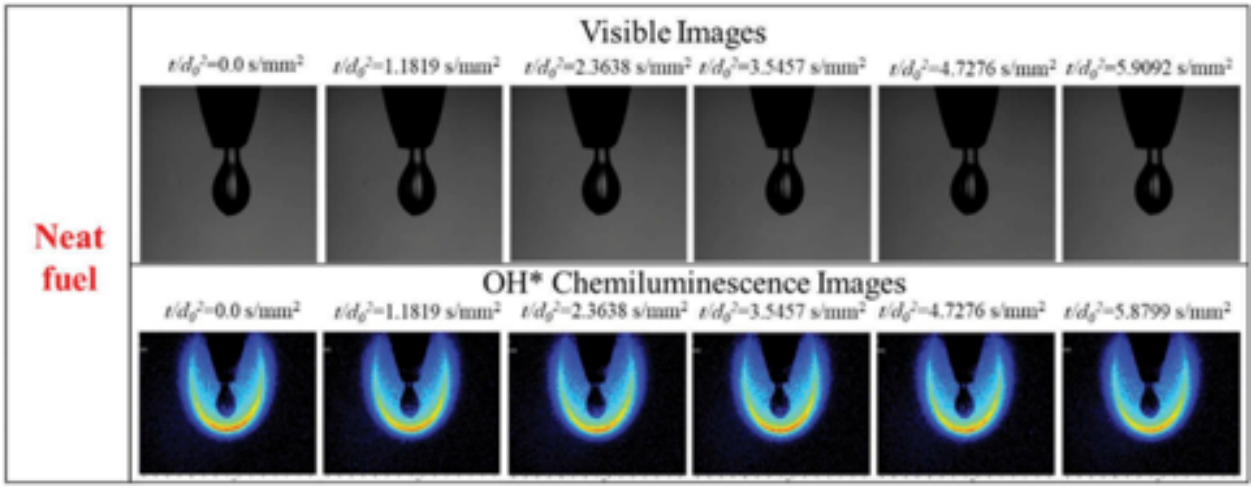

Figure 3.6: Burning sequences from visible and OH* chemiluminescence imaging of continuously fed droplets of neat ethanol with simultaneous visible (top) and OH* chemiluminescence (bottom) imaging (case III).

Additionally, Figure 3.7 shows the droplet diameter and OH* chemiluminescence intensity and flame standoff distance are effectively constant over time. In this plot, the two images represent the droplet at the beginning and end of the data shown. Pure ethanol exhibits quasi-steady combustion for approximately 20 seconds which is significantly more than that for non-fed droplets (1-2 sec.). For case III, the average burning rate constant is 0.80 $[mm^2/s]$ with a 98 percent confidence interval of $\pm$ 0.024. Similarly, to case II the average droplet diameter (1.6 mm) is larger than case I, but of course here the droplet does not recede in shape but maintains the same shape over time. The maintenance of the droplet size, in addition to potential internal recirculation within the droplet, are likely reasons for this larger burning rate constant K as compared with values for Case II, the capillary-suspended droplet without fuel feeding. The plot in Figure 3.6 also describes flame characteristics: the variation of the normalized δ_f and OH* chemiluminescent intensity are plotted in blue and red respectively. Both parameters are nearly constant for the duration of the experiment, further confirming the quasi-steadiness aspect of these experiments.

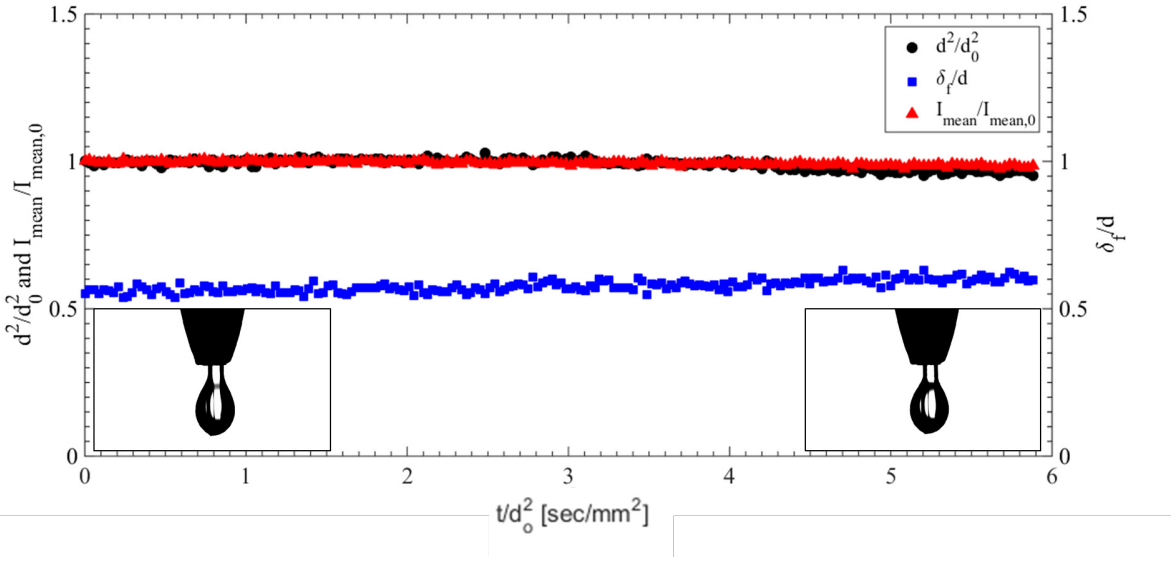

Figure 3.7: Normalized droplet diameter (black), OH* chemiluminescence intensity (red), and δ_f (blue). Additionally an initial (left) and final (right) image of the droplet are show in the plot.

3.1.4 Summary

To summarize the baseline results for the burning ethanol droplets without nano particulates, table 3.1 lists average values for K as calculated from the slope of the $(d^2/d_0)^2$ plots for cases I and II, and for case III equation 2.4 is used. While there were some differences among the different methods and results in terms of average K values, due in general to altered droplet sizes over time and different suspension diameters between the fiber and capillary, current K values are in good agreement with established values (0.82 $[mm^2/s]$ [13], 0.80 $\pm$ 0.05 $[mm^2/s]$ [41]).

	Case I	Case II	Case III
$K_{avg}[mm^2/s]$	0.81	0.74	0.80
$K_{min}[mm^2/s]$	0.79	0.72	0.75
$K_{max}[mm^2/s]$	0.82	0.77	0.84
confidence interval ($\pm$)	0.002	0.013	0.024
$d_{eqvs,avg}$ [mm]	1.3	1.5	1.89
# of tests	50	12	24

Table 3.1: Summary of the burning rate constants for neat fuel.

Case I data for the nonfed, fiber-suspended droplet produced slightly higher K values than for the nonfed, capillary-suspended droplet (case II). This was likely related to the fact that the effective droplet surface area exposed to hot gases was reduced for the capillary-suspended droplets as compared with the fiber-suspended droplets but with the same effective volume and thus effective diameter of a sphere. For the neat fuel in case III, the average K value was 0.80 $[mm^2/s]$, in contrast to K = 0.74 $[mm^2/s]$ for case II in the absence of continuous fuel delivery. Internal droplet recirculation, which is known to increase evaporative rates [18], was occasionally visible in imaging of fed droplets and could have been the reason for this systematic increase in K for case III.

3.2 Nanofuels

Next, the effects of adding energetic nAl and inert $nSiO_2$ particles to liquid ethanol will be explored. The mixture loading concentrations varied from 1-6wt% for nAl and 1-3wt% for $nSiO_2$. For case II, $nSiO_2$ was not tested since the method itself was designed to understand the effect of the diameter of the suspension capillary as compared with the quartz fiber, and this understanding was accomplished using neat ethanol. Comparisons to established values by others, obtained via fiber-suspended droplet experiments, are made for mixtures of 1wt% nAl in ethanol.

3.2.1 Case I: Droplet suspended from a quartz fiber

In this section we explore the classic burning droplet suspended from a fiber, starting with the lowest particulate concentration. Figure 3.8 illustrates simultaneous visible and OH* chemiluminescence images for 3 separate tests at three different loading concentrations of nAl, 1 wt%, 3 wt%, and 5 wt%, shown in Figures 3.8a, 3.8b, and 3.8c, respectively. Similar to neat fuel droplets, the diameter deceases systematically as the fuel evaporates, but as the combustion approached completion, burning particles were visible, likely due to the occurrence of particle ejections from the droplet as well as from the fiber, with possible passage through the flame zone, in some cases. With increasing concentration, of nAl the particle ejection/ignition appears to occur earlier and more frequently because of particle accumulation and agglomeration within the droplet. In Figure 3.8.b large aggregates of particles were found, at time 0.6233 $[mm^2/s]$, near the top of the droplet surface and adjacent to the fiber; these particles then ignite after they travel across the flame as seen in the following image. Additionally, there is some residue of nAl left on the fiber after combustion is complete, consisting potentially of reacted as well as of unreacted particles as seen in Figure 3.8.c.

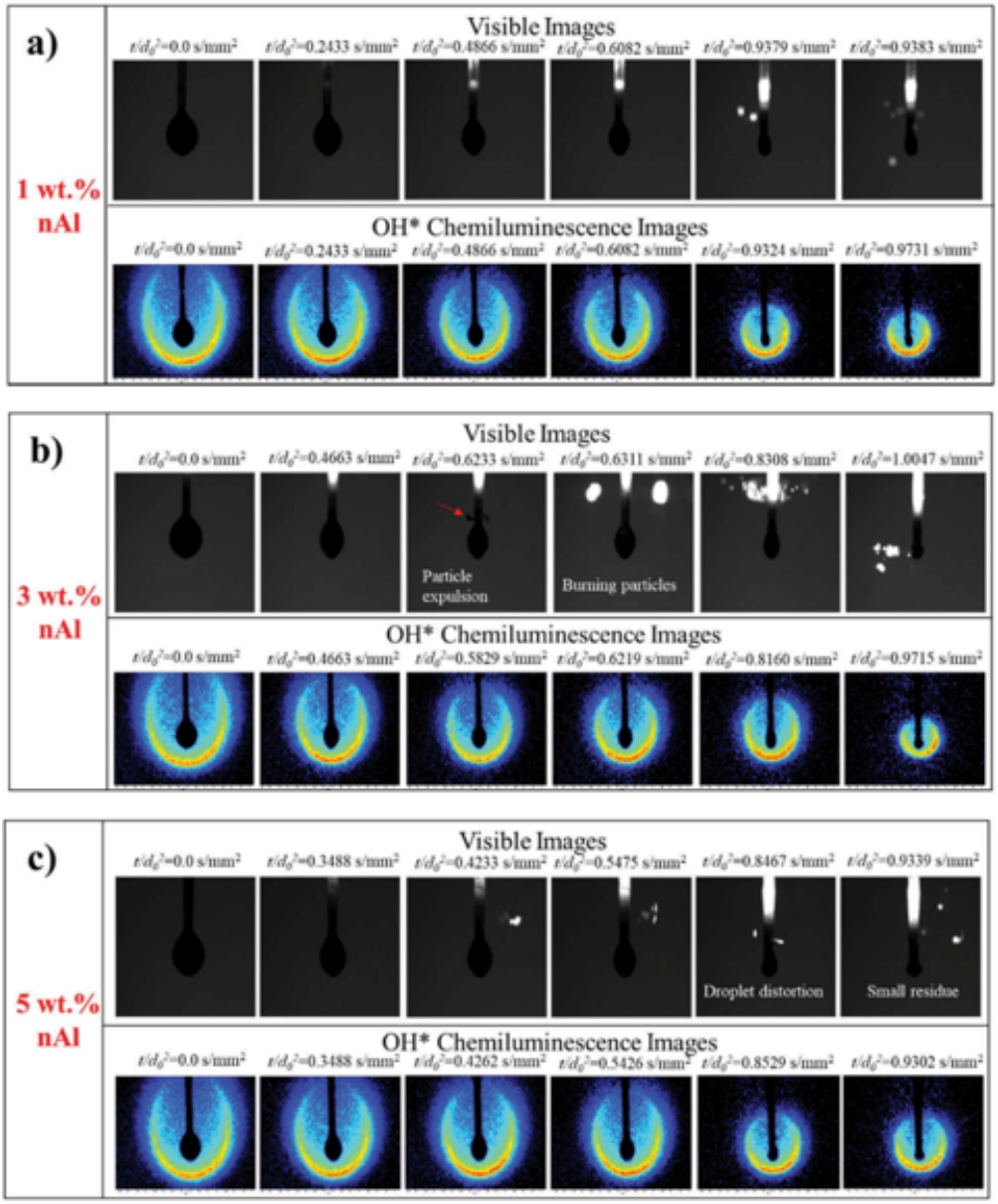

Figure 3.8: Simultaneous visible and OH* chemiluminescence images depicting the droplet regression for a mixtures of a) 1 wt%, b) 3 wt%, & c) 6 wt% nAl (case I).

As shown in Figure 3.9, the evolution of the normalized square of the droplet diameter follows the classical d squared law. Systematically larger slopes with the addition of nAl were observed when compared with that for pure ethanol, corresponding to a slight increase in K. For higher loading concentrations (4-6 wt%), the droplet regression experiences a deviation

from the d^2 law due to the distortion of the droplet, for example, as shown in Figure 3.8.c. However, only the middle 80% of the data are used to calculate K, therefore this deviation, which likely has a higher burning rate, is excluded. It is important to note that during this portion of the test, the mixture concentration of the droplet is much higher than the original quantity because of the accumulation and agglomeration of the nanoparticles. For these experiments, the increase in K with increasing nAl concentration was measurable, on the order of 8.5% as one increases concentration from 1 wt% to 6 wt%. These values will be compared to the other droplet formation methods later on.

Figure 3.10 has two plots; on the right normalized flame standoff distance (normalized by the time-variable droplet diameter) and on the left normalized intensity. For the standoff distance there is a large amount of overlap amongst the data points, giving no particular trend with respect to increasing nAl concentration. Nonetheless, the trend of increasing standoff distance with time remains as noted for neat fuel. In terms of OH* chemiluminescence intensity, the higher loading concentrations have a slightly more negative slope than neat fuel does in the second half of the droplet lifetime.

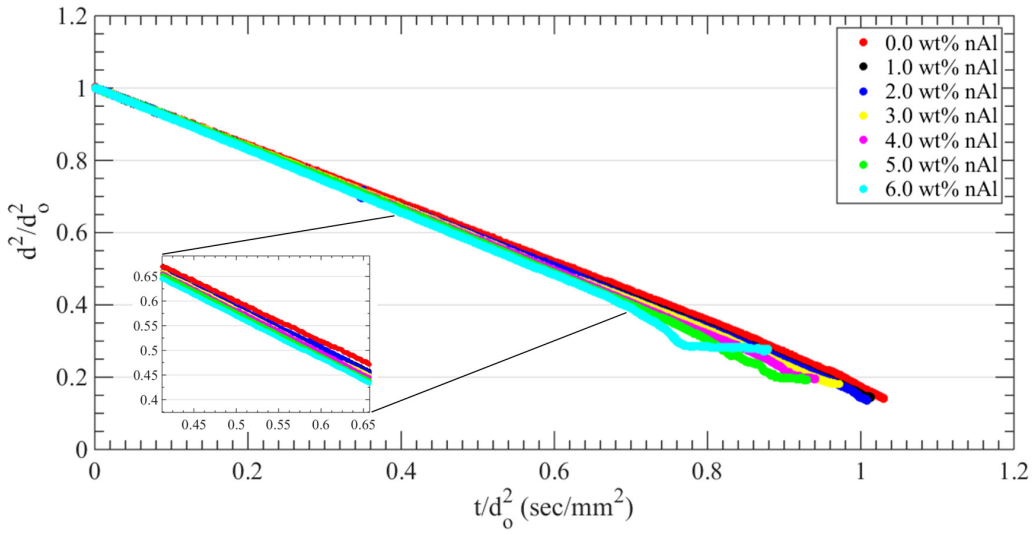

Figure 3.9: Normalized droplet diameter regression as a function of time for various nAl concentrations, ranging from 1-6 wt% (case I). One representative neat fuel case is show in red.

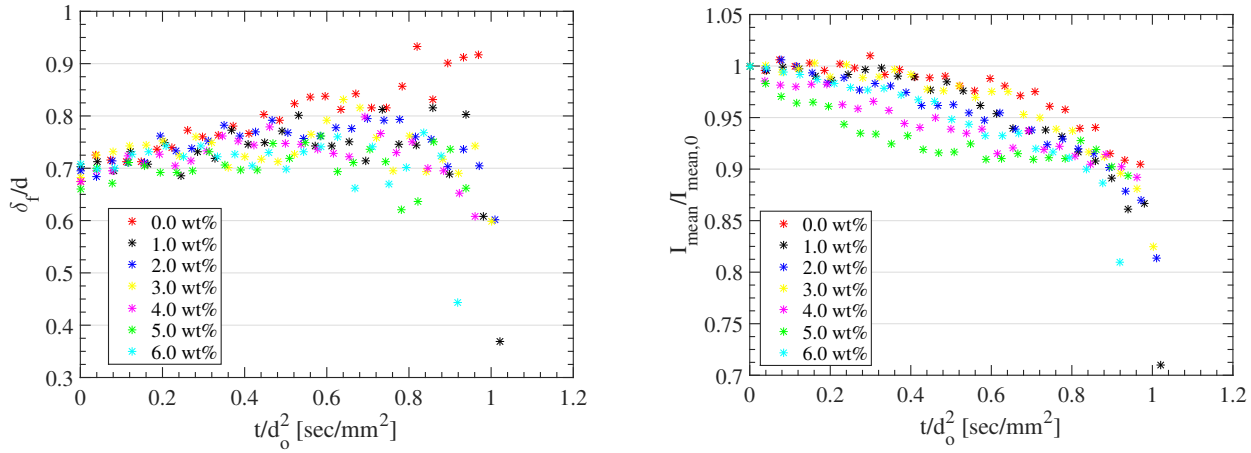

(a) (b)

Figure 3.10: Evolution of the normalized a) chemiluminescence intensity and b) flame standoff distance for nanofuels containing nAl.

Next results for the addition of inert $nSiO_2$ and agglomerate will be presented. For these mixtures only 1-3wt% was used because of the large amount of the particle build up. Figure 3.11 has simultaneous visible and OH* chemiluminescence images for concentrations of 1wt% and 3wt%. Similar to the nAl cases agglomerates can be seen ejecting from the droplet/fiber, but they do not ignite as the particles cross the flame zone due to its higher melting and ignition temperature. The $nSiO_2$ residues left on the fiber did not melt or burn at burnout of the droplet, which is quite different from the observations in the presence of nAl. At the higher loading concentrations, $nSiO_2$ residual forms a shell-like structure which can be seen in Figure 3.11.b at time 1.2873 sec. Once the shell is formed the liquid fuel continues to burn adjacent to the $nSiO_2$ shell, but the visible region in which liquid fuel exists does not change size anymore, which provides evidence that shell is porous so that fuel can diffuse through it. In fact, this structure deforms the droplet from its initially symmetric elliptical shape so that it is no longer axisymmetric and follows the d^2 law. This can be seen in the $(d/d_0)^2$ vs t/d_0^2, Figure 3.12. Burning ethanol droplets with 1 and 2 wt% $nSiO_2$ exhibit similar behavior to the nAl-laden droplets, while 3 wt% $nSiO_2$-ethanol droplet shows a flattening of the d squared plot, reflecting a constant droplet size which produces a reduction in the K

value at about 50% of the burning time when the severe droplet deformation occurs.

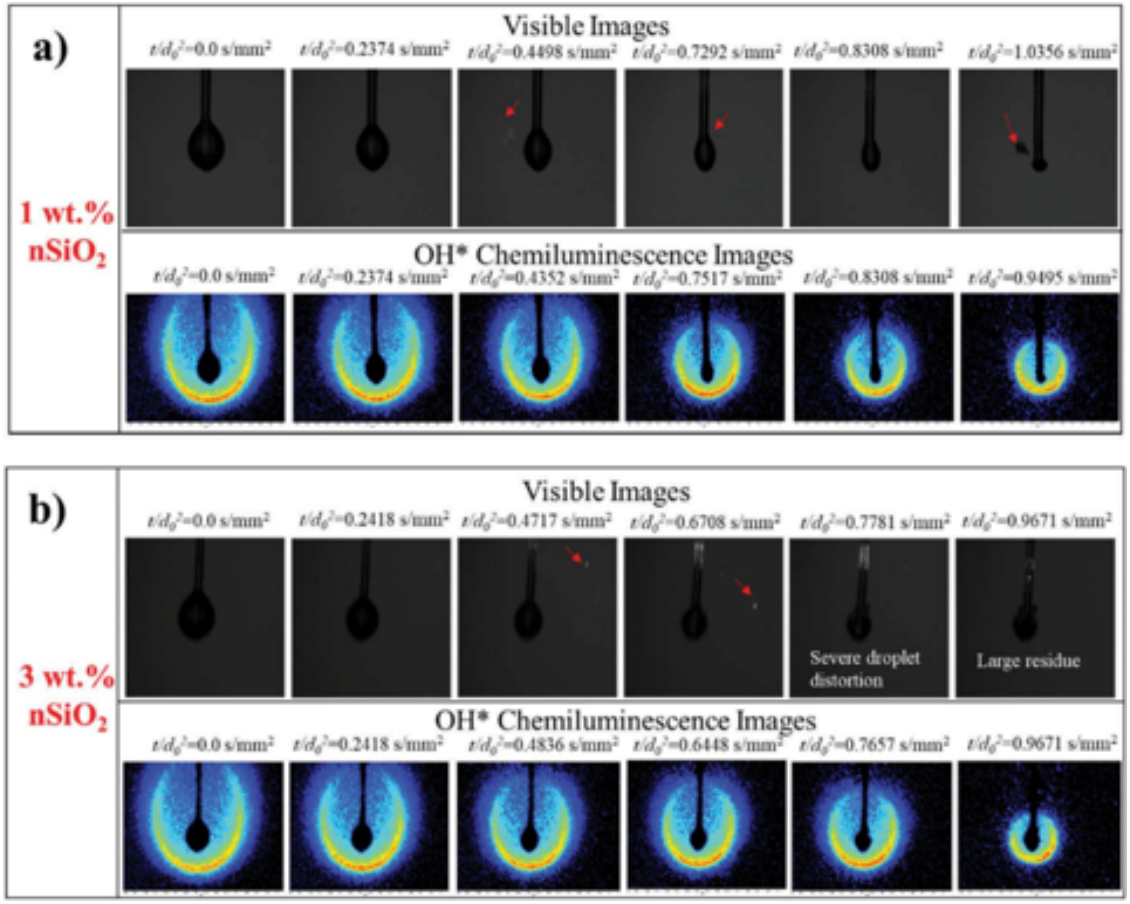

Figure 3.11: Simultaneous visible and OH* chemiluminescence images depicting the droplet regression for mixtures of a) 1 wt% & b) 3 wt% $nSiO_2$ (case I).

Figure 3.13 shows trends in flame standoff distance and evolution in chemiluminescence intensity over time. Normalized intensity profiles indicate that the addition of $nSiO_2$ have a faster decay after the initial burning of the droplet, similar to that seen for nAl additives.There is also a non-systematic reduction in intensity with increasing concentrations of $nSiO_2$, as observed for nAl, but the addition of the particles appears to indicate some level of increase in depletion of oxygen. The standoff distance shows the same tends as that of neat fuel and ethanol with nAl. Overall, however, the visible reduction in the slope of the lines

in Figure 3.12 with increasing $nSiO_2$ concentration in the early stages is not as significant as for nAl, as will be discussed below.

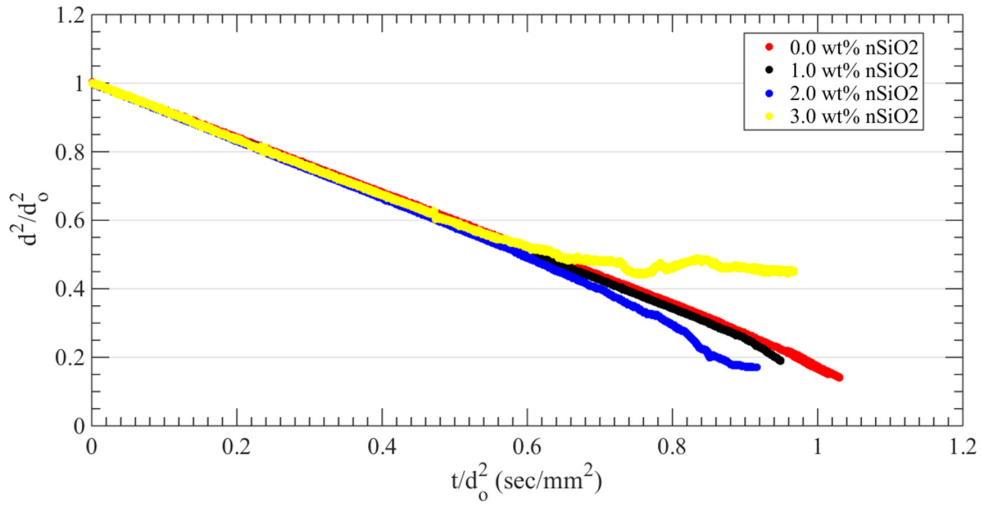

Figure 3.12: Normalized droplet diameter regression for $nSiO_2$ concentrations of 1-3 wt% (case I). One representative neat fuel case is show in red.

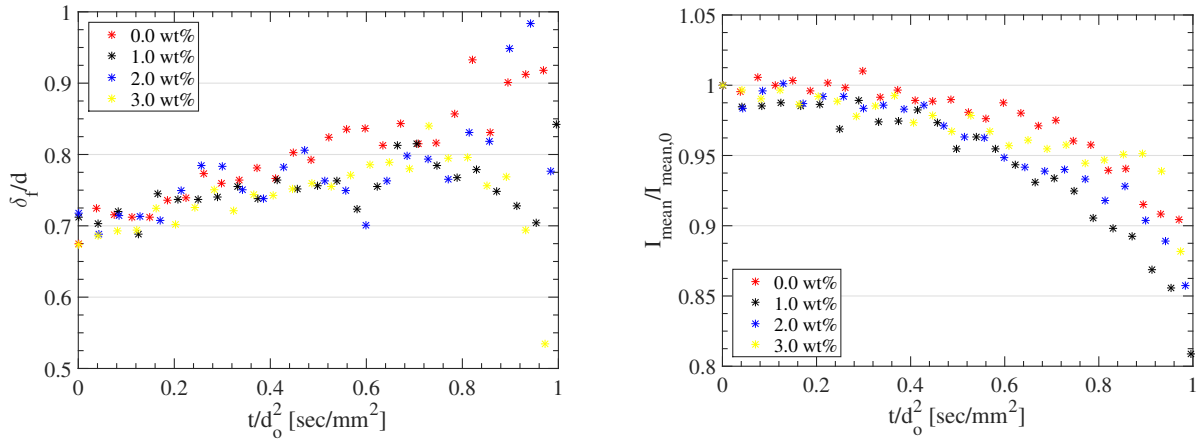

(a) (b)

Figure 3.13: Evolution of the normalized a) chemiluminescence intensity and b) flame distance for nanofuels containing $nSiO_2$.

3.2.2 Case II: Droplet suspended from a quartz capillary

Experiments for burning ethanol droplets suspended at the end of the quartz capillary but without continuous fuel delivery were performed for various concentrations of nAl, as in case I, to enable study of the effects of a larger diameter suspension device (with an outer diameter of 0.64 mm, vs. the quartz fiber diameter of 0.24 mm). When nano Aluminum additives are introduced to capillary suspended ethanol droplets the burning rates similar trends to case I were found. Figure 3.14 shows the variation in the normalized droplet diameter squared as a function of scaled time for the neat fuel and for fuel with 1, 2, 3 and 4 wt.% nAl as examples. Droplets suspended from the capillaries exhibited the same trends in the decay in diameter as in case I in that the evolution of the droplet diameter followed the d2 law prior to initiation of particle expulsion. Overall, the $(d/d_0)^2$ trends are consistent with previous case with the addition of nAl, higher loading concentrations have steeper slopes.

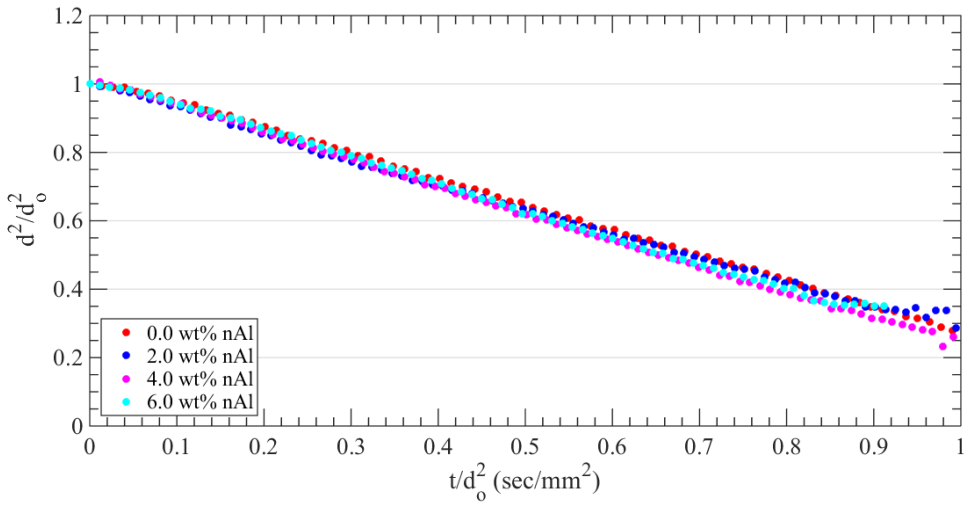

Figure 3.14: Normalized droplet diameter regression for nAl concentrations of 2, 4, 6 wt% (case II). One representative neat fuel case is show in red.

3.2.3 Case III: Continuously fed droplet via a quartz capillary

Combustion processes for fed droplets without and with inclusion of nAl and $nSiO_2$ additives are shown in Figures 3.6, 3.15, & 3.16. For continuously fed droplets with additives, two distinct stages of the burning process were identified: (1) one with quasi-steady combustion and a relatively unchanged effective droplet diameter, and (2) a stage with clearly unsteady combustion processes and a decay in droplet size due to jet/ligament ejection, causing droplet deformation. As shown in Figure 3.15.a, at 1 wt.% nAl, there was a downward jetting of fluid from the bottom of the droplet which first occurred at a scaled time (t/d 2) of 4.4201 s/mm2, followed by the appearance of distinct particle combustion near the ethanol envelope flame, which continued in time. The initiation of distinct burning particle agglomerates led to transient behavior such as droplet distortion and a reduction in effective droplet diameter. The presence of jetting transported nAl particles from the liquid into the flame zone. The associated reduction in droplet size would effectively increase the burning rate constant determined at a fixed volume flow rate. For high concentrations of nAl, jetting caused droplet–flame instabilities to be initiated sooner, more severely, and more frequently than for lower concentrations. As indicated in Figure 3.15.c, for example, OH* chemiluminescence images with 5 wt.% nAl show that the expulsion of particles and liquid ligaments from the droplet significantly perturbed the diffusion flame. At burnout, a large degree of particle residue was built up outside of the capillary for both nAl and $nSiO_2$ laden droplets.

For $nSiO_2$ additives, a concentration of 1 wt.% did not significantly alter the flame or droplet dynamics, as depicted in Figure 3.16.a. But in Figure 3.16.b, for 3 wt.% $nSiO_2$, formation of droplet ligaments as well as severe droplet deformation were apparent. Here, the particles were found to accumulate in the upper part of the droplet during combustion and formed rigid, porous structures within and at the surface of the droplet over the burning period of several seconds.

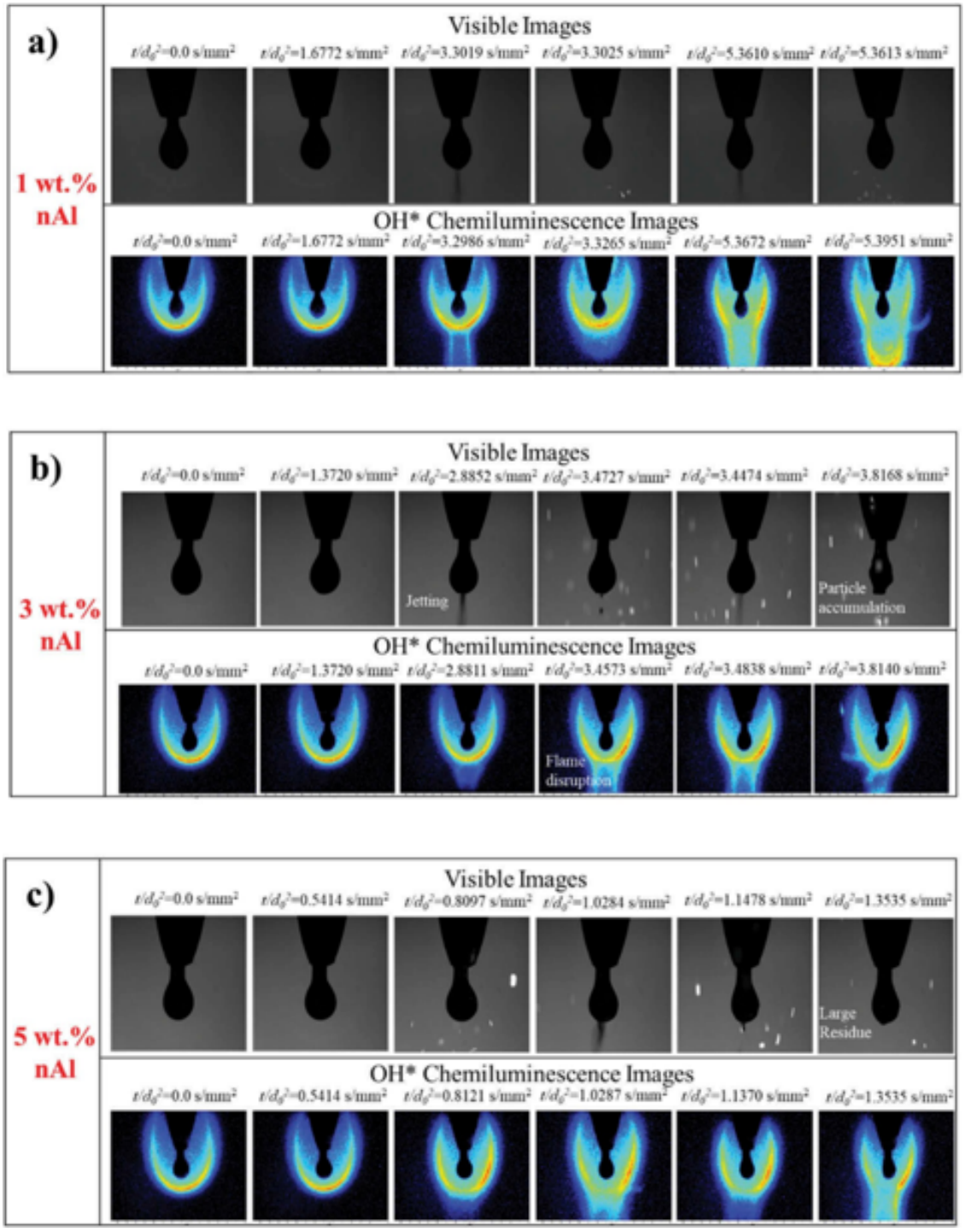

Figure 3.15: Simultaneous visible and OH* chemiluminescence images depicting the droplet regression for a mixtures of a) 1, b) 3, & c) 6 wt% nAl (case III).

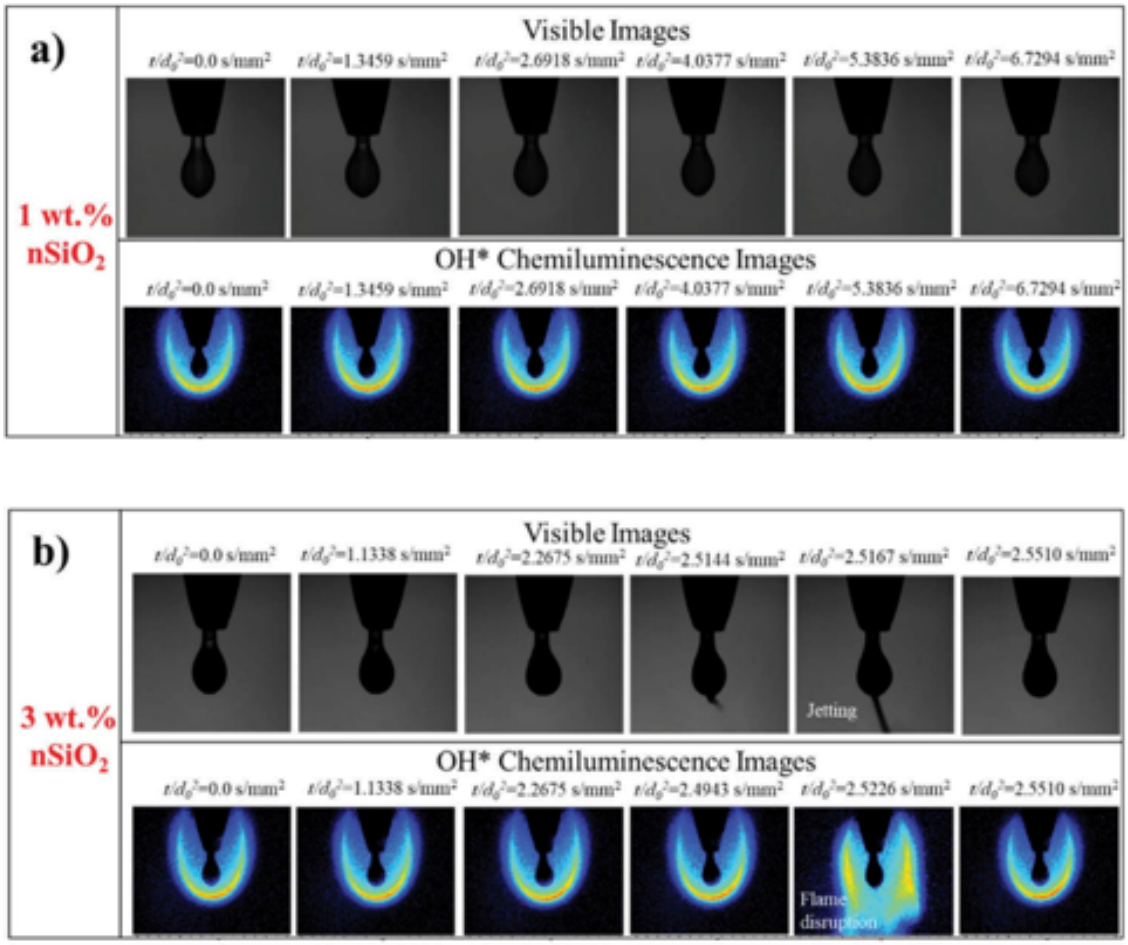

Figure 3.16: Simultaneous visible and OH* chemiluminescence images depicting the droplet regression for a mixtures of a) 1 & b)3 wt% $nSiO_2$ (case III).

Figure 3.17 and 3.18 shows the variation of the square of droplet diameter plotted as a function of scaled time for the continuously fed droplet with various concentrations of nAl and $nSiO_2$. In Figure 3.17, droplets with nAl showed quasi-steady combustion, that is, an approximately constant droplet diameter, for approximately 5–15 sec., depending on the concentration. After this, the droplet experienced swelling and shrinking cycles noted above, followed by an overall decrease in the effective droplet diameter as determined via backlit visible imaging. In contrast, for droplets with 1 and 2 wt.% $nSiO_2$ as in Figure 3.18, the droplet diameter remained nearly constant, with quasi-steady combustion for about 20

sec. without exhibiting significant droplet deformation or diameter alteration. But at 3 wt.% $nSiO_2$, abrupt changes in the diameter due to fuel jetting and other phenomena were observed, as shown in the images in Figure 3.18. Based on these later stage alterations in the droplet shape for higher loading concentrations of nAl and $nSiO_2$, the burning rate constants were extracted for case III using Eqn. 2.4 applied during the quasi-steady combustion period only, when the droplet itself was more likely to be symmetrical about the suspension rod or capillary.

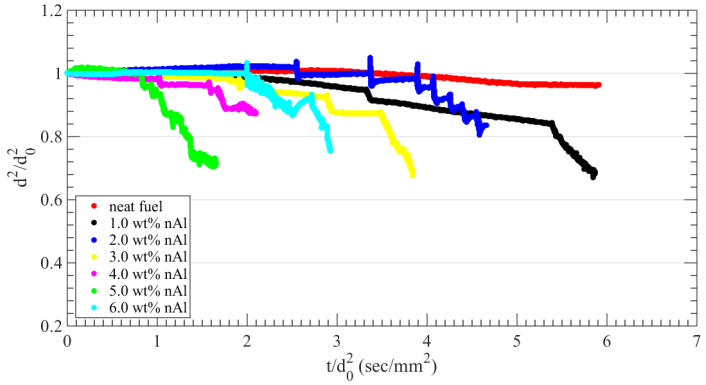

Figure 3.17: Normalized diameter vs time profiles for continuously fed nAl laden droplets (case III).

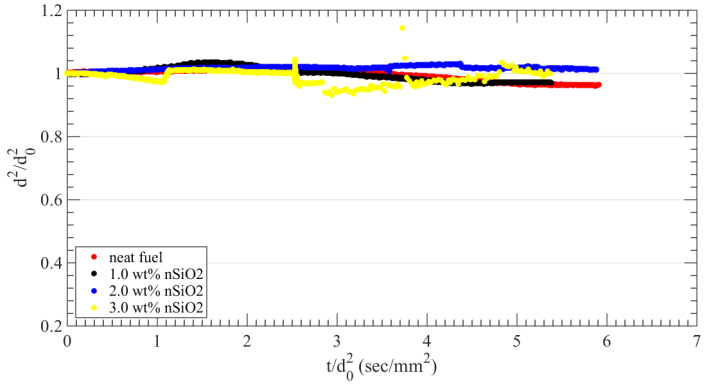

Figure 3.18: Normalized diameter vs time profiles for continuously fed $nSiO_2$ laden droplets (case III).

3.2.4 Summary

The resulting values of burning rate constant K for all the nanofuel concentrations and for the three different experimental procedures are summarized in figure 3.19 and 3.20 for nAl and $nSiO_2$, respectively. Lower concentrations of nAl (below 3 wt %) only appeared to increase K slightly for all three cases. But in the case of continuously fed burning droplets, higher concentrations of nAl, at or above 3 wt%, were observed to improve K by up to 13%, depending on the nAl concentration. Continuous feeding maintains the droplet at an effectively constant size, and the internal circulation created by feeding appears to delay the agglomeration of particulates seen in non-fed burning droplets while simultaneously enabling the nAl addition to contribute to increases in burning rates.

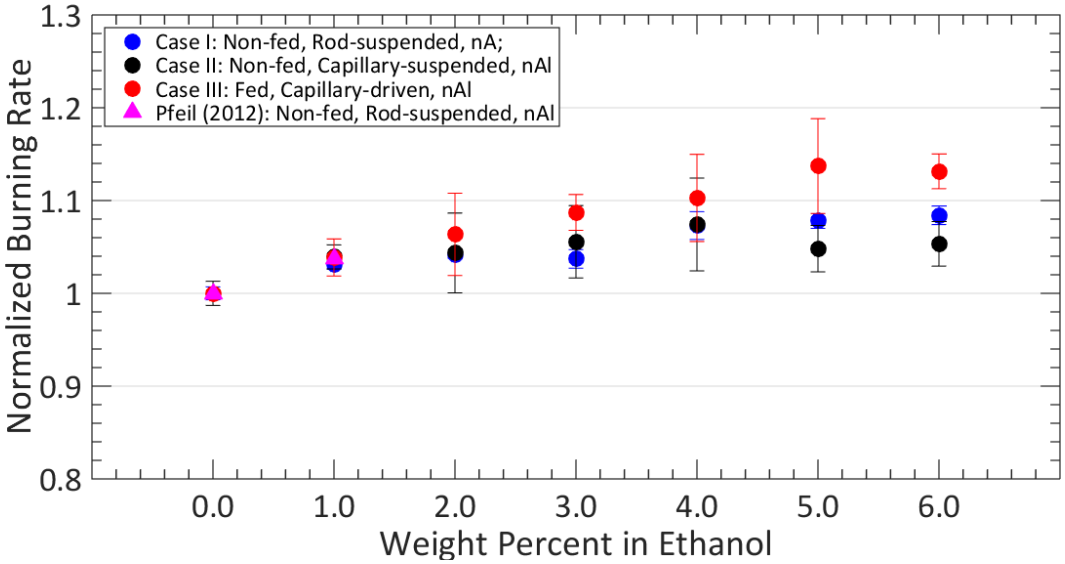

Figure 3.19: Effect of nAl additives on K with varying concentration for three different fuel delivery methods.

Figure 3.20 summarizes the burning rate of ethanol plus $nSiO_2$. In case I ($nSiO_2$), the highest enhancement of 2.5% was achieved at 2.0 wt% and there was no further increase in K at 3.0 wt%. Case III at 1 wt.% $nSiO_2$ increased the burning rate constant by 5%, whereas 2 wt% and 3 wt% did not show any enhancement in K when compared with the

baseline. The relatively small increases in burning rate constants with increasing loading concentration, even for $nSiO_2$, are consistent with separate modeling study results [32]. But increases in burning rate constant, especially with higher loading concentrations, are greater for the energetic nAl additives than for inert $nSiO_2$ additives.

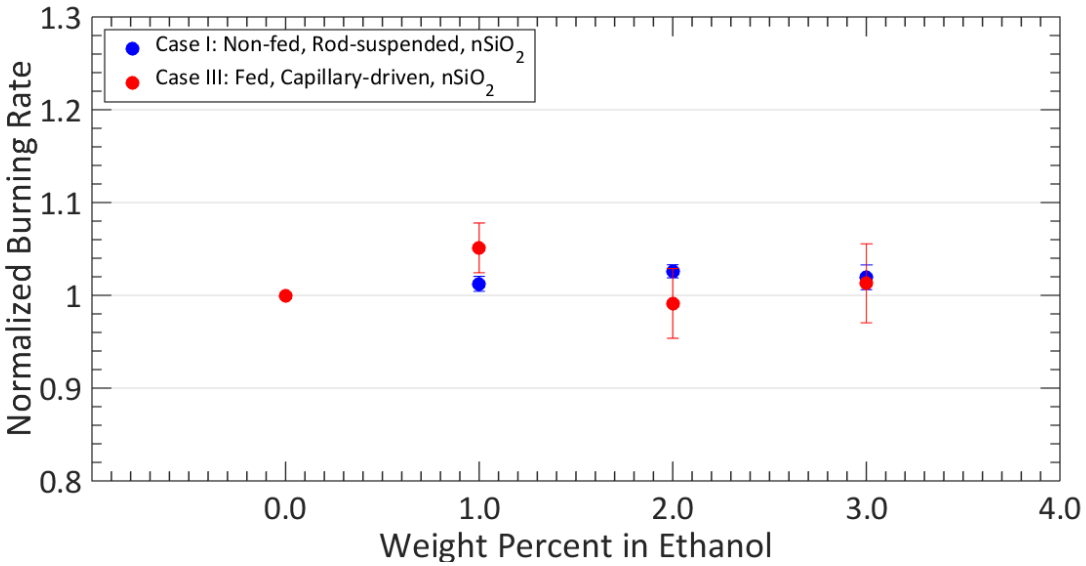

Figure 3.20: Effect of $nSiO_2$ additives on K with varying concentration for three different fuel delivery methods.

3.3 TEM Imaging

Figure 3.21 shows TEM images of nAl before and after combustion when dispersed in ethanol droplets, which can assist in interpreting the previous results. Transmission electron microscopy (TEM T12 quick cryoEM) is used to determine the microscopic morphology of nAl and their aggregates after combustion, and this imaging was performed by Dr. Hyung Sim, a postdoctoral researcher in the UCLA Energy and Propulsion Research Laboratory. The TEM image of the as-received nAl had a particle size range from a few tens of nanometers to about 100 nm as well as an oxide shell (2-5 nm) on the Al core in many cases; the advertised diameter of the nAl was 80 nm. Compared with the unreacted particles, the irregular shapes

of the reacted particles in the residue were found as clusters in the TEM images, suggesting that the oxide shell may have ruptured and that at least some of the Al core was oxidized during the combustion of the droplets. Large agglomerates of unreacted and/or partially reacted particles were also observed in the residue. There were no significant differences among the reacted residue resulting from the three different experimental methods for performing these experiments. Separate scanning electron microscope (SEM) imaging conducted by Dr. Sim will enable both surface topography and elemental analysis (via Energy Dispersive Spectroscopy or EDS) to be performed for these various samples.

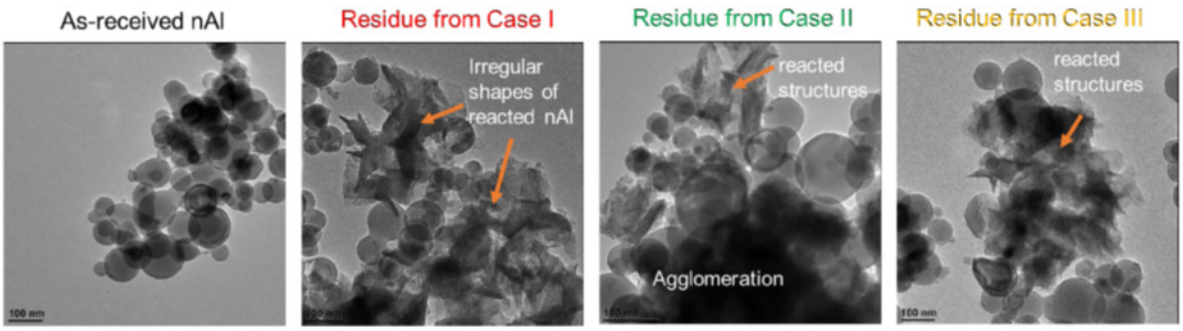

Figure 3.21: TEM images of the nAl residue from different experimental conditions.

3.4 Flame Temperature Analysis

In addition to measuring the droplet temperature, a theoretical analysis of the adiabatic flame temperature for mixtures was calculated using the NASA Chemical Equilibrium with Applications (CEA) [96] online program. Both mixtures of bulk aluminum and silica with ethanol were explored up to 6 wt%. It is assumed that the bulk material and ethanol burn simultaneously, at constant pressure (1 atm) and an initial temperature of 300 K. At an equivalence ratio of unity, most relevant to the diffusion flame in this study ($\phi = 1$), the addition of 6 wt% nAl increases the flame temperature by approximately 55 K from 2195

K to 2250 K, while the addition of 6wt% $nSiO_2$ does not change the flame temperature, 2187 K, with respect to the neat fuel case. If in fact some of the aluminum core of the nanoparticles burn in the vapor phase, per the Glassman criterion, this could cause an increase in the nanofuel droplet flame temperature. Therefore, driving the surface of the droplet to evaporate faster.

3.5 Droplet Temperature Measurements

The droplet temperature was measured for neat fuel, nAl + ethanol, and $nSiO_2$ + ethanol, explain some of the differences observed in burning rate constant K and other features of the combustion process. A history of droplet temperature was measured by forming a droplet on a thermocouple bead during droplet combustion; this method was used to replicate the conditions of case I. From table A.6 the boiling temperature of ethanol is 351 K, and it is expected that the droplet remains below this temperature during quasi-steady combustion in order to sustain a liquid droplet. Figure 3.22 depicts the results, where in the four tests shown the droplet temperature reaches a temperature of approximately 343 K at the 2-4 seconds range. This corresponds to the quasi-steady combustion of the droplet. The later part of the temperature, where the temperature spikes and then drops profile is not accurate because when the droplet becomes small the TC junction may be exposed to the flame before the droplet has fully evaporated. The addition of nanoparticles did not change the temperature of the droplet substantially, which tells us that the boiling temperature is not altered to any significant degree with the addition of low concentrations (1-6wt%) of nanoparticles. Table 3.2 has the summary of droplet temperatures during the quasi-steady combustion portion of the droplet lifetime; a minimum of three tests were used to obtain the average.

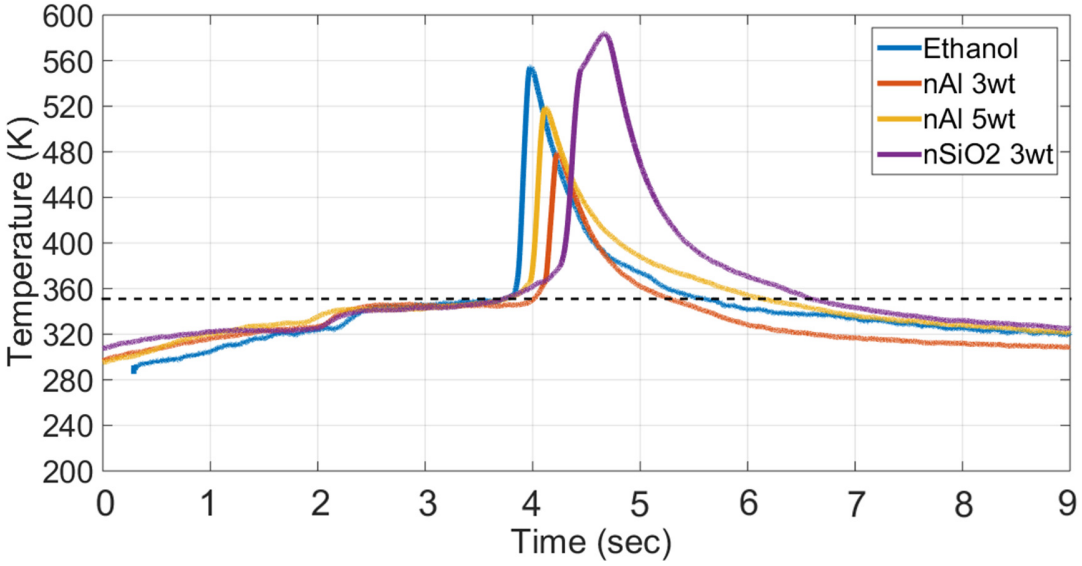

Figure 3.22: Temperature evolution of the droplet suspended from thermocouple bead for various droplet conditions (neat fuel, nAl at 3 wt% and 5 wt%, and $nSiO_2$ at 3 wt% concentration). Dashed line represents the boiling temperature of pure ethanol.

	neat fuel	1 wt% nAl	3 wt% nAl	5 wt% nAl	3 wt% $nSiO_2$
Temperature [K]	345.89	344.59	343.70	343.01	343.51

Table 3.2: Average droplet temperature for quasi-steady portion of droplet lifetime.

3.6 Theoretical Burning Rate Comparison

This section is take from recently published paper [32]. Figure 3.23 summarizes the effects of particle loading concentration, particle type, and droplet forming methods on the average K values from experimental measurements, and these results are also compared with theoretical calculations. Data were normalized by the average baseline burning rate constant without additives, $K_{noadditive}$. The average K for 1 wt.% nAl in the present fiber-suspended droplet experiments (case I) agrees well with the value of K for the same conditions and methods in the experimental studies by Pfeil et al. [41]. For case I experiments, the addition of nAl

systematically increased K by up to 8.5% with increasing loading concentration; in contrast, inclusion of $nSiO_2$ produced a maximum enhancement in K of 2.5%, achieved at 2.0 wt.% $nSiO_2$, with no further increase in K at 3.0 wt.% $nSiO_2$. For other nonfed experiments, as in case II, K was observed to increase by as much as 7.4% at 4 wt.% nAl relative to the baseline. At 5 and 6 wt.% nAl, there was no further increase in K values, likely due to formation of aggregates that appeared to influence the structure of the droplet to a greater degree than for the fiber-suspended droplets in case I. It should be noted that for nAl additives, there seems to exist a critical concentration for maximized K values, at loading concentrations around 4–5 wt.%, above which a reduction in K was observed. Per imaging results, this was likely due to the formation of aggregates, especially in the vicinity of the droplet surface, which could suppress evaporation, as noted in other studies [28].

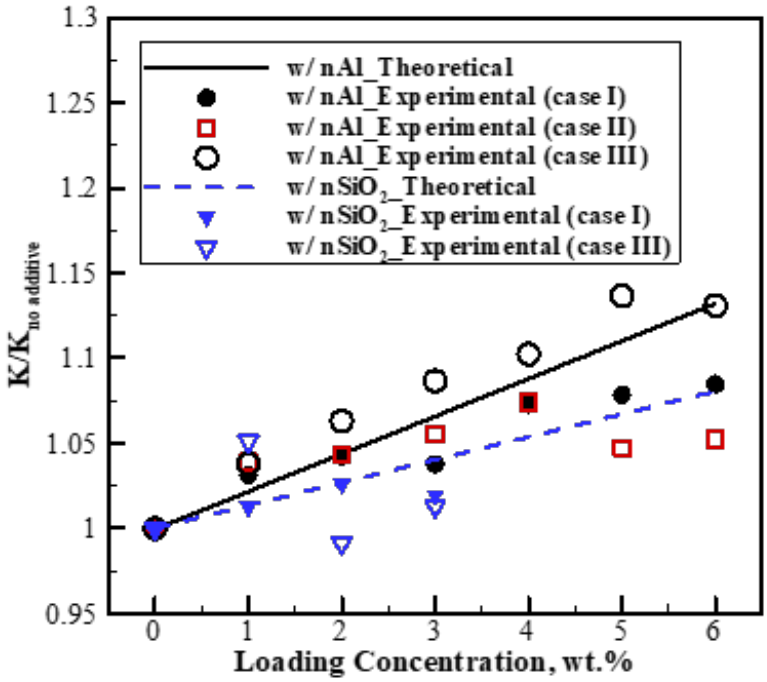

Figure 3.23: Comparison of K values for theoretical calculations and experimental measurements (from cases I to III) for burning nAl and $nSiO_2$ laden ethanol droplets at various particle concentrations.

Figure 3.23 indicates that fed droplets (case III) with nAl exhibited the same trends as the nonfed droplets in the sense that K systematically increased, by up to 13.6%, with increasing nAl concentrations. Larger values of K in fed droplets with NPs could possibly be attributed to enhanced internal circulation within the droplet during fuel delivery, with a documented delay in particulate agglomeration and aggregation which could have enabled energetic NPs to have a greater influence on the liquid droplet. In contrast, while Figure 11 shows that the inclusion of 1 wt.% $nSiO_2$ raised the burning rate constant by 5%, the addition of 2 and 3 wt.% $nSiO_2$ did not show any enhancement in K compared with the baseline. For increasing concentrations of $nSiO_2$ in ethanol, the increasingly prominent residual shell structure within and adjacent to the droplet surface appeared to reduce the effective vaporization of ethanol, especially at later times.

The theoretical (predicted) burning rate constant K_0 for nonfed burning ethanol droplets with nAl and $nSiO_2$ additives compared reasonably well with experimental measurements, as indicated in Figure 3.23. For a pure ethanol droplet, K_0 was found to be approximately 0.74 mm2/s, in reasonably good agreement with the current experimental measurements. The simple combustion model showed that inclusion of nAl particulates could increase the burning rate constant by up to 13.3% with increasing loading concentration but that the addition of $nSiO_2$ would produce a predicted maximum enhancement in K of 7.2% (associated with 6 wt.% $nSiO_2$, which was not possible to sustain in the present experiments). This theoretical approach suggested that both nAl and $nSiO_2$ could enhance thermal properties, resulting in higher vaporization rates relative to the neat fuel during combustion. But compared to inert $nSiO_2$, the energetic nAl produced an increased flame temperature and heat of combustion. Yet even $nSiO_2$ additives at low concentrations produced increases in K_0, comparable to those observed in experiments for nonfed droplets; changes in thermal conductivity appeared to be the primary reason for the increases in K.

CHAPTER 4

Reacting Jets: Experimental Setup and Methods

4.1 Facility

The present studies were performed using a newly designed fundamental atmospheric combustion facility at the Air Force Research Laboratory (AFRL/RQR) located at Edwards Air Force base. This facility was designed to study turbulent gaseous non-premixed (diffusion) flames generated by a variable exit burner with different geometries. It is equipped with a high-pressure supply line of ambient temperature nitrogen, air, oxygen, and methane. A chamber to house the jet and acoustic field sits above the burner.

Experiments were performed to explore the behavior of reacting methane jets in the presence of an acoustic field under normal atmospheric conditions. In the following subsections, a description of the acoustic chamber, gas burner, and flow system will be given. An overview of the acoustics field generation and image visualization techniques are then discussed. Next, the analysis used on the recorded high-speed images is presented. Finally, the experimental errors and their propagation to the measured quantities are discussed.

4.1.1 Acoustic Waveguide

A schematic of the experimental facility is shown in Figure 4.1. The acoustic waveguide sits on top of an optical table and is elevated 76.2 mm with four stands. The waveguide is fabricated from 6.35 mm (1/4 in.) and 12.7 mm (1/2 in.) thick aluminum sheets. The walls were made of sectional pieces of aluminum sheets so that the length could be modified

to change acoustic resonances. For this study only one configuration was used; the inner dimensions of the waveguide were 914.4 mm x 355.6 mm x 108.0 mm. Inside two horizontal baffles (not shown) were placed in the center of the channel to suppress vertical acoustic modes. These baffles are made of aluminum having dimensions of 254 mm x 104.8 mm x 3.2 mm (see Figure B.3). The burner, to be described in a later section, is located at the geometric center of the acoustic channel. The general acoustic waveguide design is motivated by the facility designed and used by O'Connor [98], and also bears similarities to the acoustic waveguide/reactive flow configuration used at UCLA for both liquid droplet and gaseous fuel jet experiments.

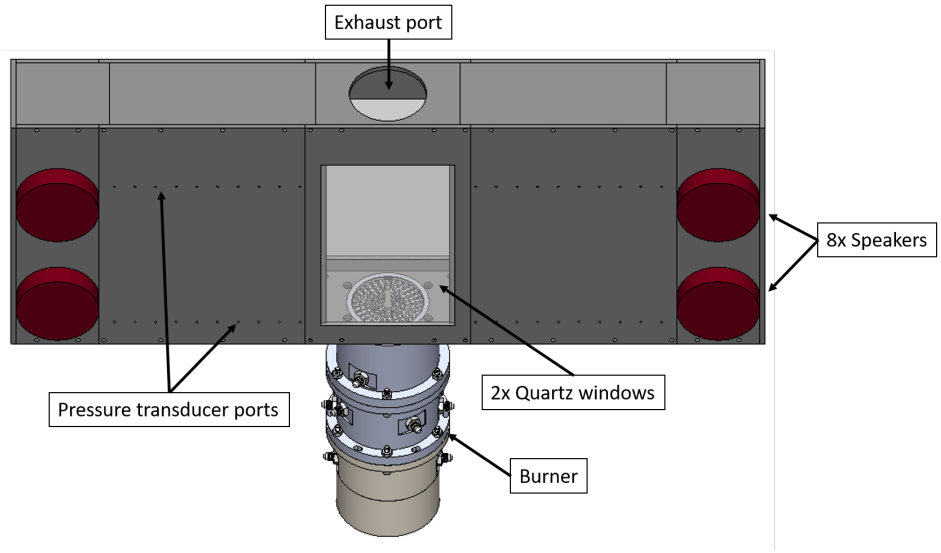

Figure 4.1: CAD assembly illustrating details of the acoustic channel and burner.

Various access points were incorporated into the design of the waveguide to accommodate data acquisition and an exhaust exit. Optical access is made possible through multiple quartz windows used for imaging and laser entry. Two large rectangular (165.1 mm x 279.4 mm x 6.35 mm) quartz windows give imaging access to the reacting jet. For pressure measurements, two rows of pressure transducer ports are located at heights of 6.35 mm and 152.4 mm in reference to the bottom floor. An exhaust port with a diameter of 88.9 mm is positioned concentrically above the burner exit. The acoustic drivers (speakers) were threaded directly

to the side walls. Threaded through holes for the speakers were machined symmetrically on both ends of the waveguide (4 on each end); the exact location of these holes is 88.9 mm from the top/bottom edge and 50.8 mm inside from the channel ends. One ignition port with diameter of 25.4 mm is located on the back side of the channel near the bottom wall. Lastly, nitrogen purges introduced near the acoustic drivers push the gases inside the channel toward the exhaust port to protect the drivers and to force variations in the speed of sound caused by the presence of the flame to remain located near the center of the channel. Appendix B includes a technical drawing of the acoustic waveguide.

4.1.2 Waveguide Characterization

The waveguide was designed to produce one-dimensional transverse acoustic waves but departures from this ideal exist due to the presence of the exhaust port and the burner volume. Initially the length of the channel was chosen based on resonance frequencies in a rectangular cavity with rigid boundaries,

$$f_a = c\sqrt{\left(\frac{n_x}{2L_x}\right)^2 + \left(\frac{n_y}{2L_y}\right)^2 + \left(\frac{n_z}{2L_z}\right)^2}, \tag{4.1}$$

where f_a relates to the waveguide dimensions, $L_{x,y,z}$, integers $n_{x,y,z}$, and the ambient speed of sound c. To create an acoustically resonant condition with maximum pressure perturbations, then the frequency must correspond to one of the frequencies in Eqn. 4.1 [99]. The reference coordinate system used for this analysis is as follows; L_x represents the length (transverse) direction, L_y represents the height, and L_z is the width of the waveguide. The goal of this study was to apply transverse forcing therefore both n_y and n_z are set to zero to find the theoretical acoustic frequency $f_{a,th}$ and wavelength λ_{th}. Equation 4.1 simply becomes

$$f_a = \frac{cn_x}{2L_x}, \tag{4.2}$$

where n odd integers correspond to the pressure node (PN) resonances (e.g. n = 1, 3, 5 etc.) and even integers correspond to the pressure anti-node (PAN) resonances (e.g. n = 2, 4, 6 etc.).

The length of the waveguide took into consideration the frequency range of the speakers and the physical space in the facility. With a length of 27.94 cm, the possible resonant frequencies (refer to table 4.1) were within the frequency range of the speakers (Galls SK144), which was reported by the manufacture to be 200-5,000 Hz. See Figure B.4 for manufacturer's published frequency response for each speaker. Just as important, the flow field could still be considered acoustically compact (where the characteristic length scale of the flow is significantly lower than that of the acoustic wavelength). Here the compactness is in reference to the transverse direction in which the acoustics were applied and the propellant injection diameters. See the third and fourth columns of table 4.1 for the detailed frequencies that are theoretically achievable in the transverse direction.

Table 4.1: Theoretical and experimental resonant frequencies and wavelengths.

Transverse Waveguide Resonance ($n_{y,z} = 0$)							
		1D Theoretical		3D COMSOL		Experimental	
n_x	L_x	$f_{a,th}$ [Hz]	λ_{th} [cm]	$f_{a,comsol}$ [Hz]	λ_{comsol}	$f_{a,exp}$ [Hz]	λ_{exp} [cm]
1	.9144	188	1.83	189	1.8	-	-
2	.9144	375	0.91	363	0.94	375	0.92
3	.9144	563	0.61	567	0.60	571	0.60
4	.9144	750	0.46	750	0.46	775	0.44
5	.9144	938	0.37	941	0.36	942	0.36
6	.9144	1125	0.30	1116	0.31	1150	0.30
7	.9144	1313	0.26	1318	0.26	1314	0.26
8	.9144	1500	0.23	-	-	-	-
9	.9144	1688	0.20	1693	0.20	-	-
10	.9144	1876	0.18	-	-	-	-
11	.9144	2063	0.17	2066	0.17	-	-

In order to investigate three dimensional effects and departure from the theoretical one dimensional frequencies a simulation of the waveguide was performed using COMSOL Multiphyics, a finite element solver. First the CAD model was imported into the software (see 4.2.a). Features such as propellant tubes, burner volume, exhaust port, and baffles were included in the model. The acoustic mode shapes of the geometry are solved using the Helmholtz equation in the frequency domain. The boundary conditions were all selected to

be hard wall boundaries. The exit port is represented by using a closed pipe with the same diameter and with an effective finite length to best represent an open flange port [99]. The (gas) used was nitrogen at standard temperature and pressure. Examples of the first two modes of the standing acoustic waves from this type of simulation are given in Figure 4.2b and 4.2c for the first pressure node condition (n = 3, frequency 567 Hz) and first pressure anti-node condition (n = 2, frequency 363 Hz), per table 4.1. See table 4.1 for other transverse modes found in this simulation.

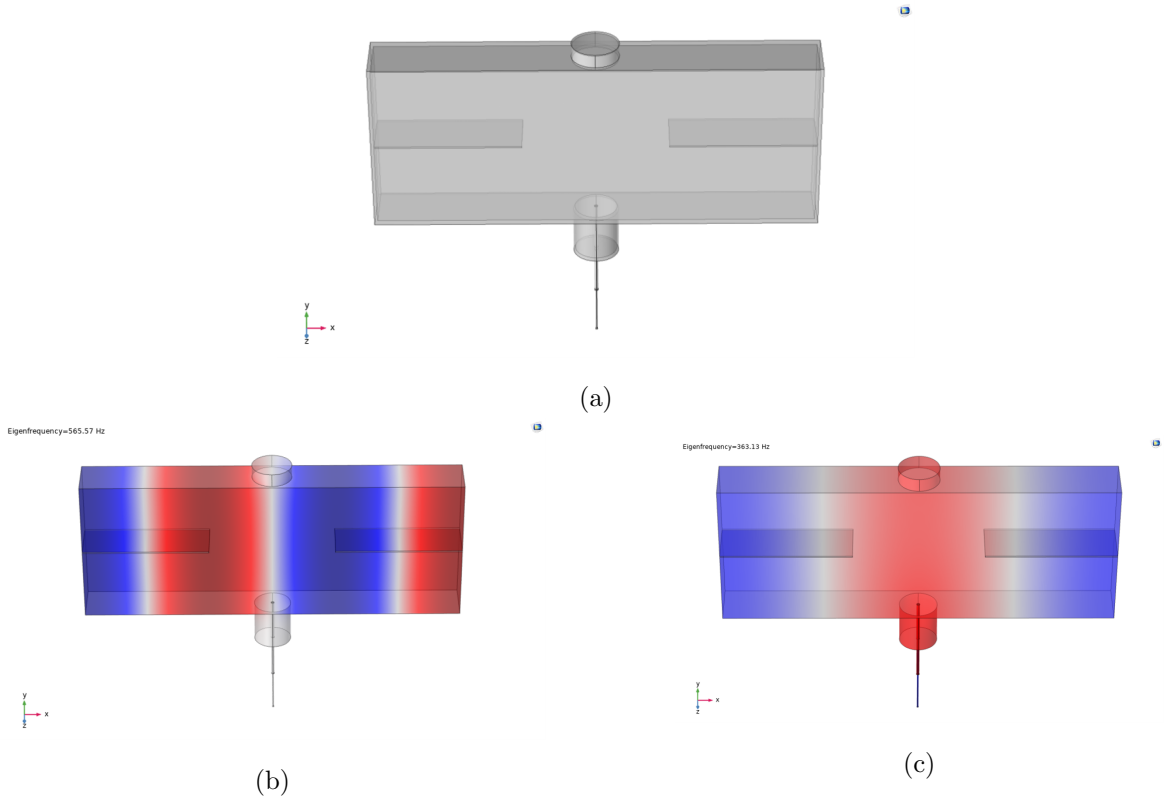

(a)

(b)

(c)

Figure 4.2: Comsol Multiphysics acoustic simulation of (a) combustion geometry, (b) amplitude of pressure fluctuations is shown for n_3 at frequency 567Hz, and (c) amplitude of pressure fluctuations is shown for n_2 at frequency 363Hz

To complete the characterization of the acoustic waveguide an experimental frequency analysis was performed without the presence of a reacting jet. First it is established that two different types of transverse standing wave modes can be established inside the waveguide,

pressure anti-node (PAN) phase or a pressure node (PN) phase. When the speakers on both ends of the channel are operated in phase ($\phi = 0°$), standing acoustic waves with a pressure anti-node (PAN) and corresponding velocity node (VN) at the center where the burner is located. Conversely, when the speakers on one end are operated out of phase ($\phi = 180$) with respect to the opposite end, standing acoustic waves with a pressure node (PN) and corresponding velocity anti-node (VAN) are established at the burner exit.

Using five Kulite (XCS-093-10D) miniature differential pressure transducers embedded at several locations along the waveguide, acoustically resonant conditions can be identified for both PAN and PN conditions at the center of the chamber. A frequency sweep over a duration of 236 seconds was used to ramp the oscillation frequency from 100 Hz to 1500 Hz while acquiring data at a rate of 50 kHz. A constant voltage (3 V) was applied to each speaker during this sweep. First the speakers were operated in phase to acquire frequency sweep results for a PAN. Figure 4.3 shows the results of the sweep in terms of a Fast Fourier Transfer (FFT) of a pressure transducer, place at the center location, to qualitatively and quantitatively show the frequencies that produced the highest amplitudes with the common input voltage, these frequencies are taken as the resonant modes of the acoustic waveguide. For PAN conditions at the center of the chamber, significant amplitudes can be achieved near the first even values of the transverse modes ($n_x = 2, 4, 6$) with values of 375 Hz, 775 Hz, and 1150 Hz. Similarly, a sweep was performed for out-of-phase speaker operation (PN), and FFT spectral results for data from two pressure transducers located 63.5 mm on both sides of the center location can be seen in Figure 4.4. For PN conditions at the center of the chamber, significant amplitudes can be achieved near the first even values of the transverse modes ($n_x = 3, 5, 7$) with values of 571 Hz, 942 Hz, and 1314 Hz. Similar results for a pressure transducer placed at the center location are located in Figure B.7. Given that this is a pressure node, there is no significant spectral content. See the last two columns of table 4.1 for the transverse modes found experimentally. There was reasonable consistency between these experimental measurements and both 1D theoretical estimates

and COMSOL-based 3D estimates.

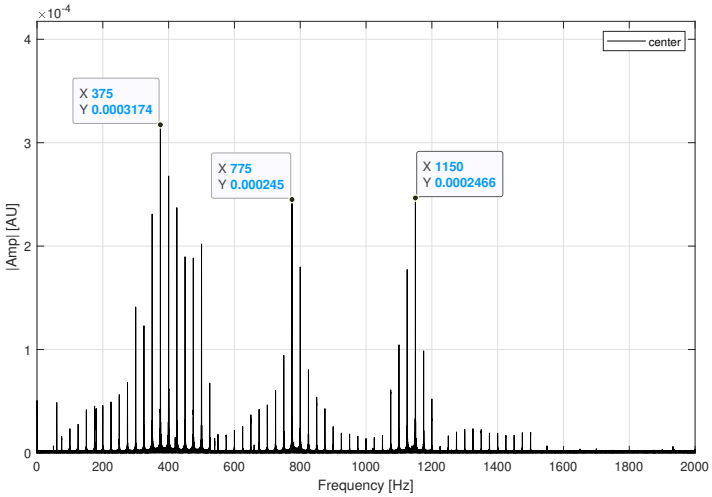

Figure 4.3: Frequency sweep with speakers operated in-phase (0°) and a PAN occurring at the center of the waveguide. A FFT of a pressure transducer located at center of the waveguide at 6.35mm from the floor (bottom row). Resonant frequencies are shown to occur near 375 Hz, 775 Hz, and 1150 Hz.

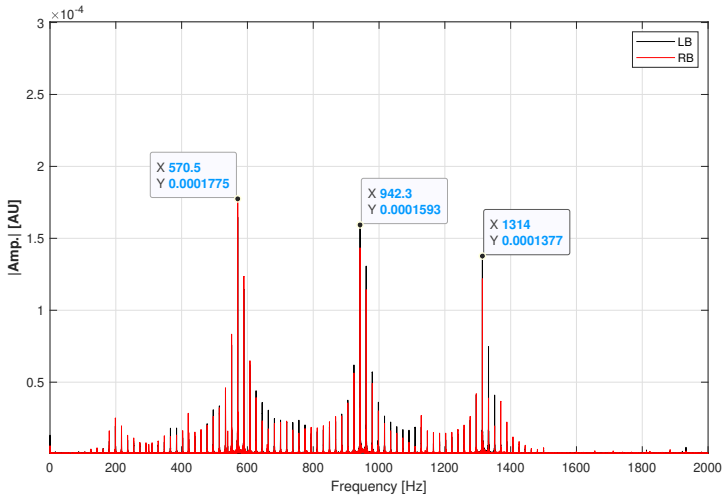

Figure 4.4: Frequency sweep with speakers operated out-of-phase (180°) and a PN occurring at the center of the waveguide. A FFT of two pressure transducer located 63.5mm to the left and right with reference to the center (6.35mm from the floor or bottom row). Resonant frequencies are shown to occur near 571 Hz, 942 Hz, and 1314 Hz.

To ensure the acoustics were in fact nearly one-dimensional standing waves at the noted phases, the waves were characterized by positioning five pressure transducers in the channel. Two transducers were positioned to the right of the jet exit on the upper and lower PT rows of the channel, two transducers were positioned to the left of the jet exit on the upper and lower PT rows, and one transducer was positioned at the jet exit on the bottom row. The wave forms from the five transducers were then examined to confirm their phase and standing nature. Two examples of typical pressure traces are shown in Figure 4.5. It may be confirmed that all wave forms were sinusoidal. For the PN case (Figure 4.5 a) the left and right pressure transducers were placed at the nearest PAN, assuming uniform channel conditions, 12.7 cm from the center. The side pressures are out-out-of-phase and of equal amplitudes as expected. For the PAN case (Figure 4.5 b), the left and right pressure transducers were located nearer to the center at 6.35 cm, too close to be at an anti-node. The side pressures were in-phase, lower in amplitude than the peak at the center, and yet at an appropriate amplitude given the locations of the transducers. Similar analyses were performed for all the frequencies above to confirm PN or PAN status for all conditions.

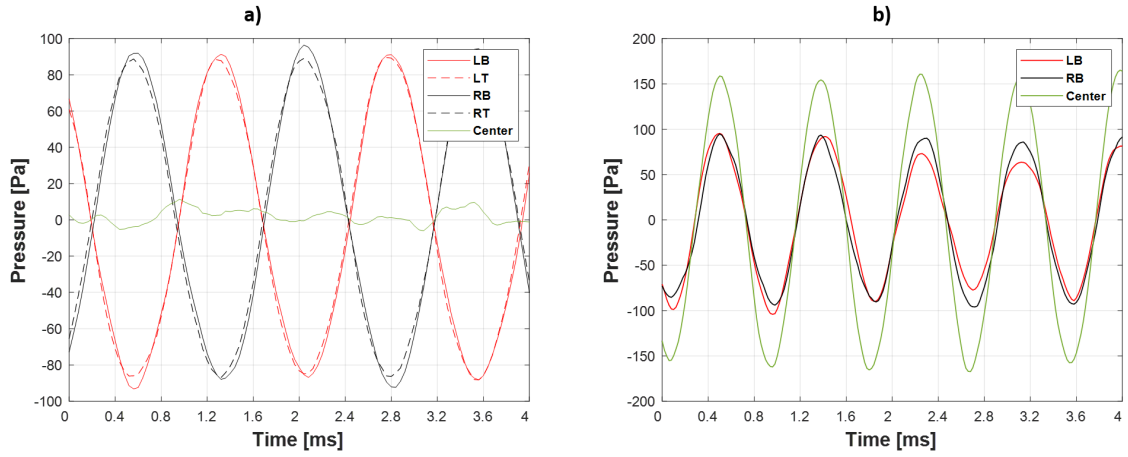

Figure 4.5: Local Pressure transducer measurements, producing a wave form analysis for (a) pressure node at 1314 Hz and (b) pressure anti-node at 1150Hz

Final resonant frequencies for reacting experiments were selected based on several factors such as speaker frequency range, mode mixing, and variability of the acoustics in the presences of a flame. Mode mixing refers to a transverse resonance that coincides with a vertical resonance and therefore both modes can interact inside the waveguide. For PN $n_x = 1$ ($n_{y,z} = 0$), 189Hz, was not used because it was out of the frequency range of the speakers. Additionally, $n_x = 5$ ($n_{y,z} = 0$), 942Hz, was also not used because of its proximity to $n_y = 2$ ($n_{x,z} = 0$) which is estimated to be 964Hz using Eqn. 4.2. Similarly, $n_x = 9$ ($n_{y,z} = 0$), 1688Hz, was not used because of its proximity to $n_z = 1$ ($n_{x,y} = 0$). For the PAN the first three modes,$n_x = 2, 4, 6$, were used without mode mixing. It is important to note that second PAN mode did have a resonance that coincided with the resonance of the center burner tube, this can be seen from the COMSOL results in Figure B.9. Lastly, the final frequencies used to apply forcing to the reacting jet were 360 Hz, 775 Hz, and 1150 Hz for the PAN. For the PN the frequencies were 581Hz, 1348Hz, and 2065Hz. The slight changes at some of the frequencies were modified because of experimental findings comes from adjusting the frequency once the flame was present inside the channel.

4.2 Burner Configuration

The burner system, which could be operated as a single burner with co-flow or a coaxial burner with co-flow consisted of two alternative configurations. Configuration 1 was for a single jet (see Figure 4.6), with a center round tube (inner diameter, $D_{1,i} = 4.0$ mm, post thickness $Tp_1 = 0.36$ mm) surrounded by a minimum velocity co-flow section (outer diameter, $D_{3,i} = 88.9$ mm) to shield the jet from outside entertainment and suppress recirculation. Configuration 2 is a coaxial jet (see Figure 4.7), with a center round tube (inner diameter, $D_{1,i} = 4.0$ mm, post thickness $Tp_1 = 0.36$ mm) and an annular tube (outer diameter, $D_{2,i} = 11.23$ mm, post thickness $Tp_2 = 0.36$ mm) which are surrounded by the same co-flow section (outer diameter, $D_{3,i} = 88.9$ mm). The two concentric tubes are circular in cross-section and were designed to have fully developed turbulent flow at the exit

($L_1 = 305$ mm $L_2 = 254$ mm), using $L/D = 4.4Re^{1/6}$ [100]. The Reynolds numbers (Re) referred to in this study corresponds to the methane jet in the center and is based on the tube exit diameter ($D_{1,i}$), bulk velocity based on mass flowrate, and fluid properties (density and dynamic viscosity) of methane calculated at chamber conditions (atmospheric). The length of the co-flow section in the axial direction is 200 mm, where the metal spheres take up 80.15 mm of the space. In addition, the honeycomb has a diameter of 88.0 mm and is 25.4 mm thick, with a cell to thickness ratio of 8:1. The co-flow is injected such that its velocities lie in the range 0.5-1 m/s. The co-flow consists of either nitrogen or a mixture of nitrogen and oxygen. Both flows are controlled by choked flow conditions upstream of the burner using sonic orifices which provide a constant mass flowrate and well-defined flow and acoustic boundary conditions. Two sets of experiments were conducted, one with configuration 1 and the other with configuration 2. The only difference between the two configuration is the addition of the annular tube with diameter D_2 and the flow of oxidizer gas through that annular region whose velocity could be varied.

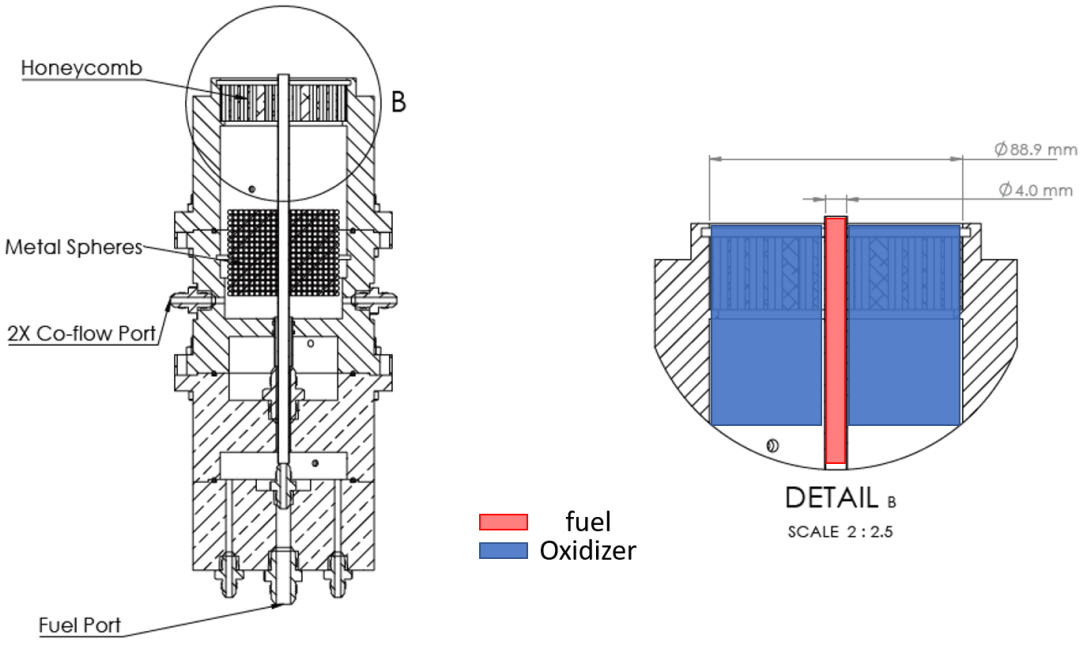

Figure 4.6: Schematic of the burner as a **Single Jet** with co-flow, configuration 1.

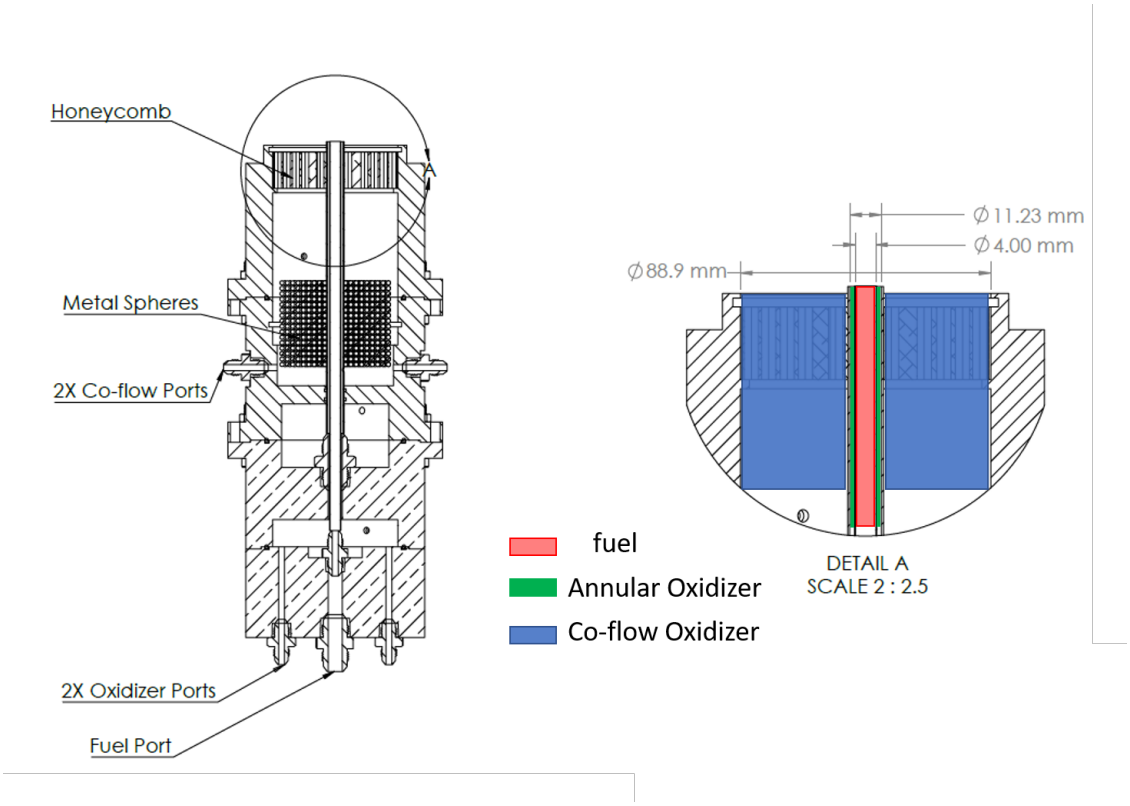

Figure 4.7: Schematic of burner as a **Coaxial Jet** with co-flow, configuration 2.

In order to understand the acoustics for the burner system itself, a simple one-dimensional analysis was used to calculate the natural resonances of the center tube, annular tube, and co-flow volume. First, the resonance of the center tube will be examined. For this analysis, the equation for a pipe that is open on both ends is used, $f = \frac{nc}{2L}$, n takes integers values, L is the length of the tube (0.295m), and c = 450 m/s for the speed of sound of methane at ambient temperature. Only the fundamental mode, 2nd harmonic, and 3rd harmonic are near the frequencies of interest in the acoustic waveguide. Those values are as follows: 763 Hz, 1,526 Hz, and 2,298 Hz. Comparing them to Table 4.1, only the first frequencies is near a transverse mode of the waveguide which was the second PAN frequencies of 775 Hz. This result is confirmed by the COMSOL simulation which did in fact show coupling between waveguide and the burner, shown in Figure B.9. For the coaxial jet where an annular tube

was used, a similar calculation to the center tube can be done but in this case L = 0.227 m and the gas is estimated to be air with c = 343 m/s. The calculation gives frequencies of 861 Hz, 1,722 Hz, and 2,584 Hz for the first three modes. In this case all of the natural burner frequencies were at least 100 Hz away from any of the chamber forcing frequencies used in this study. Lastly, the cavity between the metal spheres and honeycomb in the co-flow, and to some extent the metal spheres and honeycomb volumes as well, can act as a resonator if the right conditions are established. Assuming no acoustic resistance in the honeycomb and that the resistance of the metal spheres is large enough for the spheres to be treated as a hard boundary, the 1D resonances modes of this cavity can be roughly estimated using the formula, $f = \frac{nc}{4L}$, where n are odd integers, L is the distance from the metal spheres to the honeycomb exit, and c = 343 m/s is the speed of sound of air at ambient temperature. This gives the first three longitudinal resonant frequencies as 884 Hz, 2,651 Hz, and 4,419 Hz. Similar to the annular tube only the first resonance is near the forcing frequencies, but still more than 100 Hz away. Therefore, only the 763 Hz resonance in the center tube coincided with one of the transverse modes of the acoustic waveguide, namely PAN 775 Hz.

4.3 Flow System

For this experiment a new flow system was designed to accommodate for the different gases that needed to be supplied to the burner. These gases included nitrogen, helium, air, methane, and oxygen. The design includes control and measurement of pressure and temperature of the gas through the system. The data for flow measurement instrumentation is acquired using a data acquisition (DAQ) system from Pacific Instruments (Model 6000U). The DAQ was equipped with special modules for input/out signals which have filtering and calibration capabilities (both gain and zero calibration). The overall design was created to control flowrates using precision nozzles (O'Keefe Controls Co.) that can reach a choked condition with the appropriate upstream pressure. A notional schematic of the flow system is represented in Figure 4.8.

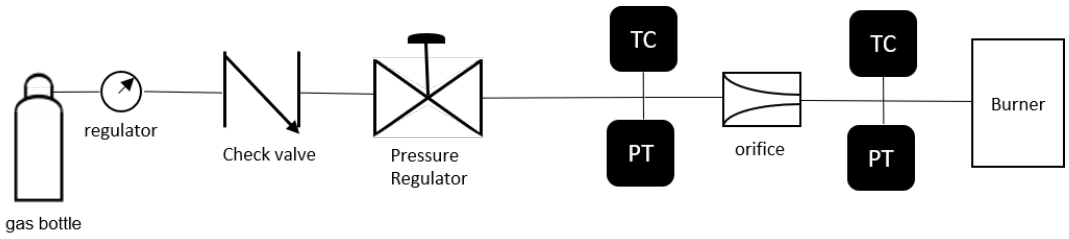

Figure 4.8: A representative flow diagram that corresponds to all the gases entering the burner.

This flow concept applies to all the gases feeding into the burner. The propellants were supplied via gas cylinders (2200-4000 psi) located outside of the test cell. The nitrogen is supplied via an in-house line at 3000 Psi. All gases were introduced into the experiment at ambient temperatures. Essential components such as check valves, filters, and pressure regulators are used on every gas supply line. With the goal of the flow system being to control the mass flowrate of an individual gas by using a precision nozzle, it is important to regulate the upstream flow to desired values. The upstream pressure is controlled using pressure regulators (Tescom) and measured with static pressure transducers (Taber 2911 Series) and E type thermocouples. Using a second set of instruments the pressure and temperature is measured downstream of the nozzle. The orifices were placed adjacent to the burner entrance ports just upstream of the final coaxial tubes. The propellant mass flowrates were in the range of 0.5-5 g/s while the nitrogen co-flow was in the range 0.5-1 g/s. A detailed Piping and Instrumentation Diagram (PID) schematic of the entire lab flow system can be found in Appendix B.

4.4 Jet Visualization

Simultaneous high-speed Schlieren and OH* chemiluminescence imaging focused near the exit of the burner were taken at 50k frames per second (fps). The field of view was approximately $20D_{1,i}$ above the center tube exit for the schlieren images and $10D_{1,i}$ for the

OH* chemiluminescence images. Figure 4.9 illustrates a top view of the imaging setup. A beam-splitter (custom made by Lattice Electro Optics) was used to have a single view angle for both camera setups. The high speed Schlieren optics were composed of a red collimated light source, formed with two spherical 4.25 inch diameter mirrors, imaged onto a Phantom Research v2511 camera with a Nikon (AF Micro-Nikkor 200 mm) lens. Simultaneously, OH* chemiluminescence was captured with a Lambert Instruments HICATT intensifier imaged directly onto a Phantom Research v1210 camera. In addition, a UV lens (F/2.8 Cerco 2178) with a Semrock (PN FF02-320/40) optical filter was used to capture the electronically excited hydroxyl radical OH* which is known to emit UV light near 308 nm.

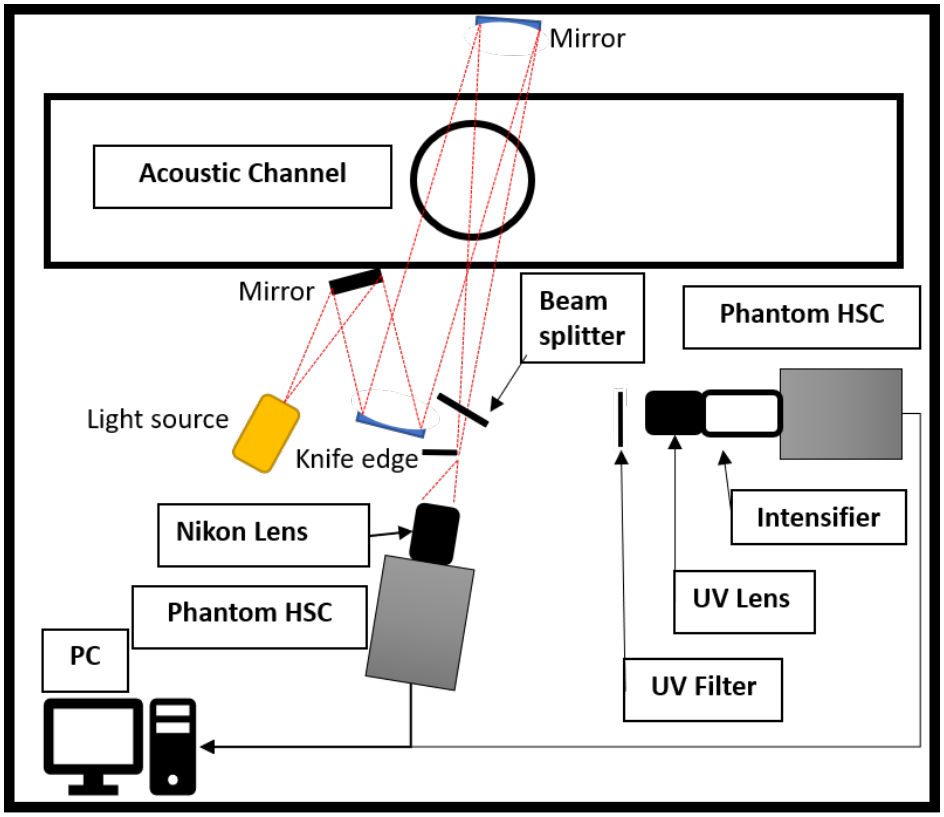

Figure 4.9: Top view schematic view of the simultaneous Schlieren and OH* chemiluminescence high-speed imaging setup.

Synchronization of the cameras and intensifier was achieved by using a pulse generator (Berkeley Nucleonics Model 577) which was used to adjust the delay of the two faster instruments to be in sync with the third. In this case the intensifier had the largest natural delay therefore the two cameras were given the appropriate delay to sync them with the intensifier. The sampling frequency was also controlled by the timing unit. Finally, the system was triggered using a mechanical switch which also triggered the data acquisition system that recorded the flow measurements and acoustic field. In addition, a universal timing unit that sends a time code was synced to the cameras and DAQ to have a time stamp associated with every acquired point of data.

4.5 Analysis Methods

4.5.1 Proper Orthogonal Decomposition

Proper Orthogonal Decomposition (POD) has been used for decades as a method to extract the most dominant mode structures of a data field obtained from dynamical flows. The POD was introduced in the context of turbulence by Lumley [101, 102]. When applied as an image analysis algorithm for flow instability, POD uses high-speed imaging results to reconstruct an approximate representation of a flow using proper orthogonal modes (POMs) which are ranked according to the energetic content of their pixel intensity variations relative to the time-average. POD can be used for analysis and synthesis of data from experiments or simulations and it permits the extraction of spatial and temporal structures judged essential according to predetermined general knowledge of the flow field. POD is often used to highlight the most energetic dynamics of a system [102].

To implement this method, the time series images must be arranged into a single 2D matrix containing all the pixel intensity values. A single image matrix (IM) contains mxn pixels and a total pixel count of $M = mn$; the image matrix may be represented by the following;

$$\mathbf{IM} = \begin{vmatrix} d_{11} & \cdots & d_{1n} \\ \vdots & \ddots & \vdots \\ d_{m1} & \cdots & d_{mn} \end{vmatrix} \tag{4.3}$$

First, each image of the data set containing N images frames are converted into a single column vector, and this is formed in order of increasing pixel columns followed by increasing pixel rows.

$$\mathbf{d}^N = [d_{11}^N \cdots d_{1n}^N, d_{21}^N \cdots d_{2n}^N \cdots d_{m1}^N \cdots d_{mn}^N]^T \tag{4.4}$$

Column vectors are then combined resulting in the matrix $\mathbf{D}$ consisting of M rows by N columns of intensity values.

$$\mathbf{D} = [\mathbf{d}^1, \mathbf{d}^2, \cdots \mathbf{d}^N] \tag{4.5}$$

In order to isolate the periodic fluctuations of coherent structures, the intensity fluctuations should be considered rather than the mean. Thus, the time-average of each pixel intensity is subtracted from the mean to produce a matrix of intensity fluctuations .

$$\tilde{\mathbf{D}}_{ij} = \mathbf{D}_{ij} - \frac{1}{N} \sum_i \mathbf{D}_{ij} \tag{4.6}$$

With the matirx $\tilde{\mathbf{D}}$ there are two general approaches that can be taken to perform the POD of this matrix.

Eigenvalues of the Covariance Matrix

The first method, snapshot POD, was introduced by Sirovich [103]. It involves finding eigenvalues of the covariance matrix $\tilde{C}$ [104],

$$\tilde{\mathbf{C}} = \tilde{\mathbf{D}}^T \tilde{\mathbf{D}} \tag{4.7}$$

and the corresponding eigenvalue problem

$$\tilde{\mathbf{C}}\mathbf{X} = \lambda \mathbf{X}^i \tag{4.8}$$

is solved. The solutions are ordered according to the size of the eigenvalues

$$\lambda^1 > \lambda^2 \cdots > \lambda^N > 0 \tag{4.9}$$

The eigenvectors of 4.8 make up a basis for constructing the POD modes ϕ^i,

$$\phi^i = \frac{\sum_{n=i}^{N} \mathbf{X}_n^i \tilde{\mathbf{D}}^n}{|| \sum_{n=i}^{N} \mathbf{X}_n^i \tilde{\mathbf{D}}^n ||} \tag{4.10}$$

where $\mathbf{X}_n^i$ is the nth component of the eigenvector corresponding to λ^i from equation 4.8 and the denominator is the discrete norm. Each snapshot can be expanded in a series of the POD modes with expansion coefficients a_i for each POD mode i. The coefficients, also called POD coefficients, are determined by projecting the fluctuating part of the velocity field onto the POD modes

$$a^n = \psi^T \tilde{\mathbf{D}} \tag{4.11}$$

where $\psi = [\phi^1 \phi^2 \cdots \phi^N]$.

Single Value Decomposition (SVD)

The second approach involves finding the singular value decomposition (SVD) of $\tilde{\mathbf{D}}$.

$$\tilde{\mathbf{D}} = \mathbf{U}\Sigma\mathbf{V}^T \tag{4.12}$$

This decomposition is used within POD to divide the complete matrix into a matrix containing temporal information $\mathbf{U}$, a matrix containing spatial information $\mathbf{V}$, and a scaling matrix Σ. Similar to the previous method mode shapes and coefficients can be extracted

from the SVD method. The modes are columns of $\mathbf{U}$, the coefficients are columns of $\mathbf{V}$, and the energy values are given by the square of diagonal entries in Σ.

For the results presented in this study, the first method of solving for POD modes and coefficients was used. Because the number of images analyzed was not extremely large (between 1000-2500 images) solving for the covariance matrix and its eigenvalues was manageable with a basic computer. If larger amounts of data need to be looked at, the SVD method should be more efficient. Results from the POD analysis are presented in the results chapter 5. In these results, spatial mode shapes, temporal coefficients corresponding to the spatial modes, and time-dependent amplitude coefficients can be used to produce power spectral density (PSD) plots corresponding to each POM. A MATLAB code written by our research group at UCLA (Andres Vargas) was used to carry out the POD snapshot method and plot the results.

4.6 Flame Standoff Distance

The OH* chemiluminescence images enable a standoff distance (δ_f) to be calculated for the cases where the flame is not fully anchored. First the images must be corrected for background noise and intensity variation for both the camera and the intensifier. A basic flat-field correction is applied to the images. To perform this method, 500 dark images are taken where the camera is operated with a lens cover, and 500 uniformly-illuminated (flat-field) images are acquired using a rectangular white light source. The following Eqn. was carried to correct the images,

$$IC = \frac{(IR - IB) * M}{IF - IB}. \tag{4.13}$$

Here IC is the calibrated image, IR is the raw frame, IB is the dark frame, IF is the uniformly-illuminated image, and M is the average pixel value of IF [105]. The flat field correction was applied to all OH* chemiluminescence images presented in this work.

In this study the tracking of the flame base (standoff distance) was done by using the

MATLAB-based Canny detection function to determine the edges of the OH* chemiluminescence intensity from the line of sight image. Figure 4.10 shows an example image where the bottom edge was located and represented by the white markers (line thickness exaggerated for illustration). Once the bottom edge was found the mean height of the points was taken to represent the instantaneous flame standoff distance (δ_f) for that frame. This method will be used in a later section to track the temporal oscillating flame behavior.

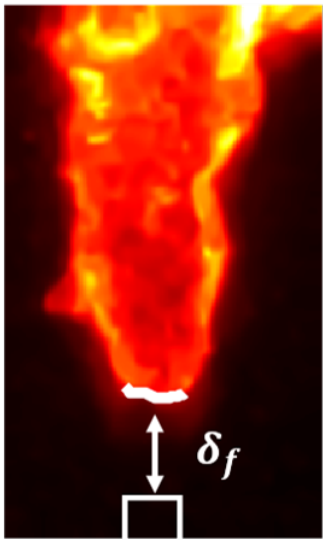

Figure 4.10: OH*chemiluminescence image showing the mean flame standoff distance (δ_f).

4.7 Measurement Uncertainty

Experimental data measurements will naturally come with some degree of inherent uncertainty. Uncertainties can arise both from bias error associated with the measurement devices or the repeatability of individual measurements commonly known as precision errors. It is important to keep track of individual measurement uncertainty and how it propagates to other parameters that are defined by the measured quantities. To determine the degree of accuracy in dependent physical quantities, error propagation is performed by taking into

consideration individual instrument error. For this error analysis the precision error of pressure and temperature will be ignored due to their small size compared to bias error. This can be justified because of (1) the repeatability of the experiments and (2) this study reports measurements as time-averaged quantities for steady flow conditions. Thus, the following error analysis will focus on bias errors.

In this study the principal quantities that were calculated based on measurements was the jet exit velocities, which depend on the measured mass flowrates, density, and exit area.

$$U_k = \frac{\dot{m}_k}{\rho_k A_k} \tag{4.14}$$

where k can be 1, 2, 3 for the inner, outer, and co-flow jet flows, respectively. Both mass flowrates and density depend on the measured temperature and static pressure in the flow system. Following the standard rule of error propagation for a function of several variables [106] and similar uncertainty analysis performed by previous members of our lab [66, 72, 107], the uncertainty in the calculated jet velocities was determined as

$$\delta U = U\sqrt{\left(\frac{\delta\dot{m}}{\dot{m}}\right)^2 + \left(\frac{\delta\rho}{\rho}\right)^2 + \left(\frac{\delta A}{A}\right)^2} \tag{4.15}$$

First the error in mass flowrate will be discussed and this analysis has been reported previously by two groups at AFRL [[108],[109]]. The mass flowrate is calculated from the relationship through a converging-diverging nozzle assuming the flow through the nozzle is compressible, isentropic, one-dimensional, and behaves as an ideal gas:

$$\dot{m} = \frac{AMp_0}{\sqrt{T_0}}\sqrt{\frac{\gamma}{R}}\left(1 + \frac{\gamma - 1}{2}M^2\right)^{\frac{-\gamma-1}{2(\gamma-1)}} \tag{4.16}$$

where p_0 is the total pressure, T_0 is the total temperature, R is the gas constant for the given gas, A is the local area, M is local mach number and γ is the ratio of specific heats [110]. For given stagnation conditions, the maximum mass flow through the nozzle throat will occur when M=1, corresponding to the throat of cross-sectional area A_t; hence Eqn. 4.16 becomes

$$\dot{m} = \frac{A_t p_0}{\sqrt{T_0}} \sqrt{\frac{\gamma}{R}} \left(\frac{\gamma + 1}{2} \right)^{\frac{-\gamma-1}{2(\gamma-1)}} \tag{4.17}$$

Based on this equation, the stagnation temperature and pressure dictate the uncertainty of this dependent quantity. For temperature measurements type E thermocouples from Omega were used. The manufacture reports bias uncertainty of 1% K for these thermocouples. The pressure measurements were made using static pressure transducers which have a less than 0.014% uncertainty according to the manufacturer. Additionally, the discharge coefficient of a specific nozzle is important to consider for mass flowrate calculations. This can be obtained from the manufacturer or by calibrating it with a known mass flowrate source. Rathsack et al. found an error around 2% can be expected in the mass flowrate from this method using similar precision nozzles.

Next, the uncertainty in the density calculation will be examined. This uncertainty depends on the temperature and pressure measurements which are used as input into NIST REFPROP tables. The exit temperature of the jet is assumed to be the same as that measured inside the burner plenums. Again this temperature is measured using a E type thermocouple. The pressure is assumed to be atmospheric. The uncertainty is around 0.014%. It is safe to say that the uncertainty of the density is mostly dependent on the temperature measurement. Lightfoot et al. report 0.11% error in density using an E type thermocouple. Lastly, the uncertainty in the exit area (A) comes from measuring the brass tubes inner diameter using pin gauges with increments of 0.0005. Sizing the correct pin can introduce human error. Once again Lightfoot et al. reported uncertainty from this method to be 0.10%. With these uncertainties and Eqn. 4.15 the error in the jet exit velocity is approximately $\pm 0.41 m/s$.

In general, appropriate experimental practices were employed with the guidance of experienced research engineers at AFRL and instrumentation vendors. For example, such guidance included using well-shielded instrumentation cables to improve signal-to-noise ratios for all pressure transducers and thermocouples. Additionally, yearly calibrations of static pressure

transducers were performed using a dead weight tester. Also, the tubing supplying the gas to the experiment had an inside diameter greater than 6 times the throat diameter of the sonic nozzle being used. Lastly, all fluid properties for flow calculation are obtained using NIST REFPROP tables [111].

CHAPTER 5

Reacting Jets: Results and Discussion

5.1 Single Jet Results

The first set of experiments utilized configuration 1 for single methane jet flames with co-flow. As noted previously, the design consisted of a center round tube (inner diameter, $D_{1,i}$ = 4 mm, post thickness Tp_1 = 0.36 mm) surrounded by a minimum velocity co-flow section (outer diameter, $D_{3,i}$ = 88.9 mm). Initially the anchoring stability of this burner configuration was explored. In the literature turbulent flame experiments have used a premixed pilot burner to keep the flame anchored to the burner [112, 113, 114]. In this study the oxygen concentration in the co-flow was enriched above the air concentration to achieve an anchored flame. Subsequently, a receptivity study was performed on a single fuel jet Reynolds number for fuel jets situated at both a pressure node and pressure anti-node location associated with a standing wave in the chamber.

5.1.1 Unforced Reacting Jet

A series of unforced reacting jet experiments were conducted to acquire an understanding of the burner at different flow conditions and natural jet flame instabilities. Initially, the reacting jet consisted of methane with air in the co-flow. However, the methane flame naturally lifted in air at a fuel Re greater than about 2,000. This can be seen in Figure 5.1, which shows a plot of the instantaneous flame standoff distance (δ_f) for different values of the oxygen enrichment concentration and jet Reynolds number. The flame standoff distance is indicated by the gray scale of the circles, as indicated by the legend. The flame standoff distance is tracked and averaged using the method described in section 4.6. The oxygen con-

centration in the co-flow was systematically increased to find conditions where an anchored flame with a turbulent jet Reynolds number could be achieved. For mixture concentrations above that for air (21% oxygen) a mixture of nitrogen and oxygen was created to control the oxygen percentage. At an oxygen concentration of 40%, a jet Reynolds number up to at least 10,000 could support an attached flame. With the goal of operating the single jet burner at turbulent flow conditions with an attached flame as a baseline, a 40% oxygen concentration in the co-flow was chosen and kept constant for the single jet flame results presented here. For Hagen-Poiseulle flow the transition to turbulence occurs at Reynolds numbers (based on diameter) 2000-3000 [115]. A turbulent Re_{fuel} of 5,300 was used for this study because companion modeling collaborators requested a turbulent Reynolds numbers (above 5,000) for the fuel exit.

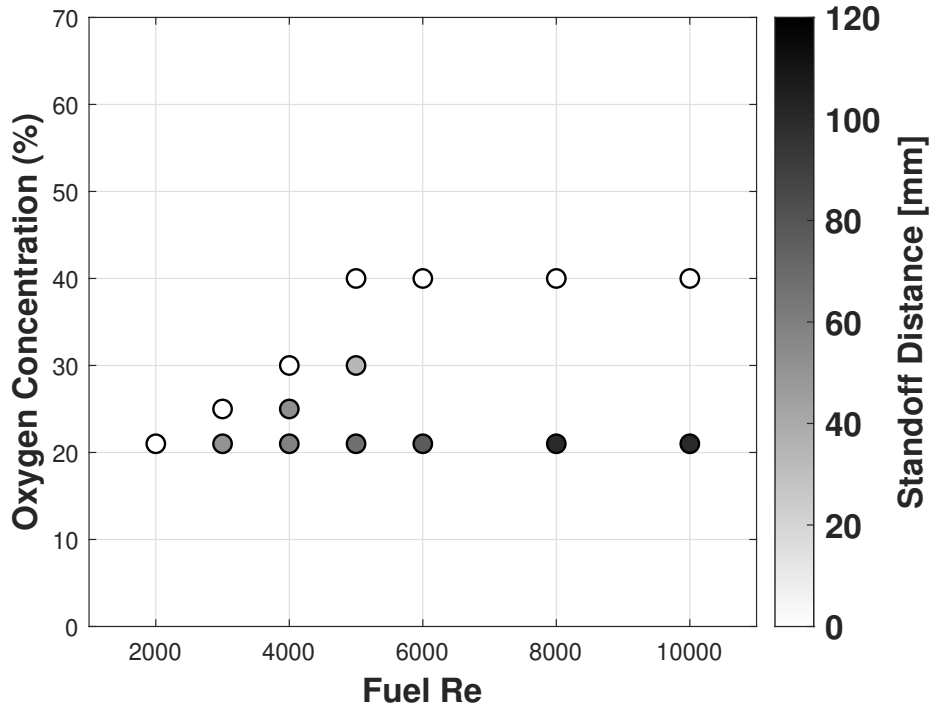

Figure 5.1: **Single Jet**: Flame standoff (δf) distance as a function of oxygen mass concentration and fuel Reynolds number. The grayscale legend indicates the magnitude of δf.

A sequence of simultaneously acquired Schlieren and OH* chemiluminescence of an unforced jet flame at the conditions previously stated (Re_{fuel} and 40% oxygen in co-flow) is shown in Figure 5.2. Recall that the two different imaging techniques are not one-to-one in terms of pixel size as a result of the different camera fields of view. The unforced jet did not show any unexpected flame/gas attributes not already documented in the literature. Schlieren images of the unforced jet in Figure 5.2a show that in the near field a highly turbulent center fuel core with a surrounding reaction zone appeared with an unstable inner fuel core. General differences in the time and length scales of the fuel core and flame zone can be seen. In Figure 5.2b, false colored images of the electronically excited OH* radicals, captured by blocking visible wavelengths using an optical bandpass filter, are presented at the same instants of time as in the Schlieren imaging, with the fuel tube shown as a white outline. Yet the reduced resolution and line-of-sight measurement eliminated the ability to see spatial details in the fuel core. The sequence of images shows an anchored flame as well as an evenly distributed flame without significant variation in the OH* chemiluminescence signal.

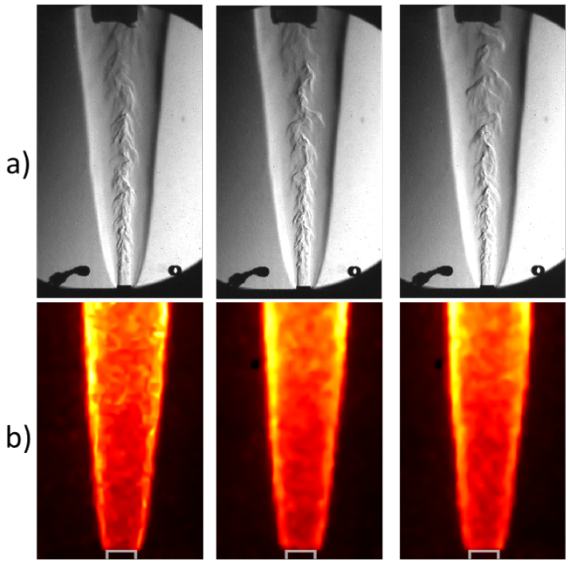

Figure 5.2: **Single Jet**: A sequence of simultaneous reacting methane jet images in the absence of acoustic forcing: a) schlieren and b) OH* chemiluminescence acquired at a frame rate of 50 kHz.

POD analysis of the OH* chemiluminescence images for the unforced jet flame are presented in Figure 5.3. These analyses were performed to search for any naturally occurring flame dynamics. The spatial modes have low energy content because of the low intensity fluctuations other than natural flickering of the flame (Figure 5.3a). The PSD of the temporal coefficients corresponding to each spatial mode, Figure 5.3b, does not show any dominant frequencies in the coefficients. The purpose of this analysis to later compare this case to acoustically forced jets at the same Re_{fuel}.

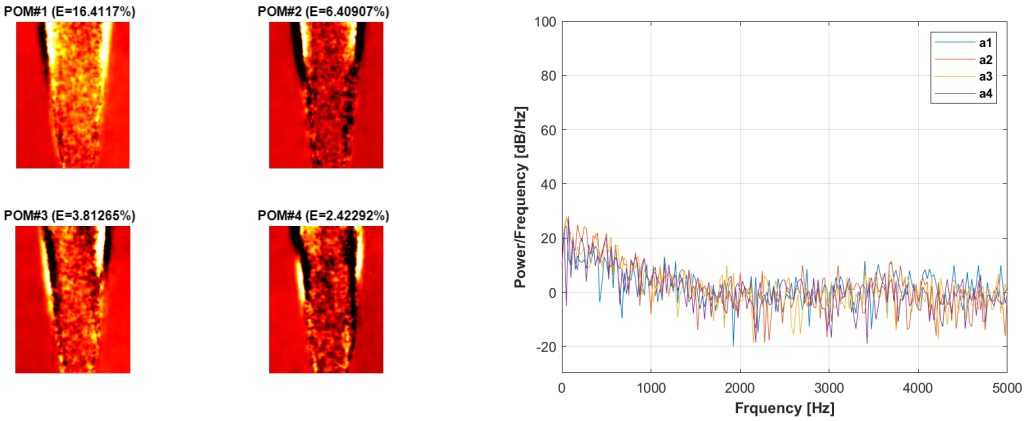

(a) (b)

Figure 5.3: **Single Jet**: POD analysis results for an unforced single jet. Results include (a) the first four POD spatial modes with associated percentage of energetic content, and where the color denotes strength of the mode scaled by its own norm and (b) the power spectral density associated with the first four POD modes.

5.1.2 Pressure Node Forcing

Pressure node forcing for three frequencies of 581 Hz, 1,348 Hz and 2,065 Hz at various forcing amplitudes was explored. The acoustic forcing amplitude for the PN is represented by the estimated local perturbation velocity u'_{max} rather than the measured pressure perturbation pressure p', measured at the PAN closest to the pressure node and thus corresponding to p'_{max}. This is done because pressure amplitudes are approximately zero at the waveguide

center and the jet is instead perturbed by acoustic velocity fluctuations, so the local velocity perturbation, rather than the adjacent PAN pressure perturbation, reveals more information. In order to estimate the amplitude of the velocity fluctuations from the pressure measurements, two pressure transducers were placed at the adjacent PANs located at y = $\lambda/4$ and y = $-\lambda/4$ for each respective frequency. The velocity amplitude at the pressure node can be estimated from

$$u'_{max} = \frac{p'_{max}}{\rho c}, \tag{5.1}$$

where p'_{max} is the average of the maximum pressure perturbation amplitudes at the adjacent PANs, (ρ) is the density and (c) speed of sound atmospheric conditions. This relationship for the velocity perturbation assumes the acoustic waves are linear and one-dimensional, which is supported by the experimental observations in section 4.1.2. The forcing amplitudes in the PN forcing produced theoretical velocities amplitudes ranging from 0.3 to 3 m/s, for reference the vertical jet velocity was U_{fuel} = 24 m/s, hence the velocity perturbations in comparison were almost negligible except at the very highest amplitude excitation cases.

The PN forced flame was characterized by transverse oscillatory (sinusoidal) bulk motion of the flame and flow. The transverse standing wave induces a sinuous response of the fuel jet core and the gases surrounding it. Additionally, jet distortion was observed from the planar images taken in this study and from visual observations out-of-plane. The distortion included jet flattening and spreading of the jet at higher forcing frequencies. The flame "flattened" into an ellipsoidal shape, with a narrow axis in the direction of the acoustic waves. Although this phenomena was seen for all PN cases it was not examined in detail because a second out-of-plane view would have been necessary. To characterize the coupling between the jet flames and applied acoustic forcing, an example for each frequency will be discussed next.

For comparison purposes a common forcing amplitude was chosen to illustrate the significance of modifying the frequency at a constant forcing amplitude (u'_{max}). First an example of PN forcing at 581 Hz with an amplitude of u'_{max} = 1.9 m/s (corresponding to p'_{max} = 600

Pa) is shown in Figure 5.4. A time sequence of images, equally spaced over one acoustic period, for both Schlieren and OH* chemiluminescence are presented in Figure 5.4a and 5.4b respectively. The Schlieren images in Figure 5.4a show that the methane core has a sinuous wave-like pattern. The gases surrounding the fuel core were also forced transversely, in a bulk like motion. In addition, the OH* chemiluminescence images in Figure 5.4b show the OH* radical to have sinuous boundaries, unlike the unforced images which show nearly straight symmetric expanding boundaries. An outline of the exit tube is drawn on the images to illustrate that flames at a PN remain anchored for the entire period.

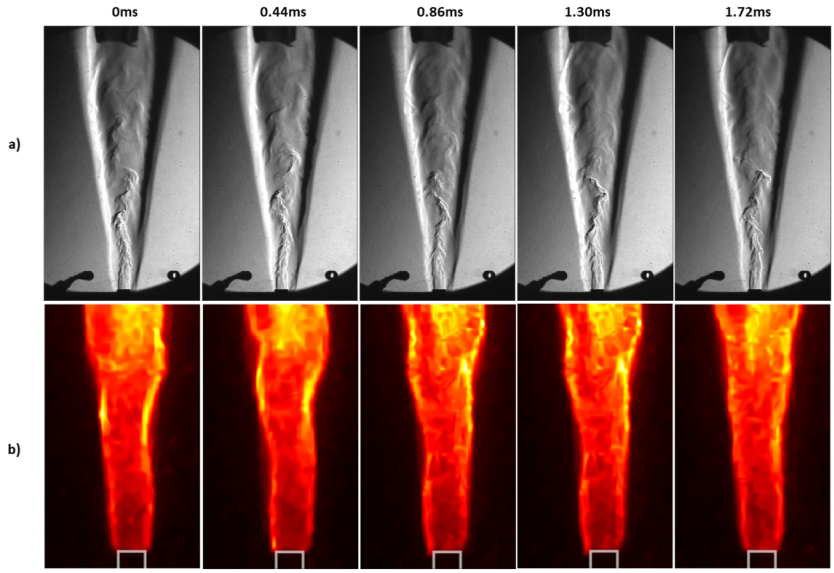

Figure 5.4: **Single Jet**: Equally spaced images over one time/acoustic period corresponding to a PN forcing frequency at **581 Hz** with forcing amplitude of $u' = 1.9$ m/s. (a) depicts Schlieren images and (b) depicts OH* chemiluminescence images in false color.

When increasing the forcing frequency at a constant forcing amplitude ($u'_{max} = 1.9m/s$) to 1,348 Hz and 2,065 Hz, the sinuous motion of the flame diminishes along with a reduced core length, though the core appears to have a sinuous response. Similar results of a reduction in the intact core length have been previously reported for PN forcing by Leyva et al. [71]. Figure 5.5 illustrates one complete acoustic period for forcing at 1,348 Hz. The response of

the jet to this frequency can be seen in both sets of images, with the fuel core being reduced compared to the core length for forcing at the lower frequency. It is also observed that the sinuous response in the OH* chemiluminescence images is more subtle than at the lower frequency. If the frequency is further increased to the last resonant mode used in this study, 2,065 Hz, Figure 5.6 shows that the sinuous response of the flame is almost non-existent. Conversely, the methane fuel core still shows a strong sinuous oscillatory response. While the bulk motion of the flame has diminished, the jet is still responsive at the jet exit where it is able to impact the center fuel jet the most. The forcing creates jet spreading approximately $4D_{1,i}$ downstream of the exit. For all PN cases the flame anchoring stability did not change, and the flame remained anchored despite the transverse acoustic forcing. At the two higher frequencies the oscillations in the OH* chemiluminescence boundaries are not as pronounced and have of smaller wavelengths, as would be expected. Results for the response of the single fuel jet to additional forcing amplitudes are shown in appendix C for different frequencies.

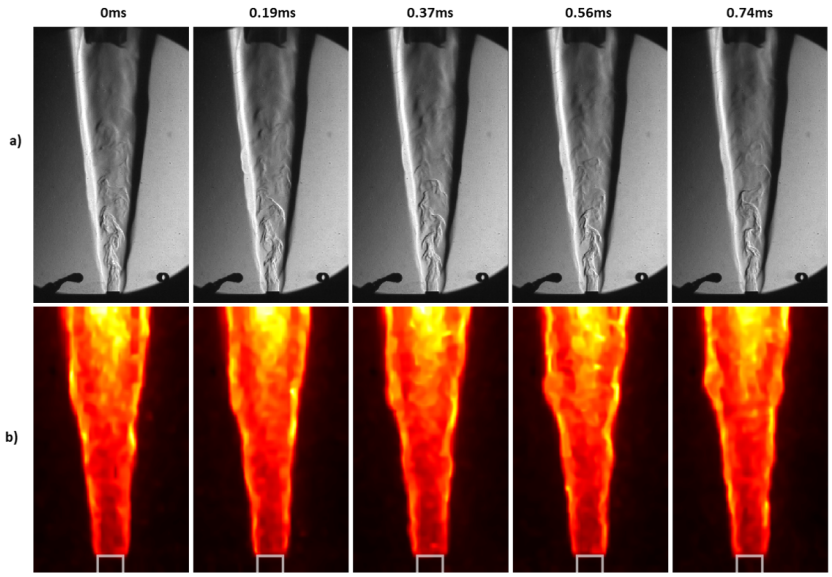

Figure 5.5: **Single Jet**: Equally spaced images over one time/acoustic period corresponding to a PN forcing frequency at **1,348 Hz** with forcing amplitude of $u'_{max} = 1.9$ m/s. (a) depicts Schlieren images and (b) depicts OH* chemiluminescence images in false color.

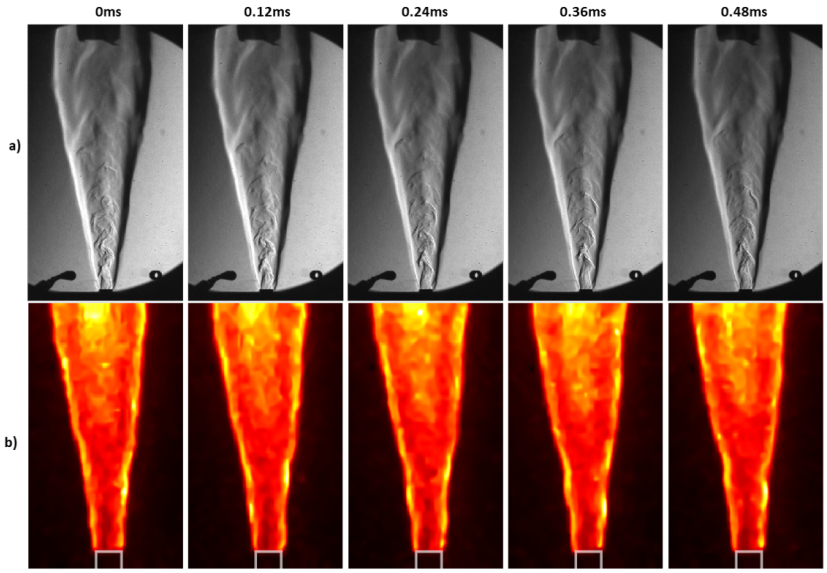

Figure 5.6: **Single Jet**: Equally spaced images over one time/acoustic period corresponding to a PN forcing frequency at **2,065 Hz** with forcing amplitude of $u'_{max} = 1.9$ m/s. (a) depicts Schlieren images and (b) depicts OH* chemiluminescence images in false color.

Next the POD analysis of the three different forcing conditions corresponding to results presented in Figures 5.4-5.6 will be reviewed. Once again for all three cases the forcing amplitude was $u'_{max} = 1.9$ m/s. Results analogous to those in Figure 5.3 for the case of PN forcing enable exploration of the influence of acoustic forcing at the different frequencies by looking at the dominant modes and dynamical nature the reacting jets. Figure 5.7 shows the four highest ranked POD mode structures along with there corresponding energy percentage for $u'_{max} = 1.9$ m/s excitation amplitude. The energy content presented relates to the pixel intensity variations relative to the time-average. There was a clear dominance in proper orthogonal mode (POM) 1 which suggests it represents the bulk oscillatory, sinuous motion of the flame. Additionally, POM 2 represents the sinuous response of the flame edge. Spectral analysis of the four temporal coefficients, corresponding to of each spatial modes, is done using a power spectral density (PSD) plot shown in Figure 5.7b. A clear peak at the applied frequency (581 Hz) for POM modes 1 and 2 can be seen. The spectral response of the two higher modes suggest that the "weaker" dynamics in these modes are at harmonics of the

applied frequency. The PSD results suggests that the oscillating flame has predominately locked-in to the applied acoustics. Since no clear natural oscillations of the flame were found, lock-in to applied excitation was achieved at relatively low excitation, as one would typically see in a convectively unstable shear layer [55]. Additionally, when POD mode coefficients are plotted against each other it can help illustrate relationships between the different modes which might indicate that the flame dynamics are dominated by a linear combination of each other and thus correspond to traveling wave behavior. For this forcing amplitude the plot of

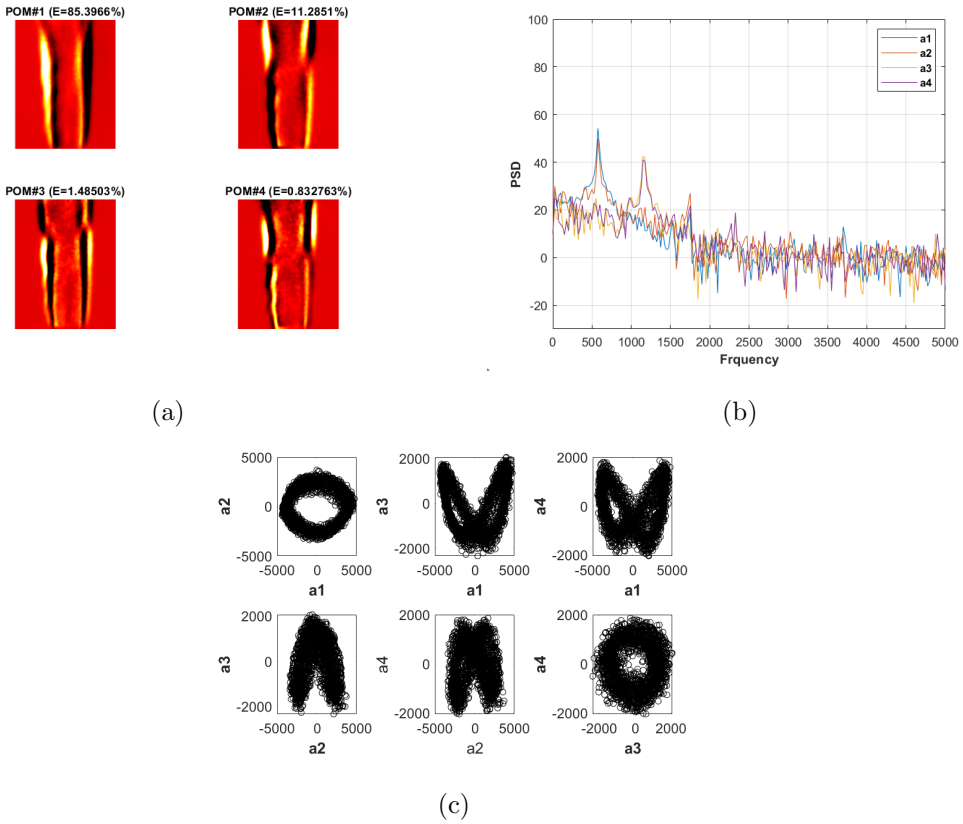

Figure 5.7: **Single Jet**: POD analysis results for **581 Hz** excitation at an amplitude of $u' = 1.9$ m/s at a PN. Results include (a) the first four POD spatial modes with associated percentage of energetic content, and where the color denotes strength of the mode scaled by its own norm, (b) the power spectral density associated with the four POD modes, and (c) sample plots of the POD mode coefficients against one another for the first four modes.

the coefficients a1 vs. a2, for example, produced clear periodicity and an oval shape. The behavior of these first two mode coefficients is similar to the findings of others, e.g., for the non-reactive jet in crossflow [116, 104], indicating that when the first two coefficients create a circular pattern, then the structure in question is a periodic traveling wave that is characterized by linear combinations of the two modes. Similarly, a3 vs. a4 show periodicity because they are at the same frequency. The combination of the modes that showed different peak frequencies show more complex patterns, but still with oscillatory behavior and relatively symmetric phase plots. In a recent paper by our group at UCLA, Sim et al. [49], laminar microjet diffusion flames were subjected to pressure node forcing. The POD results presented were remarkably similar to the phase portraits presented here in Figure C.28c. This suggests that jet flames subjected to pressure node acoustics are highly susceptible to the applied forcing, resulting in an interesting interplay in the visible dynamics of the flame.

Figures 5.8 and 5.9 show results for the two higher frequencies of forcing with the same amplitude of excitation. Similar to the 581 Hz case, the first two modes represent the sinuous motion of the jet flame. Only the forcing frequency is extracted from the PSD of each mode and the correlation between the modes is only seen in modes 1 and 2. The lesser responsiveness of the flame to higher frequency excitation shown in the OH* and Schlieren images in Figures 5.5 and 5.6 are also manifested in the phase portraits, where only the first two modes yield what appear to be periodic behavior, with smearing of the portraits that suggests a lesser degree of locking in to the applied frequency at a fixed forcing amplitude. These results help illustrate the susceptibility of the jet to the different frequencies. More examples of the flame dynamics at a PN can be found in appendix C for the higher forcing amplitudes at each frequency.

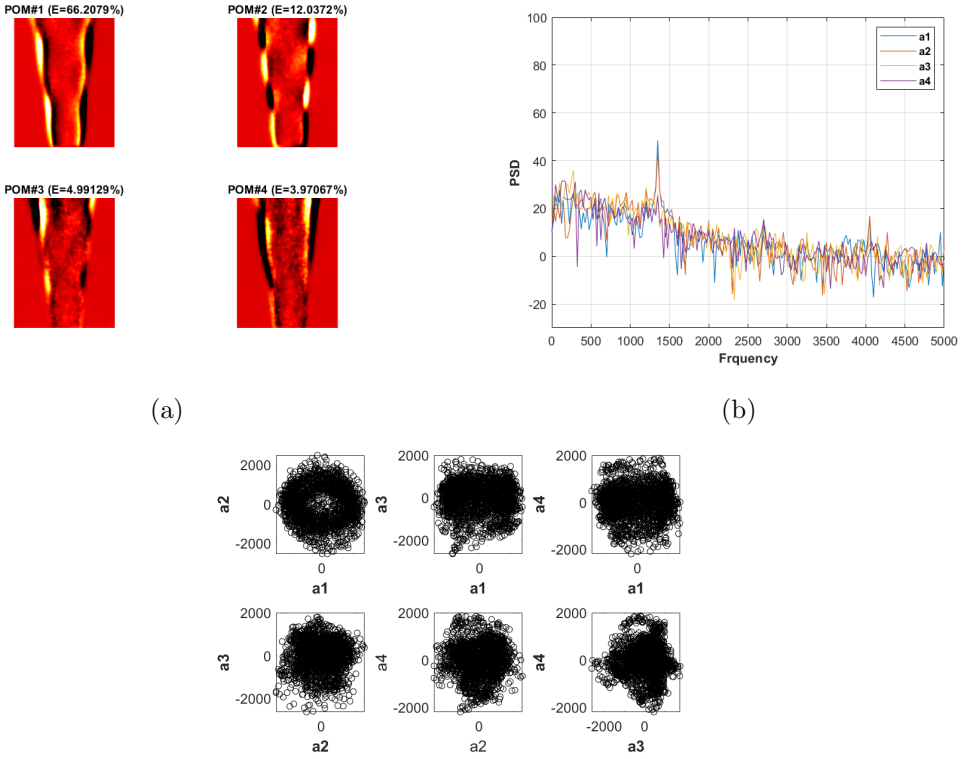

(a) (b)

(c)

Figure 5.8: **Single Jet**: POD analysis results for 1,348 Hz excitation at an amplitude of $U' = 1.9$ m/s at a PN. Results include (a) the first four POD spatial modes with associated percentage of energetic content, and where the color denotes strength of the mode scaled by its own norm, (b) the power spectral density associated with the four POD modes, and (c) sample plots of the POD mode coefficients against one another for the first four modes.

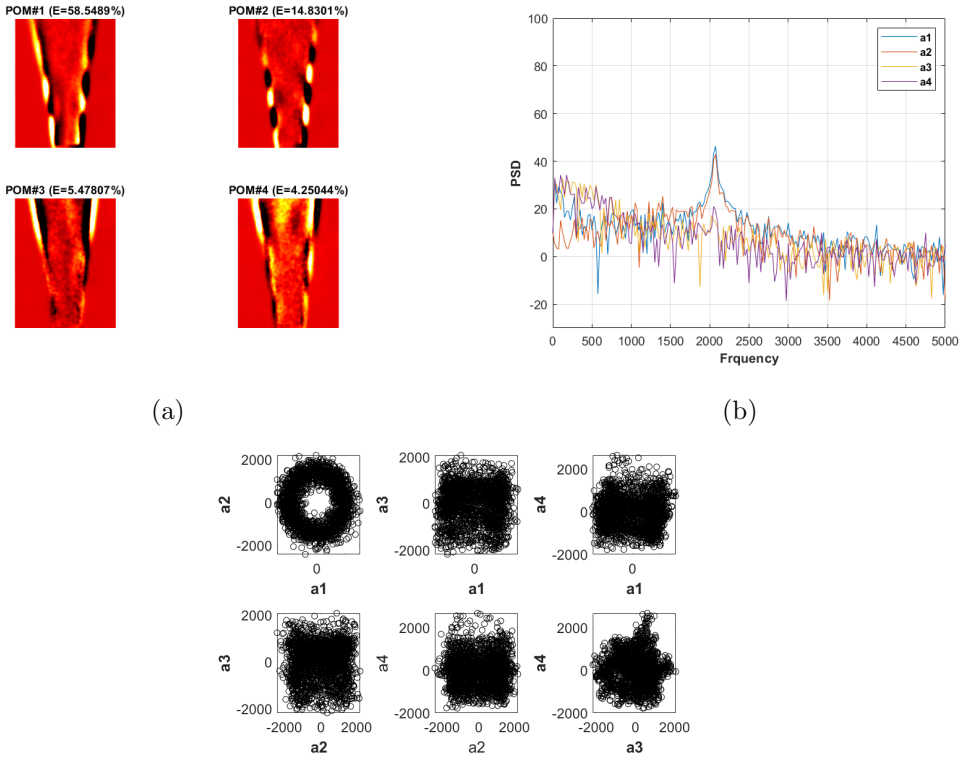

(a) (b)

(c)

Figure 5.9: **Single Jet**: POD analysis results for 2,065 Hz excitation at an amplitude of $U' = 1.9$ m/s at a PN. Results include (a) the first four POD spatial modes with associated percentage of energetic content, and where the color denotes strength of the mode scaled by its own norm, (b) the power spectral density associated with the four POD modes, and (c) sample plots of the POD mode coefficients against one another for the first four modes.

5.1.3 Pressure Anti-Node Forcing

At a pressure anti-node, three chamber resonant frequencies were investigated, 360 Hz, 775 Hz, and 1,150 Hz. Under PAN forcing, the flame-acoustic coupling was characterized by symmetric, puff-like behavior of the reacting jet. Unlike PN, forcing no ellipsoidal distortion or "flattening" effect was observed for the PAN forcing. As mentioned in section 4.1.2 the transverse chamber acoustic mode at 775 Hz coupled with the center fuel tube. It is also important to note for reference that for the PAN cases the forcing amplitude will be presented as P'_{max} in units of Pa, reflective of the fact that pressure oscillations dominate at the PAN; this was a direct measurement using a differential pressure transducer located at the pressure anti-node (i.e., jet center line).

Figure 5.10 illustrates the axisymmetric response of the jet to PAN forcing at 360Hz. Three regimes were found when increasing the forcing amplitude at each frequency: stable (anchored) flames exhibiting axisymmetric flame wrinkling (Figure 5.10a), periodically lifted (red arrows) and reattached flames with more pronounced axisymmetric flame wrinkling (Figure 5.10b), and flames that were permanently lifted by the acoustic field (Figure 5.10c). For the jet to respond, a minimum forcing amplitude of approximately $P'_{max} = 175Pa$ needed to be achieved at 360 Hz. Continually increasing the applied forcing amplitude, the first transition was seen at approximately 300 Pa and the second transition was first seen at an amplitude of $P'_{max} = 450Pa$ (about 0.5% of the chamber pressure). At the higher forcing frequencies, the minimum forcing amplitudes for periodic lift off and permanent lift off increased. It is noteworthy to state that when the flames were lifted by the acoustics alone, the flames returned to an anchored position when the acoustics were removed, with no apparent hysteresis. Later discussion will examine the corresponding OH* chemiluminescence images corresponding to Figure 5.10b and 5.10c to further characterize the flame liftoff.

Next, the flame standoff distance for these periodically lifted cases was quantified. The flame standoff distance is calculated based on the procedure using MATLAB described in

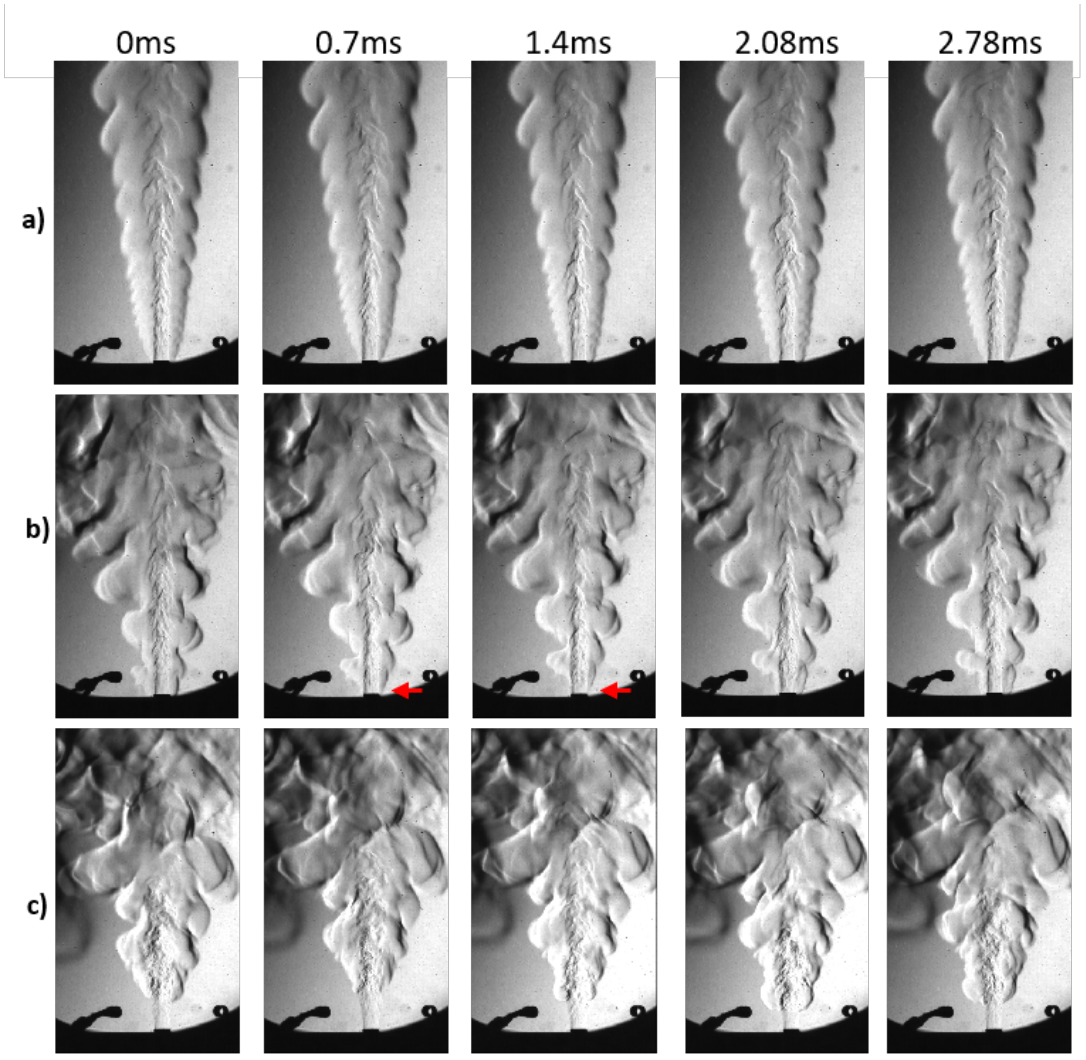

Figure 5.10: **Single Jet**: Equally spaced Schlieren images of the forced jet flame over one time/acoustic period for a PAN at 360Hz with increasing forcing amplitudes of (a) $P'_{max} = 175Pa$, (b) $P'_{max} = 300Pa$, and (c) $P'_{max} = 450Pa$.

section 4.6. Figure 5.11 tracks the flame standoff distance over two periods of a PAN forcing condition at 360Hz at a forcing amplitude of $P'_{max} = 300Pa$, and compares it to the simultaneously acquired pressure signal. OH* chemiluminescence images equally spaced over the two periods are shown in Figure 5.11a, where the flame is periodically lifting (green arrows) and reattaching. Below these images in Figure 5.11b is the instantaneous standoff distance

of all images within the two periods. The oscillations resemble a sine wave which is clipped at the bottom during the times when the flame is attached. Additionally, Figure 5.11c plots the pressure signal vs. the flame standoff distance for 10 cycles. This gives an elliptic orbit that signifies that there is a nearly out-of-phase relationship between the acoustic pressure field and the flame oscillations. The flame standoff distance reaches a maximum when the pressure reaches a minimum, or when the pressure drops across the nozzle exit reaches a maximum. The maximum pressure drop would produce a maximum flow rate, which would be consistent with the observed maximum flame standoff distance at that instant.

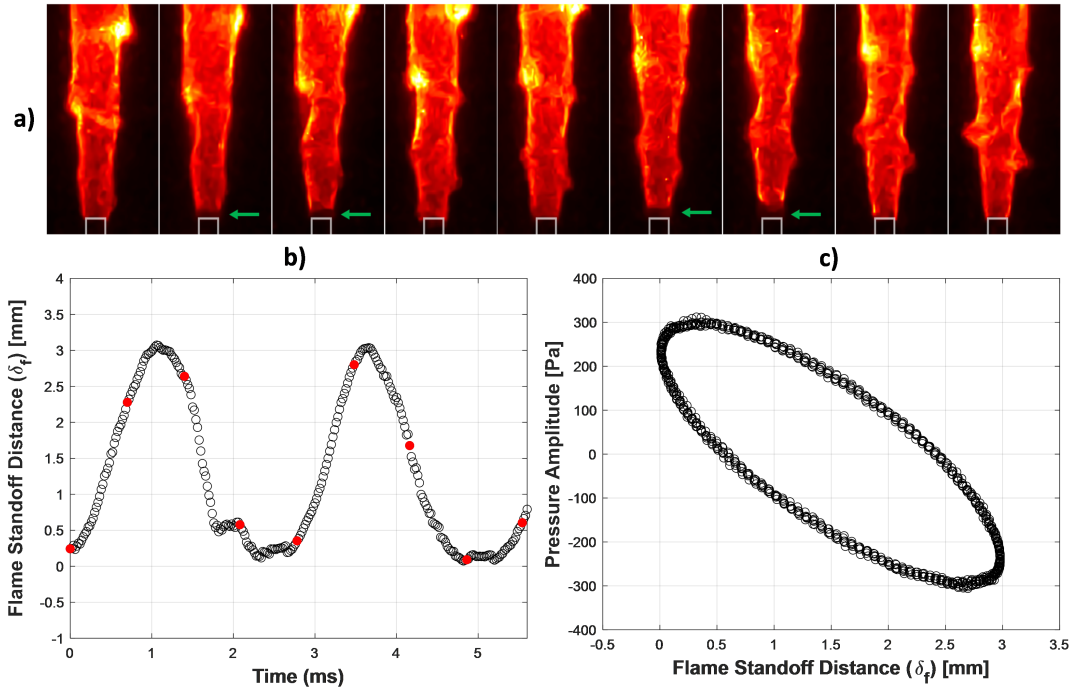

Figure 5.11: **Single Jet**: Cyclical processes of flame liftoff and reattachment at PAN with a frequency of **360Hz** and forcing amplitude of $P'_{max} = 300Pa$. (a) Equally spaced OH* chemiluminescence images over two periods (in false color). (b) Time series plot of the flame standoff distance (red markers correspond to the OH* chemiluminescence images above). (c) Pressure measurements in Pa vs. standoff distance in mm.

Corresponding results for PAN forcing at the same frequency (360 Hz) but at a higher

forcing amplitude of $P'_{max} = 450Pa$ are shown in Figure 5.12. At this higher forcing amplitude, the flame is lifted at all times at a mean standoff distance of about 7.6 mm ($1.6D_{1,i}$), but the standoff distance still oscillates. Figure 5.12b shows that the oscillations for this permanently lifted case still occur, but at a larger amplitude than in Figure 5.11. Once again, the flame oscillations and pressure oscillations follow an elliptic orbit with an out-of-phase relationship, as in Figure 5.11, which is consistent with the flame standoff distance reaching a maximum when the flow rate reaches a maximum. The pressure vs standoff distance plot in Figure 5.11c has more variation because the lifted flame has its own natural oscillations and tracking the flame base becomes more difficult. Nevertheless, there still is clear periodicity in an elliptic shape, suggesting that the flame standoff distance still oscillates with the applied frequency.

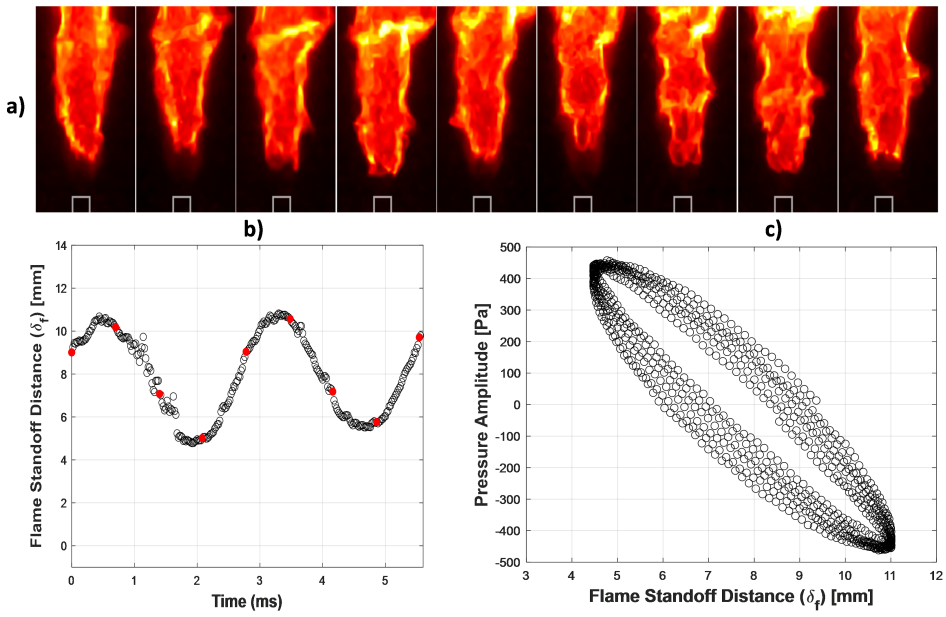

Figure 5.12: **Single Jet**: Cyclical processes of flame liftoff and reattachment at PAN with a frequency of **360Hz** and forcing amplitude of $P'_{max} = 450Pa$. (a) Equally spaced OH* chemiluminescence images over two periods (in false color). (b) Time series plot of the flame standoff distance (red markers correspond to the OH* chemiluminescence images above). (c) Pressure measurements in [Pa] vs. standoff distance in mm.

Similar results for PAN forcing of the single jet at 1,150 Hz that illustrate periodic liftoff and full liftoff are shown in Figures 5.13 and 5.14. The results for this higher forcing frequency are consistent with those at 360Hz in terms of the liftoff behavior, with the standoff distance out of-phase with the pressure signal. The clear difference is that the forcing amplitude required to reach the periodic liftoff regime is greater, around 600 Pa for 1,150 Hz. Additionally, the standoff distance (δ_f) has diminished compared to the liftoff cases at 360Hz. POD results can be found in the appendix C for the 360Hz and 1,150Hz cases, shown in, Figures C.12-C.20. Although the modes were not able to capture much of the dynamics, likely due to the line-of-sight image, but the forcing frequencies were present in the first modes.

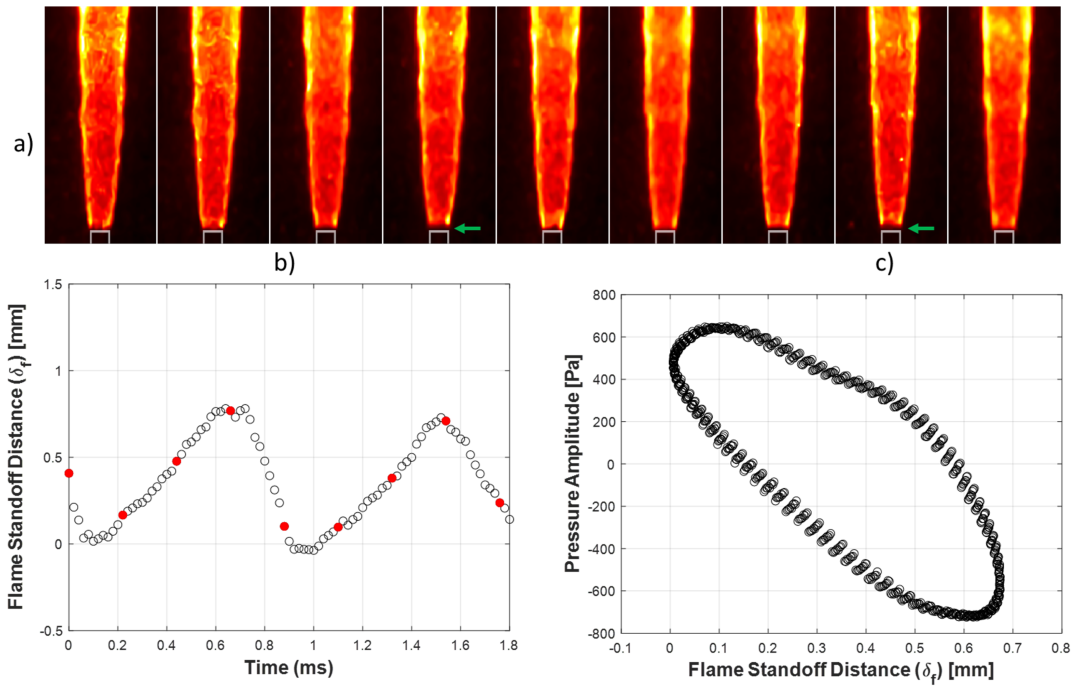

Figure 5.13: **Single Jet**: Cyclical processes of flame liftoff and reattachment at PAN with a frequency of **1,150Hz** and forcing amplitude of $P'_{max} = 650Pa$. (a) Equally spaced OH* chemiluminescence images over two periods (in false color). (b) Time series plot of the flame standoff distance (red markers correspond to the OH* chemiluminescence images above). (c) Pressure measurements in [Pa] vs. standoff distance in mm.

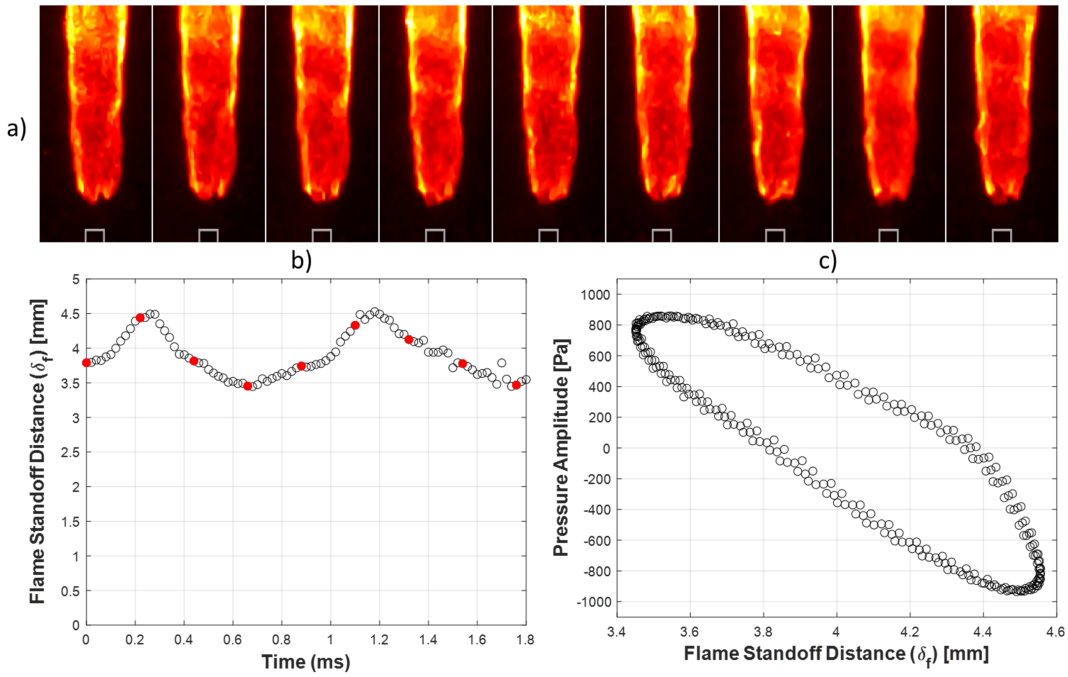

Figure 5.14: **Single Jet**: Cyclical processes of flame liftoff and reattachment at PAN with a frequency of **1,150Hz** and forcing amplitude of $P'_{max} = 900Pa$. (a) Equally spaced OH* chemiluminescence images over two periods (in false color). (b) Time series plot of the flame standoff distance (red markers correspond to the OH* chemiluminescence images above). (c) Pressure measurements in [Pa] vs. standoff distance in mm.

The results also indicate that not only are the mean standoff distances reduced as frequency increases, the magnitudes of the fluctuations in standoff distance also decrease. Figure 5.15 shows a series of OH* chemiluminescence images for permanently lifted flames at the three frequencies. The lowest frequency (360 Hz) shown in Figure 5.15a experiences the largest response to the acoustics with a mean standoff distance of 7.6 mm ($1.6D_{1,i}$) and an amplitude of 5.5 mm (peak to peak). In Figure 5.15b, for a frequency of 775 Hz the OH* chemiluminescence signal moves closer to the tube exit (mean δ_f is 4 mm) and the oscillations of the flame base are noticeable with a standoff distance amplitude of 2.0 mm. Lastly, Figure 5.15c represents a frequency of 1,150 Hz, which shows little to no oscillations in the flame base. The mean δ_f is 4 mm with an amplitude of 0.2 mm.

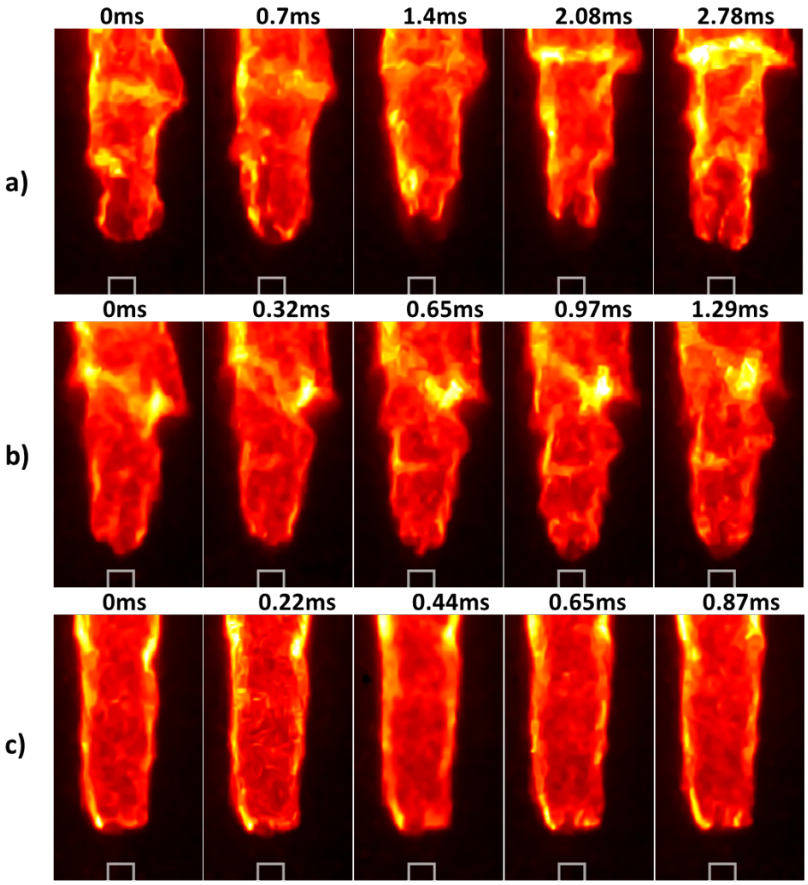

Figure 5.15: **Single Jet**: OH* chemiluminescence images equally spaced over one time/acoustic period for three different frequencies (a) $P'_{max} = 450Pa$ at 360Hz (St = 0.06), (b) $P'_{max} = 570Pa$ at 775Hz (St = 0.13), and (c) $P'_{max} = 890Pa$ at 1,150Hz (St = 0.19).

As previously mentioned, PAN forcing exhibited three regimes of flame response: anchored (stabilized) flames, periodically lifting flames, and permanently lifted flames. The entire set of results explored here for all the frequencies will be presented next in a single plot that summarizes the flame response. All three lift off regimes previously mentioned were still encountered at these higher frequencies as well. However, while the flames continued to respond at the frequency of the pressure forcing, the amplitude of the forcing required to produce equivalent lift off behavior (i.e., periodic or permanent) tended to increase with frequency, and the resulting mean flame standoff distance tended to decrease. This effect is plotted in Figure 5.16.

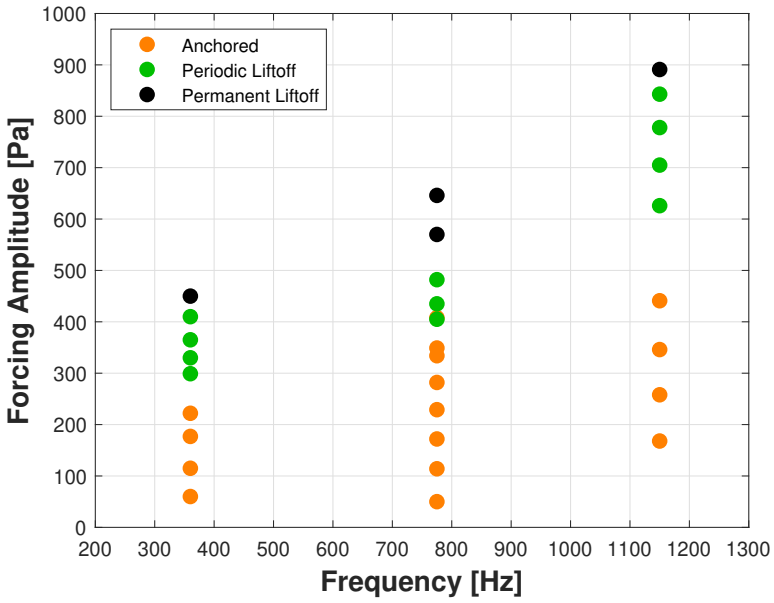

(a)

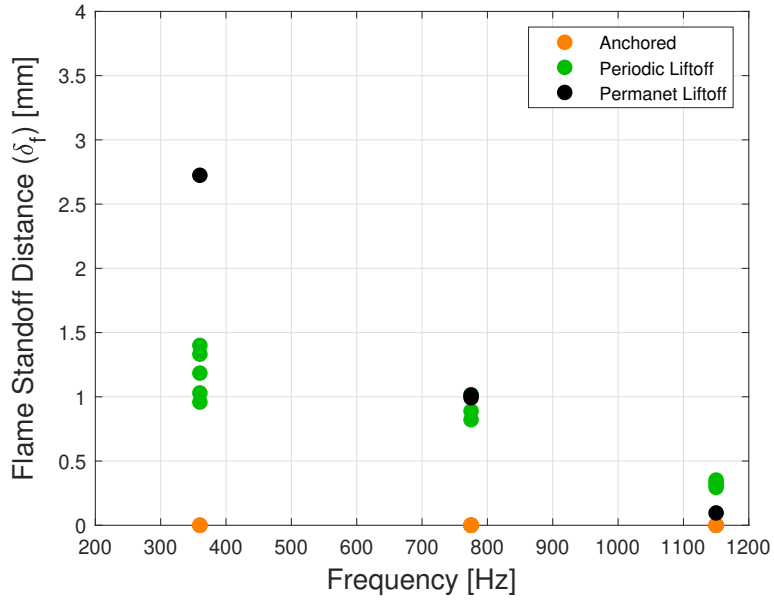

(b)

Figure 5.16: **Single Jet**: Flame response to PAN forcing for various frequencies and forcing amplitudes. (a) Forcing amplitude vs frequency. (b) Flame standoff distance amplitude (peak-peak) as a function of frequency.

In Figure 5.16a, a susceptibility diagram that plots the forcing amplitude vs forcing frequency was created to map the three different anchoring stability regimes. The lifting condition is indicated by the color of the markers. This plot shows that it takes increasingly greater forcing to periodically lift and then permanently lift the jet as the frequency increases. The lesser degree of responsiveness of a diffusion flame exposed to high frequency excitation, as compared with lower frequency excitation at the same amplitude, is well-known [62, 117, 118, 119]. The increase in the required forcing amplitude for both lifting conditions (periodic and permanent) is roughly linear with frequency, increasing from about 300 Pa to 600 Pa in the case of periodic liftoff. All liftoff behavior required a forcing amplitude greater than 400Pa. Figure 5.16b plots additional standoff distance amplitude (peak-peak) data that validates how the coupling between the acoustics and the flame is dependent on frequency. With increasing frequency, the standoff distance amplitude of both periodically and permanently lifted flames are reduced.

5.2 Coaxial Jet Results

The second set of experiments utilized configuration 2 for a shear coaxial jet, which consists of a central methane jet and outer thin annular region with oxygen-enriched air. As noted in Chapter 4, the design consisted of a center tube (inner diameter, $D_{1,i} = 4$ mm, post thickness $Tp_1 = 0.36$ mm) and an annular tube (outer diameter, $D_{2,i} = 12$ mm, post thickness $Tp_2 = 0.36$ mm) which are surrounded by the same co-flow section (outer diameter, $D_{2,i} = 88.9$ mm) as in configuration 1. This study was intended to be an extension of the single jet flames studied in the previous sections. The flow condition for the center fuel jet were matched to have at $Re_{fuel} = 5,300$. The outer co-flow was also kept constant at 1 m/s. The parameter that was varied, other than the forcing, was the annular exit velocity which carried the enriched air. For both the annular flow and co-flow the same oxidizer mixture ($60\%N_2 + 40\%O_2$) was used, and each was controlled independently using sonic nozzles. A similar receptivity study was performed to that done on the single jet (configuration 1).

5.2.1 Unforced Reacting Jet

Three different annular-to-jet velocity ratios (R) were examined for this configuration. Both the center fuel velocity ($U_{1,fuel}$) and co-flow velocity $U_{3,coflow}$ were kept constant at 24 m/s and 1 m/s, respectively. The outer (annular) velocity ($U_{2,ox}$) was increased from 1 m/s to 6.5 m/s. With the highest $U_{2,ox}$ a mass ratio (MR), defined by ($\dot{m}_{ox}/\dot{m}_{fuel}$), of 3.25 was achieved. A mass ratio of 3.25 theoretically gives the best rocket chamber performance in terms of I_{sp} [6]. Table 5.1 has the details for the 3 cases examined in this study.

Case	$\dot{m}_{fuel}$ [g/s]	$U_{1,fuel}$ [m/s]	$Re_{1,fuel}$	$\dot{m}_{ox}$ [g/s]	$U_{2,ox}$ [m/s]	$Re_{2,ox}$	R	MR
1	0.18	24	5,300	0.09	1	1,100	0.05	0.5
2	0.18	24	5,300	0.36	4	3,200	0.17	1.89
3	0.18	24	5,300	0.56	6.5	4,500	0.30	3.25

Table 5.1: Flow conditions for coaxial jet configuration.

For the coaxial jet configuration, two shear layers, inner and outer, are established which produce natural dynamics that can be control the stability of the jet and how it responds to external perturbations. As the outer (annular) flow is increased the inner shear layer that is created between the methane and oxidizer mixture has a more significant role in the flow field. Additionally, in a vertical reacting jet, the flame changes the density profile and hence the velocity profile of the jet through the action of buoyancy. Depending on the degree to which the two profiles are modified, the jet flames can become more or less stable. This happens because buoyancy and heat release can alter the velocity profile and therefore changes the Kelvin–Helmholtz shear layer instability [55], in addition to the fact that the outer-to-inner velocity ratio variation can affect whether the instabilities are more like a shear layer or a wake, depending on the thickness of the tube [120].

Figure 5.17 illustrates a sequential series of images for an unforced reacting jet at R = 0.05 (case 1). The Schlieren images show a turbulent fuel core surrounded by uniform gases which can be described as laminar. Similarly, the OH* chemiluminescence images show a

symmetric flame. This case was one which was in theory similar to the single jet because the bulk exit velocities of the annular and co-flow were all matched. However, physical differences remained present. One was the outer tube post thickness which could change the dynamics between the co-flow and annular flow by adding wake-like behavior. Another difference was adding the natural impedance of an annular tube into the system.

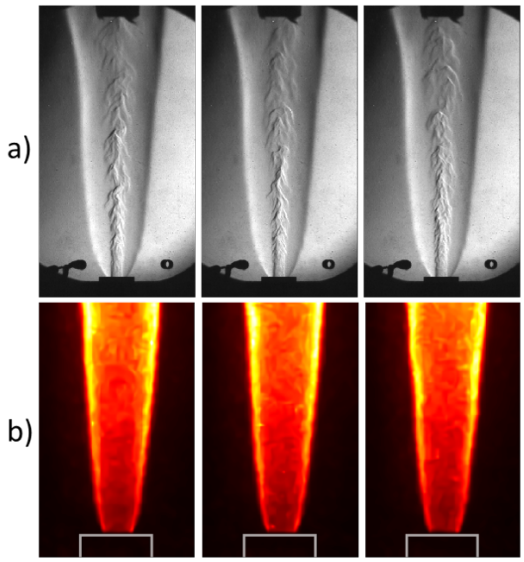

Figure 5.17: **Coaxial Jet**: A sequence of simultaneous reacting jet images a) Schlieren and b) OH* chemiluminescence acquired at a frame rate of 50 kHz. This was for an unforced condition at a velocity ratio R = 0.05.

Next, Figure 5.18 represents a higher velocity ratio of R = 0.17 (case 2). The Schlieren images illustrate a turbulent fuel core surrounded a developing shear layer between the inner and outer flow, about five fuel diameters downstream the surrounding gases becomes turbulent. In the OH* chemiluminescence images minimal disturbances are seen near the top of the images, corresponding to a region at which the surrounding shear layer is turbulent. Lastly, Figure 5.19 presents a similar time series of images but for the highest velocity ratio R = 0.3 (case 3). The shear layer between the inner and outer flow has more apparent disturbances closer to the injection point and now the OH* chemiluminescence images have distortion near the top of the field of view correspond to the shear layer disturbances. The

green arrows reference the inflection point near the top of the OH* chemiluminescence and its corresponding location in the Schlieren image.

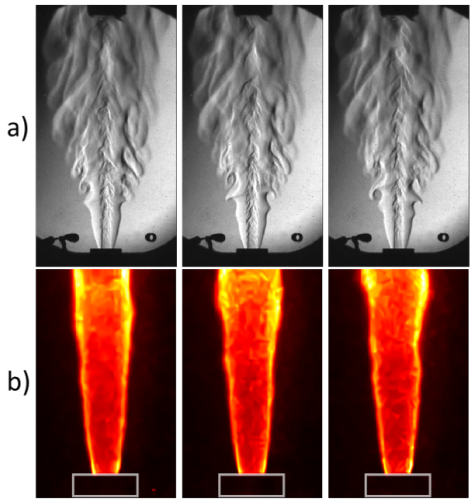

Figure 5.18: **Coaxial Jet**: A sequence of simultaneous reacting jet images a) Schlieren and b) OH* chemiluminescence acquired at a frame rate of 50 kHz. This was for an unforced condition at a velocity ratio R = 0.17.

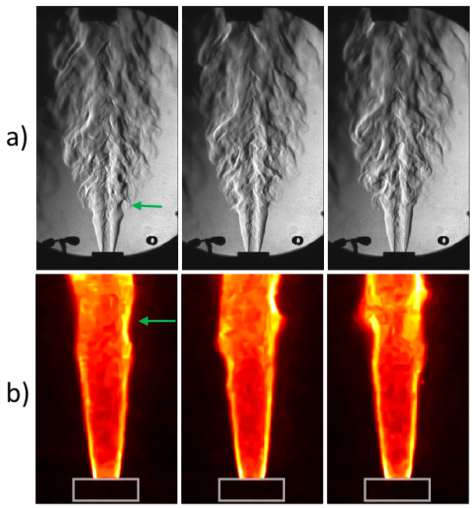

Figure 5.19: **Coaxial Jet**: A sequence of simultaneous reacting jet images a) Schlieren and b) OH* chemiluminescence acquired at a frame rate of 50 kHz. This was for an unforced condition at a velocity ratio R = 0.3.

Spectral analysis of the unforced coaxial reacting jets was performed on the flame to extract any naturally occurring flow dynamics. First, POD analysis was performed on the OH* chemiluminescence images similar to the single jet results, but no distinct frequency peaks were found in these unforced cases, although the lesser resolution of such images made it difficult to extract meaningful data here. A second approach was taken to find any natural frequencies from the Schlieren images where the shear layer is noticeable. Frequencies were extracted by taking power spectral densities (PSD) of integrated intensity signal, of small windows, near the visible shear layer of the Schlieren images over a sequence of 2000 snapshots. Spectral results for R = 0.05, R = 0.17 and R = 0.3 are shown in Figures 5.20, 5.21, and 5.22, respectively.

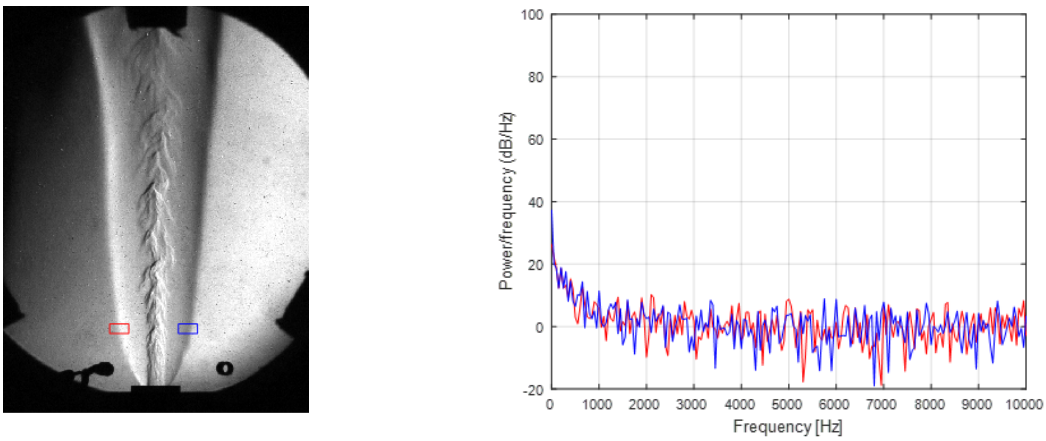

(a) (b)

Figure 5.20: **Coaxial Jet**: PSD analysis on shear layer for unforced reacting jets at R = 0.05. (a) is still frame with the pixel windows used as the signal and (b) is the resulting spectra plot from 2000 snapshots

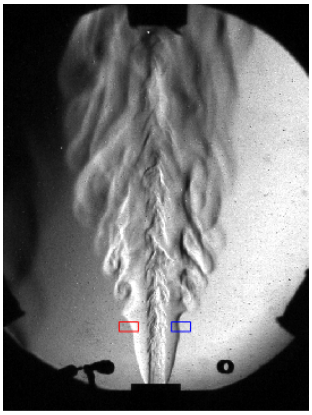

(a)

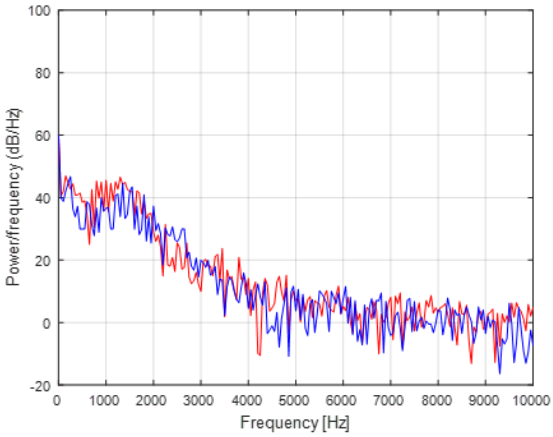

(b)

Figure 5.21: **Coaxial Jet**: PSD analysis on shear layer for unforced reacting jets at R = 0.17. (a) is still frame with the pixel windows used as the signal and (b) is the resulting spectra plot from 2000 snapshots

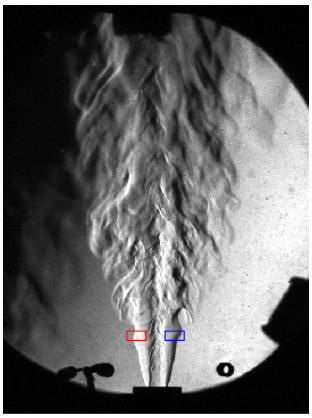

(a)

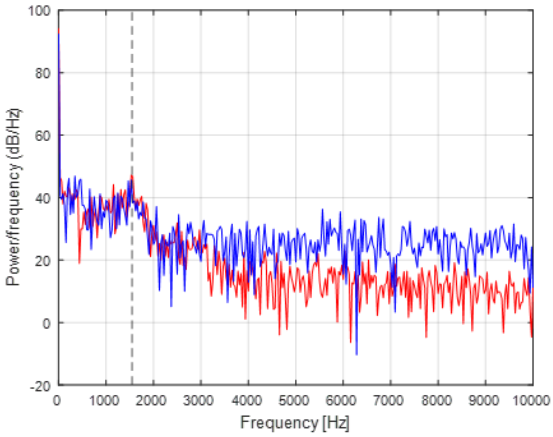

(b)

Figure 5.22: **Coaxial Jet**: PSD analysis on shear layer for unforced reacting jets at R = 0.3. (a) is still frame with the pixel windows used as the signal and (b) is the resulting spectra plot from 2000 snapshots

Case 3 (R = 0.3) revealed the most pronounced frequency peak near 1500 Hz, shown in Figure 5.22. In case 2 (R = 0.17), there was no sharp peak in the spectrum but rather a

broad response in the frequencies range of 1000Hz - 1500Hz. For case 1 (R = 0.05) no clear frequencies were extracted from the images; this is similar to the single jet results, which involved roughly the same flow conditions as in case 1. It can be difficult to pick up subtle dynamics from planar images; this could signify that the two lower velocity ratios could have clear natural frequencies not detected by the methods applied here. The natural instabilities for the higher velocity ratio case suggests that these are associated with shear layer modes rather than wake modes, but further examination for different tube thicknesses would enable verification.

5.2.2 Pressure Node Forcing

When forcing the coaxial jets at a pressure node, the flame behaved similar to the case of the single jet configuration. The flame behavior is still characterized by transverse oscillatory (sinusoidal) bulk motion of the flame. For all PN cases the flame anchoring stability did not change (that is, there was an anchored flame for all conditions). Conditions for all three velocity ratios were completed. Similar qualitative features of the flame response were observed with few visual differences in the Schlieren images. The reacting jets do experience the flattening behavior described previously which is most notable at the lower forcing frequency. These results are discussed below.

First, qualitative results in the form of time series images are presented for a velocity ratio of R = 0.17. Results for case 1 with R = 0.05 are not included here because of the similarity to those of the single jet when situated at a PN. Two sets of figures, with simultaneous Schlieren and OH* chemiluminescence imaging, compare the response of the jet flame for R = 0.17 at frequencies of 581 Hz (Figure 5.23), 1,348 Hz (Figure 5.24), and 2,065 Hz (Figure 5.25). A common chamber perturbation velocity forcing amplitude of 1.2 m/s ($P'_{max} = 450Pa$) was chosen because of the availability to compare to the higher velocity ratio results. Figure 5.23 demonstrates the response of the jet to a forcing frequency of 581 Hz; focusing near the jet exit the shear layer is being moved transversely back and forth in a sinuous manner.

The shear layer is responding to the acoustics as can be seen from the periodic structures progressing downstream along the shear layer. In the OH* chemiluminescence images the transverse oscillations are present but not to as significant degree as for the single jet, where the edges of the flame took on a sinuous pattern. Increasing the forcing frequency to 1,348 Hz (see Figure 5.24) results in a diminishing response of the jet to the applied acoustic forcing. Finally, at the highest forcing frequency 2,065 Hz (see Figure 5.25) in this study shows similar diminishing trends in terms of the jet transverse motion. Notably, the shear layer disturbances do not begin developing near the jet exit as they did in the lower forcing frequency. Additionally, the flattening of the jet in the transverse direction is not as evident at the higher frequencies, seen in Figures 5.24c and 5.25c. Interestingly, the center fuel core appear to more response as frequency is increased, as seen the Schlieren images.

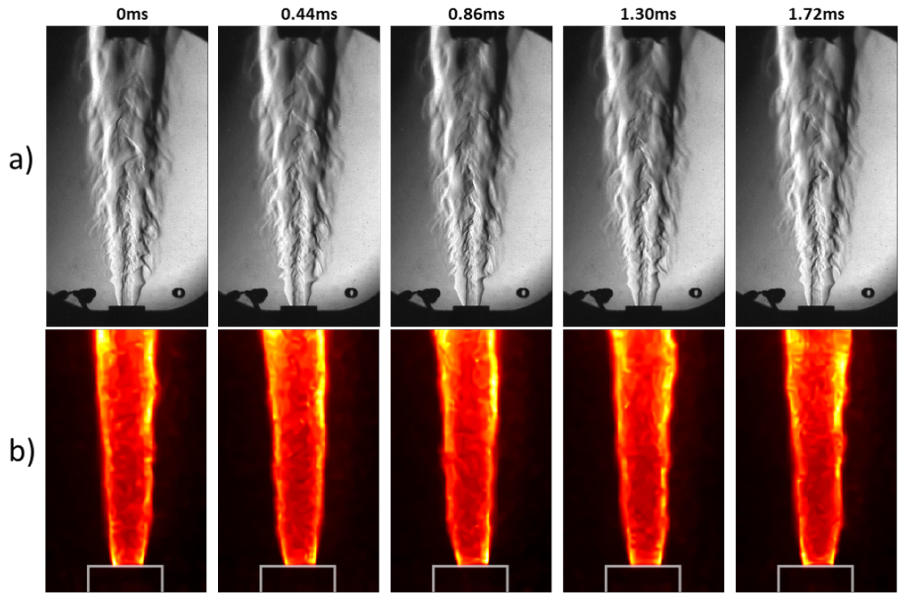

Figure 5.23: **Coaxial Jet (R = 0.17)**: Equally spaced images over one time/acoustic period corresponding to a PN forcing frequency at **581 Hz** with forcing amplitude of $u'_{max} = 1.2$ m/s. (a) depicts Schlieren images and (b) depicts OH* chemiluminescence images in false color.

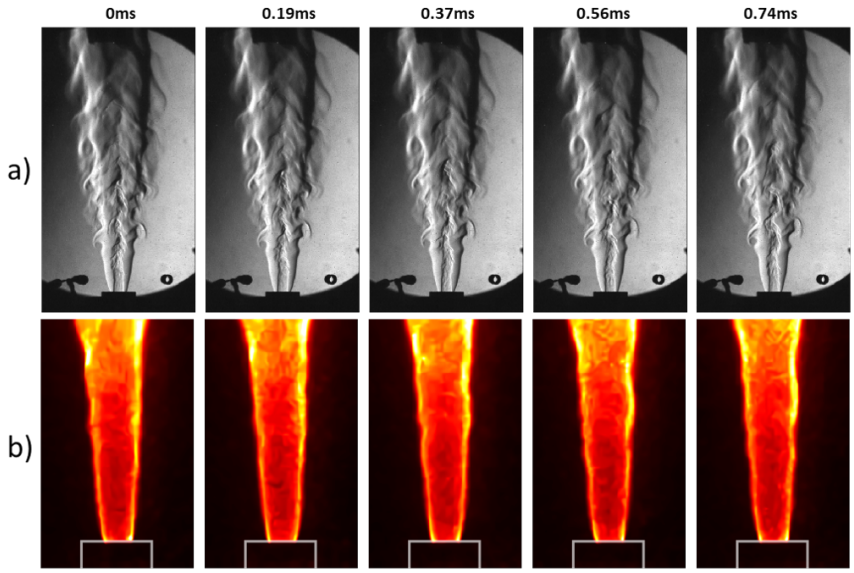

Figure 5.24: **Coaxial Jet (R = 0.17)**: Equally spaced images over one time/acoustic period corresponding to a PN forcing frequency at **1,348 Hz** with forcing amplitude of $u'_{max} = 1.2$ m/s. (a) depicts Schlieren images and (b) depicts OH* chemiluminescence images in false color.

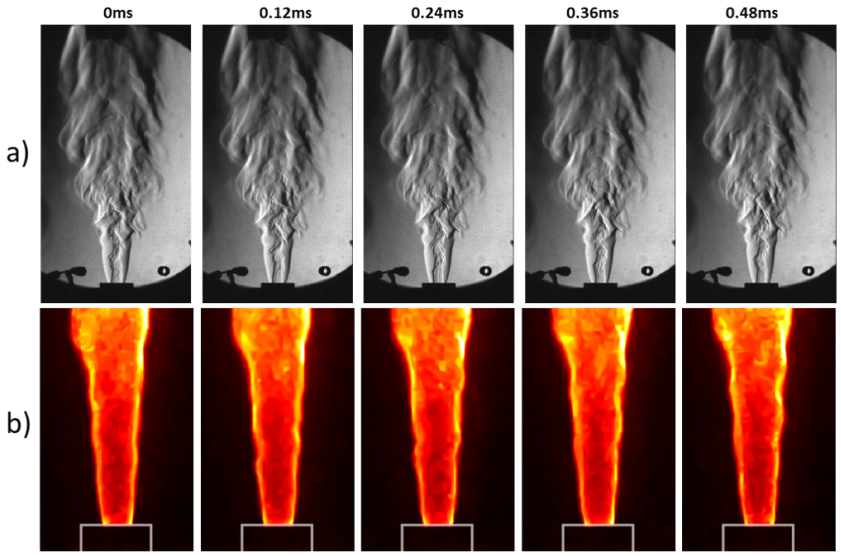

Figure 5.25: **Coaxial Jet (R = 0.17)**: Equally spaced images over one time/acoustic period corresponding to a PN forcing frequency at **2,065 Hz** with forcing amplitude of $u'_{max} = 1.2$ m/s. (a) depicts Schlieren images and (b) depicts OH* chemiluminescence images in false color.

Next, results are shown for a velocity ratio of R = 0.3. Figures 5.26, 5.27 and 5.28 help illustrate the coaxial jet's responsiveness to PN forcing at two frequencies, 581 Hz, 1,348 Hz, and 2,065 Hz. Recall that for this case (R = 0.3), the unforced jet showed a natural instability at a frequency around 1500 Hz. Figure 5.26 is for a forcing amplitude of 1.2 m/s and frequency 581 Hz, where it is clear that both Schlieren and OH* chemiluminescence show the dominant periodic flame structure arising from the transverse oscillations (more so than at R = 0.17), which appear visibly to be more vigorous oscillations as compared with the natural oscillations indicated in Figure 5.19.

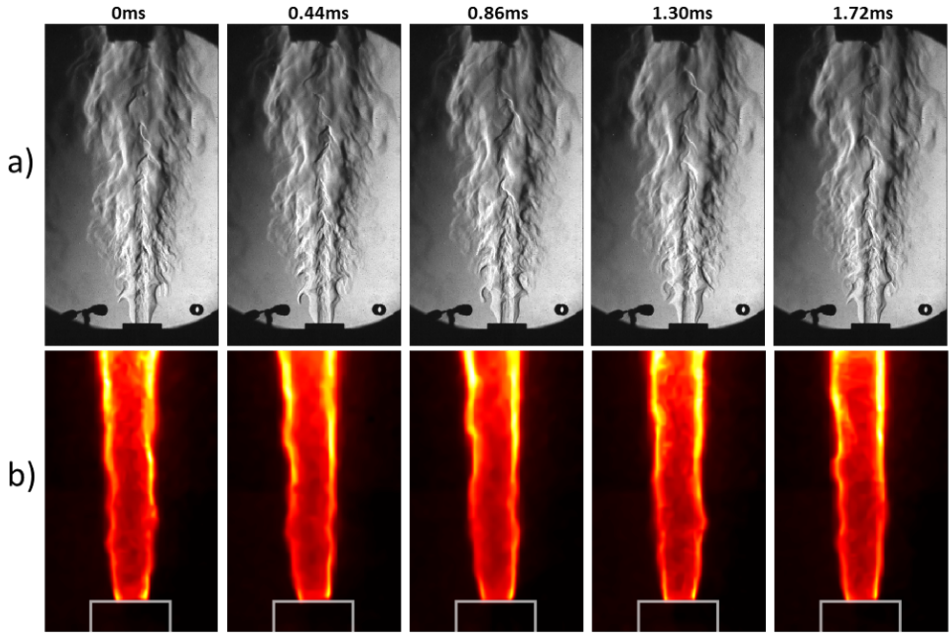

Figure 5.26: **Coaxial Jet (R = 0.3)**: Equally spaced images over one time/acoustic period corresponding to a PN forcing frequency at **581 Hz** with forcing amplitude of $u'_{max} = 1.2$ m/s. (a) depicts Schlieren images and (b) depicts OH* chemiluminescence images in false color.

In the intermediate forcing frequency (1,348Hz) case, with imaging shown in Figure 5.27, there are also some clear differences to be noted. First the OH* chemiluminescence images show how the jet is not flattened to the degree that it was in Figure 5.26b when

there is a change in the forcing frequency. Comparing the Schlieren images with those at lower frequency forcing in Figure 5.26, it appears that the shear layer instabilities have been initiated further downstream. Yet as in Figure 5.26, forcing at the higher frequency did result in shear layer disturbances and jet oscillatory structures that appeared to be more vigorous than in the naturally unstable coaxial jet in Figure 5.19. Lastly, at 2,065 Hz (see Figure 5.28) the shear layer disturbances have moved into the turbulent region and therefore less evident. Naturally increasing the annular flow create a more compact flame as compared to R = 0.17, but even so the jet flattening characteristic diminishes with increasing frequency for the higher velocity ratio as it did for the lower one. Next, POD analysis will be applied for the for different flow and forcing conditions.

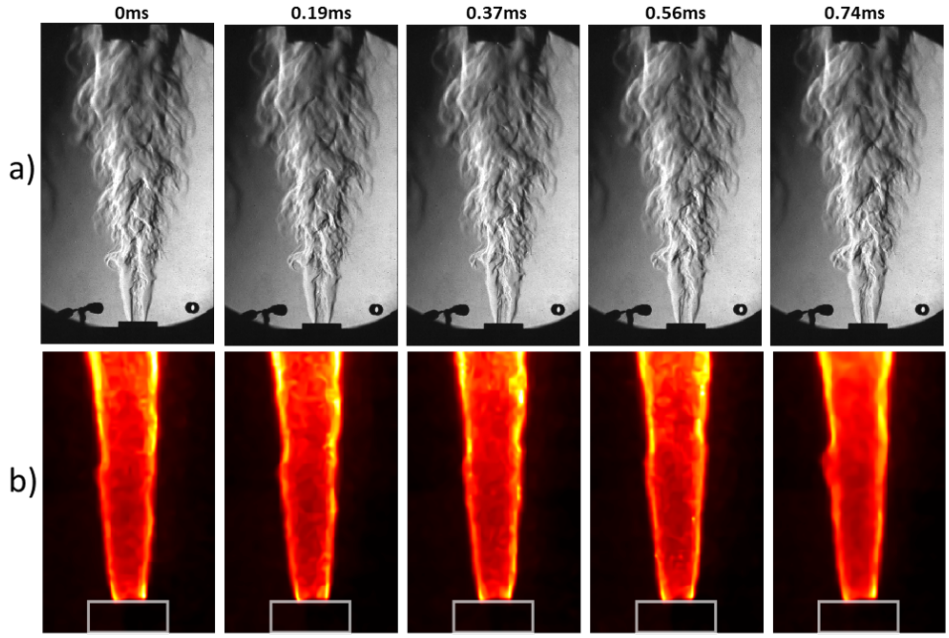

Figure 5.27: **Coaxial Jet (R = 0.3)**: Equally spaced images over one time/acoustic period corresponding to a PN forcing frequency at **1,348 Hz** with forcing amplitude of $u'_{max} = 1.2$ m/s. (a) depicts Schlieren images and (b) depicts OH* chemiluminescence images in false color.

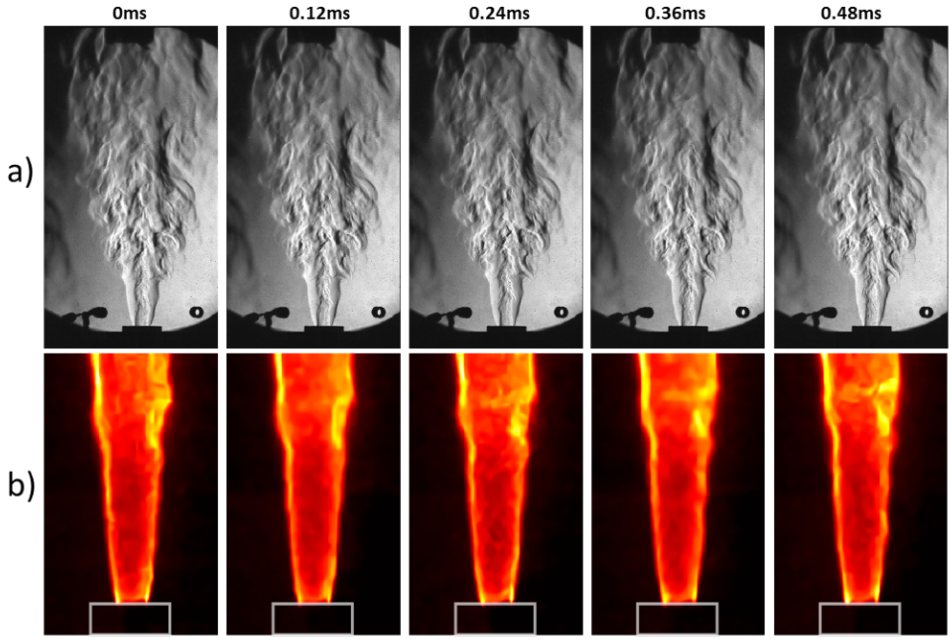

Figure 5.28: **Coaxial Jet (R = 0.3)**: Equally spaced images over one time/acoustic period corresponding to a PN forcing frequency at **2,065 Hz** with forcing amplitude of $u'_{max} = 1.2$ m/s. (a) depicts Schlieren images and (b) depicts OH* chemiluminescence images in false color.

Two sets of flow conditions were chosen to illustrate the acoustic-flame coupling, using POD analysis, when the flame is forced at a PN (Figures C.23 and C.26 have 2,065 Hz results). First, a velocity ratio of R = 0.17 was examined at two forcing amplitudes, $u'_{max} = 1.2$ m/s (corresponding to Figure 5.23) and $u'_{max} = 2.6$ ($P'_{max} = 900Pa$), while keeping the forcing frequency at 581 Hz. Figure 5.29 at the lower forcing amplitude shows that the bulk flame oscillation takes place at the applied forcing frequency of 581 Hz, is described by mode 1. Both the energy content of the modes indicated in Figure 5.29a and the phase portraits in Figure 5.29c suggest that modes 1 and 2 make up the dominant oscillatory behavior of the flame. Increasing the forcing amplitude to $u'_{max} = 2.6$ in Figure 5.30 shows similar behavior in modes 1 and 2 as seen at the lower amplitude. Figure 5.30c shows more significant dynamical coupling between the modes, including higher modes than 1 and 2, likely due to the strongly pronounced first harmonic related to modes 3 and 4. Similar results to these

data sets were seen in the single jet PN forcing conditions as well (see Figure 5.7). This reinforces the notion that the dynamic behavior of the flame can be captured to some extent by using POD analysis, at least for the most energetic modes which for PN forcing typically have been modes 1 and 2 and perhaps a few higher modes.

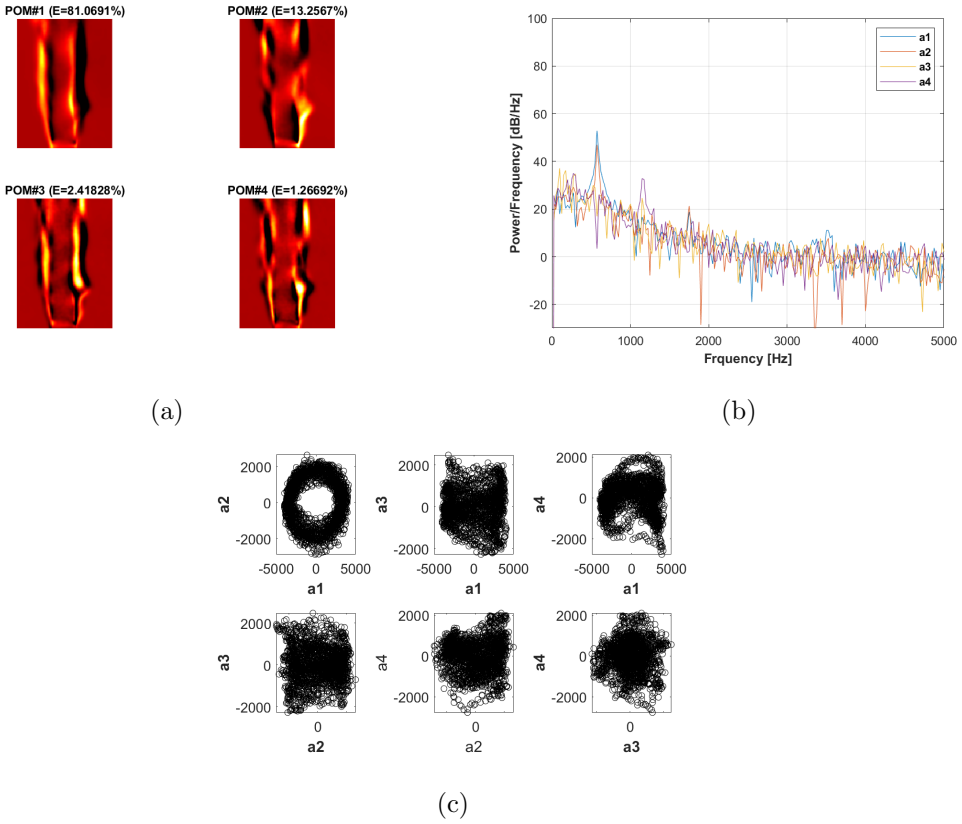

(a) (b)

(c)

Figure 5.29: **Coaxial jet (R = 0.17)**: POD analysis results for 581 Hz excitation at an amplitude of $u' = 1.2$ m/s at a PN. Results include (a) the first four POD mode structures with associated percentage of energetic content, and where the color denotes strength of the mode scaled by its own norm, (b) the power spectral density associated with the first POD mode, and (c) sample plots of the POD mode coefficients against one another for the first four modes.

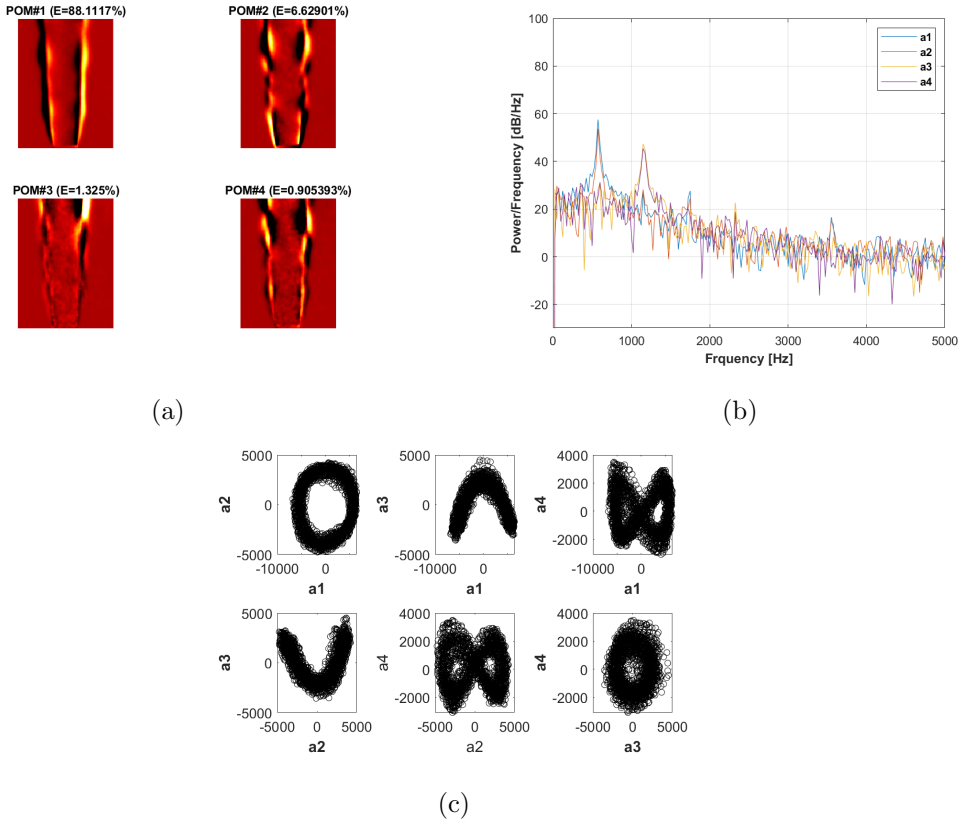

(a) (b)

(c)

Figure 5.30: **Coaxial jet (R = 0.17)**: POD analysis results for 581 Hz excitation at an amplitude of $u' = 2.6$ m/s at a PN. Results include (a) the first four POD mode structures with associated percentage of energetic content, and where the color denotes strength of the mode scaled by its own norm, (b) the power spectral density associated with the first POD mode, and (c) sample plots of the POD mode coefficients against one another for the first four modes.

Two additional sets of results in Figures 5.31 and 5.32 are presented to examine the higher velocity ratio jet, with R = 0.3. The results here are similar to those in Figures 5.29 and 5.30 for the lower velocity ratio, in that they demonstrate that the jet is oscillating at the applied 581 Hz and that modes 1 and 2 describe the bulk motion. Phase portraits in Figures 5.31c and 5.32c indicate that there is a clear dynamical lock-in to the applied frequency and its harmonics, with characteristic signatures that are similar to those for the single jet, both in the present experiments and in corresponding experiments at UCLA at much lower Reynolds numbers [49]. Higher frequency results can be found in appendix C, Figures C.21-C.26, with consistency to the results shown here.

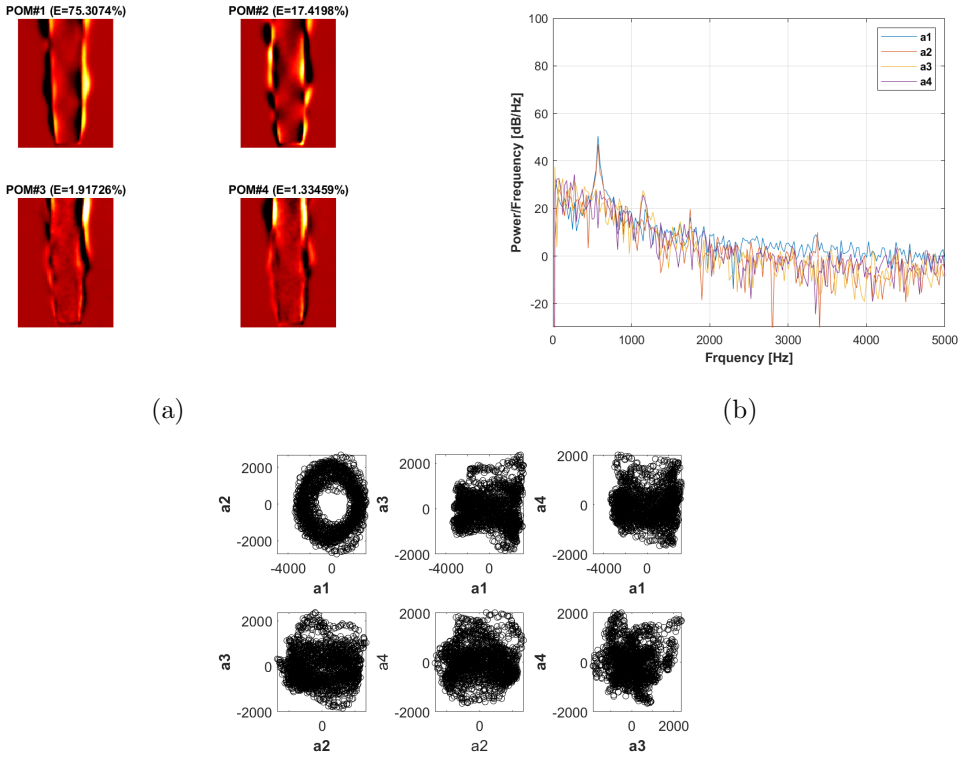

Figure 5.31: **Coaxial jet (R = 0.3)**: POD analysis results for 581 Hz excitation at an amplitude of $u' = 1.2$ m/s at a PN. Results include (a) the first four POD mode structures with associated percentage of energetic content, and where the color denotes strength of the mode scaled by its own norm, (b) the power spectral density associated with the first POD mode, and (c) sample plots of the POD mode coefficients against one another for the first four modes.

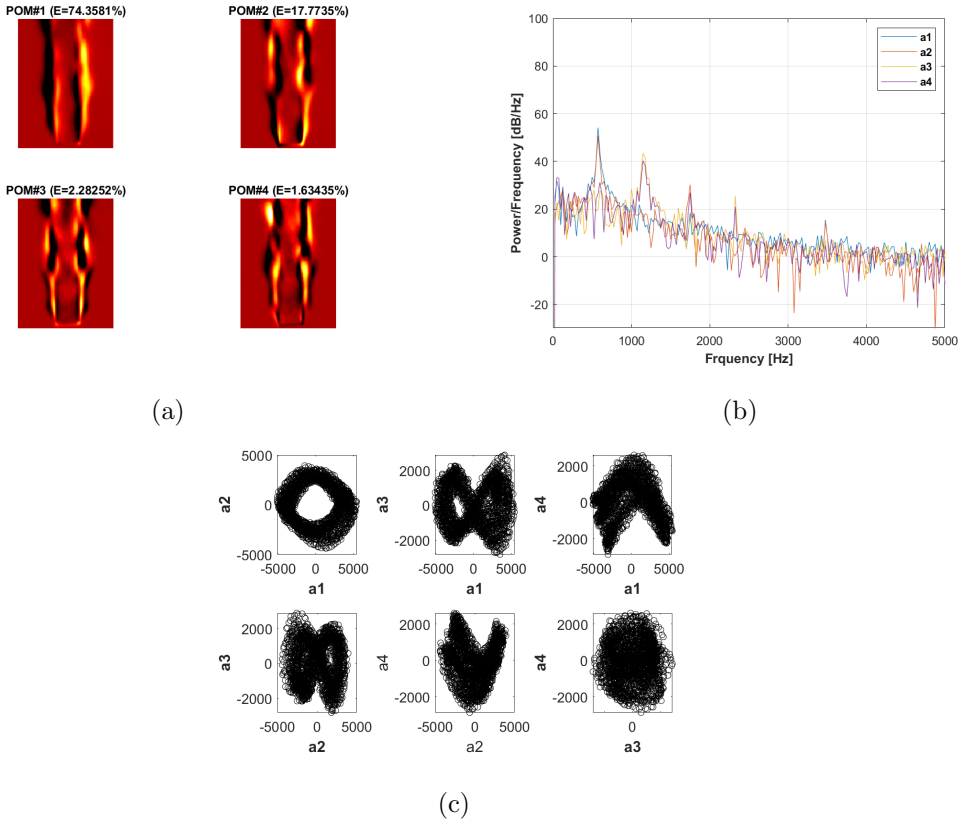

(a) (b)

(c)

Figure 5.32: **Coaxial jet (R = 0.3)**: POD analysis results for 581 Hz excitation at an amplitude of $u' = 2.6$ m/s at a PN. Results include (a) the first four POD mode structures with associated percentage of energetic content, and where the color denotes strength of the mode scaled by its own norm, (b) the power spectral density associated with the first POD mode, and (c) sample plots of the POD mode coefficients against one another for the first four modes.

5.2.3 Pressure Anti-Node Forcing

Subjecting the coaxial jet to acoustic forcing at a PAN (at the waveguide center) produced a different susceptibility diagram compared to the one that was found for the single jet under presumably identical conditions. The acoustic-flame coupling regimes of anchored flames, periodic lifting flames, and permanently lifted flames were observed for the different velocity ratio cases, but the forcing amplitude required to transition through the regimes, interpreted here as susceptibility, had the opposite trend to that of the previous single jet results. A summary of the general findings is given next where results are focused on the PAN resonant

modes of 360 Hz and 1,150 Hz; results for 775 Hz which were complicated by the resonance of the manifold of the center jet and only used for susceptibility diagram.

Schlieren imaging showing a time series of jet responses for the R = 0.05 and R = 0.3 cases to forcing at 360 Hz for a common forcing amplitude is shown in Figure 5.33. Clear flow structures are evident when comparing these two cases, to be expected as in the unforced results, but the overall bulk axial oscillations are present for both velocity ratios. The amplitudes for this frequency were applied as high as 1,000 Pa and no clear liftoff, periodic or permanent, was detected. In between the oscillation cycle the jet appears to wrap around the exit tube as a vortex appears to form; green arrows show this part of the acoustic period. The long wavelength oscillations help the coaxial jet flames anchor better than the single jet. These findings were consistent for all three velocity ratios examined in this study. A summary of the forcing conditions will be given and discussed below.

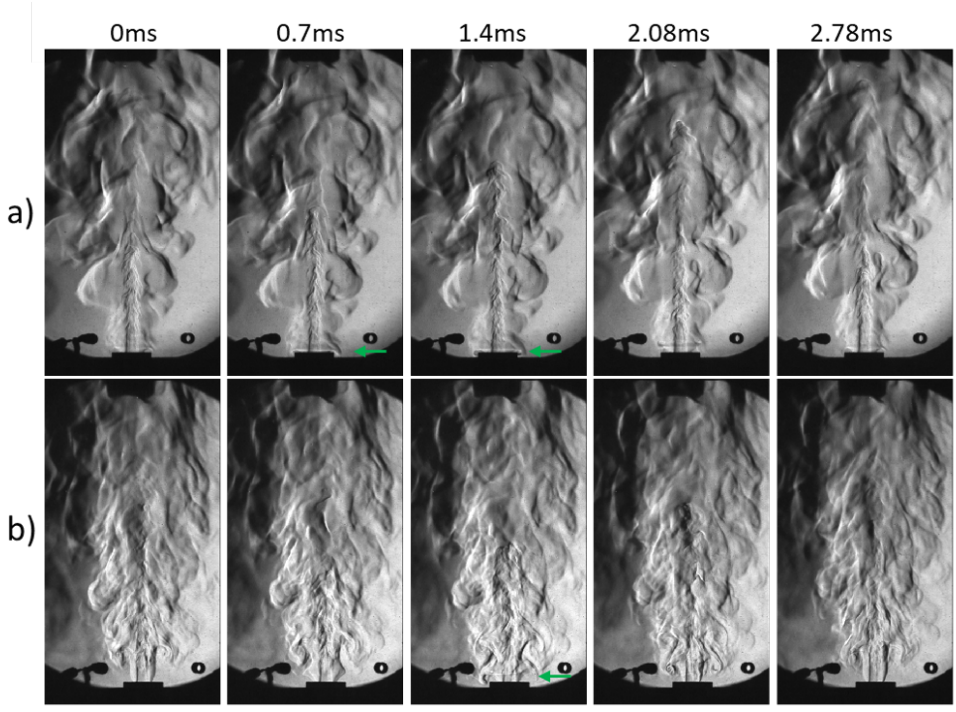

Figure 5.33: **Coaxial Jet**: Equally spaced Schlieren images of the forced jet flame over one time/acoustic period for a PAN at 360Hz with forcing amplitude of 500 Pa at velocity ratios of (a) R = 0.05 and (b) R = 0.30.

At the highest forcing frequency, 1,150 Hz, the flame was susceptible to lifting as seen in the single jet. A time series of Schlieren images for both R = 0.05 and 0.3 in Figure 5.34 illustrate a forcing amplitude just before periodic liftoff for case 1 and case 3. The bulk axisymmetric, puff-like oscillations are more pronounced at the lower velocity ratio where large structures are formed around the center fuel jet, indicated in Figure 5.34a. Figure 5.34b illustrates a highly turbulent reacting jet where the shear layer has oscillations created by the acoustic field but the overall puff-like structures are not as prominent in the surrounding gases. These visualizations suggest that at the larger velocity ratios where a clear shear layer instabilities between the inner fuel and outer (annular) flow are present, the acoustics can have an influence, depending on frequency and amplitude. Further increasing the forcing amplitude leads to periodic lifted and permanently lifted flames.

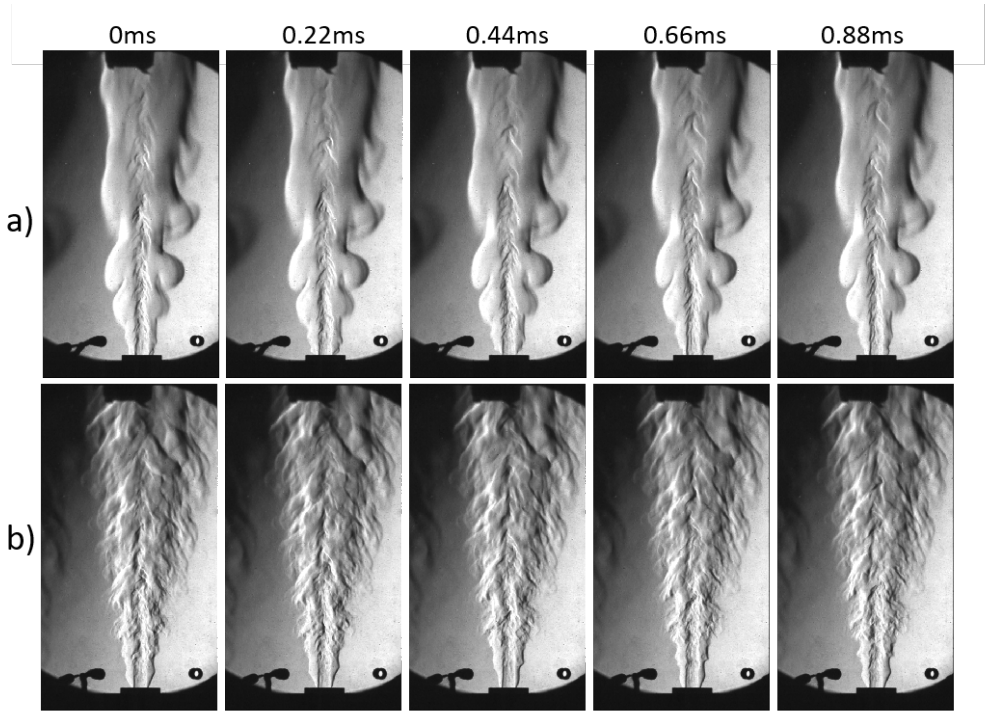

Figure 5.34: **Coaxial Jet**: Equally spaced Schlieren images of the forced jet flame over one time/acoustic period for a PAN at 1,150Hz with forcing amplitude of 150 Pa at velocity ratios of (a) R = 0.05 and (b) R = 0.30.

Flame anchoring stability becomes important beyond a threshold forcing amplitude at the higher frequencies. For case 1 (R = 0.05), PAN forcing above a threshold forcing amplitude of P' = 200 Pa causes the flame to lift periodically and transition to a fully lifted flame within a narrow range of forcing amplitude. For example, Figure 5.35 tracks the flame standoff distance over two periods of a PAN forcing condition at 360Hz at a forcing amplitude of P' = 200 Pa, and compares it to the simultaneously acquired pressure signal. One can match sequential OH* chemiluminescence images equally spaced over the two periods, shown in Figure 5.35a, to the red markers corresponding to flame and pressure oscillations in Figure 5.35b. The green arrows in the images refer to the point of the period where the flame is lifted. Lastly, the plot in Figure 5.35c of the pressure signal vs. the flame standoff distance once again displays an elliptic orbit that signifies that there is a nearly out-of-phase

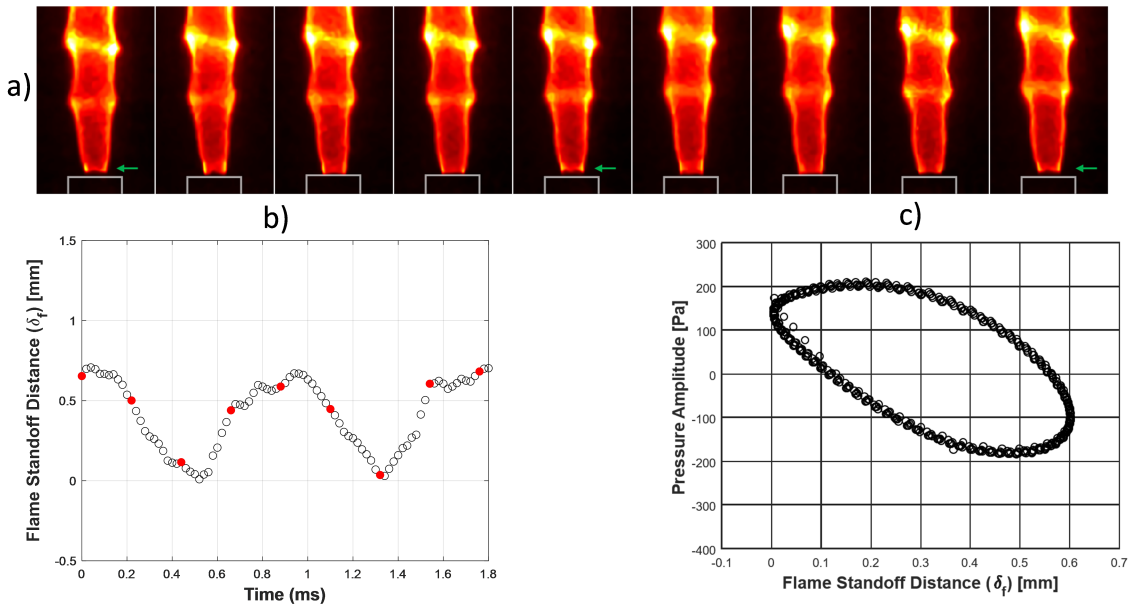

Figure 5.35: **Coaxial Jet (R = 0.05)**: Cyclical processes of flame liftoff and reattachment at PAN with a frequency of 1,150 Hz and forcing amplitude of $P'_{max} = 200Pa$. (a) Equally spaced OH* chemiluminescence images over two periods (in false color). (b) Time series plot of the flame standoff distance (red markers correspond to the OH* chemiluminescence images above). (c) Pressure measurements in Pa vs. standoff distance in mm.

relationship between the acoustic pressure field and the flame standoff oscillations, the latter of which are inversely related to the heat release, consistent with the Rayleigh criterion for combustion instabilities. Referring back to the single jet results in section 5.1.3 the results found for the coaxial jet have similar phasing between the applied acoustics and flame liftoff oscillations. Figure 5.36 has similar results for a periodically lifting flame but a higher velocity ratio case 3 (R = 0.3). The frequency of focus is still 1,150Hz for a forcing amplitude of $P'_{max} = 250Pa$. A direct forcing amplitude comparison is difficult for PAN excitation because of the different regimes that flame experiences. The coupling between the flame liftoff height and the pressure is out-of phase. In general for the cases where the coaxial jet configuration did experience periodic liftoff the coupling behavior was consistent with these findings. POD analysis of the different flame liftoff regimes is presented in appendix C.

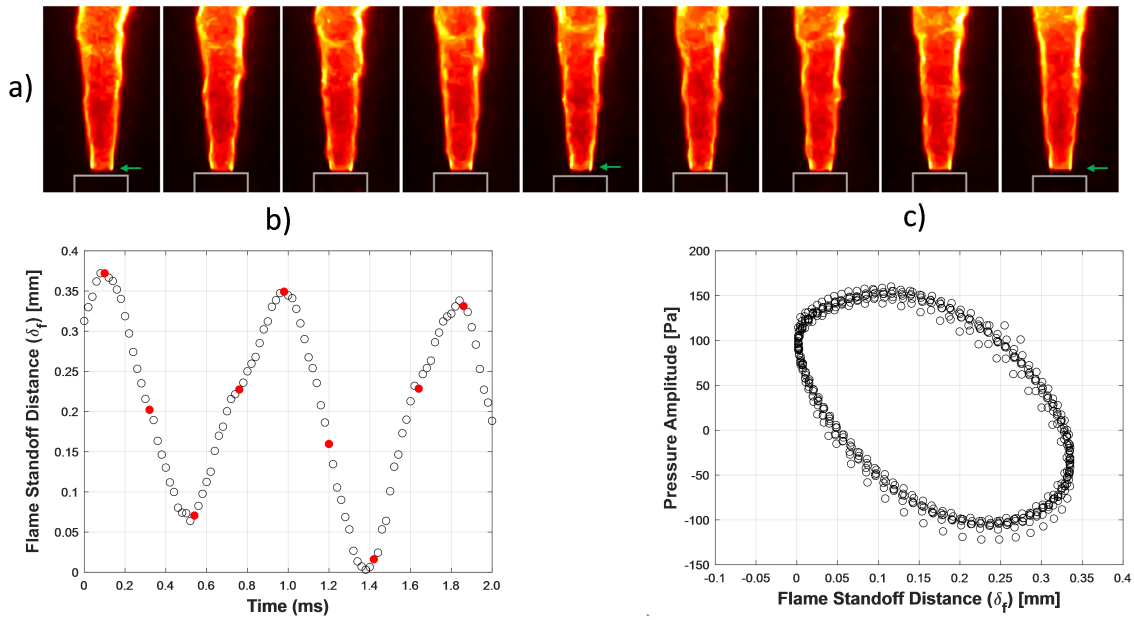

Figure 5.36: **Coaxial Jet (R = 0.3)**: Cyclical processes of flame liftoff and reattachment at PAN with a frequency of 1,150 Hz and forcing amplitude of $P'_{max} = 250Pa$. (a) Equally spaced OH* chemiluminescence images over two periods (in false color). (b) Time series plot of the flame standoff distance (red markers correspond to the OH* chemiluminescence images above). (c) Pressure measurements in Pa vs. standoff distance in mm.

A Summary of the PAN results are put into forcing amplitude vs frequency plots in Figures 5.37-5.39, similar to that in Figure 5.16a for the single jet. In case 1 for the coaxial jet (R = 0.05) the flame was more stable and less responsive to the lower forcing frequencies and became less stable (i.e., more responsive to forcing) with regards to flame anchoring as the frequencies were shifted to the two higher resonant modes. At the lowest PAN frequency of 360Hz the flame remained stable, but still with a puff-like response, for the maximum acoustic amplitude that could be achieved by the speakers which was around 1000 Pa. At the higher forcing frequencies periodic and permanently lifted flames were achieved at above 400 Pa for 775Hz and 200 Pa for 1,150Hz the latter of which was closest to the natural instability frequency of around 1500 Hz. It is important to note that the results found here were for one test campaign but were reproduced on different testing days for the same flow conditions, including after the burner was disassembled and reassembled.

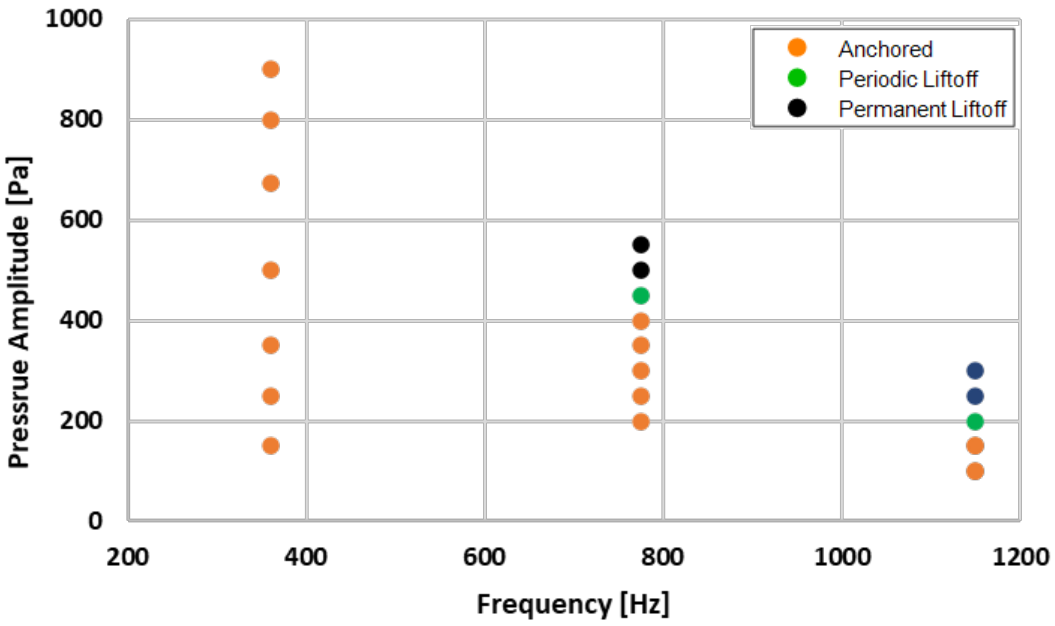

Figure 5.37: **Coaxial Jet (R = 0.05)**: Flame response to PAN forcing for various frequencies and forcing amplitudes.

Increasing the outer (annular) flow to 4 m/s (case 2) for a velocity ratio of R = 0.17 showed similar trends to the lower velocity ratio, shown in Figure 5.38. Once again, no flame liftoff response was seen for the maximum level of excitation produced at 360Hz. At 775Hz the forcing amplitude required to transition from the unstable flame was near 450 Pa for periodic liftoff and above 600 Pa for permanently lifted flames. For the highest frequency forcing at 1,150Hz, amplitudes about 200 Pa destabilized the anchored flame. Figure 5.39 displays the results for the largest velocity ratio studied, R = 0.3. In this flow regime the results for the three cases discussed have a similar susceptibility diagrams, but it becomes increasing more difficult to destabilize an anchored flame (that is, to cause flame distortion via forcing) at the higher velocity ratios. These results suggest that if the facility was capable of producing larger forcing amplitudes (greater than 1,000 Pa) at 360 Hz perhaps the regime change from anchored flames to lifted flames could take place.

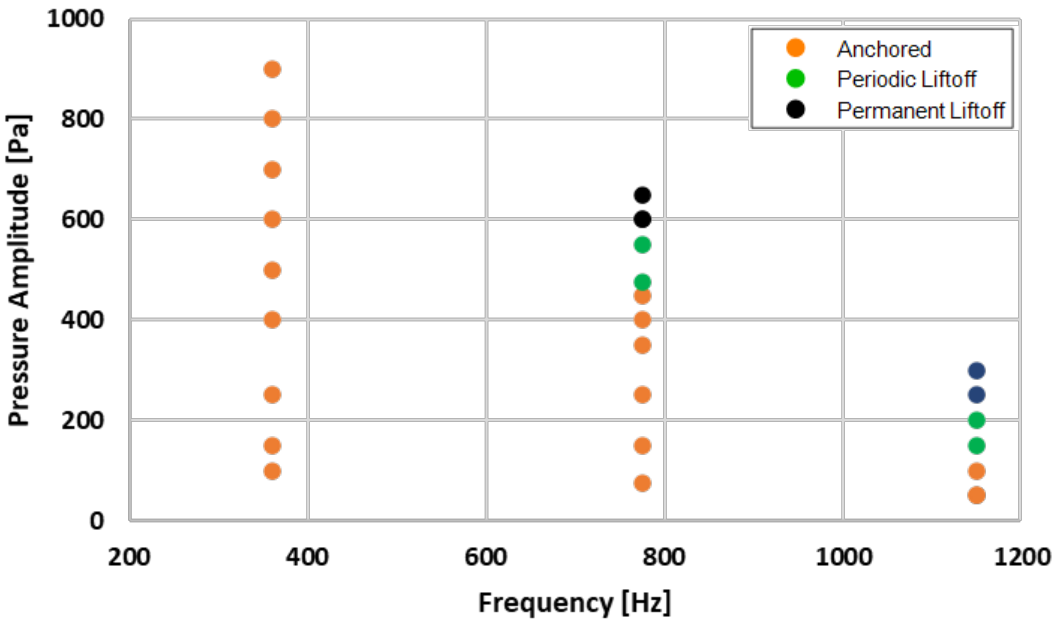

Figure 5.38: **Coaxial Jet (R = 0.17)**: Flame response to PAN forcing for various frequencies and forcing amplitudes.

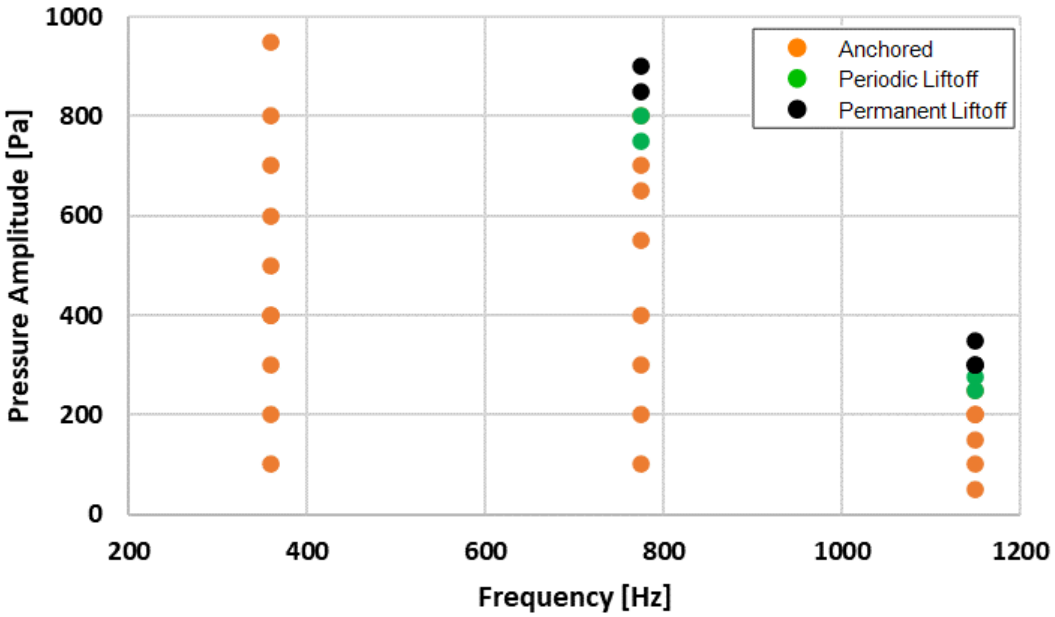

Figure 5.39: **Coaxial Jet (R = 0.3)**: Flame response to PAN forcing for various frequencies and forcing amplitudes.

One hypothesis for the difference in the receptivity of this coaxial jet to transverse acoustic forcing compared to the single jet is that natural frequencies of the shear layer may be at play. In the single jet no obvious natural instability could be extracted from the methods used in this work which could suggest that either its spectral character is more broadband and with lower natural perturbations to the jet, as is common to convectively unstable jet shear layers. In contrast, the coaxial jet is observed to have an unstable shear layer, especially at higher velocity ratios, with a preferred mode/frequency. This phenomenon, where applied forcing can affect natural instabilities, is typically described in a "V" shaped lock-in diagram of amplitude vs. frequency [55, 121]. The "V" is formed by the minimum amplitude necessary for the system to lock-in to applied forcing at a given frequency. The natural frequency is located at the lowest point of the "V" because lock-in at that frequency should be relatively easy to achieve; at forcing frequencies well above or well below the natural frequency, it becomes more difficult to affect the jet with external excitation. The results presented above

show that the jet becomes more responsive to excitation and is susceptible to liftoff as the frequency increases toward the natural frequency, which is close to 1500 Hz, as indicated in section 5.2.1. The current test matrix does not include higher forcing frequencies that are necessary to explore this conjecture in more detail, but a speculation could be made that forcing at frequencies beyond 1,150 Hz might establish the "V" shape lock-in type diagram describing the transitions from an anchored flame to a periodically lifted flame and ultimately a fully lifted flame.

CHAPTER 6

Conclusions and Recommendations for Future Work

6.1 Droplet Combustion

This work explored the effects of reactive nAl and inert $nSiO_2$ particulate additives on combustion characteristics of ethanol droplets for three alternative types of experimental procedures. The different experimental methods performed in this study produced similar trends and magnitudes in K, the standoff distance, and OH* chemiluminescent intensity when nanoparticles (NPs) were added to ethanol but with a few quantitative differences. The key findings of this work can be summarized as follows:

For nonfed droplets, the evolution of equivalent droplet diameter followed the classical d2 law during the majority of the droplet's lifetime, but toward the end of combustion, there were deviations from the law associated with particulate- generated droplet deformation and particle expulsion, occurring sooner for higher loading concentrations of nAl and $nSiO_2$. Fed droplets with nAl additives experienced a much longer period of quasi-steady-state combustion yet showed instabilities such as jetting from the droplet, a periodic droplet shrink and growth cycle, and subsequent particle expulsion and burning. Increasing concentrations of nAl produced systematic enhancements in quantified values of K, by up to 13% with 6 wt.% loading. The addition of the inert nano-particulate $nSiO_2$ led to somewhat inconsistent trends in K with increasing concentration, although relatively small increases in K, for example, by around 5% for the addition of 1 wt.% $nSiO_2$, were documented. Droplets with nAl additives had consistently higher K values than either neat ethanol or $nSiO_2$-laden droplets at a given concentration, but the increases were not on the order of magnitude suggested by some groups (e.g., Tanvir and Qiao [38]), highly likely resulting from radiation absorption

effects for others' exploration of a fuel droplet stream with nanoparticulates.

A simple droplet combustion model demonstrated similar trends in K to the experimental observations with increasing loading concentration of nAl and even $nSiO_2$. The model suggested that alterations in thermal properties of the base fuel produced by adding nAl, especially alterations in the heat of combustion, thermal conductivity, and flame temperature, could be responsible for higher vaporization rates with increasing concentrations. The differences between the reactive and inert NP additives corresponded principally to the nAl's energetic content, as expected, but the differences in agglomeration and residual structure also affected global droplet properties. TEM and SEM images provided insights into these differences in residual structure between nAl and $nSiO_2$ formed on the fiber or capillary after combustion.

The current experimental configuration for droplet combustion studies not only enables exploration of the effects of alternative fuels and additives to condensed-phase combustion but combined with simple model scaling as well as TEM and SEM imaging and EDS analysis could provide a systematic means for designing new energetic fuel additives for aerospace propulsion systems.

6.2 Reacting Jets

Turbulent nonpremixed methane jet flames were subjected to transverse acoustic forcing. Two separate burner configurations were used in this receptivity study: (1) a single jet surrounded by a co-flow and (2) a coaxial jet that was also surrounded by a co-flow. The reacting jets could be situated at either a pressure node or a pressure anti-node location, which was controlled by the phase between the speakers. Based on the findings from the single jet burner, a mixture consisting of 60% Nitrogen and 40% oxygen was used as the oxidizer for both studies. The results were visualized using high speed simultaneous Schlieren and OH* chemiluminescence imaging.

Under PN forcing, sinuous motion (i.e., a transverse sinusoidal oscillation) of the flame was observed, which created flame wrinkling as seen from the OH* chemiluminescence images. The Schlieren imaging showed that the fuel core developed a wave-like pattern that caused the intact core length to shorten. At the pressure node at higher frequencies the center fuel jet was changed by the acoustic field more than the flame. The flame remained anchored for all forcing conditions studied at the PN. These qualitative features of the flame response were present in both burner configurations. POD analysis of the flame dynamics was performed, revealing differences in the POD mode shapes and coefficient plots, as well as the dominant mode frequencies as the amplitude of applied acoustic excitation was increased. For most cases, the bulk asymmetric motion of the jet was described by the first two POD modes which described the asymmetric motion of the flame across the burner axis and the flame wave patterns developed on the flame edges. Additionally, jet distortion was observed from the planar images taken in this study. The distortion included jet flattening and spreading of the jet at higher forcing frequencies. The flame "flattened" into an ellipsoidal shape, with a narrow axis in the direction of the acoustic waves. The reacting jet were able to respond at the frequency of the unsteady acoustic field even at higher frequencies, but with a diminishing response of the flame. No changes in the flame anchoring stability were observed; the flame remained anchored for all forcing conditions studied.

Conversely, at a pressure anti-node, the coupling of the acoustics and flame gave rise to an axisymmetric response (puff-like oscillations), which prompted the flame to become unstable at the anchoring region. Three regimes were found: stable attached flames exhibiting axisymmetric flame puff-like wrinkling, periodically lifting and reattaching flames with more pronounced symmetric flame wrinkling, and flames that were permanently lifted by the acoustic field. In general, the reacting jets experienced this behavior but there were notable differences between the single jet and coaxial jet configuration.

The single jet demonstrated flame response at all three forcing frequencies, but succeedingly larger amplitudes were required to produce corresponding liftoff behavior (periodic or

permanent) as the frequency increased, and the resulting fluctuations in the flame standoff distance decreased. The boundaries of the susceptibility diagram for the corresponding liftoff behaviors increased roughly linearly with frequency. This proved that the single jet configuration behaves similar to basic diffusion flames under external forcing. Higher frequencies required increasing larger amplitudes to achieve flame response, which is consistent with periodically strained flame theory [117, 118, 119, 62]. Further exploration of the PAN case, beyond the qualitative features and liftoff boundary, revealed more details regarding how the periodically lifting flame regime and the fully lifted flame regime was coupled to the acoustic field. Results revealed that the liftoff behavior was tightly coupled with the pressure field; both periodic lifting and permanently lifted flames were out-of-phase with the pressure signal acquired at the jet exit. This behavior was consistent with large standoff distances being caused by maximum flow rates when the pressure was minimized, which caused the pressure drop and the resulting flow rate to be maximized.

The reacting coaxial jet configuration revealed different susceptibility diagrams compared to the single jet. The three velocity ratios explored in this study were more susceptible to acoustic forcing at higher frequencies, which is the opposite trend of what was found for the single jet. These results were found for all three velocity ratios explored in this study. A total of three frequencies were explored, same ones as for the single jet, where the lifting regimes only appeared at the two higher frequencies (775 Hz and 1150 Hz). It is likely that liftoff behavior could have been achieved at the lowest frequency with larger forcing amplitudes, but the current system was not capable of producing such amplitudes. This difference in flame-acoustic coupling signifies that there are more complex flow instabilities involved that could not be determined with the current methods. The different susceptibility diagrams suggest the possibility that the coaxial jet has a natural frequency larger than the largest one explored here (1150 Hz). Spectral results extracted from the unforced images revealed that the R = 0.3 had a frequency around 1500 Hz in the shear layer between the inner flow and annular flow. If indeed the coaxial jets have instabilities at higher frequencies, then a

hypothesis for results found here is that a lock-in diagram exist where the jet is only able to achieve liftoff at a given threshold amplitude at a given frequency. The farther way the applied forcing is from the natural frequency the more difficult it is for the jet respond. This is consistent the three frequencies applied to the reacting coaxial jets. Lastly, in the cases were periodic liftoff and full liftoff were seen, the standoff distance behaved similar to the single jet where an out-of-phase relationship with the pressure signal existed.

6.3 Future Work

This dissertation has described extensive experiments relevant to combustion of droplets and jets. While both studies have brought fundamental insight into the dynamics of the nanofuel characterization and the behavior of reacting jets under acoustic forcing, there remain a number of issues on which future studies should focus. Recommendations will focus on the reacting jet experiment given that the droplet experiments have ended and the reacting jet is a new experiment.

There is a lot of opportunity to continue to study reacting jets using this experimental setup. First when it comes to characterization of the exit flow conditions, it would be recommended that hot-wire anemometry or particle image velocimetry be performed to correctly predict the velocity profiles and map the natural frequencies more precisely. Having this data will be crucial to continue the study of the coaxial jet based on the results presented. Another recommendation that will help to further explore the stability of this jet is to change the chamber transverse length, which will give different harmonic frequencies for both PN and PAN that will not couple with the center tubes as was found for one frequency in this study. Lastly, given that reacting jet can be well characterized it would be interesting to incorporate heat exchangers to the fuel and oxidizer lines to have control over the exit temperatures, this was one idea that was of interest to our group but was not accomplished in this study.

Appendix A

Droplet Combustion Data

A.1 Ethanol Properties

Fuel Property	Ethanol
Chemical Formula	C_2H_5OH
Molecular Weight [kg/kmol]	46.17
Stoichiometric Air-Fuel Ratio	8.948
Specific Heat Capacity* [kJ/(kg-K)]	2.42
Thermal Conductivity* [W/(m-K)]	0.179
Kinematic Viscosity* $[mm^2/s]$	1.452
Mass Density* $[g/cm^3]$	0.79
Boiling Temperature [K]	351
Freezing Temperature [K]	158
Heat of Vaporization [kJ/kg]	841
Heat of Combustion [kJ/g]	27
Energy Density $[kJ/m^3]$	21.3

* Calculated for T $\approx$ 295 K and P $\approx$ 101,325 Pa

Table A.1: Thermodynamic Properties of liquid Ethanol [61]

A.2 Burning Rate Constant Tables for Case I, II, and III

Loading Concentration (wt %)	Min	Max	Average	Uncertainty (±)
0	0.792	0.822	0.808	0.007
1	0.823	0.841	0.833	0.005
2	0.838	0.848	0.842	0.004
3	0.826	0.851	0.838	0.010
4	0.844	0.891	0.867	0.015
5	0.858	0.888	0.871	0.008
6	0.865	0.898	0.876	0.010

Table A.2: Burning Rate Constant Statistics for Case I (nAl)

Loading Concentration (wt %)	Min	Max	Average	Uncertainty (±)
0	0.792	0.822	0.808	0.007
1	0.801	0.829	0.818	0.009
2	0.811	0.836	0.829	0.008
3	0.797	0.839	0.823	0.014

Table A.3: Burning Rate Constant Statistics for Case I ($nSiO_2$)

Loading Concentration (wt %)	Min	Max	Average	Uncertainty (±)
0	0.717	0.765	0.742	0.013
1	0.735	0.811	0.771	0.013
2	0.747	0.814	0.774	0.043
3	0.758	0.811	0.783	0.039
4	0.774	0.812	0.797	0.050
5	0.756	0.811	0.777	0.025
6	0.744	0.819	0.781	0.024

Table A.4: Burning Rate Constant Statistics for Case II (nAl)

Loading Concentration (wt %)	Min	Max	Average	Uncertainty (±)
0	0.754	0.841	0.797	0.024
1	0.805	0.858	0.828	0.017
2	0.807	0.919	0.848	0.042
3	0.839	0.912	0.866	0.022
4	0.838	0.972	0.879	0.049
5	0.860	0.964	0.906	0.043
6	0.871	0.923	0.902	0.016

Table A.5: Burning Rate Constant Statistics for Case III (nAl)

Loading Concentration (wt %)	Min	Max	Average	Uncertainty (±)
0	0.754	0.841	0.797	0.024
1	0.811	0.863	0.838	0.020
2	0.749	0.831	0.790	0.032
3	0.770	0.846	0.808	0.031

Table A.6: Burning Rate Constant Statistics for Case III ($nSiO_2$)

Appendix B

Reacting Jets

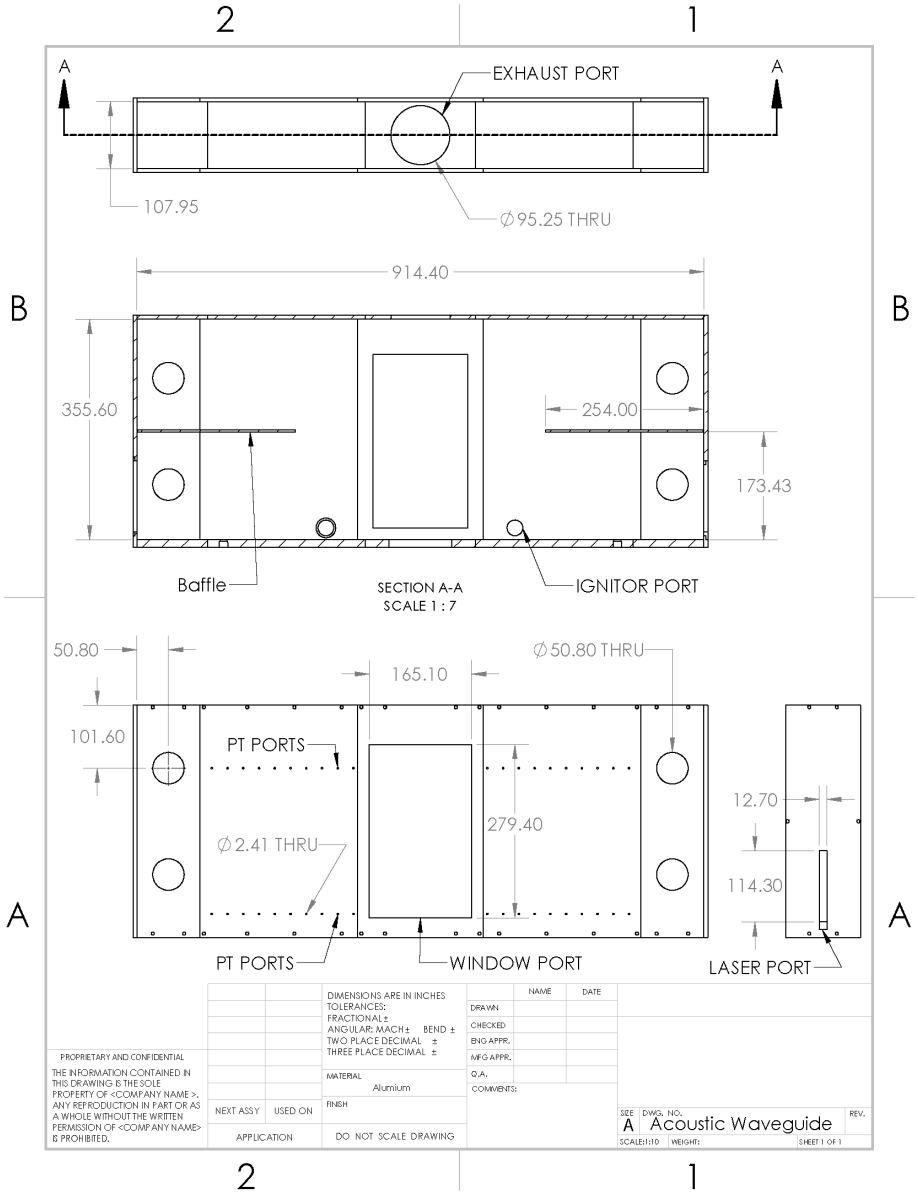

Figure B.1: Drawings of the acoustic waveguide used for the reacting jet experiments.

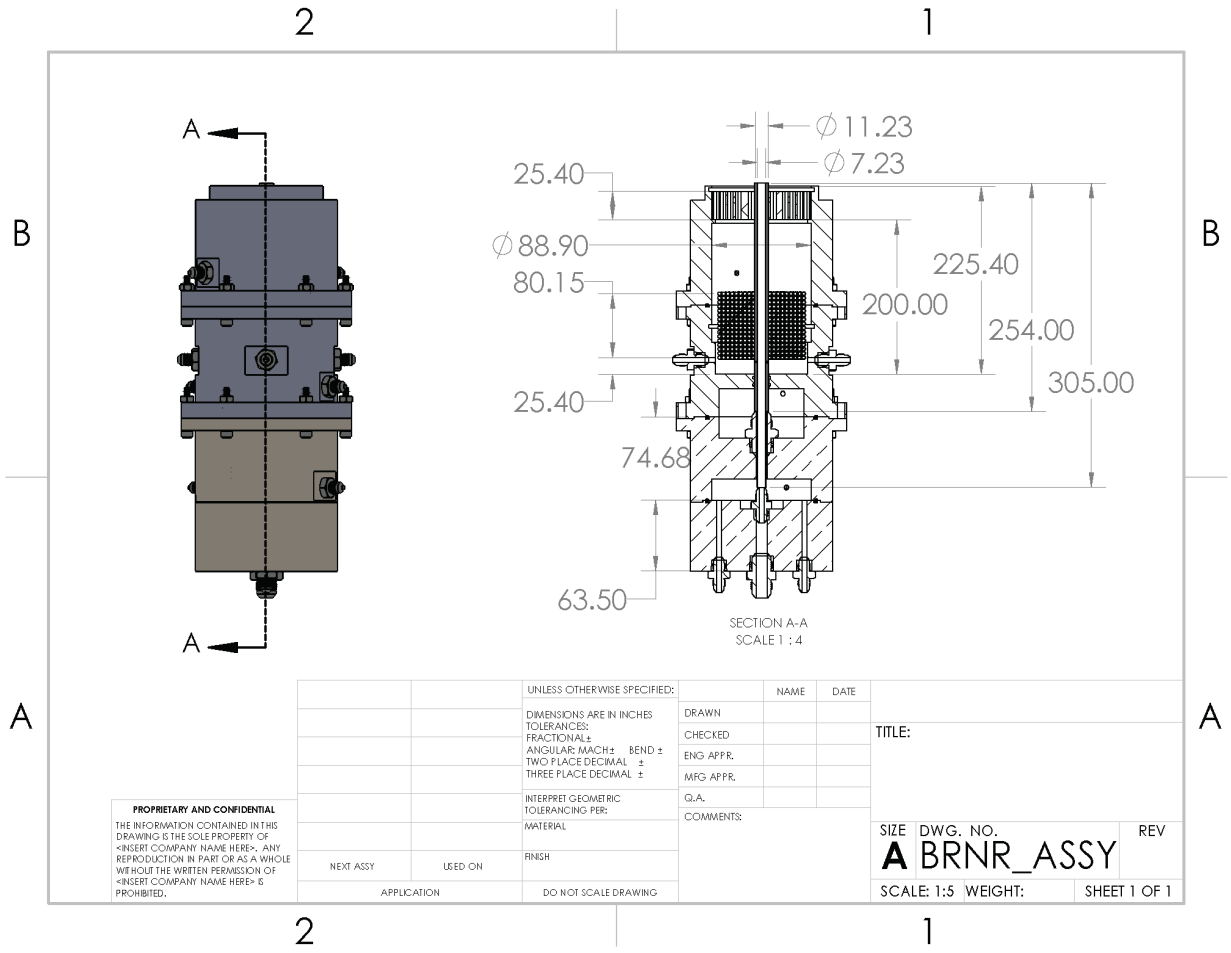

Figure B.2: Detailed drawings of the Burner.

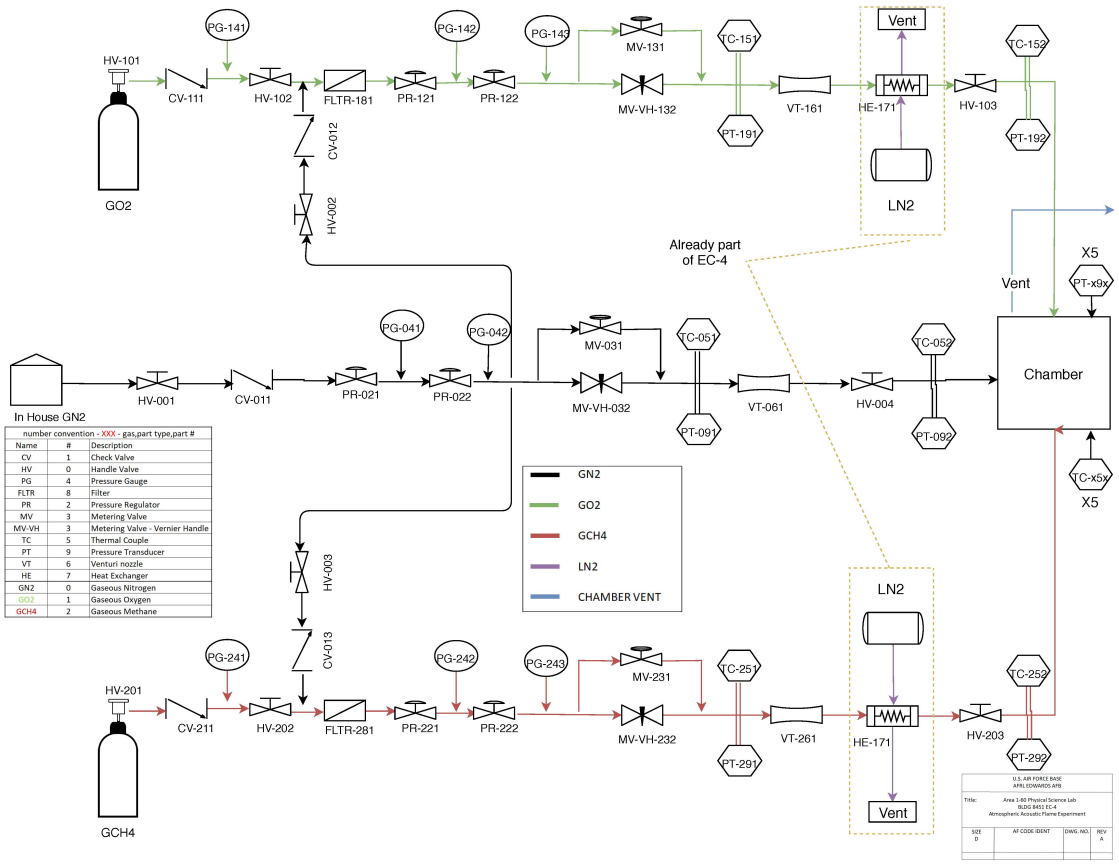

Figure B.3: PID of complete flow system used in test cell 4 for the fundamental acoustic combustion experiment.

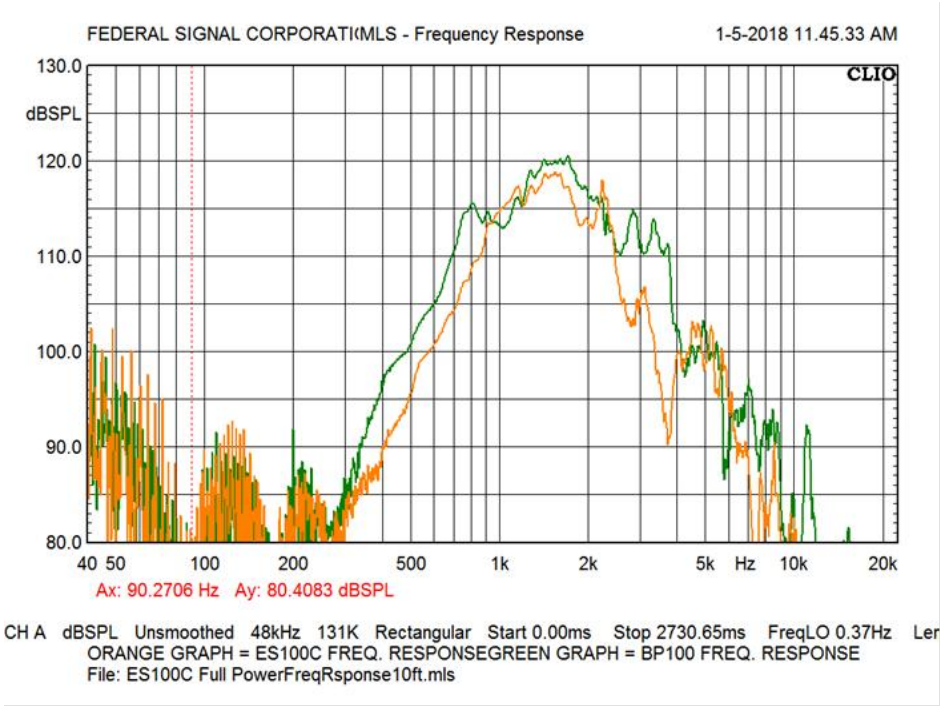

Figure B.4: Galls 100W Speaker (SK144) frequency response as reported by the manufacturer.

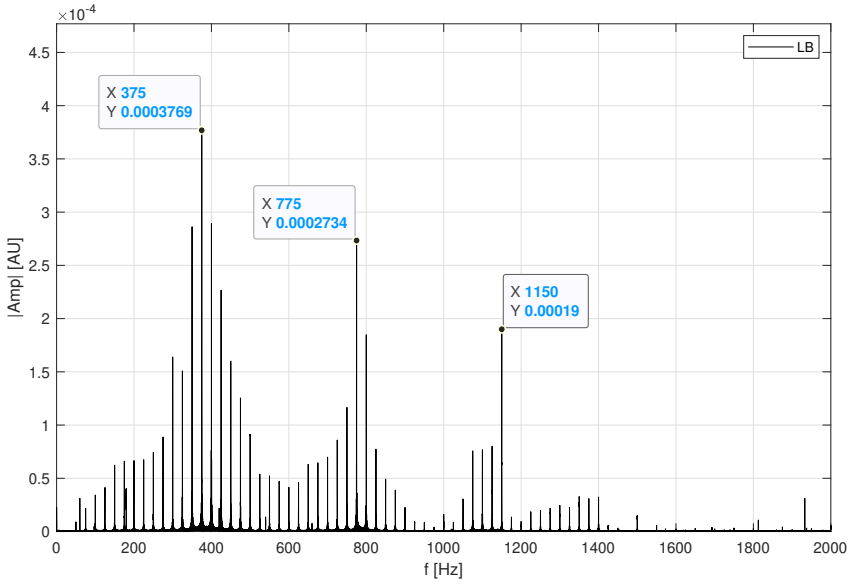

Figure B.5: Frequency sweep with speakers operated in-phase (0°) and a PAN occurring at the center of the waveguide. A FFT of a pressure transducer located 63.5mm to the left of the center and 6.35mm from the floor (bottom row). Resonant frequencies are shown to occur near 375 Hz, 775 Hz, and 1150 Hz.

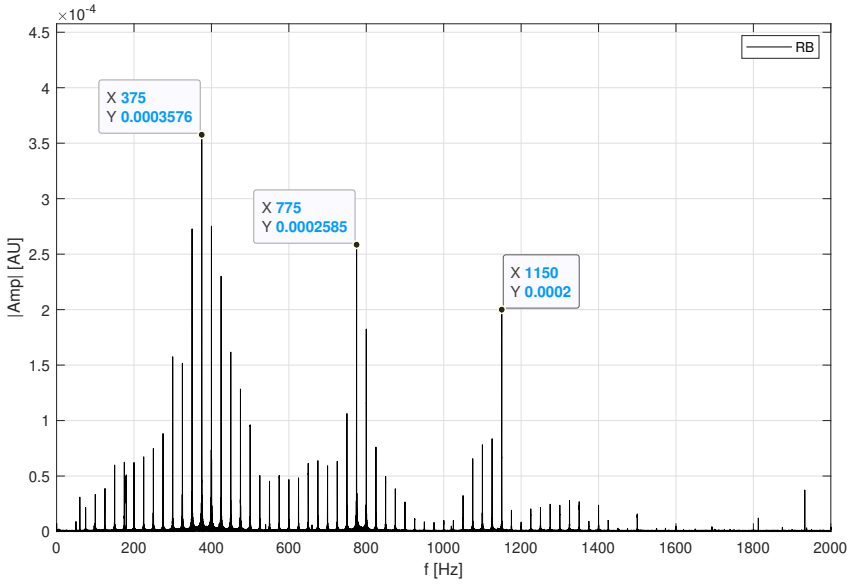

Figure B.6: Frequency sweep with speakers operated in-phase (0°) and a PAN occurring at the center of the waveguide. A FFT of a pressure transducer located 63.5mm to the right of the center and 6.35mm from the floor (bottom row). Resonant frequencies are shown to occur near 375 Hz, 775 Hz, and 1150 Hz.

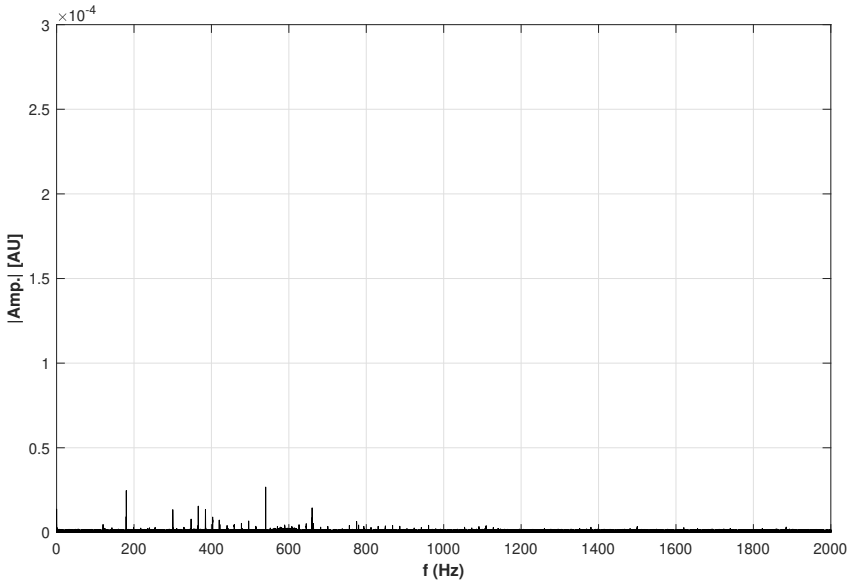

Figure B.7: Frequency sweep with speakers operated out-of-phase (180°) and a PN occurring at the center of the waveguide. A FFT of a pressure transducer located at the center and 6.35mm from the floor (bottom row). Resonant frequencies are shown to occur near 571 Hz, 942 Hz, and 1314 Hz.

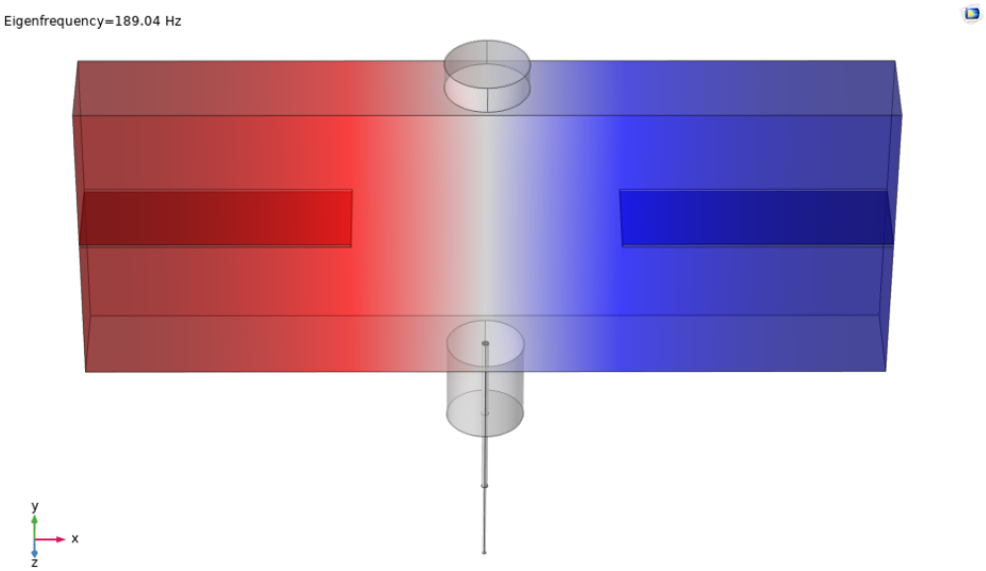

Figure B.8: Comsol Multiphysics acoustic simulation, amplitude of pressure fluctuations is shown for n_1 at frequency 189Hz.

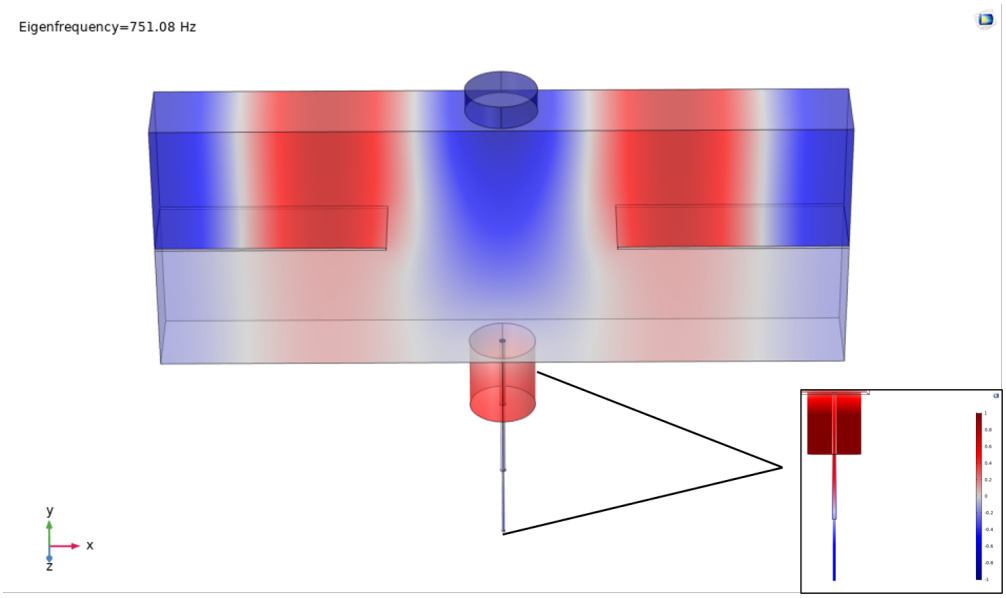

Figure B.9: Comsol Multiphysics acoustic simulation, amplitude of pressure fluctuations is shown for n_4 at frequency 750Hz.

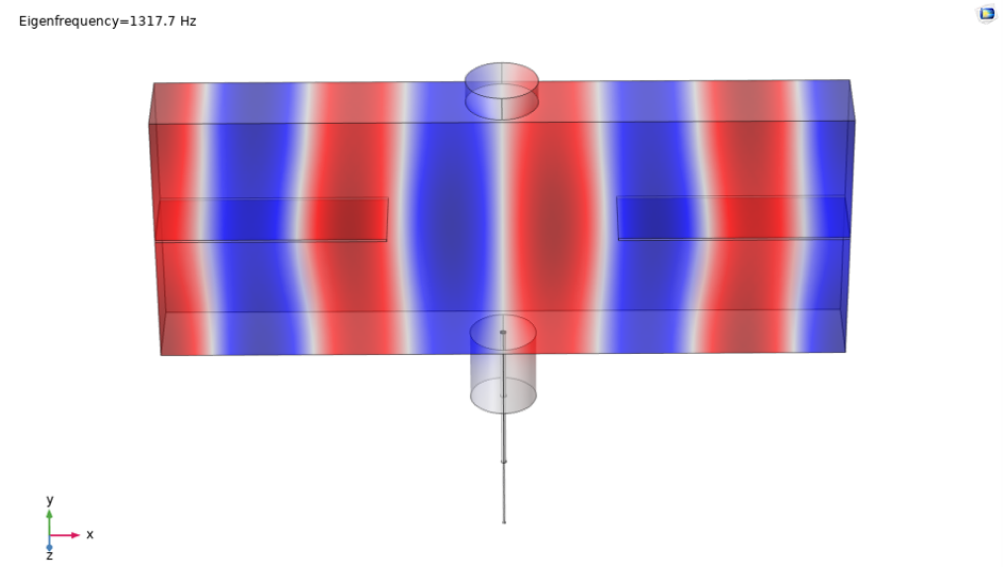

Figure B.10: Comsol Multiphysics acoustic simulation, amplitude of pressure fluctuations is shown for n_5 at frequency 941Hz.

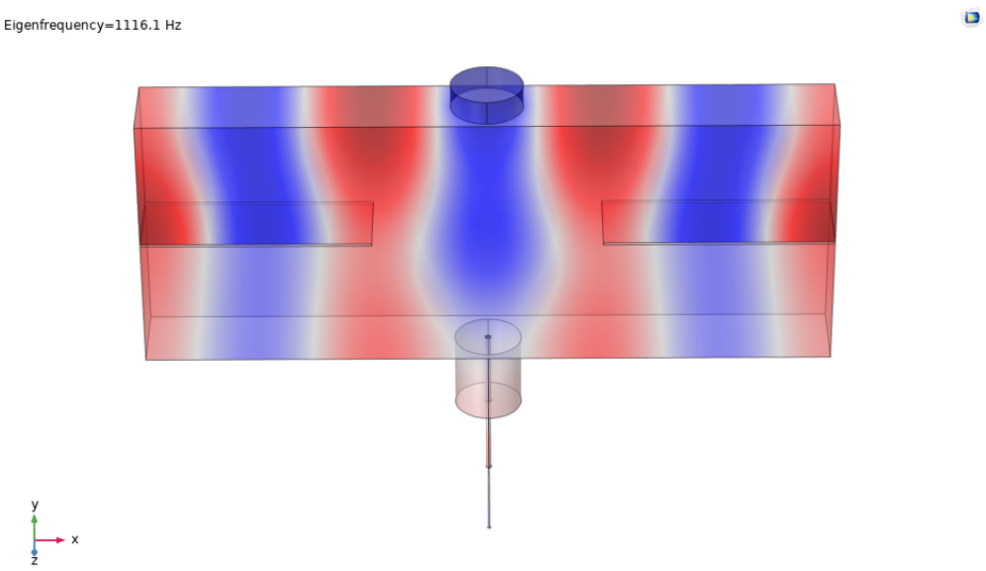

Figure B.11: Comsol Multiphysics acoustic simulation, amplitude of pressure fluctuations is shown for n_6 at frequency 1116Hz.

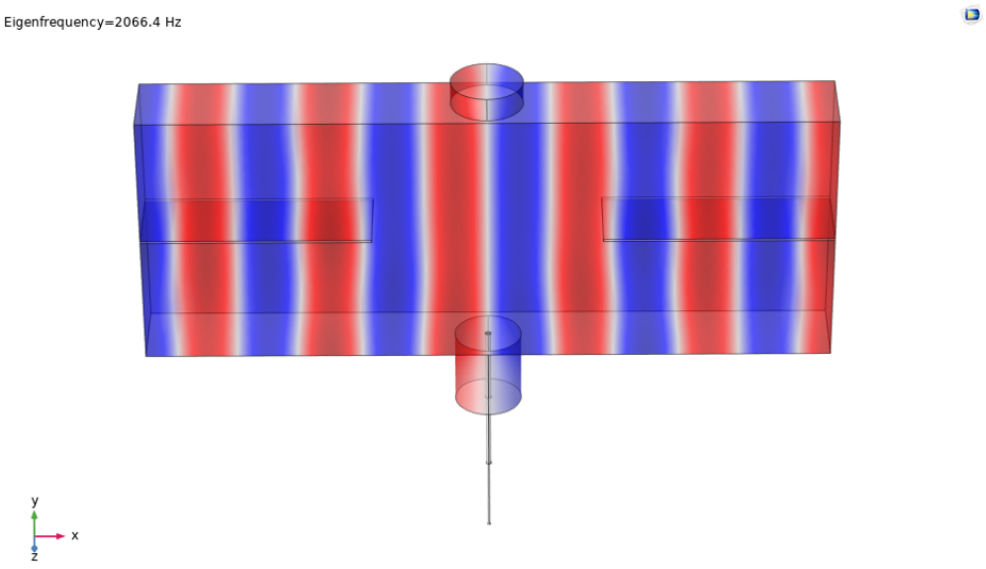

Figure B.12: Comsol Multiphysics acoustic simulation, amplitude of pressure fluctuations is shown for n_{11} at frequency 2066Hz.

Appendix C

Reacting Jets: Additional Results

C.1 Additional Single Jet Results

C.1.1 Pressure Node

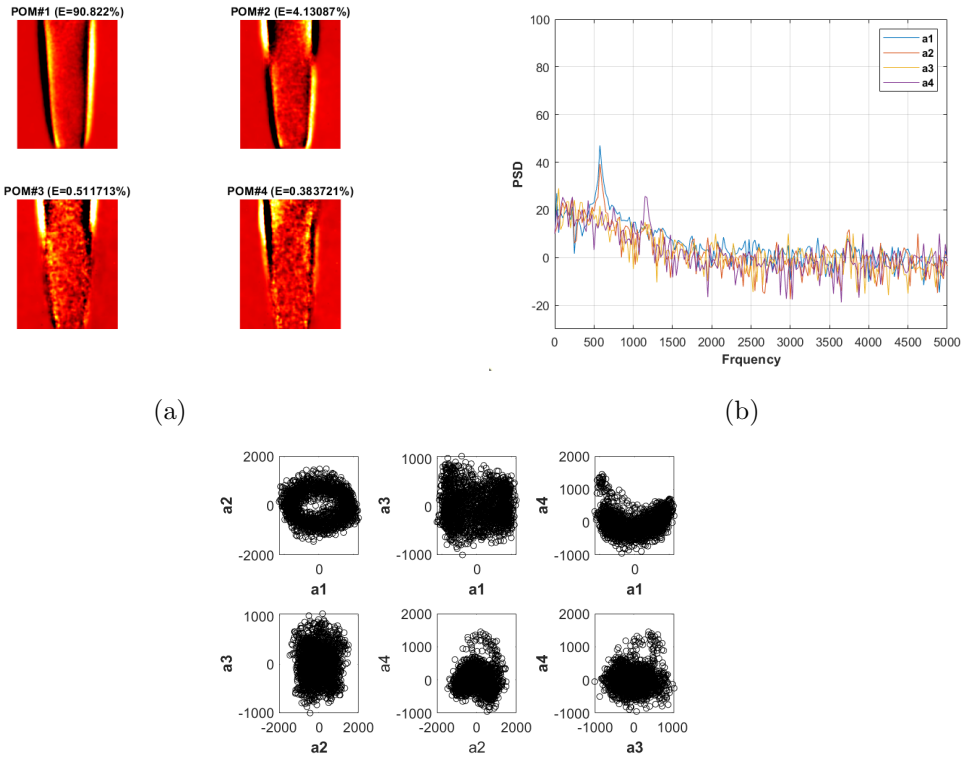

(a) (b)

(c)

Figure C.1: **Single Jet**: POD analysis results for 581 Hz excitation at an amplitude of $u' = 0.8$ m/s at a PN. Results include (a) the first four POD mode structures with associated percentage of energetic content, and where the color denotes strength of the mode scaled by its own norm, (b) the power spectral density associated with the four POD modes, and (c) sample plots of the POD mode coefficients against one another for the first four modes. $Re_{fuel} = 5,300$, $40\%O_2$.

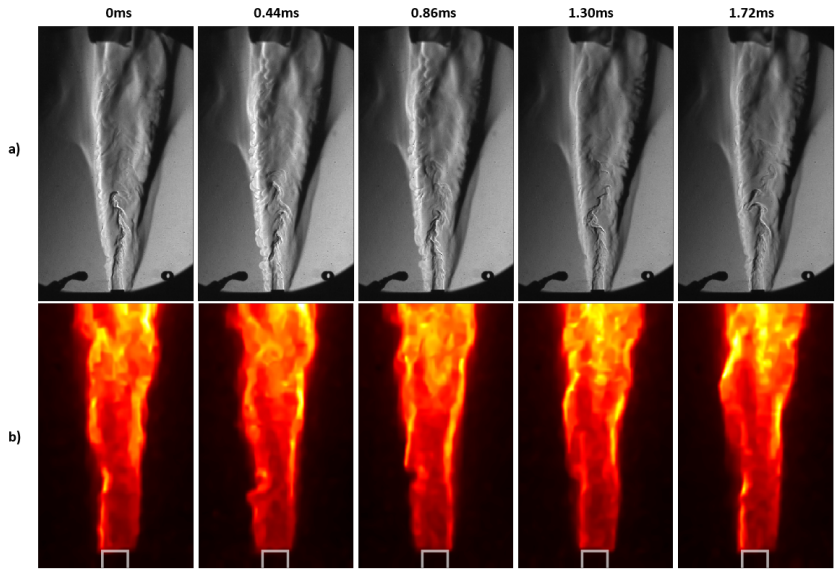

Figure C.2: **Single Jet**: Equally spaced images over one time/acoustic period corresponding to a PN forcing frequency at 581Hz with forcing amplitude of $u' = 2.6$ m/s. (a) depicts Schlieren images and (b) depicts OH* chemiluminescence images in false color.

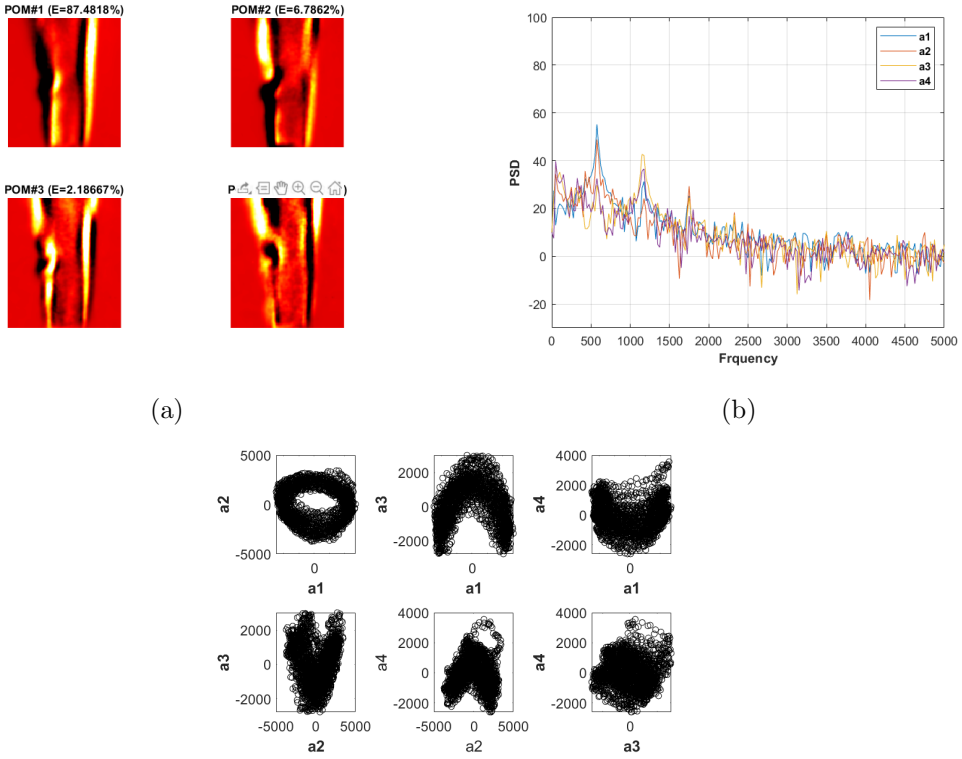

(a) (b)

(c)

Figure C.3: **Single Jet**: POD analysis results for 581 Hz excitation at an amplitude of $u' = 2.6$ m/s at a PN. Results include (a) the first four POD mode structures with associated percentage of energetic content, and where the color denotes strength of the mode scaled by its own norm, (b) the power spectral density associated with the four POD modes, and (c) sample plots of the POD mode coefficients against one another for the first four modes.

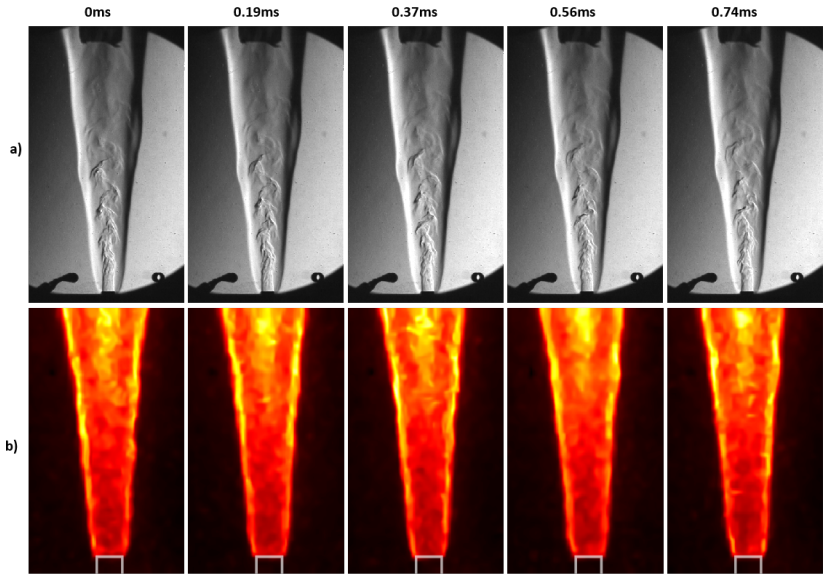

Figure C.4: **Single Jet**: Equally spaced images over one time/acoustic period corresponding to a PN forcing frequency at 1348Hz with forcing amplitude of $U^{'} = 0.8$ m/s. (a) depicts Schlieren images and (b) depicts OH* chemiluminescence images in false color.

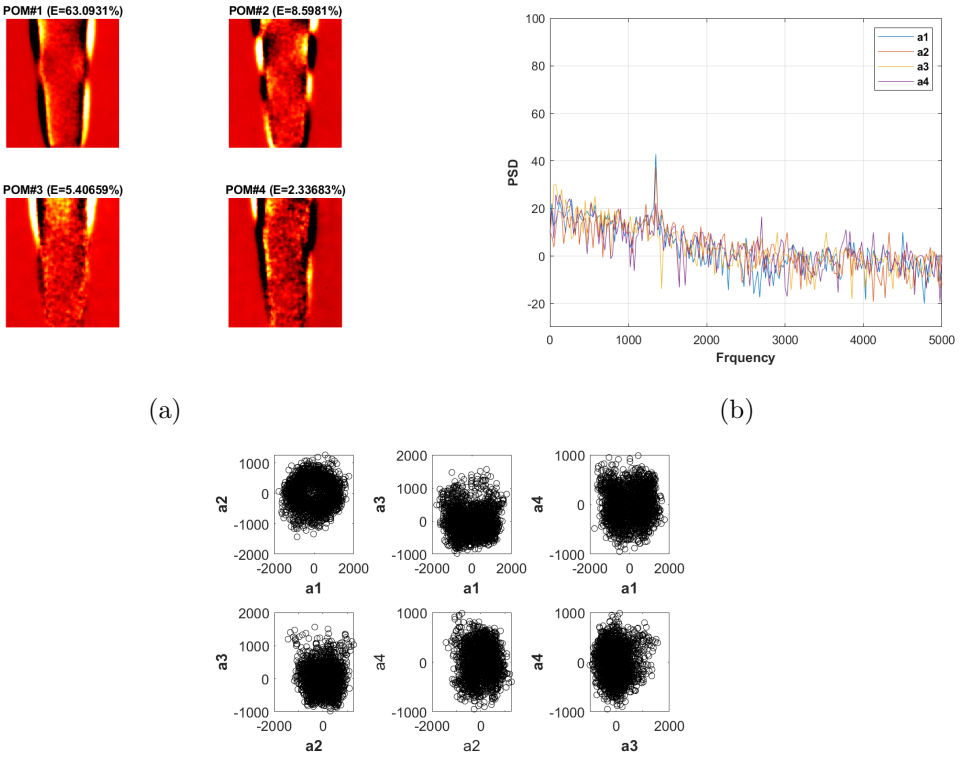

(a) (b)

(c)

Figure C.5: **Single Jet**: POD analysis results for 1348 Hz excitation at an amplitude of $U' = 0.8$ m/s at a PN. Results include (a) the first four POD mode structures with associated percentage of energetic content, and where the color denotes strength of the mode scaled by its own norm, (b) the power spectral density associated with the four POD modes, and (c) sample plots of the POD mode coefficients against one another for the first four modes.

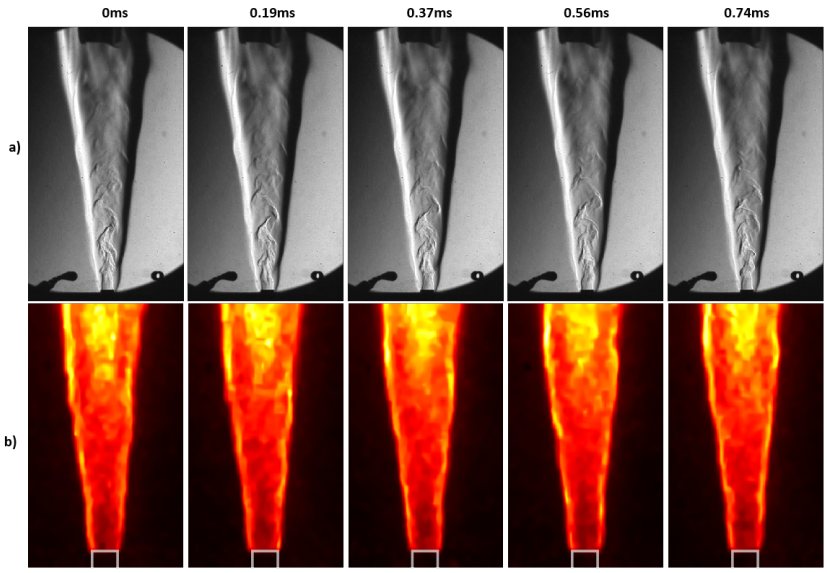

Figure C.6: **Single Jet**: Equally spaced images over one time/acoustic period corresponding to a PN forcing frequency at 1348Hz with forcing amplitude of $U^{'} = 2.6$ m/s. (a) depicts Schlieren images and (b) depicts OH* chemiluminescence images in false color.

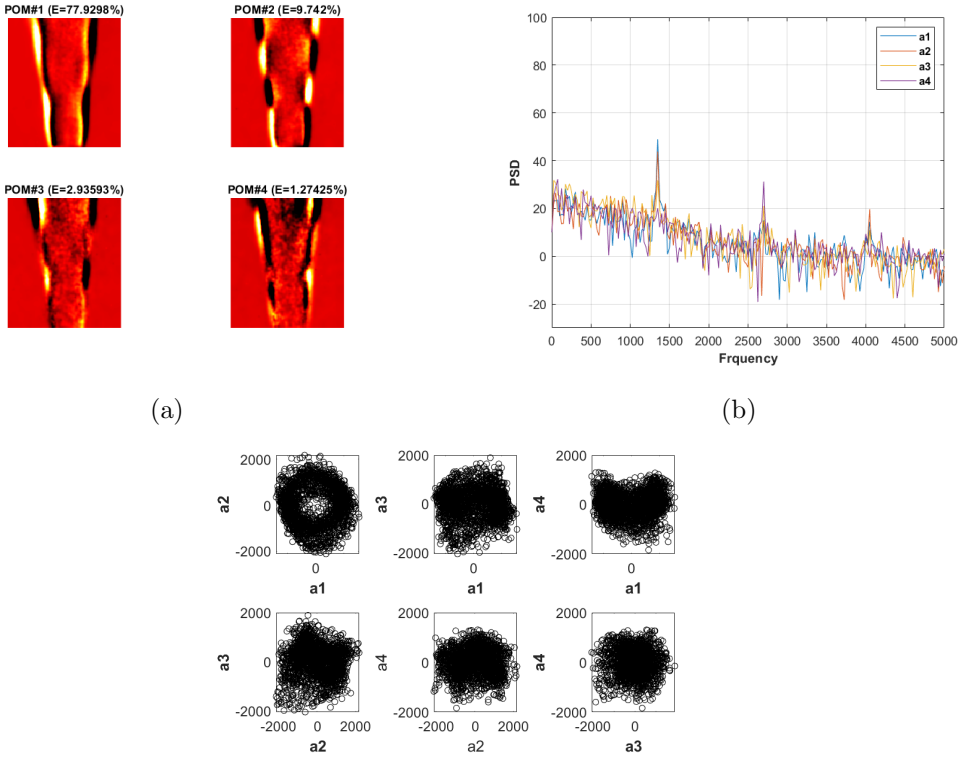

(a) (b)

(c)

Figure C.7: **Single Jet**: POD analysis results for 1348 Hz excitation at an amplitude of $U' = 2.6$ m/s at a PN. Results include (a) the first four POD mode structures with associated percentage of energetic content, and where the color denotes strength of the mode scaled by its own norm, (b) the power spectral density associated with the four POD modes, and (c) sample plots of the POD mode coefficients against one another for the first four modes.

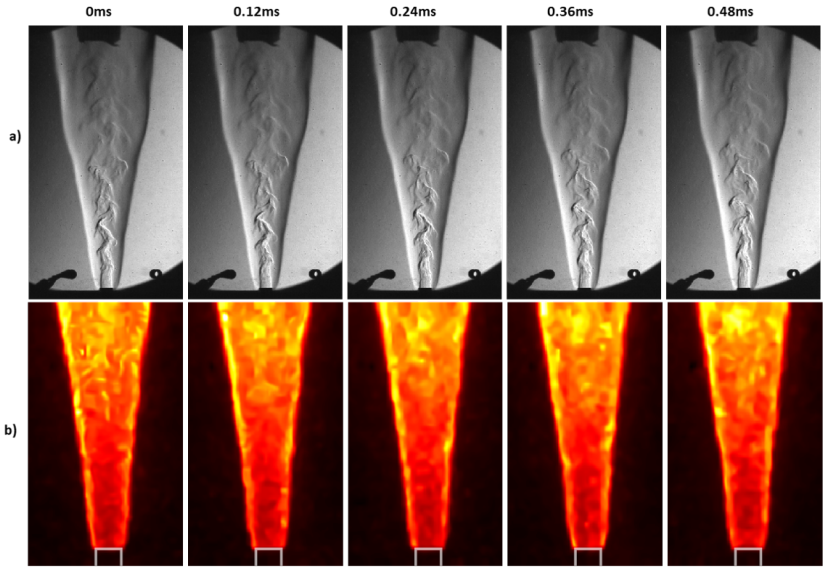

Figure C.8: **Single Jet**: Equally spaced images over one time/acoustic period corresponding to a PN forcing frequency at 2065Hz with forcing amplitude of $U^{'} = 0.8$ m/s. (a) depicts Schlieren images and (b) depicts OH* chemiluminescence images in false color.

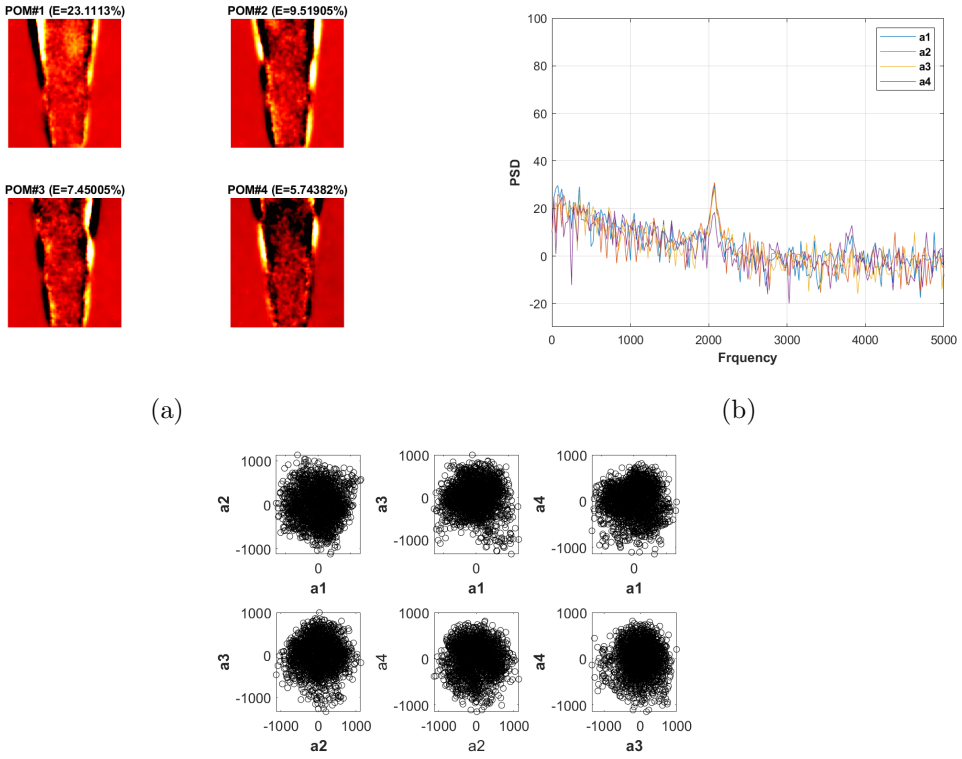

(a) (b)

(c)

Figure C.9: **Single Jet**: POD analysis results for 2065 Hz excitation at an amplitude of $U' = 0.8$ m/s at a PN. Results include (a) the first four POD mode structures with associated percentage of energetic content, and where the color denotes strength of the mode scaled by its own norm, (b) the power spectral density associated with the four POD modes, and (c) sample plots of the POD mode coefficients against one another for the first four modes.

C.1.2 Pressure Anti-node

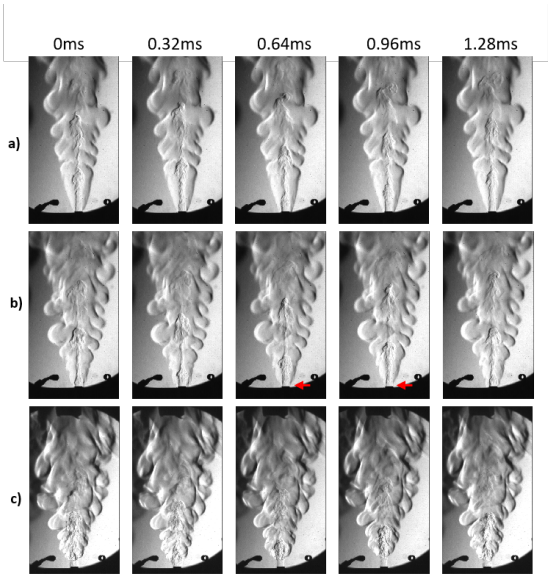

Figure C.10: **Single Jet**: Equally spaced Schlieren images of the forced jet flame over one time/acoustic period for a PAN at 775Hz with increasing forcing amplitudes of (a) $p'_{max} = 280Pa$, (b) $p'_{max} = 450Pa$, and (c) $p'_{max} = 550Pa$.

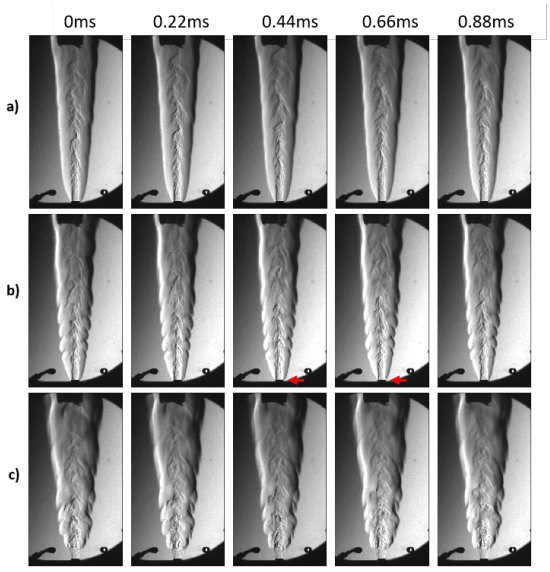

Figure C.11: **Single Jet**: Equally spaced Schlieren images of the forced jet flame over one time/acoustic period for a PAN at 1150Hz with increasing forcing amplitudes of (a) $p'_{max} = 300Pa$, (b) $p'_{max} = 650Pa$, and (c) $p'_{max} = 900Pa$.

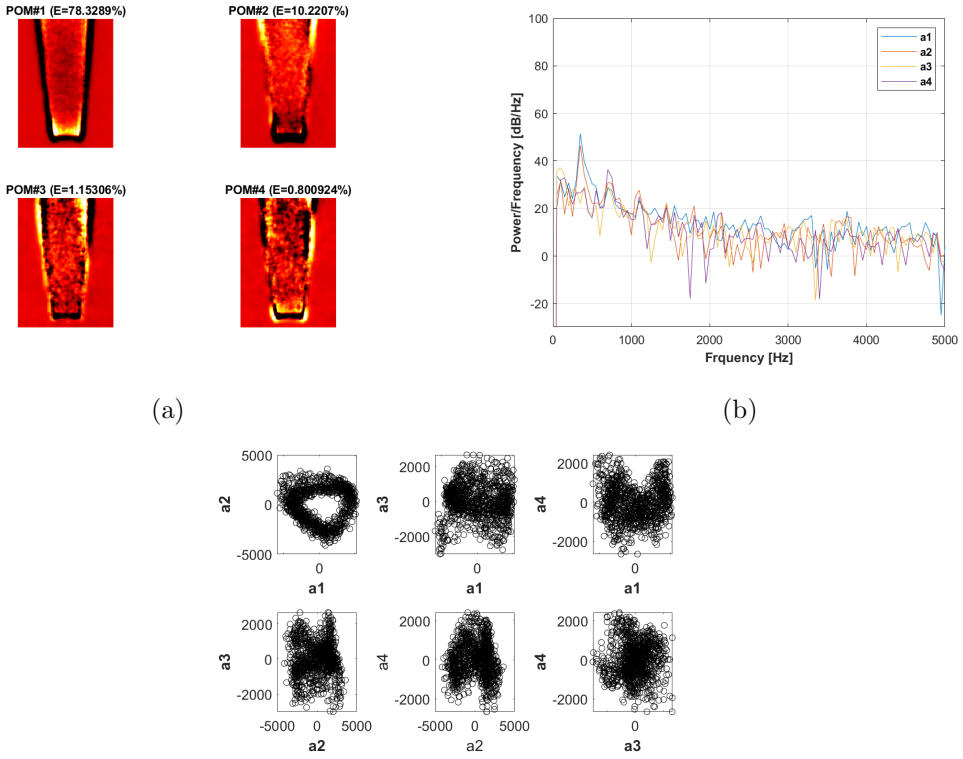

(a) (b)

(c)

Figure C.12: **Single Jet**: POD analysis results for 360 Hz excitation at an amplitude of $p'_{max} = 175$ Pa at a PAN. Results include (a) the first four POD mode structures with associated percentage of energetic content, and where the color denotes strength of the mode scaled by its own norm, (b) the power spectral density associated with the four POD modes, and (c) sample plots of the POD mode coefficients against one another for the first four modes.

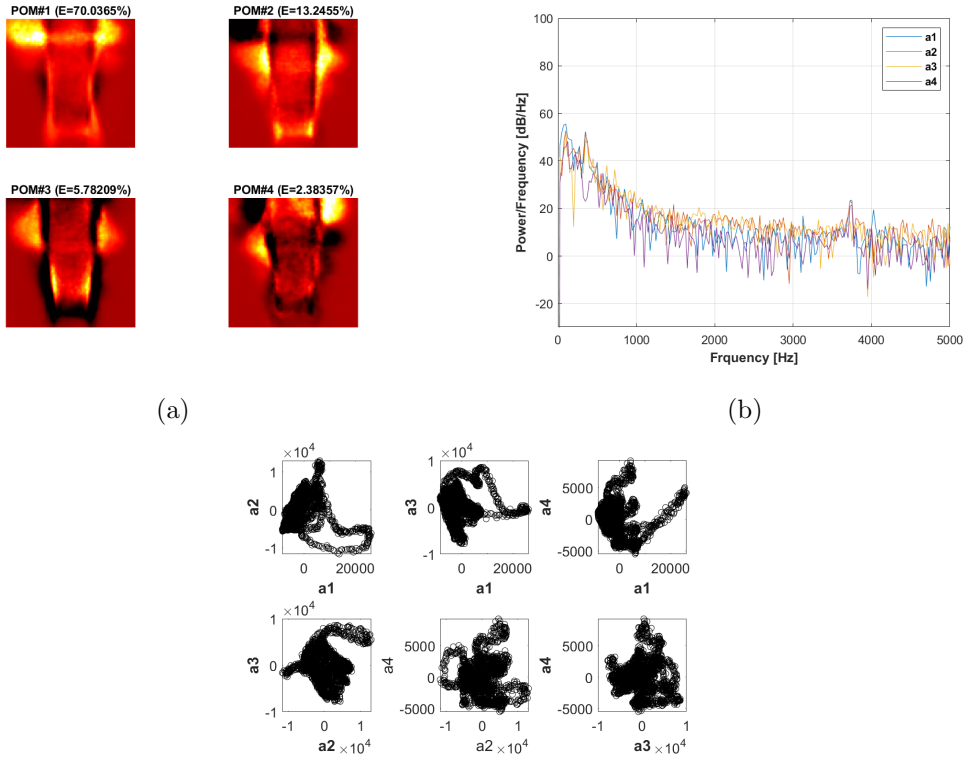

(a) (b)

(c)

Figure C.13: **Single Jet**: POD analysis results for 360 Hz excitation at an amplitude of $p'_{max} = 300$ Pa at a PAN. Results include (a) the first four POD mode structures with associated percentage of energetic content, and where the color denotes strength of the mode scaled by its own norm, (b) the power spectral density associated with the four POD modes, and (c) sample plots of the POD mode coefficients against one another for the first four modes.

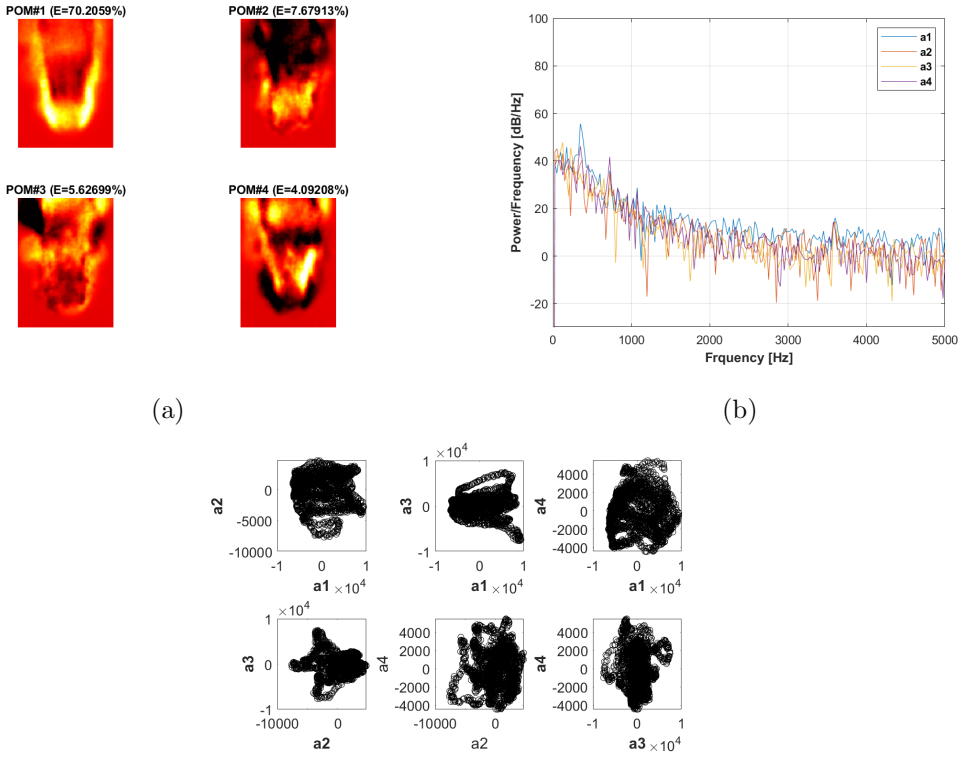

(a) (b)

(c)

Figure C.14: **Single Jet**: POD analysis results for 360 Hz excitation at an amplitude of $p'_{max} = 450$ Pa at a PAN. Results include (a) the first four POD mode structures with associated percentage of energetic content, and where the color denotes strength of the mode scaled by its own norm, (b) the power spectral density associated with the four POD modes, and (c) sample plots of the POD mode coefficients against one another for the first four modes.

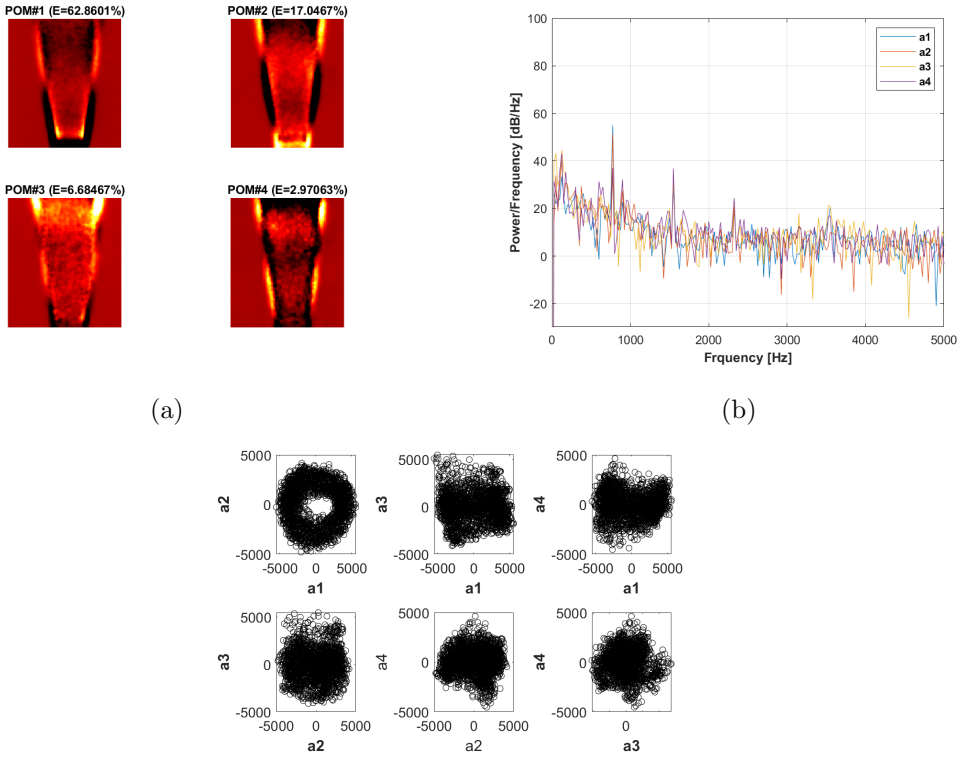

(a) (b)

(c)

Figure C.15: **Single Jet**: POD analysis results for 775 Hz excitation at an amplitude of $p'_{max} = 280$ Pa at a PAN. Results include (a) the first four POD mode structures with associated percentage of energetic content, and where the color denotes strength of the mode scaled by its own norm, (b) the power spectral density associated with the four POD modes, and (c) sample plots of the POD mode coefficients against one another for the first four modes.

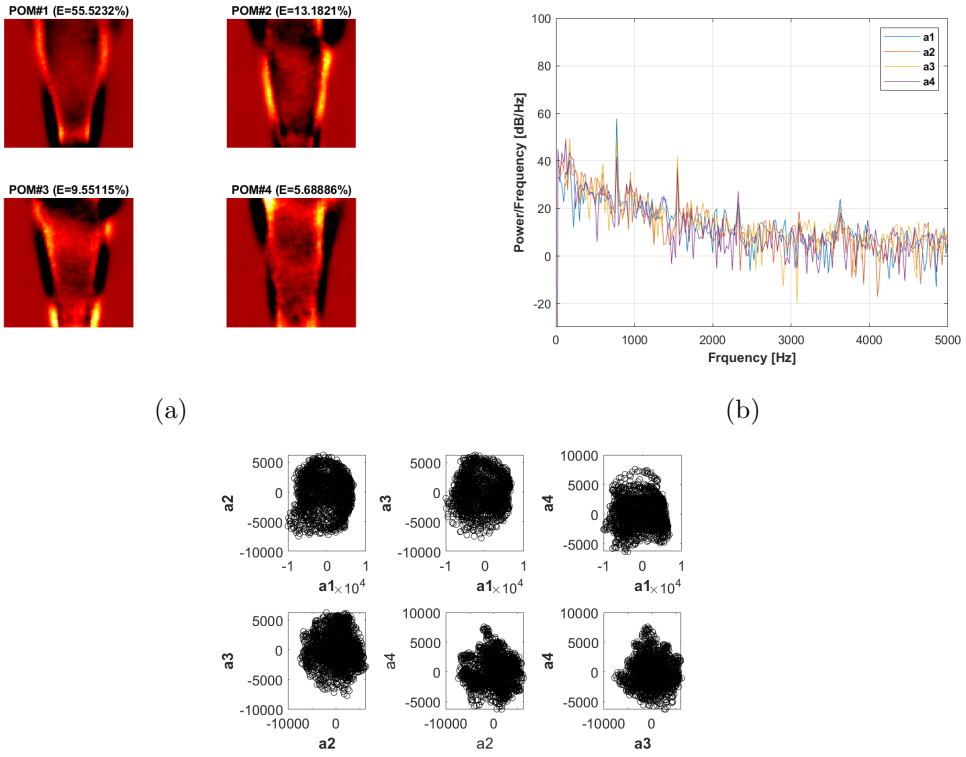

(a) (b)

(c)

Figure C.16: **Single Jet**: POD analysis results for 775 Hz excitation at an amplitude of $p'_{max} = 450$ Pa at a PAN. Results include (a) the first four POD mode structures with associated percentage of energetic content, and where the color denotes strength of the mode scaled by its own norm, (b) the power spectral density associated with the four POD modes, and (c) sample plots of the POD mode coefficients against one another for the first four modes.

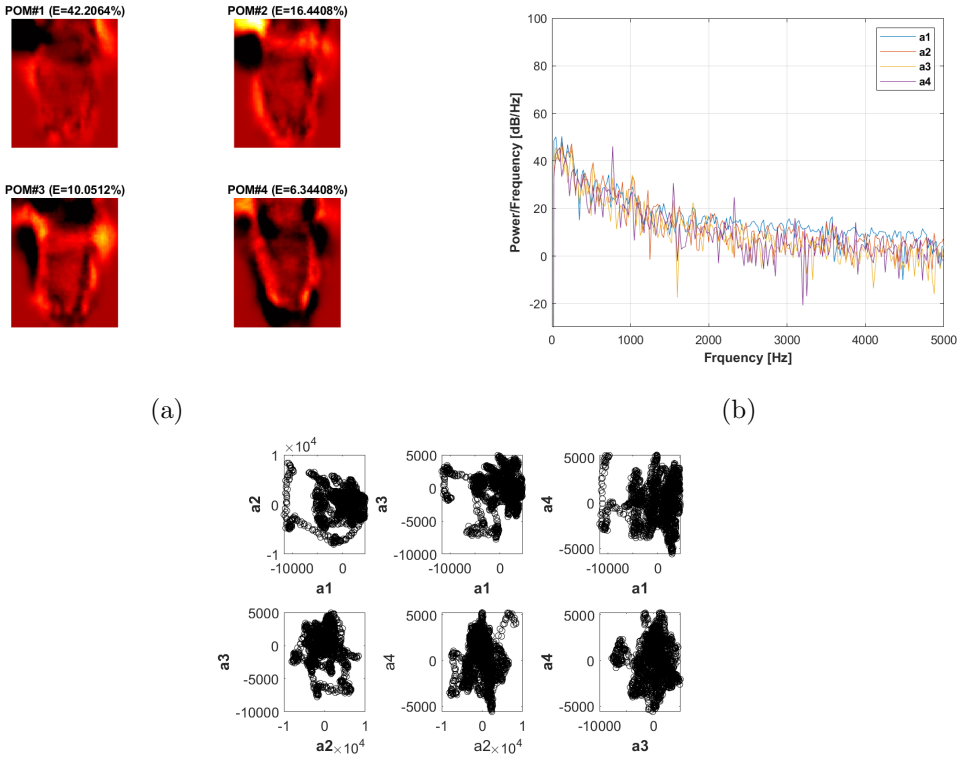

Figure C.17: **Single Jet**: POD analysis results for 775 Hz excitation at an amplitude of $p'_{max} = 550$ Pa at a PAN. Results include (a) the first four POD mode structures with associated percentage of energetic content, and where the color denotes strength of the mode scaled by its own norm, (b) the power spectral density associated with the four POD modes, and (c) sample plots of the POD mode coefficients against one another for the first four modes.

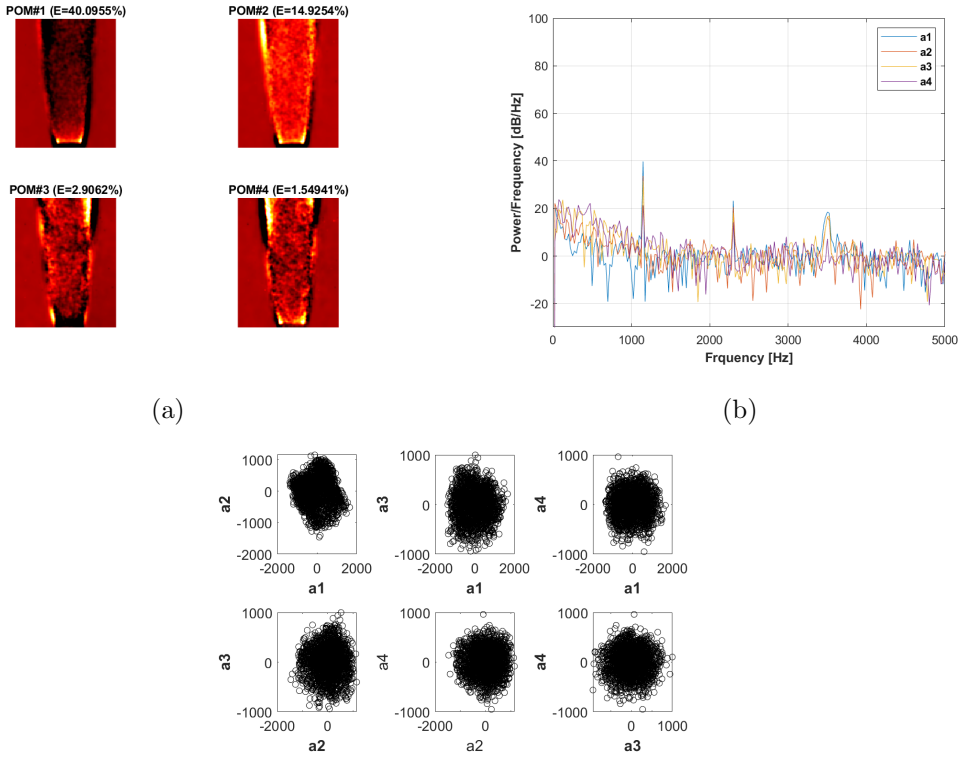

(a) (b)

(c)

Figure C.18: **Single Jet**: POD analysis results for 1150 Hz excitation at an amplitude of $p'_{max} =$ 300 Pa at a PAN. Results include (a) the first four POD mode structures with associated percentage of energetic content, and where the color denotes strength of the mode scaled by its own norm, (b) the power spectral density associated with the four POD modes, and (c) sample plots of the POD mode coefficients against one another for the first four modes.

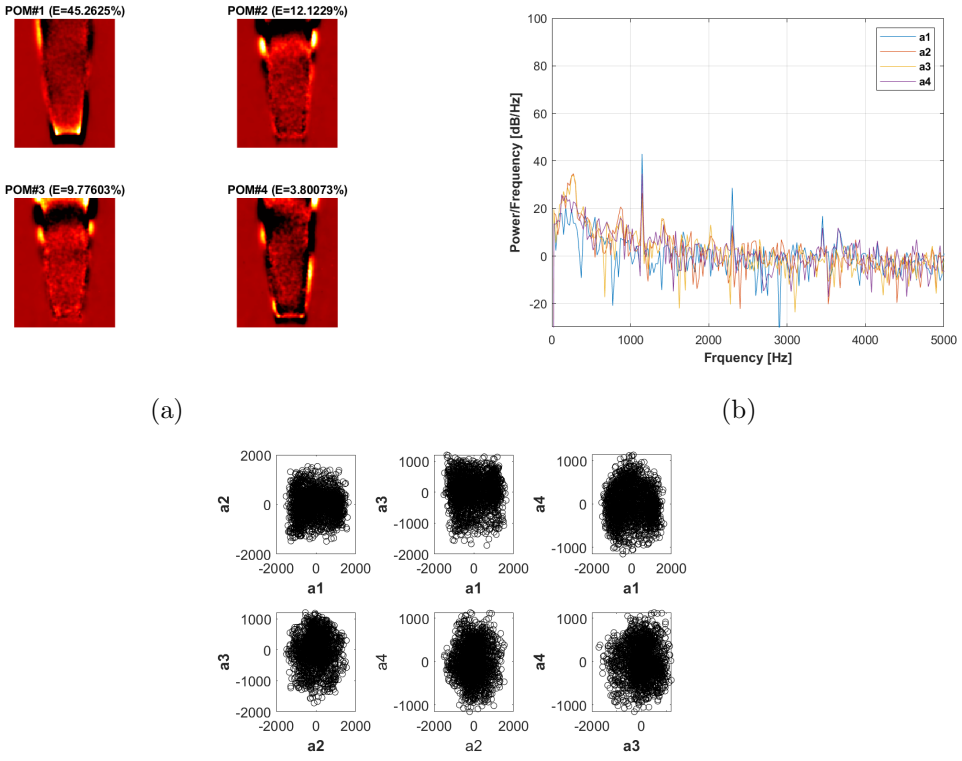

(a) (b)

(c)

Figure C.19: **Single Jet**: POD analysis results for 1150 Hz excitation at an amplitude of $p'_{max} =$ 650 Pa at a PAN. Results include (a) the first four POD mode structures with associated percentage of energetic content, and where the color denotes strength of the mode scaled by its own norm, (b) the power spectral density associated with the four POD modes, and (c) sample plots of the POD mode coefficients against one another for the first four modes.

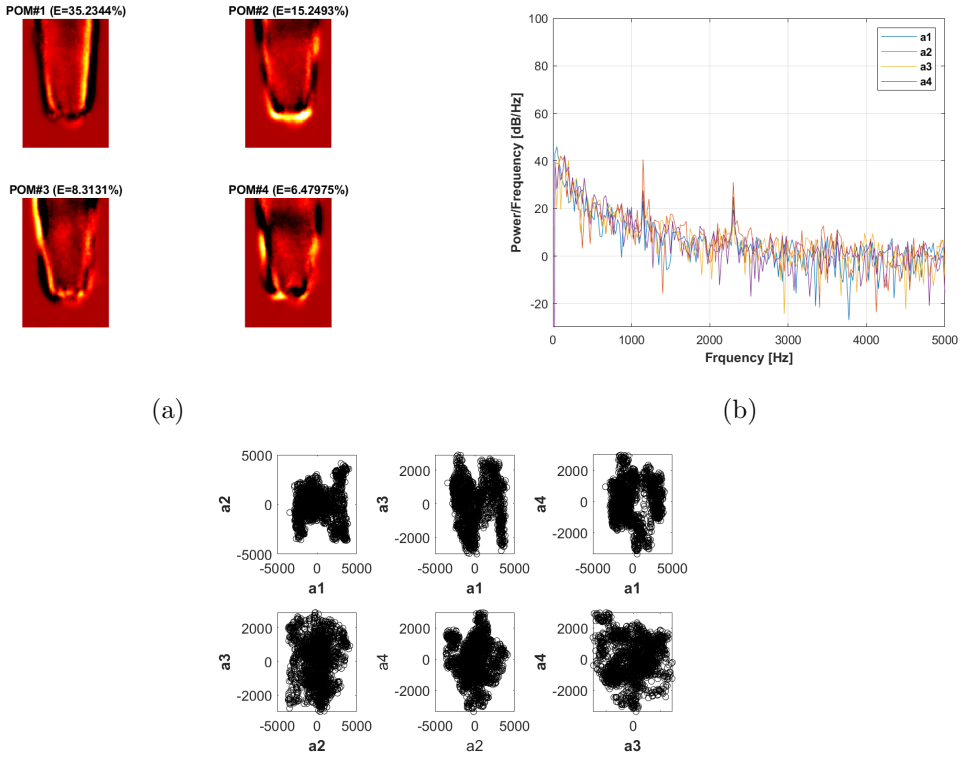

(a) (b)

(c)

Figure C.20: **Single Jet**: POD analysis results for 1150 Hz excitation at an amplitude of $p'_{max} =$ 900 Pa at a PAN. Results include (a) the first four POD mode structures with associated percentage of energetic content, and where the color denotes strength of the mode scaled by its own norm, (b) the power spectral density associated with the four POD modes, and (c) sample plots of the POD mode coefficients against one another for the first four modes.

C.2 Additional Coaxial Jet Results

C.2.1 PN

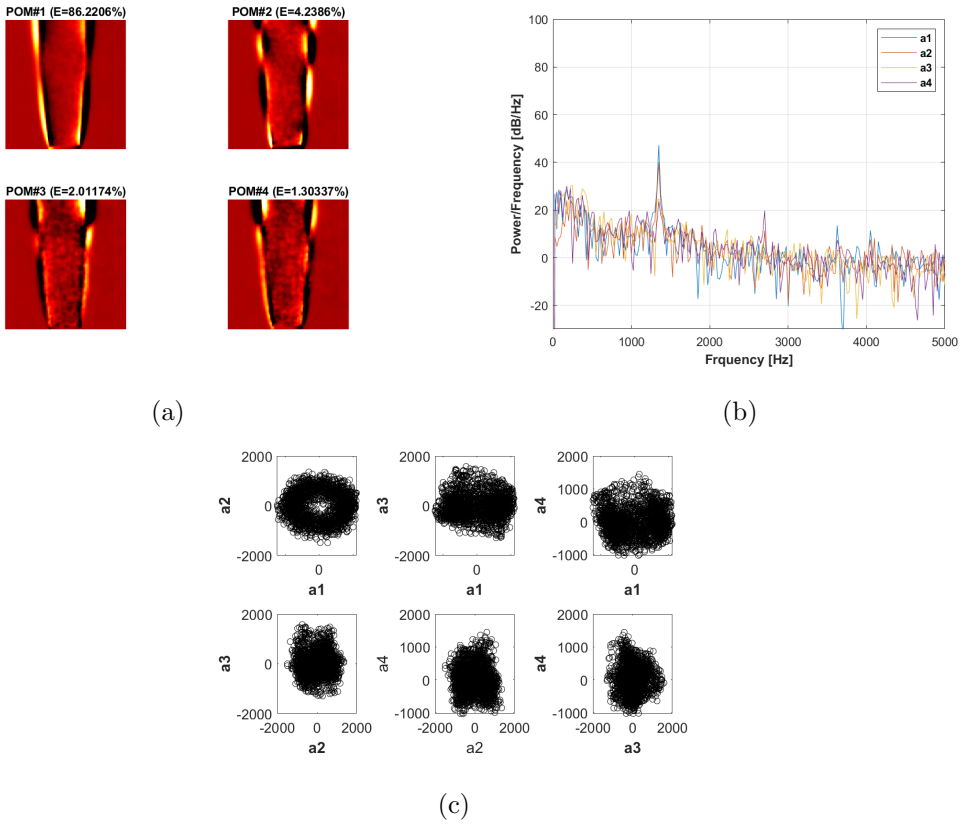

(a) (b)

(c)

Figure C.21: **Coaxial jet (R = 0.17)**: POD analysis results for 1348 Hz excitation at an amplitude of $u' = 1.2$ m/s at a PN. Results include (a) the first four POD mode structures with associated percentage of energetic content, and where the color denotes strength of the mode scaled by its own norm, (b) the power spectral density associated with the first POD mode, and (c) sample plots of the POD mode coefficients against one another for the first four modes.

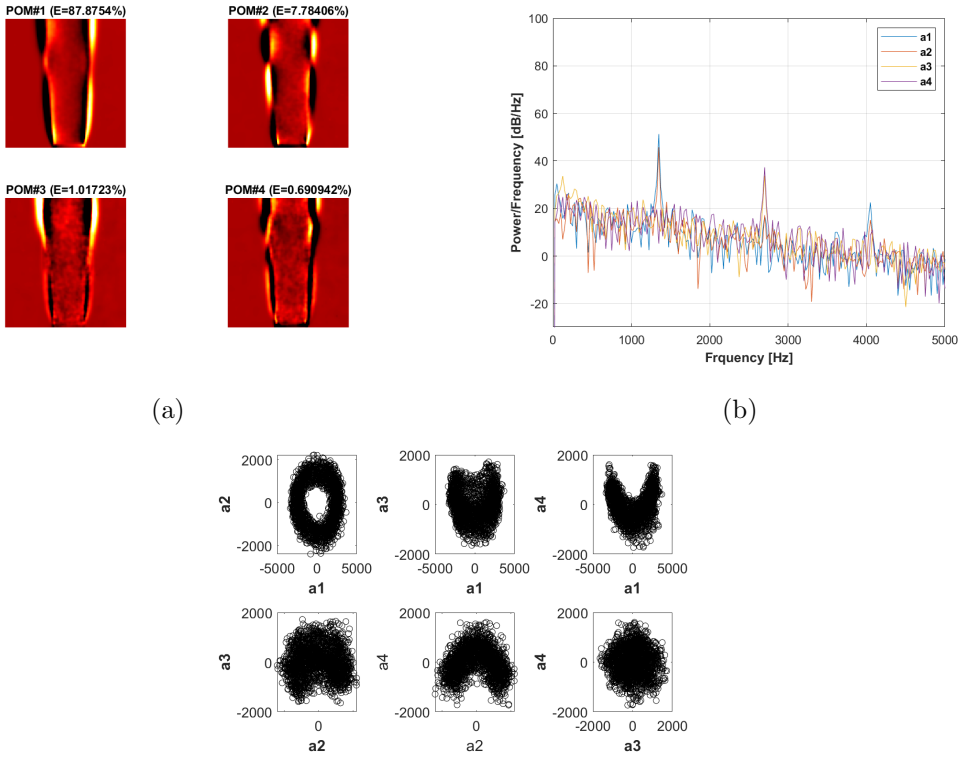

(a) (b)

(c)

Figure C.22: **Coaxial jet (R = 0.17)**: POD analysis results for 1348 Hz excitation at an amplitude of $u' = 1.6$ m/s at a PN. Results include (a) the first four POD mode structures with associated percentage of energetic content, and where the color denotes strength of the mode scaled by its own norm, (b) the power spectral density associated with the first POD mode, and (c) sample plots of the POD mode coefficients against one another for the first four modes.

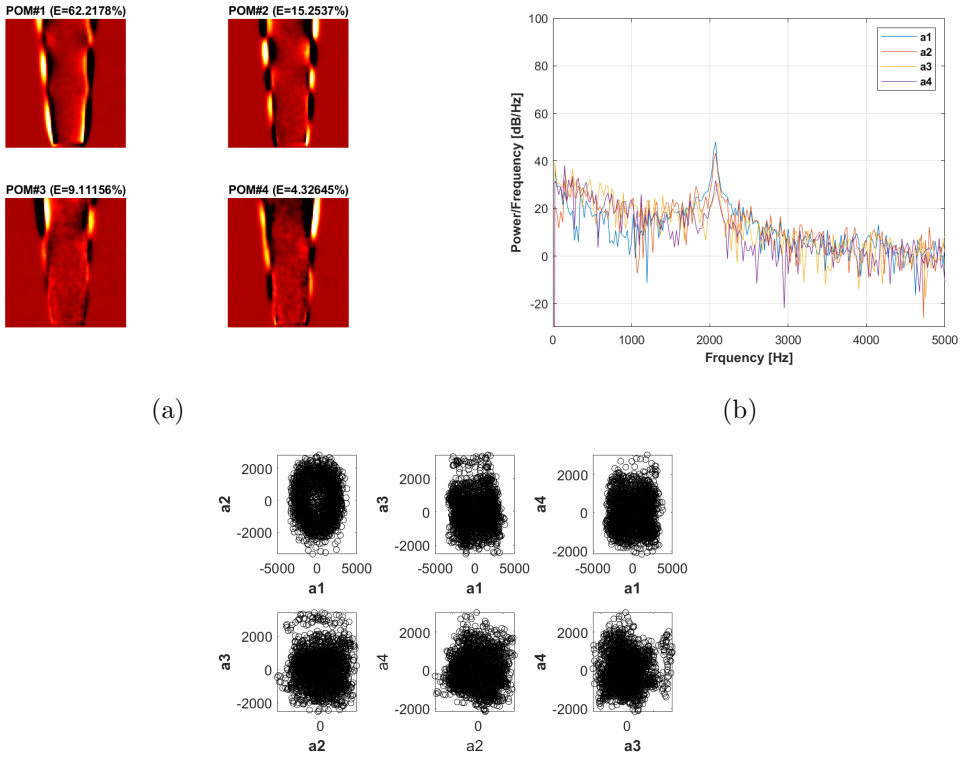

(a) (b)

(c)

Figure C.23: **Coaxial jet (R = 0.17)**: POD analysis results for 2065 Hz excitation at an amplitude of $u' = 1.2$ m/s at a PN. Results include (a) the first four POD mode structures with associated percentage of energetic content, and where the color denotes strength of the mode scaled by its own norm, (b) the power spectral density associated with the first POD mode, and (c) sample plots of the POD mode coefficients against one another for the first four modes.

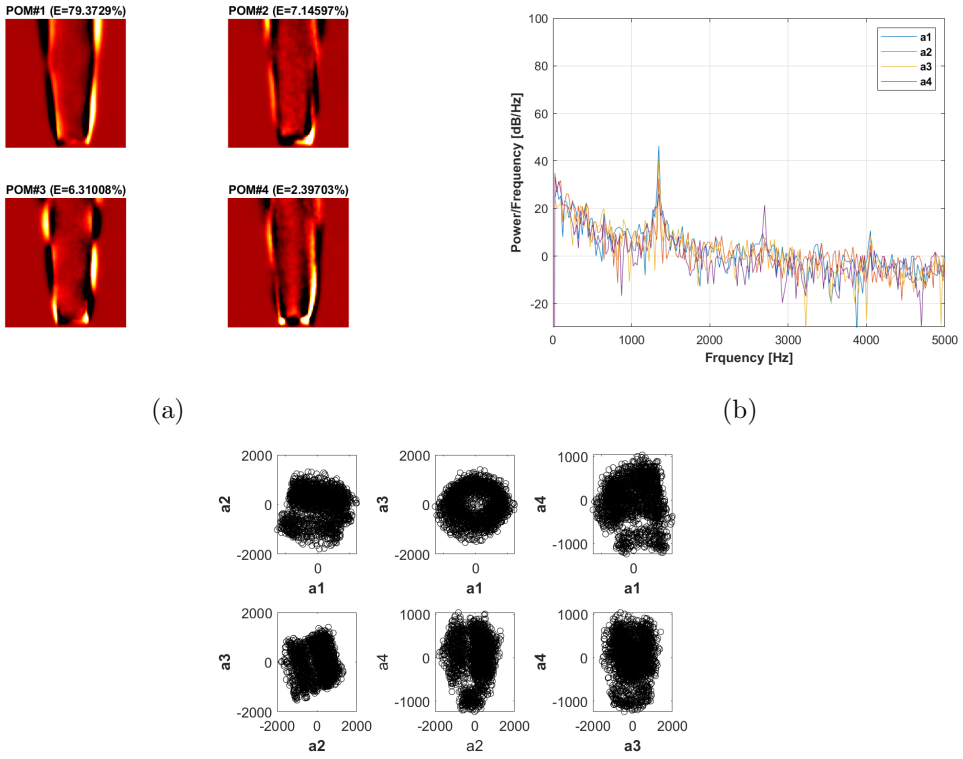

(a) (b)

(c)

Figure C.24: **Coaxial jet (R = 0.3)**: POD analysis results for 1348 Hz excitation at an amplitude of $u' = 1.2$ m/s at a PN. Results include (a) the first four POD mode structures with associated percentage of energetic content, and where the color denotes strength of the mode scaled by its own norm, (b) the power spectral density associated with the first POD mode, and (c) sample plots of the POD mode coefficients against one another for the first four modes.

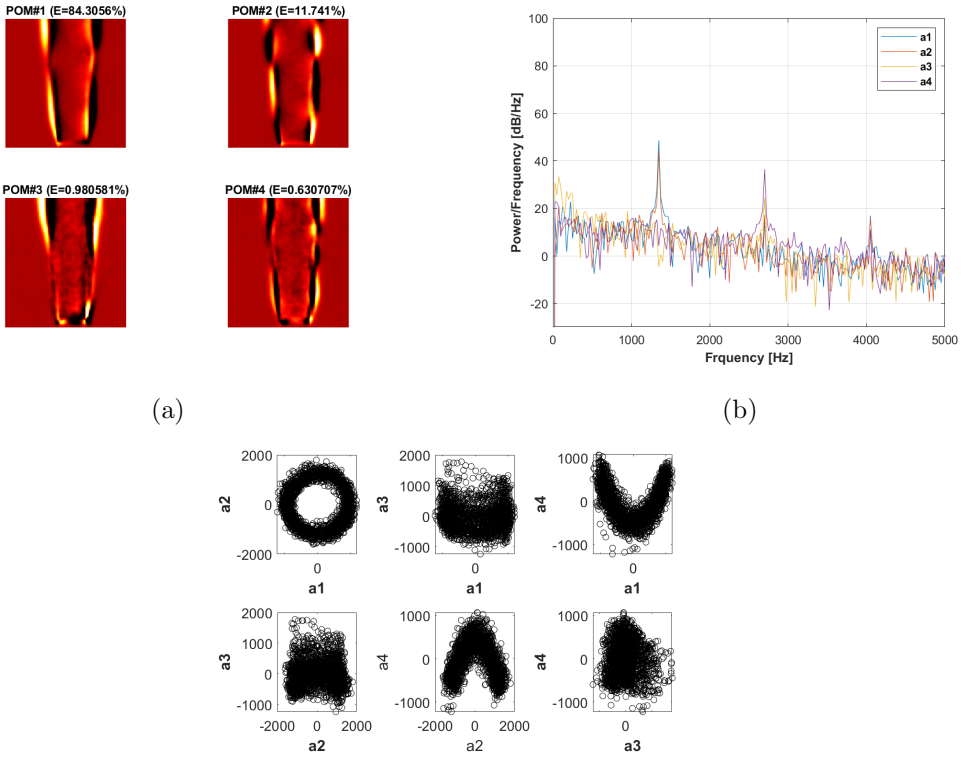

(a) (b)

(c)

Figure C.25: **Coaxial jet (R = 0.3)**: POD analysis results for 1348 Hz excitation at an amplitude of $u' = 1.6$ m/s at a PN. Results include (a) the first four POD mode structures with associated percentage of energetic content, and where the color denotes strength of the mode scaled by its own norm, (b) the power spectral density associated with the first POD mode, and (c) sample plots of the POD mode coefficients against one another for the first four modes.

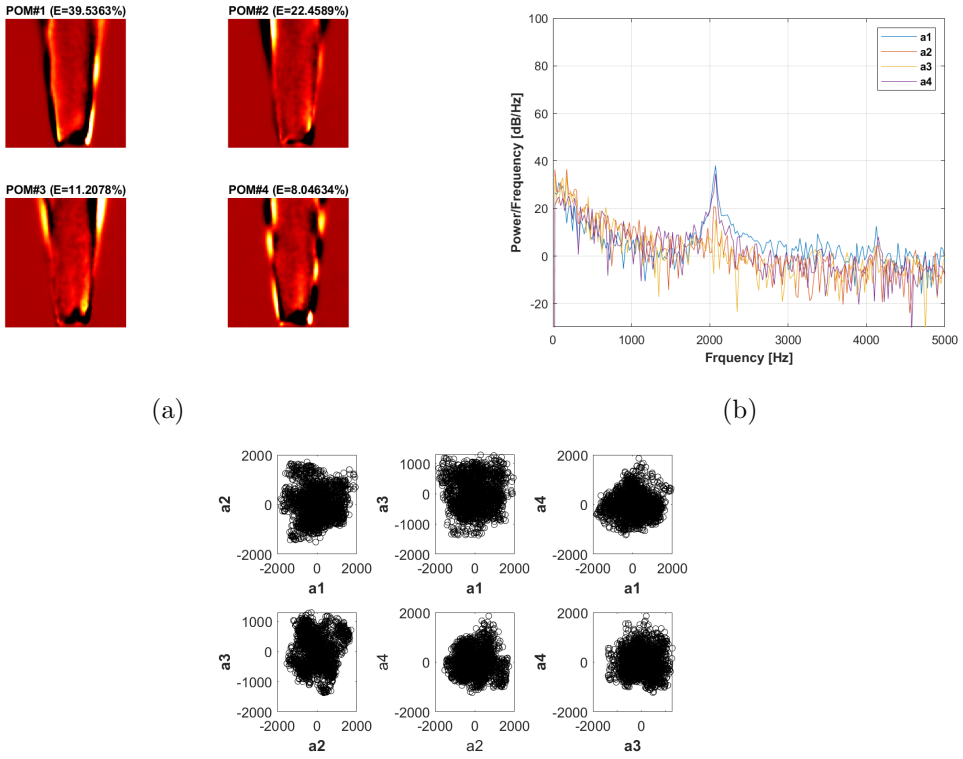

(a) (b)

(c)

Figure C.26: **Coaxial jet (R = 0.3)**: POD analysis results for 2065 Hz excitation at an amplitude of $u' = 1.2$ m/s at a PN. Results include (a) the first four POD mode structures with associated percentage of energetic content, and where the color denotes strength of the mode scaled by its own norm, (b) the power spectral density associated with the first POD mode, and (c) sample plots of the POD mode coefficients against one another for the first four modes.

C.2.2 PAN

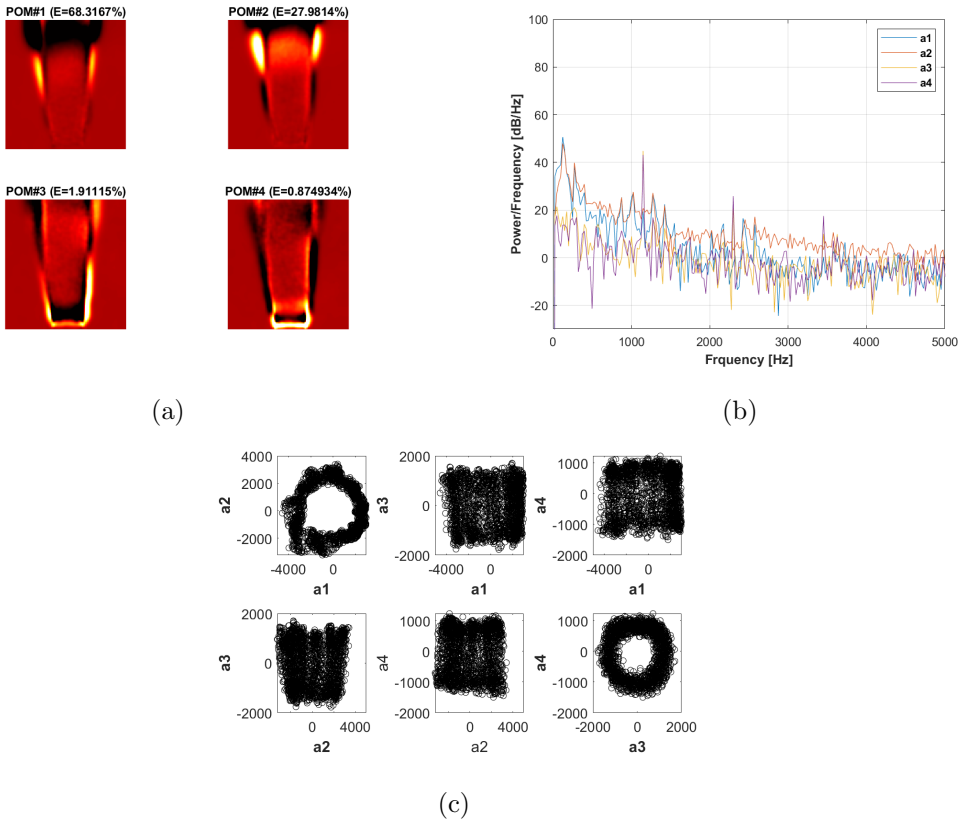

Figure C.27: **Coaxial jet (R = 0.05)**: POD analysis results for 1150 Hz excitation at an amplitude of $p' = 200$ Pa at a PAN. Results include (a) the first four POD mode structures with associated percentage of energetic content, and where the color denotes strength of the mode scaled by its own norm, (b) the power spectral density associated with the first POD mode, and (c) sample plots of the POD mode coefficients against one another for the first four modes.

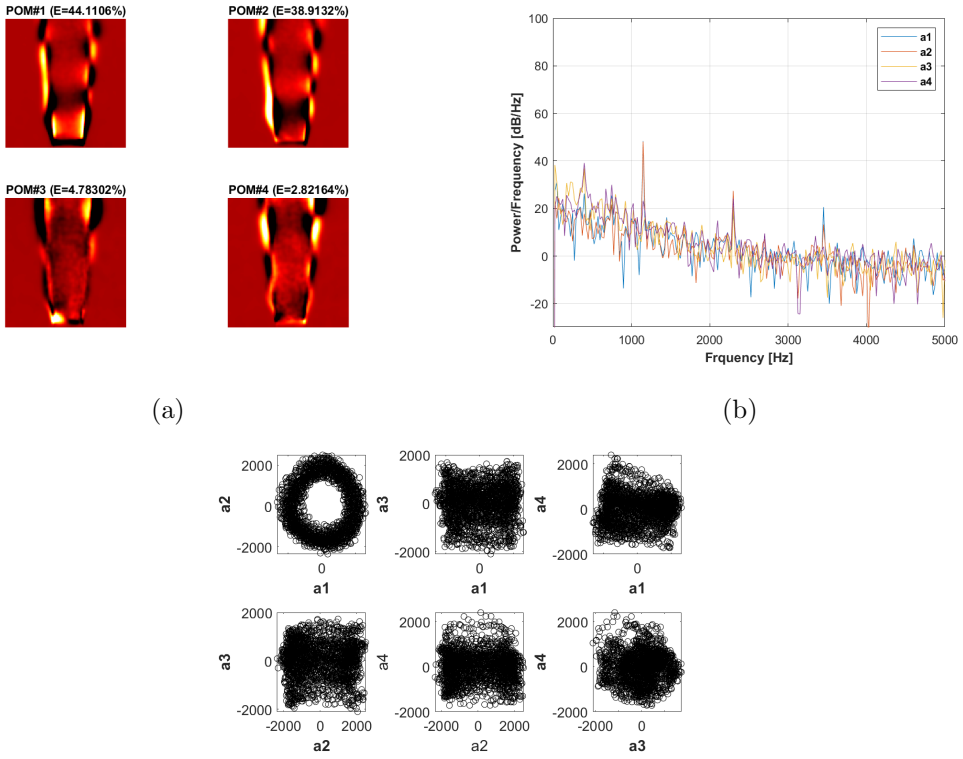

(a) (b)

(c)

Figure C.28: **Coaxial jet (R = 0.3)**: POD analysis results for 1150 Hz excitation at an amplitude of $p' = 250$ Pa at a PAN. Results include (a) the first four POD mode structures with associated percentage of energetic content, and where the color denotes strength of the mode scaled by its own norm, (b) the power spectral density associated with the first POD mode, and (c) sample plots of the POD mode coefficients against one another for the first four modes.

Bibliography

[1] H. S. Sim, M. A. Plascencia, A. Vargas, and A. R. Karagozian. Acoustically forced droplet combustion of liquid fuel with reactive aluminum nanoparticulates. *Combustion Science and Technology*, 192(5):761–785, 2019.

[2] D. T. Harrje and Fr. H. Reardon. Liquid propellant rocket combustion instability. Technical report, National Aeronautics and Space Administration, Washington D.C., 1972.

[3] J. C. Oefelein and Y. Vigor. Comprehensive review of liquid-propellant combustion instabilities in F-1 engines. *Journal of Propulsion and Power*, 9(5):657–677, 1993.

[4] F. E. C. Culick and V. Yang. Overview of combustion instabilities in liquid propellant rocket engines. *Progress in Astronautics and Aeronautics*, 169:3–38, 1995.

[5] T. C. Lieuwen and V. Yang. Combustion instabilities in gas turbine engines: operational experience, fundamental mechanisms, and modeling. *Progress in Astronautics and Aeronautics*, 210, 2006.

[6] G. P. Sutton and O. Biblarz. *Rocket Propulsion Elements (9th Edition)*. John Wiley and Sons, 2017.

[7] N. A. Chigier. The atomization and burning of liquid fuel sprays. *Progress in Energy and Combustion Science*, 2(2):97–114, 1976.

[8] I. Glassman and R. A. Yetter. *Combustion (Fifth Edition)*. Elsevier Inc., 2008.

[9] W. Mayer and H. Tamura. Propellant injection in a liquid oxygen/gaseous hydrogen rocket engine. *Journal of Propulsion and Power*, 12(6):1137–1147, 1996.

[10] W. A. Sirignano. Fuel droplet vaporization and spray combustion theory. *Progress in Energy and Combustion Science*, 9(4):291–322, 1983.

[11] S.R. Turns. *An Introduction to Combustion: Concepts and Applications*. McGraw-Hill, 1996.

[12] S.D. Heister, W.E. Anderson, T.L. Pourpoint, and R.J. Cassady. *Rocket Propulsion*. Cambridge Aerospace Series. Cambridge University Press, 2019.

[13] G. A. E. Godsave. Studies of the combustion of drops in a fuel spray-the burning of single drops of fuel. *Symposium (International) on Combustion*, 4(1):818–830, 1953.

[14] D. B. Spalding. The combustion of liquid fuels. *Symposium (International) on Combustion*, pages 847–864, 1953.

[15] G. M. Faeth. Current status of droplet and liquid combustion. *Progress in Energy and Combustion Science*, 1977.

[16] W. A. Sirignano. *Fluid dynamics and transport of droplets and sprays*. Cambridge University Press, 1999.

[17] C. K. Law. *Combustion Physics*. Cambridge University Press, 2010.

[18] C. K. Law. Recent advances in droplet vaporization and combustion. *Progress in Energy and Combustion Science*, 1982.

[19] C. K. Law and G. M. Faeth. Opportunities and challenges of combustion in microgravity. *Progress in Energy and Combustion Science*, 20(1):65–113, 1994.

[20] A. J. Marchese, F. L. Dryer, V. Nayagam, and R. O. Colantonio. Hydroxyl radical chemiluminescence imaging and the structure of microgravity droplet flames. *Symposium (International) on Combustion*, 26(1):1219–1226, 1996.

[21] M. Goldsmith and S. S. Penner. On the burning of single drops of fuel in an oxidizing atmosphere. *Journal of Jet Propulsion*, 24(4):245–251, 1954.

[22] He. Wise, J. Lorell, and B. J. Wood. The effects of chemical and physical parameters on the burning rate of a liquid droplet. In *Symposium (International) on Combustion*, pages 132–141, 1955.

[23] P. M. Struk, M. Ackerman, V. Nayagam, and D. L. Dietrich. On calculating burning rates during fibre supported droplet combustion. *Microgravity Science and Technology*, 11, 1998.

[24] D. Sundaram, V. Yang, and R. A. Yetter. Metal-based nanoenergetic materials: synthesis, properties, and applications. *Progress in Energy and Combustion Science*, 61:293–365, 2017.

[25] R. A. Yetter, G. A. Risha, and S. F. Son. Metal particle combustion and nanotechnology. *Proceedings of the Combustion Institute*, 32:1819–1838, 2009.

[26] M. Pfeil, S. Rosen, Y. Yu, W. Anderson, and S. Son. Effects of nanoaluminum on droplet combustion and combustion instabilities in a single element rocket combustor. *46th AIAA-ASME-SAE-ASEE Joint Propulsion Conference Exhibit*, 2010.

[27] Y. Gan and L. Qiao. Combustion characteristics of fuel droplets with addition of nano and micron-sized aluminum particles. *Combustion and Flame*, 158:354–368, 2011.

[28] S. Tanvir and L. Qiao. Effect of addition of energetic nanoparticles on droplet-burning rate of liquid fuels. *Journal of Propulsion and Power*, 31(1):408–415, 2015.

[29] I. Javed, S. W. Baek, and K. Waheed. Autoignition and combustion characteristics of heptane droplets with the addition of aluminium nanoparticles at elevated temperatures. *Combustion and Flame*, 162(1):191–206, 2015.

[30] I. Javed, S. W. Baek, and K. Waheed. Autoignition and combustion characteristics of kerosene droplets with dilute concentrations of aluminum nanoparticles at elevated temperatures. *Combustion and Flame*, 162(3):774–787, 2015.

[31] P. M. Guerieri, J. B. DeLisio, and M. R. Zachariah. Nanoaluminum/nitrocellulose microparticle additive for burn enhancement of liquid fuels. *Combustion and Flame*, 176:220–228, 2017.

[32] H. S. Sim, M. A. Plascencia, A. Vargas, J. W. Bennewitz, O. I. Smith, and A. R. Karagozian. Effects of inert and energetic nanoparticles on burning liquid ethanol droplets. *Combustion Science and Technology*, 191(7):1079–1100, 2019.

[33] J. W. Bennewitz, A. Badakhshan, and D. G. Talley. Combustion characteristics of suspended hydrocarbon fuel droplets with various nanoenergetic additives. *Combustion Science and Technology*, pages 1–26, 2020.

[34] Y. Gan, Y. S. Lim, and L. Qiao. Combustion of nanofluid fuels with the addition of boron and iron particles at dilute and dense concentrations. *Combustion and Flame*, 159:1732–1740, 2012.

[35] M. N. Bello, M. L. Pantoya, K. Kappagantula, W. S. Wang, S. A. Vanapalli, D. J. Irvin, and L. M. Wood. Reaction dynamics of rocket propellant with magnesium oxide nanoparticles. *Energy and Fuels*, 2015.

[36] M. Ghamari and A. Ratner. Combustion characteristics of colloidal droplets of jet fuel and carbon based nanoparticles. *Fuel*, 188:182–189, 2017.

[37] J. B. Ooi, H. M. Ismail, V. Swamy, X. Wang, A. K. Swain, and J. R. Rajanren. Graphite oxide nanoparticle as a diesel fuel additive for cleaner emissions and lower fuel consumption. *Energy and Fuels*, 30:1341–1353, 2016.

[38] S. Tanvir and L. Qiao. Droplet burning rate enhancement of ethanol with the addition of graphite nanoparticles: Influence of radiation absorption. *Combustion and Flame*, 166:34–44, 2016.

[39] A. Miglani and S. Basu. Coupled mechanisms of precipitation and atomization in burning nanofluid fuel droplets. *Scientific Reports*, 5:1–9, 2015a.

[40] A. Miglani and S. Basu. Effect of particle concentration on shape deformation and secondary atomization characteristics of a burning nanotitania dispersion droplet. *Journal of Heat Transfer*, 137:1–8, 2015b.

[41] M. A. Pfeil, L. J. Groven, R. P. Lucht, and S. F. Son. Effects of ammonia borane on the combustion of an ethanol droplet at atmospheric pressure. *Combustion and Flame*, 160(10):2194–2203, 2013.

[42] S. Basu and A. Miglani. Combustion and heat transfer characteristics of nanofluid fuel droplets: A short review. *International Journal of Heat and Mass Transfer*, 96:482–503, 2016.

[43] A. Miglani, S. Basu, and R. Kumar. Suppression of instabilities in burning droplets using preferential acoustic perturbations. *Combustion and Flame*, 161(12):3181–3190, 2014.

[44] K. Pandey, K. Chattopadhyay, and S. Basu. Combustion dynamics of low vapour pressure nanofuel droplets. *Physics of Fluids*, 29(7), 2017.

[45] M. A. Pfeil, S. F. Son, and W. E. Anderson. Influence of ammonia borane on the stability of a liquid rocket combustor. *Journal of Propulsion and Power*, 30(2):290–297, 2014.

[46] L. Rayleigh. The explanation of certain acoustical phenomena. *Nature*, 18:319–321, 1878.

[47] A. Ghosh, Q. Diao, and K. H. Yu. Effect of flow parameters on the acoustic susceptibility of shear-coaxial flames. *Journal of Propulsion and Power*, 32(2):295–304, 2016.

[48] Q Diao, A Ghosh, and K.H. Yu. Acoustic stability of model injector flames using H2-CH4 fuel mixture. *44th AIAA/ASME/SAE/ASEE Joint Propulsion Conference Exhibit*, (July):1–15, 2008.

[49] H. S. Sim, A. Vargas, D. D. Ahn, and A. R. Karagozian. Laminar microjet diffusion flame response to transverse acoustic excitation. *Combustion Science and Technology*, 192(7):1292–1319, 2020.

[50] W. Pun, S. L. Palm, and F. E.C. Culick. Combustion dynamics of an acoustically forced flame. *Combustion Science and Technology*, 175(3):499–521, 2003.

[51] Ja. O'Connor and T. Lieuwen. Disturbance field characteristics of a transversely excited burner. *Combustion Science and Technology*, 183(5):427–443, 2011.

[52] J. O'Connor and T. Lieuwen. Recirculation zone dynamics of a transversely excited swirl flow and flame. *Physics of Fluids*, 24(7), 2012.

[53] Ja. O'Connor. Visualization of shear layer dynamics in a transversely forced flow and flame. *Journal of Propulsion and Power*, 31(4):1127–1136, 2015.

[54] A. Saurabh and C. O. Paschereit. Dynamics of premixed swirl flames under the influence of transverse acoustic fluctuations. *Combustion and Flame*, 182:298–312, 2017.

[55] M. P. Juniper, L. K. B. Li, and J. W. Nichols. Forcing of self-excited round jet diffusion flames. *Proceedings of the Combustion Institute*, 32 I(1):1191–1198, 2009.

[56] A. M. A. Rocha, J. A. Carvalho, and P. T. Lacava. Gas concentration and temperature in acoustically excited Delft turbulent jet flames. *Fuel*, 87(15-16):3433–3444, nov 2008.

[57] Y. Ch. Chao and J. Ming-Shan. Behavior of the lifted jet flame under acoustic excitation. *Symposium (International) on Combustion*, 24(1):333–340, 1992.

[58] D. Demare and F. Baillot. Acoustic enhancement of combustion in lifted nonpremixed jet flames. *Combustion and Flame*, 139(4):312–328, 2004.

[59] L. Zheng, S. Ji, and Y. Zhang. Lifted and reattached behaviour of laminar premixed flame under external acoustic excitation. *Experimental Thermal and Fluid Science*, 98(1):683–692, 2018.

[60] S. Dattarajan, A. Lutomirski, R. Lobbia, O. I. Smith, and A. R. Karagozian. Acoustic excitation of droplet combustion in microgravity and normal gravity. *Combustion and Flame*, 144(1):299–317, 2006.

[61] C. I. Sevilla-Esparza, J. L. Wegener, S. Teshome, J. I. Rodriguez, O. I. Smith, and A. R. Karagozian. Droplet combustion in the presence of acoustic excitation. *Combustion and Flame*, 2014.

[62] J. W. Bennewitz, D. Valentini, M. A. Plascencia, A. Vargas, H. S. Sim, B. Lopez, O. I. Smith, and A. R. Karagozian. Periodic partial extinction in acoustically coupled fuel droplet combustion. *Combustion and Flame*, 189:46–61, 2017.

[63] S. Dattarajan. *Acoustic excitation of droplet combustion in microgravity and normal gravity*. PhD thesis, University of California, Los Angeles, 2004.

[64] J. I. Rodriguez. *Acoustic excitation of liquid fuel droplets and coaxial jets*. PhD thesis, University of California, Los Angeles, 2009.

[65] T. Sophonias. *Droplet combustion and non-reactive shear-coaxial jets with transverse acoustic excitation*. PhD thesis, University of California, Los Angeles, 2012.

[66] J. L. Wegener. *Multi-phase combustion and transport processes under the influence of acoustic excitation*. PhD thesis, University of California, Los Angeles, 2014.

[67] C. I. Sevilla-Esparza. *Oscillatory flame response in acoustically coupled fuel droplet combustion*. M.S. Thesis, University of California, Los Angeles, 2013.

[68] H. S. Sim, M. A. Plascencia, A. Vargas, J. W. Bennewitz, and A. R. Karagozian. Effects of aluminum nanoparticle additives on liquid fuel droplet combustion with and

without acoustic excitation. In *10th U.S. National Combustion Meeting*, pages 1–6, 2017.

[69] B. Chehroudi and D. W. Davis. Shear-coaxial jets from a rocket-like injector in a transverse acoustic field at high pressure. In *44th AIAA Aerospace Sciences Meeting and Exhibit*, 2006.

[70] I. A. Leyva, B. Chehroudi, and D. G. Talley. Dark core analysis of coaxial injectors at sub-, near-, and supercritical pressures in a transverse acoustic field. *Collection of Technical Papers - 43rd AIAA/ASME/SAE/ASEE Joint Propulsion Conference*, 5(July):4342–4359, 2007.

[71] I. A. Leyva, J. I. Rodriguez, B. Chehroudi, and D. Talley. Preliminary results on coaxial jet spread angles and the effects of variable phase transverse acoustic fields. *46th AIAA Aerospace Sciences Meeting and Exhibit*, (January):1–15, 2008.

[72] J. I. Rodriguez, I. A. Leyva, B. Chehroudi, and D. G. Talley. Results on subcritical one-phase coaxial jet spread angles and subcritical to supercritical acoustically-forced coaxial jet dark core lengths. *44th AIAA/ASME/SAE/ASEE Joint Propulsion Conference and Exhibit*, (July):1–12, 2008.

[73] J. Wegener, D. J. Forliti, I. A. Leyva, and D. G. Talley. Receptivity of a cryogenic coaxial liquid jet to acoustic disturbances. In *26th ILASS Americas*, Dearborn, MI, 2014.

[74] D. J. Forliti, A. Badakhshan, J. Wegener, I. A. Leyva, and D. G. Talley. The response of cryogenic h2/o2 coaxial jet flames to acoustic disturbances. In *53rd AIAA Aerospace Sciences Meeting*, number January, pages 1–13, 2015.

[75] M. Roa, J. W. Bennewitz, S. A. Schumaker, and D. G. Talley. A study of acoustic forcing on gas-centered swirl-coaxial reacting flows. *AIAA SciTech Forum - 55th AIAA Aerospace Sciences Meeting*, (January):1–16, 2017.

[76] M. Roa and D. G. Talley. Wave dynamic mechanisms in coaxial hydrogen/liquid-oxygen jet flames. *Journal of Propulsion and Power*, 35(2):369–381, 2019.

[77] M. Roa and D. G. Talley. Transverse acoustic forcing of gaseous hydrogen/liquid oxygen turbulent shear coaxial flames. *Journal of Propulsion and Power*, pages 1–15, 2020.

[78] D. Valentini. *Modelling and testing of chemical propulsion rocket subsystems.* PhD thesis, University of Pisa, 2016.

[79] G. Huelsz and F. López-Alquicira. Hot-wire anemometry in acoustic waves. *Experiments in Fluids*, 30(3):283–285, 2001.

[80] A. Gaydon. *The Spectroscopy of Flames.* Chapman and Hall, London, England, 1st edition, 1957.

[81] J. Diederichsen and R.D. Gould. Combustion instability: radiation from premixed flames of variable burning velocity. *Combustion and Flame*, 9(1):25–31, 1965.

[82] H. Anders, M. Christensen, B. Johansson, A. Franke, M. Richter, and M. Alden. A study of the homogeneous charge compression ignition combustion process by chemiluminescence imaging. *SAE Technical Paper 1999-01-3680*, 1999.

[83] C.J. Lawn. Distributions of instantaneous heat release by the cross-correlation of chemiluminescent emissions. *Combustion and Flame*, 123(1):227–240, 2000.

[84] L.C. Haber, U. Vandsburger, W.R. Saunders, and V.K. Khanna. An experimental examination of the relationship between chemiluminescent light emissions and heat-release rate under non-adiabatic conditions. Technical report, DTIC Document, 2001.

[85] B.H. Timmerman and P.J. Bryanston-Cross. Optical investigation of heat release and nox production in combustion. *Journal of Physics Conference series*, 85, 2007.

[86] S. Sardeshmukh, M. Bedard, and W. Anderson. The use of oh* and ch* as heat release markers in combustion dynamics. *International Journal of Spray and Combustion Dynamics*, 9(4):409–423, 2017.

[87] C.K. Law and F.A. Williams. Kinetics and convection in the combustion of alkane droplets. *Combustion and Flame*, 19(3):393–405, 1972.

[88] C. H. Li and G. P. Peterson. Experimental investigation of temperature and volume fraction variations on the effective thermal conductivity of nanoparticle suspensions (nanofluids). *Journal of Applied Physics*, 99(8), 2006.

[89] S. I. Abu-Eishah. Correlations for the thermal conductivity of metals as a function of temperature. *International Journal of Thermophysics*, 22(6):1855–1868, 2001.

[90] E. H. Buyco and F. E. Davis. Specific heat of aluminum from zero to its melting temperature and beyond equation for representation of the specific heat of solids. *Journal of Chemical and Engineering Data*, 15(4):518–523, 1970.

[91] J. Gmehling, J.and Rarey, , and J Menke. Dortmund Data Bank. *Oldenbg*, pages 119–129, 2008.

[92] B. S. Hemingway. Quartz; heat capacities from 340 to 1000 K and revised values for the thermodynamic properties. *American Mineralogist*, 72(3-4):273–279, 04 1987.

[93] P. J. Linstrom and W. G Mallard. NIST Chemistry WebBook, NIST Standard Reference Database Number 69. 2011.

[94] H. E. Seemann. The thermal and electrical conductivity of fused quartz as a function of temperature. *PHYSICAL REVIEW*, 31:119–129, 1928.

[95] J. G. Speight. *Lange's Handbook Of Chemistry*. McGraw-Hill, New York, 16th edition, 2005.

[96] B. J. McBride and S. Gordon. Computer program for calculation of complex chemical equilibrium compositions and applications ii. users manual and program description. *NASA RP 1311*, 1996.

[97] C. K. Law, S. H. Chung, and N. Srinivasan. Gas-phase quasi-steadiness and fuel vapor accumulation effects in droplet burning. *Combustion and Flame*, 38:173–198, 1980.

[98] J. O'Connor. *Response of a swirl-stabilized flame to transverse acoustic excitation* . PhD thesis, Georgia Institute of Technology, 2012.

[99] L. Kinsler, A. Frey, A. Coppens, and J. Sanders. *Fundamentals of Acoustics*. Wiley, 4 edition, 1999.

[100] B.R. Munson, A.P. Rothmayer, T.H. Okiishi, and W.W. Huebsch. *Fundamental Fluid Mechanics*. Wiley, 5 edition, 2005.

[101] J.L. Lumley. Coherent structures in turbulence. In Richard E. M., editor, *Transition and Turbulence*, pages 215–242. Academic Press, 1981.

[102] G. Berkooz, P. Holmes, and J. L. Lumley. The proper orthogonal, decomposition in the analysis of turbulent flows. *Annual Review of Fluid Mechanics*, 25:539–575, 1993.

[103] L. Sirovich. Turbulence and the dynamics of coherent structures. *Quarterly of Applied Mathematics*, XLV(3):561–571, 1987.

[104] K. E. Meyer, J. M. Pedersen, and O. Ozcan. A turbulent jet in crossflow analysed with proper orthogonal decomposition. *Journal of Fluid Mechanics*, 583:199–227, 2007.

[105] Flat-field correction. http://www.princetoninstruments.com/cms/index.php/ccd-primer/152-flat-field-correction. Accessed: 2021-5-01.

[106] J. R. Taylor. An introduction to error analysis: The study of uncertainties in physical measurements. *University Science Books*, (2):57–58, 1982.

[107] Sophonias T. *Droplet combustion and non-reactive shear-coaxial jets with transverse acoustic excitation*. PhD thesis, University of California, Los Angeles, 2012.

[108] T. C. Rathsack, B. R. Bigler, J. W. Bennewitz, S. A. Danczyk, and W. A. Hargus. Laboratory flow measurement in rotating detonation rocket engines. *AIAA SciTech Forum*, (January):1–13, 2020.

[109] M.D.A. Lightfoot, S.A. Danczyk, J.M. Watts, and S.A. Schumaker. Accuracy and best practices for small-scale rocket engine testing. 2011.

[110] J. D. Anderson. *Modern Compressible Flow With Historical Perspective*. McGraw-Hill Publishing, 5 edition, 2003.

[111] National Institute of Standards and Technologyy. Thermophysical properties of fluid systems. 583, 2011.

[112] S.H. Starner and R.W. Bilger. Characteristics of a piloted diffusion flame designed for study of combustion turbulence interactions. *Combustion and Flame*, 61(1):29–38, 1985.

[113] M. J. Dunn, A. R. Masri, and R. W. Bilger. A new piloted premixed jet burner to study strong finite-rate chemistry effects. 151:46–60, 2007.

[114] S. Meares and A. R. Masri. A modified piloted burner for stabilizing turbulent flames of inhomogeneous mixtures. *Combustion and Flame*, 161(2):484–495, 2014.

[115] F.M. White. *Viscous Fluid Flow*. McGraw-Hill, 2006.

[116] L. Gevorkyan, T. Shoji, W. Y. Peng, and A. R. Karagozian. Influence of the velocity field on scalar transport in gaseous transverse jets. *Journal of Fluid Mechanics*, 834:173–219, 2018.

[117] A. F. Ghoniem, M. C. Soteriou, O. M. Knio, and B. Cetegen. Effect of steady and periodic strain on unsteady flamelet combustion. *Symposium (International) on Combustion*, 24(1):223–230, 1992. Twenty-Fourth Symposium on Combustion.

[118] F. N. Egolfopoulos and C. S. Campbell. Unsteady counterflowing strained diffusion flames: diffusion-limited frequency response. *Journal of Fluid Mechanics*, 318:1–29, 1996.

[119] T. Selerland and A. R. Karagozian. Ignition, burning and extinction of a strained fuel strip with complex kinetics. *Combustion Science and Technology*, 131(1-6):251–276, 1998.

[120] H. R. D. A. Quintanilha and L. S. D. B. Alves. On the existence of multiple self-excitation frequencies in the instability of interacting planar mixing layer and wake. *31st Congress of the International Council of the Aeronautical Sciences*, 31, 2018.

[121] T. Shoji, E. W. Harris, A. Besnard, S.G. Schein, and A. R. Karagozian. Transverse jet lock-in and quasiperiodicity. *Phys. Rev. Fluids*, 5:013901, Jan 2020.

[122] L. Crocco and S. Cheng. Theory of combustion instability in liquid propellant rocket motors. *Journal of Fluid Mechanics*, 2(1):100–104, 1957.

[123] S. Candel. Combustion instabilities coupled by pressure waves and their active control. *Symposium (International) on Combustion*, 24(1):1277–1296, 1992.

[124] S. Candel. Combustion dynamics and control: progress and challenges. *Proceedings of the Combustion Institute*, 29(1):1–28, 2002.

[125] Ann R. Karagozian. Acoustically coupled combustion of liquid fuel droplets. *Applied Mechanics Reviews*, 68(4):40801–40811, 2016.

[126] A. S H Kwan and N. W M Ko. The initial region of subsonic coaxial jets. *Journal of Fluid Mechanics*, 73(2):305–332, 1976.

[127] W.J.A Dahm, E.F Clifford, and G Tryggvason. Vortex structure and dynamics in the near field of a coaxial jet. *J. Fluid Mech.*, 241:371–402, 1992.

[128] N. Zong and V. Yang. A numerical study of high-pressure oxygen/methane mixing and combustion of a shear coaxial injector. *AIAA Aerospace Sciences Meeting and Exhibit*, 43(January):15, 2005.

[129] N. Okong'o, K. Harstand, and J. Bellan. Direct numerical simulations of o2/h2 temporal mixing layers under supercritical conditions. *AIAA Journal*, 40:914–926, 2002.

[130] G. Singla, P. Scouflaire, C. Rolon, and S. Candel. Planar laser-induced fluorescence of oh in high-pressure cryogenic lox/gh2 jet flames. *Combustion and Flame*, 144(1-2):151–169, 2006.

[131] M. Roa, D. Forliti, A. Badakhsahn, and D. G. Talley. Acoustically forced coaxial hydrogen / liquid oxygen jet flames. In *26th ILASS Americas*, Dearborn, MI, 2016.

[132] M. Roa and D. G. Talley. Vortex dynamic mechanisms in coaxial hydrogen/lox jet flames. *2018 AIAA Aerospace Sciences Meeting*, (January), 2018.